

**Multimetallic Supramolecular Complexes: Synthesis,
Characterization, Photophysical Studies and Applications in Solar
Energy Utilization and Photodynamic Therapy**

Ran Miao

Dissertation submitted to the Faculty of the
Virginia Polytechnic Institute and State University
in partial fulfillment of the requirements for the degree of

Doctor of Philosophy

in

Chemistry

Prof. Karen J. Brewer, Chair

Prof. Paul A. Deck

Prof. Brian E. Hanson

Prof. Larry T. Taylor

Prof. Gordon T. Yee

December 4, 2007

Blacksburg, VA

Keywords: multimetallic, supramolecular, ruthenium, osmium, platinum, DNA,
photodynamic therapy, charge separation, photocatalysis, hydrogen, solar energy conversion.

Multimetallic Supramolecular Complexes: Synthesis, Characterization, Photophysical Studies and Applications in Solar Energy Utilization and Photodynamic Therapy

Ran Miao

The goal of this research work is to develop an understanding of how ruthenium and osmium polyazine building blocks function when incorporated within mixed-metal, mixed-ligand supramolecular assemblies. The knowledge is further applied to couple reactive Pt metal center and design multifunctional supramolecules applicable for photocatalysis of hydrogen generation from water and photodynamic therapy.

This thesis describes the study of a series of multimetallic supramolecules containing varied metals and ligands, synthesized by a building block method and characterized by mass spectrometry, electronic absorption spectroscopy, and electrochemistry. Incorporating different functional units into complex systems allowed these multimetallic supramolecules to perform various light activated tasks including DNA cleavage and hydrogen generation from water.

The complex $[\{(\text{bpy})_2\text{Os}(\text{dpp})\}_2\text{Ru}_2(\text{dpq})](\text{PF}_6)_{12}$ and $[\{(\text{bpy})_2\text{M}(\text{dpp})\}_2\text{Ru}(\text{BL})\text{PtCl}_2](\text{PF}_6)_6$ were synthesized ($\text{M} = \text{Os}^{\text{II}}$ or Ru^{II} ; $\text{BL} = \text{dpp}$ or dpq ; $\text{bpy} = 2,2'$ -bipyridine, $\text{dpp} = 2,3$ -bis(2-pyridyl)pyrazine, $\text{dpq} = 2,3$ -bis(2-pyridyl)quinoxaline). The building blocks displayed varied electrochemical properties upon complexation. The bridging ligands dpp and dpq display their reduction potentials shifted to less negative values when they changed from monochelating to bischelating. The electronic absorption spectra of the multimetallic systems displayed transitions of each contributing chromophore, with overlapping metal to ligand charge transfer (MLCT) transitions in visible region of spectrum. Spectroelectrochemistry revealed the nature of MLCTs and helped to identify fingerprint

features of complex supramolecules. Photophysical measurements include emission spectroscopy with quantum yield measurements and emission lifetime measurements. Photophysical data provided detailed information to aid in developing an understanding of excited state properties of these complexes. Supported by the electrochemical data and spectroelectrochemistry, the hexametallic complex was suggested to have a HOMO localizing in the peripheral Os and a LUMO localizing in the central dpq, separating by a Ru energy barrier. This research systematically investigated photophysical properties of some building blocks and the mixed-metal, mixed-ligand supramolecules constructed by a variety of building blocks coupling light absorbing subunits to a reactive Pt metal center. Preliminary studies suggested $[\{(bpy)_2Ru(dpp)\}_2Ru(dpq)PtCl_2](PF_6)_6$ was a photocatalyst for H_2 production from water in the presence of a sacrificial electron donor. The complex $[\{(bpy)_2Ru(dpp)\}_2Ru(dpq)PtCl_2](PF_6)_6$ had been studied for its catalytic ability in generating hydrogen and was found to have 34 product turnovers after 3 h photolysis. Photolysis and gel electrophoresis revealed that the tetrametallic complexes were able to bind to and then photocleave DNA through an oxygen mediated mechanism. The independence of ionic strength variation when $[\{(bpy)_2Ru(dpp)\}_2Ru(dpp)PtCl_2](PF_6)_6$ interacted with DNA, suggested the covalent interaction nature of the complex. These results suggest future work on understanding the excited state properties of supramolecular complexes is suggested. The designs of future photocatalysts for hydrogen production from water and anticancer photodynamic therapy drugs are also proposed.

Acknowledgements

I would like to thank my father, Zenghua Miao; my mother, Meiyong Huang, my big sister, Ying Miao, and my niece, Yuanyi Lin, for all their help and encouragement on this journey toward my Ph.D. I could not have done this without them.

I am especially grateful to Prof. Karen J. Brewer for her supportive mentoring and continuous encouragement. Her guidance has been essential to my education and success in graduate school. I must also thank the members of my committee, Prof. Paul A. Deck, Prof. Brian E. Hanson, Prof. Larry T. Taylor, Prof. Gordon T. Yee and Prof. Mark Anderson, all of whom were of great assistance to me. I would be remiss if I did not acknowledge the help of Prof. Brenda S. J. Winkel for her instruction and discussions with respect to the DNA project, as well as Mr. David F. Zigler for his cooperative work in metal complexes-DNA interaction studies. I appreciate Mr. Shengliang Zhao's help in analyzing the NMR data. I would also like to thank Ms. Laurie Good and Mr. Jeffrey Bowers for their editorial assistance.

In closing, I consider myself fortunate to have been able to spend five very productive and happy years here at Virginia Tech in Blacksburg, Virginia. GO HOKIES!

Table of Contents

Title	i
Abstract	ii
Acknowledgements	iv
Table of Contents	v
List of Figures	viii
List of Tables	xiii
List of Abbreviations	xiv
Chapter 1. Introduction	1
1.1 Solar Energy Utilization and Photosynthesis	1
1.2 Overview of Supramolecular Chemistry	2
1.3 Ruthenium and Osmium Polyazine Complexes	3
1.3.1 Overview	3
1.3.2 Impact of Structural Variation on Properties	5
of Polyazine Transition Metal Complexes	
1.3.2.1 Variation of the Metal Center	5
1.3.2.2 Terminal Ligands	6
1.3.2.3 Bridging Ligands	7
1.3.2.4 Dendrimers	7
1.3.3 Electrochemistry	9
1.3.4 Spectroscopic Properties of Ru and Os Polyazine Complexes	12
1.3.5 Correlation Between Redox and Spectroscopic Properties	15
1.3.6 Excited State Properties	17
1.3.6.1 Excited State Properties of Ru and Os Polyazine Complexes	17
1.3.6.2 Energy Transfer	20
1.3.6.3 Electron Transfer	22
1.4 Applications of Ru and Os Polyazine Complexes	25
1.4.1 Charge Separation	25

1.4.2	Metal Complex Interactions with DNA and Photodynamic Therapy	27
1.4.3	Photocatalyst for Hydrogen Production from Water	31
1.5	Statement of Purpose	33
Chapter 2. Experiments		37
2.1	Materials and Solvents	37
2.2	Instrumentation	38
2.2.1	Elemental Analysis	38
2.2.2	Mass Spectrometry	38
2.2.3	NMR Analysis	38
2.2.4	Electrochemical Analysis	38
2.2.5	Electronic Absorption Spectroscopy	41
2.2.6	Spectroelectrochemistry	42
2.2.7	Emission Spectroscopy	43
2.2.7.1	Emission Spectroscopy	43
2.2.7.2	Quantum Yield Measurement	43
2.2.8	Excited State Emission Lifetime Measurement	44
2.2.9	Hydrogen Production	45
2.2.9.1	Photolysis	45
2.2.9.2	Gas Chromatography to Quantify Hydrogen	47
2.2.10	DNA Photocleavage Assay (carried out by Mr. David F. Zigler)	49
2.2.11	Impact of DNA on Emission Spectroscopy	50
2.3	Synthesis and Characterization	50
2.3.1	Modified Preparations of Literature Complexes	50
2.3.2	Preparations of New Supramolecular Complexes	57
Chapter 3. Results and Discussions		62
3.1	Synthesis	62
3.2	Discussion of the Isomers	63
3.3	Characterization	67

3.3.1	Mass Spectrometry	67
3.3.2	Electrochemical Analysis	71
3.3.2.1	General Electrochemical Considerations	71
3.3.2.2	Electrochemistry of	72
	[({(bpy) ₂ Os(dpp)} ₂ Ru) ₂ (dpq)](PF ₆) ₁₂ and [{{(bpy) ₂ Os(dpp)} ₂ Ru(dpq)}](PF ₆) ₆	
3.3.3	Electronic Absorption Spectroscopy of	86
	[({(bpy) ₂ Os(dpp)} ₂ Ru) ₂ (dpq)](PF ₆) ₁₂ and [{{(bpy) ₂ Os(dpp)} ₂ Ru(dpq)}](PF ₆) ₆	
3.3.4	Spectroelectrochemistry of	91
	[({(bpy) ₂ Os(dpp)} ₂ Ru) ₂ (dpq)](PF ₆) ₁₂ and [{{(bpy) ₂ Os(dpp)} ₂ Ru(dpq)}](PF ₆) ₆	
3.3.5	Electronic Absorption Spectroscopy of the Tetrametallic Complexes	94
3.3.6	Spectroelectrochemistry of	97
	[{{(bpy) ₂ Ru(dpp)} ₂ Ru(dpp)}](PF ₆) ₆ and [{{(bpy) ₂ Ru(dpp)} ₂ Ru(dpp)PtCl ₂ }](PF ₆) ₆	
3.3.7	Emission Spectroscopy	100
3.3.8	Excited State Emission Lifetime Measurement	103
3.3.9	Energy Diagram	104
3.3.10	Preliminary Investigation of the Photochemical Properties	110
3.3.10.1	Stern-Volmer Emission Quenching Analysis	110
3.3.10.2	Hydrogen Production	114
3.4	DNA Photocleavage Assay	119
3.4.1	DNA Photocleavage Study	119
3.4.2	Emission Quenching Experiment	122
Chapter 4.	Conclusions and Future Work	124
4.1	Conclusions	124
4.2	Future Work	127
References	129
Appendix	134

List of Figures

Figure 1.1	Solar spectrum	1
Figure 1.2	Structural representation of $[\text{Ru}(\text{bpy})_3]^{2+}$	3
Figure 1.3	Structures of bpy, dpp and dpq	4
Figure 1.4	Block molecular orbital diagram for a typical	5
	octahedral d^6 metal complex with π acceptor ligands	
Figure 1.5	Typical geometries of transition metal complexes	6
Figure 1.6	Structures of terminal ligands: bpy, phen, biq and tpy	7
Figure 1.7	Structures of bridging ligands: dpp, dpq and dpb	7
Figure 1.8	Structures of the decanuclear compounds	8
Figure 1.9	Synthetic pathway using protection/deprotection of bridging ligands	9
Figure 1.10	Cyclic voltammograms of $[\text{Os}(\text{bpy})_2(\text{L})](\text{PF}_6)_2$	10
	complexes measured in a 0.1 M Bu_4NPF_6 in CH_3CN at room temperature	
Figure 1.11	Electronic absorption spectra of $[\text{Os}(\text{bpy})_2(\text{L})](\text{PF}_6)_2$	14
	complexes measured in CH_3CN solvent at room temperature	
Figure 1.12	Electronic absorption spectra of $[\{(\text{bpy})_2\text{Os}\}_2(\text{L})](\text{PF}_6)_4$	14
	complexes measured in CH_3CN solvent at room temperature	
Figure 1.13	Correlation between the spectroscopic energy	15
	of $^1\text{MLCTs}$ and electrochemical potential of $[\{(\text{bpy})_2\text{Os}\}_2(\text{L})](\text{PF}_6)_4$	
Figure 1.14	Visible region of the electronic spectra of $[\{(\text{bpy})_2\text{Ru}\}_2(\text{dpp})]^{(4-n)+}$	16
Figure 1.15	Visible region of the electronic spectra of $[\{(\text{bpy})_2\text{Ru}\}_2(\text{dpq})]^{(4-n)+}$	17
Figure 1.16	Energy state diagram of $[\{(\text{bpy})_2\text{Ru}\}_2(\text{dpp})]^{4+}$	18
Figure 1.17	Energy state diagram of $[(\text{bpy})_2\text{Ru}(\text{dpp})\text{Os}(\text{bpy})_2]^{4+}$	21
Figure 1.18	Energy migration patterns in tetranuclear compounds	22
Figure 1.19	Energy migration patterns in decanuclear compounds	22
Figure 1.20	Structure of $[(\text{Phen})_2\text{Ru}(\text{tatpp})\text{Ru}(\text{phen})_2]^{4+}$	23
Figure 1.21	Energy state diagram of $[(\text{phen})_2\text{Ru}(\text{tatpp})\text{Ru}(\text{phen})_2]^{4+}$	24
Figure 1.22	Electron transfer in $[\{(\text{bpy})_2\text{Ru}(\mu\text{-dpp})\}_2\text{Ru}(\text{bpy-TTF})](\text{PF}_6)_6$	26

Figure 1.23	Interfacial and intramolecular electron transfer processes in $[\text{Ru}(\text{dcb})_2(\text{Cl})\text{-bpa-Os}(\text{bpy})_2\text{Cl}]^{2+}$ anchored on TiO_2	27
Figure 1.24	Structures of $[\text{Ru}(\text{phen})_3]^{2+}$ and $[\text{Ru}(\text{DIP})_3\text{Cl}_2]^{2+}$	28
Figure 1.25	Emission spectra of $[\text{Ru}(\text{phen})_3]^{2+}$ and $[\text{Ru}(\text{DIP})_3]^{2+}$ in both the absence of and presence of B-form calf thymus DNA	29
Figure 1.26	Structure of $[(\text{tpy})\text{RuCl}(\text{dpp})\text{PtCl}_2]^+$	30
Figure 1.27	DNA binding studies for $[\text{Pt}(\text{NH}_3)_2\text{Cl}_2]$ and $[(\text{tpy})\text{RuCl}(\text{dpp})\text{PtCl}_2](\text{PF}_6)$... by agarose gel electrophoresis using linearized pBluescript DNA	30
Figure 1.28	Structure of $[\text{Ru}(\text{bpy})_2\{\text{m-bpy}-(\text{CONH}-(\text{CH}_2)-\text{NH}_2)_2\}\text{PtCl}_2]^{2+}$	31
Figure 1.29	Structure of the trimetallic photocatalyst $[\{(\text{bpy})_2\text{Ru}(\text{dpp})\}_2\text{Rh}^{\text{III}}\text{Cl}_2]^{5+}$	33
Figure 1.30	Schematic representation of a long-distance intramolecular charge separation: $[\{[(\text{bpy})_2\text{Os}(\text{dpp})]_2\text{Ru}\}_2(\text{dpq})](\text{PF}_6)_{12}$	34
Figure 1.31	3-D representation of a long-distance intramolecular charge separation: $[\{[(\text{bpy})_2\text{Os}(\text{dpp})]_2\text{Ru}\}_2(\text{dpq})](\text{PF}_6)_{12}$	35
Figure 1.32	Schematic representation of $[\{(\text{bpy})_2\text{Ru}(\text{dpp})\}_2\text{Ru}(\text{dpq})\text{PtCl}_2](\text{PF}_6)_6$	36
Figure 1.33	3-D representation of $[\{(\text{bpy})_2\text{Ru}(\text{dpp})\}_2\text{Ru}(\text{dpq})\text{PtCl}_2](\text{PF}_6)_6$	36
Figure 2.1	Potential waveform of cyclic voltammetry	40
Figure 2.2	Potential waveform of Barker square wave voltammetry and Osteryoung square wave voltammetry	41
Figure 2.3	An H-type spectroelectrochemical cell	42
Figure 2.4	Correction file for Hamamatsu 1527 photomultiplier response	43
Figure 2.5	Emission lifetime measurement system	45
Figure 2.6	A 3 rd generation eight-LED array	47
Figure 2.7	Calibration curve for hydrogen analysis using GC	48
Figure 2.8	Stoichiometric control of supramolecular synthesis producing $[\{(\text{bpy})_2\text{Os}(\text{dpp})\}_2\text{Ru}(\text{dpq})](\text{PF}_6)_6$ or $[\{[(\text{bpy})_2\text{Os}(\text{dpp})]_2\text{Ru}\}_2(\text{dpq})](\text{PF}_6)_{12}$	59
Figure 2.9	Synthetic scheme of preparing $[\{(\text{bpy})_2\text{Ru}(\text{dpp})\}_2\text{Ru}(\text{dpp})\text{PtCl}_2](\text{PF}_6)_6$	60

Figure 3.1	Stereoisomer of $[(\text{phen})_2\text{Ru}(\mu\text{-tpphz})]_3\text{Ru}(\text{PF}_6)_8$: $[(\Lambda\text{-}(\text{phen})_2\text{Ru}(\mu\text{-tpphz}))_3\text{-}\Delta\text{-Ru}](\text{PF}_6)_8$ ($\Delta\Lambda_3$)	64
Figure 3.2	Representative isomers of $[\{(\text{bpy})_2\text{Ru}(\text{dpp})\}_2\text{Ru}(\text{dpq})\text{PtCl}_2](\text{PF}_6)_6$	65
Figure 3.3	Number of isomers of $[\{(\text{bpy})_2\text{Ru}(\text{dpp})\}_2\text{Ru}(\text{dpq})\text{PtCl}_2](\text{PF}_6)_6$	66
Figure 3.4	Number of isomers of $[\{(\text{bpy})_2\text{Os}(\text{dpp})\}_2\text{Ru}_2(\text{dpq})](\text{PF}_6)_{12}$	66
Figure 3.5	MALDI-TOF-MS of $[\{(\text{bpy})_2\text{Ru}(\text{dpp})\}_2\text{Ru}(\text{dpp})\text{PtCl}_2](\text{PF}_6)_6$	67
Figure 3.6	Cyclic voltammogram of $[\{(\text{bpy})_2\text{Os}(\text{dpp})\}_2\text{Ru}_2(\text{dpq})](\text{PF}_6)_{12}$ and $[\{(\text{bpy})_2\text{Os}(\text{dpp})\}_2\text{Ru}(\text{dpq})](\text{PF}_6)_6$	74
Figure 3.7	Square wave voltammogram of $[\{(\text{bpy})_2\text{Os}(\text{dpp})\}_2\text{Ru}_2(\text{dpq})](\text{PF}_6)_{12}$ and $[\{(\text{bpy})_2\text{Os}(\text{dpp})\}_2\text{Ru}(\text{dpq})](\text{PF}_6)_6$	75
Figure 3.8	Electrochemical mechanism for $[\{(\text{bpy})_2\text{Os}(\text{dpp})\}_2\text{Ru}_2(\text{dpq})](\text{PF}_6)_{12}$	78
Figure 3.9	Square wave voltammogram of $[\{(\text{bpy})_2\text{Ru}(\text{dpp})\}_2\text{Ru}(\text{dpp})](\text{PF}_6)_6$ and $[\{(\text{bpy})_2\text{Ru}(\text{dpp})\}_2\text{Ru}(\text{dpp})\text{PtCl}_2](\text{PF}_6)_6$	80
Figure 3.10	Electrochemical mechanism for $[\{(\text{bpy})_2\text{Ru}(\text{dpp})\}_2\text{Ru}(\text{dpp})\text{PtCl}_2](\text{PF}_6)_6$	82
Figure 3.11	Square wave voltammogram of the trimetallic complexes as well as the tetrametallic complexes	84
Figure 3.12	Electronic absorption spectra of $[\{(\text{bpy})_2\text{Os}(\text{dpp})\}_2\text{Ru}_2(\text{dpq})](\text{PF}_6)_{12}$ and $[\{(\text{bpy})_2\text{Os}(\text{dpp})\}_2\text{Ru}(\text{dpq})](\text{PF}_6)_6$	87
Figure 3.13	Normalized electronic absorption spectra of $[\{(\text{bpy})_2\text{Os}(\text{dpp})\}_2\text{Ru}_2(\text{dpq})](\text{PF}_6)_{12}$, $[\{(\text{bpy})_2\text{Os}(\text{dpp})\}_2\text{Ru}(\text{dpq})](\text{PF}_6)_6$ and the subtraction of trimetallic from hexametallic complex	89
Figure 3.14	Oxidative spectroelectrochemistry of $[\{(\text{bpy})_2\text{Os}(\text{dpp})\}_2\text{Ru}_2(\text{dpq})](\text{PF}_6)_{12}$ and $[\{(\text{bpy})_2\text{Os}(\text{dpp})\}_2\text{Ru}(\text{dpq})](\text{PF}_6)_6$	93
Figure 3.15	Difference spectra of the Os^{III} forms of $[\{(\text{bpy})_2\text{Os}^{\text{III}}(\text{dpp})\}_2\text{Ru}^{\text{II}}_2(\text{dpq})]^{16+}$, $[\{(\text{bpy})_2\text{Os}^{\text{III}}(\text{dpp})\}_2\text{Ru}^{\text{II}}(\text{dpq})]^{8+}$ and the subtraction of trimetallic from hexametallic complex	94
Figure 3.16	Electronic absorption spectra of $[\{(\text{bpy})_2\text{Ru}(\text{dpp})\}_2\text{Ru}(\text{dpp})\text{PtCl}_2](\text{PF}_6)_6$ and $[\{(\text{bpy})_2\text{Ru}(\text{dpp})\}_2\text{Ru}(\text{dpp})](\text{PF}_6)_6$	95

Figure 3.17	Electronic absorption spectra of the tetrametallic complexes	96
Figure 3.18	Oxidative spectroelectrochemistry of	99
	$[\{(bpy)_2Ru(dpp)\}_2Ru(dpp)PtCl_2](PF_6)_6$	
Figure 3.19	Reductive spectroelectrochemistry of	100
	$[\{(bpy)_2Ru(dpp)\}_2Ru(dpp)PtCl_2](PF_6)_6$	
Figure 3.20	Uncorrected room temperature emission spectra of	102
	$[(bpy)_2Ru(dpp)Ru(bpy)_2](PF_6)_4$, $[\{(bpy)_2Ru(dpp)\}_2Ru(dpp)](PF_6)_6$ and	
	$[\{(bpy)_2Ru(dpp)\}_2Ru(dpp)PtCl_2](PF_6)_6$	
Figure 3.21	Uncorrected 77 K emission spectra of	102
	$[\{(bpy)_2Ru(dpp)\}_2Ru(dpp)PtCl_2](PF_6)_6$ and $[\{(bpy)_2Ru(dpp)\}_2Ru(dpp)](PF_6)_6$	
Figure 3.22	Energy state diagrams of $[\{(bpy)_2Ru(dpp)\}_2Ru(dpp)](PF_6)_6$	106
	and $[\{(bpy)_2Ru(dpp)\}_2Ru(dpp)PtCl_2](PF_6)_6$	
Figure 3.23	Energy state diagrams of $[\{(bpy)_2Ru(dpp)\}_2Ru(dpq)](PF_6)_6$	109
	and $[\{(bpy)_2Ru(dpp)\}_2Ru(dpq)PtCl_2](PF_6)_6$	
Figure 3.24	Possible mechanism for the photocatalysis of hydrogen production	111
	with $[\{(bpy)_2Ru(dpp)\}_2Ru(dpp)PtCl_2](PF_6)_6$ and	
	$[\{(bpy)_2Ru(dpp)\}_2Ru(dpq)PtCl_2](PF_6)_6$	
Figure 3.25	Stern-Volmer plots for DMA quenching experiments on	114
	$[\{(bpy)_2Ru(dpp)\}_2Ru(dpp)PtCl_2](PF_6)_6$ and	
	$[\{(bpy)_2Ru(dpp)\}_2Ru(dpq)PtCl_2](PF_6)_6$	
Figure 3.26	Hydrogen generated vs. photolysis time for	118
	$[\{(bpy)_2Ru(dpp)\}_2Ru(dpq)PtCl_2](PF_6)_6$	
Figure 3.27	Comparison of electronic absorption spectra prior to and after	119
	the photocatalytic production of H ₂ for $[\{(bpy)_2Ru(dpp)\}_2Ru(dpq)PtCl_2](PF_6)_6$	
Figure 3.28	DNA interaction studies of $[\{(bpy)_2Ru(dpp)\}_2Ru(dpp)PtCl_2](PF_6)_6$,	120
	<i>cis</i> -[Pt(NH ₃) ₂ Cl ₂] and $[\{(bpy)_2Ru(dpp)\}_2Ru(dpp)](PF_6)_6$	
Figure 3.29	Ionic strength effect on the interaction of DNA with	122
	$[\{(bpy)_2Ru(dpp)\}_2Ru(dpp)PtCl_2](PF_6)_6$ and $[\{(bpy)_2Ru(dpp)\}_2Ru(dpp)](PF_6)_6$	

Figure A.1	400 MHz ^1H NMR of $[(\text{bpy})_2\text{Ru}(\text{dpp})](\text{PF}_6)_2$ in CD_3CN	136
Figure A.2	400 MHz ^1H NMR of $[(\text{bpy})_2\text{Os}(\text{dpp})](\text{PF}_6)_2$ in CD_3CN	136
Figure A.3	400 MHz ^1H NMR of $[\{(\text{bpy})_2\text{Os}(\text{dpp})\}_2\text{Ru}(\text{dpq})](\text{PF}_6)_6$ in DMSO	137
Figure A.4	400 MHz ^1H NMR of $[\{(\text{bpy})_2\text{Ru}(\text{dpp})\}_2\text{Ru}(\text{dpp})](\text{PF}_6)_6$ in DMSO	137
Figure A.5	400 MHz ^1H NMR of $[\{[(\text{bpy})_2\text{Os}(\text{dpp})]_2\text{Ru}\}_2(\text{dpq})](\text{PF}_6)_{12}$ in DMSO ...	138
Figure A.6	Cyclic voltammogram of the tetrametallic complex	139
	$[\{(\text{bpy})_2\text{Ru}(\text{dpp})\}_2\text{Ru}(\text{dpp})\text{PtCl}_2](\text{PF}_6)_6$ and the trimetallic complex	
	$[\{(\text{bpy})_2\text{Ru}(\text{dpp})\}_2\text{Ru}(\text{dpp})](\text{PF}_6)_6$	
Figure A.7	Cyclic voltammogram of the trimetallic complex	140
	$[\{(\text{bpy})_2\text{Ru}(\text{dpp})\}_2\text{Ru}(\text{dpq})](\text{PF}_6)_6$ and the tetrametallic complex	
	$[\{(\text{bpy})_2\text{Ru}(\text{dpp})\}_2\text{Ru}(\text{dpq})\text{PtCl}_2](\text{PF}_6)_6$	
Figure A.8	Electronic absorption spectra of $[\{(\text{bpy})_2\text{Ru}(\text{dpp})\}_2\text{Ru}(\text{dpp})](\text{PF}_6)_6$,	141
	$[\{(\text{bpy})_2\text{Ru}(\text{dpp})\}_2\text{Ru}(\text{dpq})](\text{PF}_6)_6$ and $[\{(\text{bpy})_2\text{Os}(\text{dpp})\}_2\text{Ru}(\text{dpq})](\text{PF}_6)_6$	
Figure A.9	DMA quenching experiments on room temperature emission	141
	of the tetrametallic complex $[\{(\text{bpy})_2\text{Ru}(\text{dpp})\}_2\text{Ru}(\text{dpp})\text{PtCl}_2](\text{PF}_6)_6$	
Figure A.10	DMA quenching experiments on room temperature emission	142
	of the tetrametallic complex $[\{(\text{bpy})_2\text{Ru}(\text{dpp})\}_2\text{Ru}(\text{dpq})\text{PtCl}_2](\text{PF}_6)_6$	
Figure A.11	FAB-MS spectrum of $[\{(\text{bpy})_2\text{Os}(\text{dpp})\}_2\text{Ru}(\text{dpq})](\text{PF}_6)_6$	143
Figure A.12	MALDI-TOF-MS spectrum of $[\{(\text{bpy})_2\text{Os}(\text{dpp})\}_2\text{Ru}(\text{dpq})](\text{PF}_6)_6$	144
Figure A.13	FAB-MS spectrum of $[\{(\text{bpy})_2\text{Ru}(\text{dpp})\}_2\text{Ru}(\text{dpp})](\text{PF}_6)_6$	145
Figure A.14	FAB-MS spectrum of $[\{(\text{bpy})_2\text{Ru}(\text{dpp})\}_2\text{Ru}(\text{dpq})](\text{PF}_6)_6$	146
Figure A.15	FAB-MS spectrum of $[\{[(\text{bpy})_2\text{Os}(\text{dpp})]_2\text{Ru}\}_2(\text{dpq})](\text{PF}_6)_{12}$	147
Figure A.16	MALDI-TOF-MS spectrum of $[\{[(\text{bpy})_2\text{Os}(\text{dpp})]_2\text{Ru}\}_2(\text{dpq})](\text{PF}_6)_{12}$...	148
Figure A.17	FAB-MS spectrum of $[\{(\text{bpy})_2\text{Ru}(\text{dpp})\}_2\text{Ru}(\text{dpp})\text{PtCl}_2](\text{PF}_6)_6$	149
Figure A.18	MALDI-TOF-MS spectrum of $[\{(\text{bpy})_2\text{Ru}(\text{dpp})\}_2\text{Ru}(\text{dpp})\text{PtCl}_2](\text{PF}_6)_6$...	150
Figure A.19	FAB-MS spectrum of $[\{(\text{bpy})_2\text{Ru}(\text{dpp})\}_2\text{Ru}(\text{dpq})\text{PtCl}_2](\text{PF}_6)_6$	151
Figure A.20	FAB-MS spectrum of $[\{(\text{bpy})_2\text{Os}(\text{dpp})\}_2\text{Ru}(\text{dpq})\text{PtCl}_2](\text{PF}_6)_6$	152

List of Tables

Table 1.1	Electrochemical data summary of selected Ru or Os polyazine complexes	11
Table 1.2	Electronic absorption data summary of Ru or Os polyazine complexes	13
Table 1.3	Photophysical properties of selected Ru or Os polyazine complexes	19
Table 3.1	Mass spectral data of $[\{(bpy)_2Os(dpp)\}_2Ru(dpq)](PF_6)_6$	69
Table 3.2	Mass spectral data of $[\{(bpy)_2Os(dpp)\}_2Ru)_2(dpq)](PF_6)_{12}$	70
Table 3.3	Mass spectral data of $[\{(bpy)_2Ru(dpp)\}_2Ru(dpp)PtCl_2](PF_6)_6$	71
Table 3.4	Electrochemical properties of $[\{(bpy)_2Os(dpp)\}_2Ru)_2(dpq)](PF_6)_{12}$, $[\{(bpy)_2Os(dpp)\}_2Ru(dpq)](PF_6)_6$ and related systems	76
Table 3.5	Electrochemical properties of $[\{(bpy)_2Ru(dpp)\}_2Ru(dpp)PtCl_2](PF_6)_6$ and related systems	81
Table 3.6	Electrochemical properties of trimetallic and tetrametallic complexes	85
Table 3.7	Electronic absorption spectra data summary of $[\{(bpy)_2Os(dpp)\}_2Ru)_2(dpq)](PF_6)_{12}$, $[\{(bpy)_2Os(dpp)\}_2Ru(dpq)](PF_6)_6$ and related systems	90
Table 3.8	Electronic absorption spectra data summary of $[\{(bpy)_2Ru(dpp)\}_2Ru(dpp)](PF_6)_6$, $[\{(bpy)_2Ru(dpp)\}_2Ru(dpp)PtCl_2](PF_6)_6$, $[\{(bpy)_2Ru(dpp)\}_2Ru(dpq)PtCl_2](PF_6)_6$ and $[\{(bpy)_2Os(dpp)\}_2Ru(dpq)PtCl_2](PF_6)_6$	97
Table 3.9	Photophysical properties of $[(bpy)_2Ru(dpp)Ru(bpy)_2](PF_6)_4$, $[\{(bpy)_2Ru(dpp)\}_2Ru(dpp)](PF_6)_6$, $[\{(bpy)_2Ru(dpp)\}_2Ru(dpq)](PF_6)_6$, $[\{(bpy)_2Ru(dpp)\}_2Ru(dpp)PtCl_2](PF_6)_6$ and $[\{(bpy)_2Ru(dpp)\}_2Ru(dpq)PtCl_2](PF_6)_6$	104
Table 3.10	Photocatalytic studies of H ₂ production using tetrametallic complexes, trimetallic complexes and some related controls	117
Table 3.11	Comparative DNA quenching experiments on $[\{(bpy)_2Ru(dpp)\}_2Ru(dpp)](PF_6)_6$ and $[\{(bpy)_2Ru(dpp)\}_2Ru(dpp)PtCl_2](PF_6)_6$	123

List of Abbreviations

biq	2,2'-biquinoline
bpy	2,2'-bipyridine
bpy-TTF	tetrathiafulvalene-substituted bipyridine
BL	bridging ligand
BP	base pair
bpa	1,2-bis(4-pyridyl)ethane
CT	charge transfer
CV	cyclic voltammetry
dcb	2,2'-bipyridine-4,4'-dicarboxylic acid
DIP	4,7-diphenyl-1,10-phenanthroline
DMA	N,N'-dimethylaniline
DMB	4-(dimethylamino)-N-methyl-N-phenyl-benzenemethanamine
dpb	2,3-bis(2-pyridyl)benzoquinoxaline
dpp	2,3-bis(2-pyridyl)pyrazine
dpq	2,3-bis(2-pyridyl)quinoxaline
dpb	2,3-bis(2-pyridyl)benzoquinoxaline
et	electron transfer
eV	electron volt
FAB	fast atom bombardment
GS	ground state
HOMO	highest occupied molecular orbital
ic	internal conversion
I.D.	inner diameter
IL	intra ligand
isc	intersystem crossing
LF	ligand field

LUMO	lowest unoccupied molecular orbital
MALDI	matrix assisted laser desorption/ionization
MC	metal complex
MLCT	metal to ligand charge transfer
MS	mass spectrometry
NADP	nicotinamide adenine dinucleotide phosphate
nr	nonradiative decay
OSWV	Osteryoung square wave voltammetry
r	radiative decay
phen	1,10-phenanthroline
RT	room temperature
TL	terminal ligand
TMB	N,N,N',N'-tetramethyl[1,1'-biphenyl]-4,4'-diamine
TOF	time of flight
tatpp	9,11,20,22-tetraazatetrapyrido[3,2-a:2'3'-c:3'',2''-l:2'''',3''''-n]pentacene
tpy	2,2',6',2''-terpyridine
TMB	tetramethylbenzidine
UV	ultraviolet
Vis	visible

Chapter 1. Introduction

1.1 Solar Energy Utilization and Photosynthesis

Solar radiation reaches the Earth's upper atmosphere at a rate of 1367 watts per square meter (W/m^2). Sunlight is attenuated by the Earth's atmosphere so that less power arrives at the surface - to 1,000 watts per directly exposed square meter in clear conditions when the Sun is near its zenith.¹ The sunlight radiation translates to a total 8.9×10^{16} W of solar energy falling on the planet's surface (Figure 1.1). While it is not plausible to capture all, or most, of the sunlight, capturing less than 0.02% would be enough to meet our current energy needs. Learning from plant photosynthesis, it is possible to harvest sunlight and convert it into chemical energy.

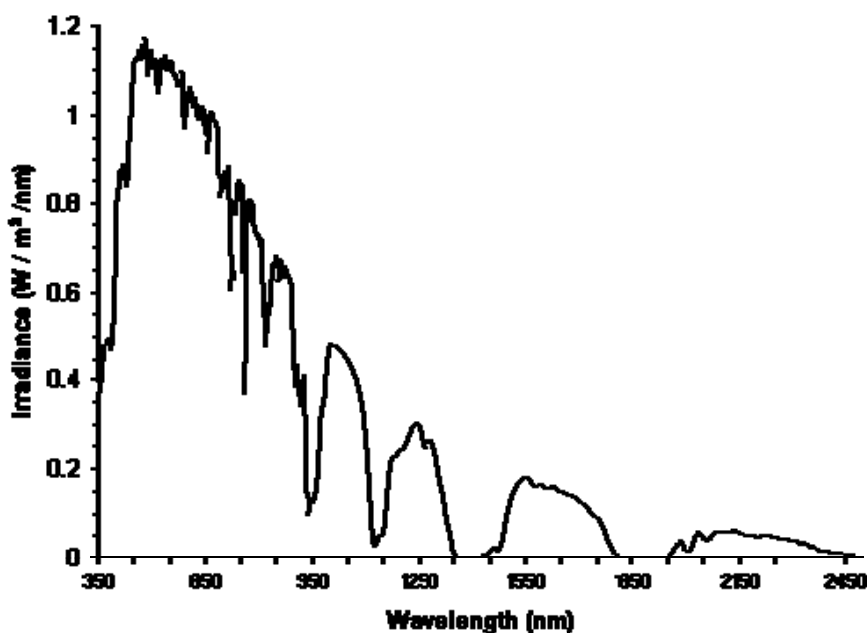
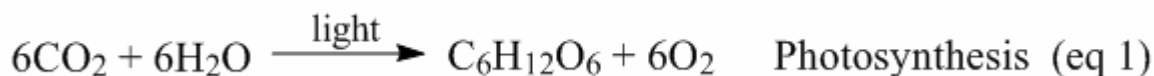


Figure 1.1 Solar spectrum. (http://fsf.nerc.ac.uk/img/asd_grph.gif)

Billions of years ago, after gaseous oxygen had been used up in the combustion (or oxidation) of materials when the Earth was very hot, life began to originate in a thin atmosphere consisting of methane, carbon dioxide, and water vapor. Over a long evolutionary process, several primal organisms began to use solar energy to synthesize large molecules from small molecules. Eventually, green plants learned how to utilize solar light, consume carbon dioxide and water vapor in the atmosphere to generate sugar, while at the same time

releasing an element essential for more complex organisms: oxygen (eq 1).



Green plants are able to convert solar energy into chemical energy. Using antenna chlorophyll, green plants capably harvest sunlight and generate photoinduced charge transfer. The charge is then transferred to a cytochrome *b6f* complex, then to NADP (nicotinamide adenine dinucleotide phosphate), where carbon dioxide is reduced by electrons so that it can react with water to form sugar.

The antenna and charge separation are two vital components in the process of photosynthesis. The antenna chlorophyll absorbs almost the entire visible region of light (except green) and generates charge separation by transferring the photoinduced electron to cytochrome *b6f* complex. Because this process is so essential, much of the research in solar energy utilization focuses on discovering efficient antennas and generating efficient charge separation.

1.2 Overview of Supramolecular Chemistry

Supramolecular chemistry focuses on the noncovalent interactions of molecules.² The importance of supramolecular chemistry was greatly recognized when the 1987 Nobel Prize in chemistry was awarded to Donald J. Cram, Jean-Marie Lehn and Charles J. Pedersen in acknowledgement of their work in this area. According to Jean-Marie Lehn, supramolecular chemistry is “the chemistry of intermolecular bond, covering the structures and functions of the entities formed by association of two or more chemical species.” The conceptual feature that differentiates supramolecules from other molecules is not the size, but rather the possibility of splitting the species into molecular components that have an individual existence and particular function.

The coordination motif allows designing and preparing the predetermined macromolecules due to the rigidity of transition metals coordination environment and the availability of various building blocks. In 1987, Balzani proposed the idea of using supramolecular species as molecular devices for various photoinitiated processes including

energy and electron transfer.³ The “supramolecules” consist of several components that somehow retain their individual properties in the assembly and perform individual functions; however, together they carry out complex functions. The composition of supramolecules can be either organic or inorganic moieties.

1.3 Ruthenium and Osmium Polyazine Complexes

1.3.1 Overview

Over the past several decades, researchers have been investigating supramolecular assemblies designed as molecular photochemical devices.³ Particularly, supramolecules involving ruthenium and osmium transition metal centers, coordinated by polyimine, cyanide and amine ligands, have shown considerable promise.³⁻⁸ In 1936, Burstall first synthesized the well-known $[\text{Ru}(\text{bpy})_3]^{2+}$ (bpy = 2,2'-bipyridine) (Figure 1.2),⁹ which later led to numerous Ru polyazine complexes.

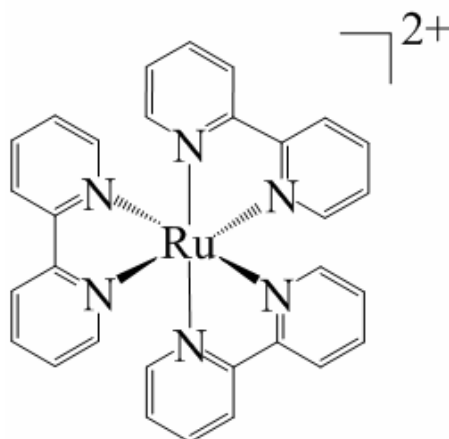


Figure 1.2 Structural representation of $[\text{Ru}(\text{bpy})_3]^{2+}$ (bpy = 2,2'-bipyridine).

A variety of polyazine bridging ligands have been synthesized and used to assemble supramolecular complexes,⁶ including the highly studied dpp (2,3-bis(2-pyridyl)pyrazine) and dpq (2,3-bis(2-pyridyl)quinoxaline) (Figure 1.3).^{4, 5, 10-16} The energy of the π^* acceptor orbital decreases from bpy to dpp to dpq, because of the increasing π conjugated system. This orbital is further stabilized when bridging ligands, like dpp or dpq, connect two metal centers, which is likely due to the decreasing of electron density on the ligand when bound to metals.⁵

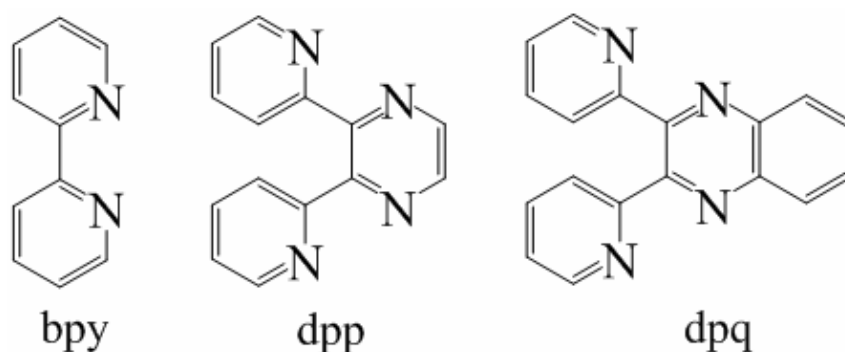


Figure 1.3 Structures of bpy, dpp and dpq. bpy = 2,2'-bipyridine, dpp = 2,3-bis(2-pyridyl)pyrazine, dpq = 2,3-bis(2-pyridyl)quinoxaline.

Ru^{II} and Os^{II} polyazine complexes are efficient light absorbers with tunable chromophores. Typically they display $\pi \rightarrow \pi^*$ based intraligand (IL) transitions in the ultraviolet region, and metal-to-ligand charge transfers (MLCT) in the visible region. Figure 1.4 illustrates a typical block MO diagram for an octahedral complex with π accepting ligands. Ligand field (LF) transitions correspond to electron transitions from the lower d orbitals (t_{2g}) of metal centers to the higher d orbitals (e_g), while IL transitions correspond to ligand based electronic transitions from π orbitals to π^* orbitals. MLCT transitions correspond to electrons moving from metal-based d orbitals to ligand-based π^* orbitals. Ligand-to-metal charge transfer (LMCT) transitions correspond to the electrons moving from ligand-based π orbitals to metal-based d orbitals. These MLCT chromophores find applications in many areas due to their ability to undergo efficient excited state energy and electron transfer as well as their often emissive $^3\text{MLCT}$ states. The introduction of polyazine bridging ligands has led to the development of interesting supramolecular complexes with efficient energy or electron transfer processes, which is characteristic of these MLCT chromophores.^{3, 5, 11}

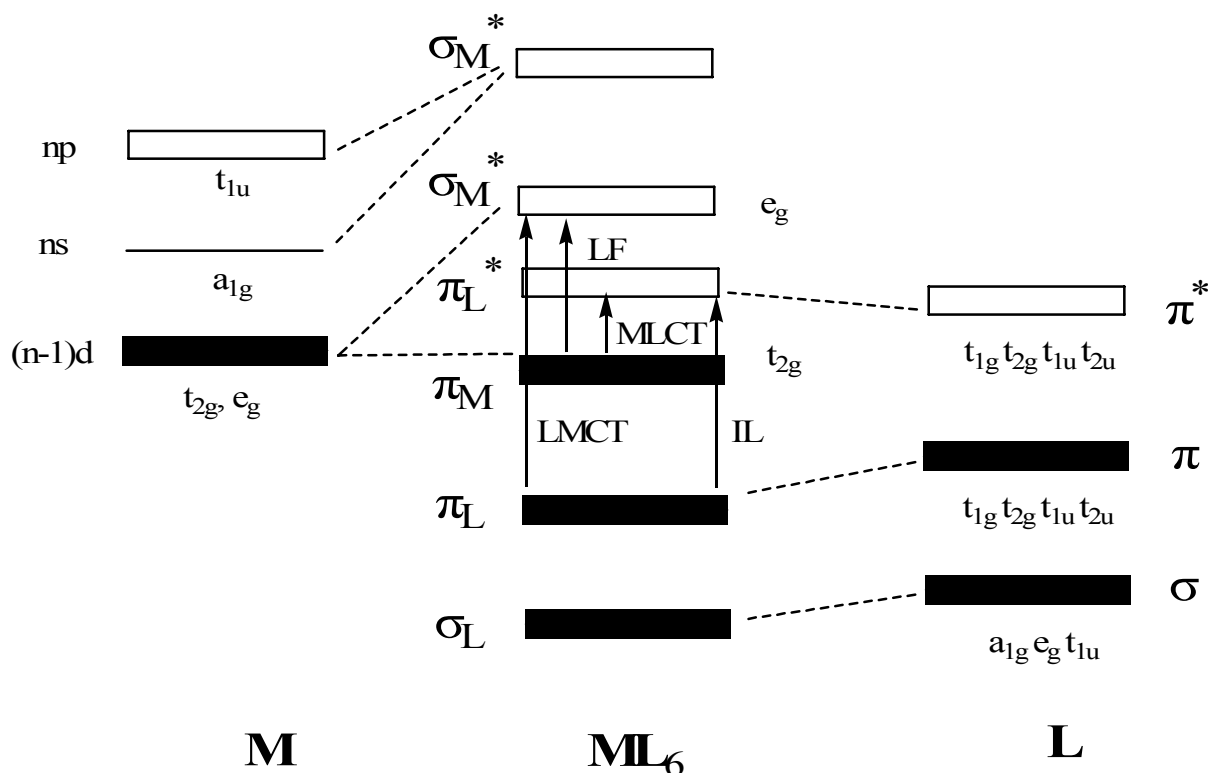


Figure 1.4 Block molecular orbital diagram for a typical octahedral d^6 metal complex with π acceptor ligands. Shaded blocks are filled orbitals and unshaded blocks are vacant ones.

1.3.2 Impact of Structural Variation on Properties of Polyzine Transition Metal Complexes

1.3.2.1 Variation of The Metal Center

Besides the widely studied Ru^{II} complex such as the early $[Ru(bpy)_3]^{2+}$,⁹ other metal centers like Os^{II} and Pt^{II} have also been studied.^{5, 11, 21-35} Os analogues typically display similar MLCT transitions in the visible region of the spectrum, but shift to the red region of the spectrum due to higher energy d orbitals on Os vs. Ru . Due to increased spin-orbit coupling for late transition metals, Os analogues typically display 3MLCT absorptions at lower energy with enhanced intensity, compared to Ru analogues.^{5, 21, 27, 36} The choice of transition metals enables the MLCT excited state energy to be regulated as needed.³⁷⁻⁴⁰ In addition, incorporation of Pt^{II} allows for biological and photochemical applications,⁴¹⁻⁴⁷ in which Pt^{II} displays a square planar geometry in lieu of the octahedral coordination displayed by Os^{II} and Ru^{II} , Figure 1.5.

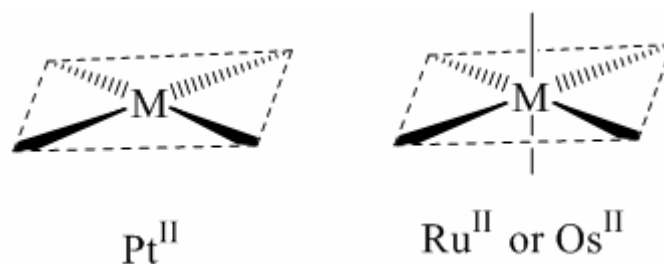


Figure 1.5 Typical geometries of transition metal complexes.

1.3.2.2 Terminal Ligands

Terminal ligands are those bound to only one metal center. Terminal polyazine ligands include 2,2'-bipyridine (bpy), the most common bidentate example (Figure 1.6).

Electrochemical and spectroscopic studies show that bpy has the ability to act as both a σ -donor and a π -acceptor, forming very stable metal complexes with electron-rich, weakly Lewis-acidic late transition metals. With a more extended π conjugated structure, phen (1,10-phenanthroline) is a stronger π electron acceptor.⁴⁸ Another common terminal ligand is 2,2'-biquinoline (biq) which is frequently incorporated into large dendritic systems.⁴⁹ 2,2',6',2''-Terpyridine (tpy)⁵⁰ is the most common tridentate terminal ligand, which lowers the energy level of the MLCT excited states of Ru and Os complexes due to the enlarged π conjugated system, compared to the bpy analogues. When used as the terminal ligand, tpy limits the stereoisomerization of the metal center, eliminating the possibility of generating Δ and Λ isomers common to tris diimine complexes like $[\text{Ru}(\text{bpy})_3]^{2+}$. Typically, the metal to bpy or tpy charge transfer states occur at higher energy than the metal to bridging μ -dpp or μ -dpq charge transfer states, because the π^* orbitals in bpy or tpy are higher in energy than those in μ -dpp or μ -dpq.

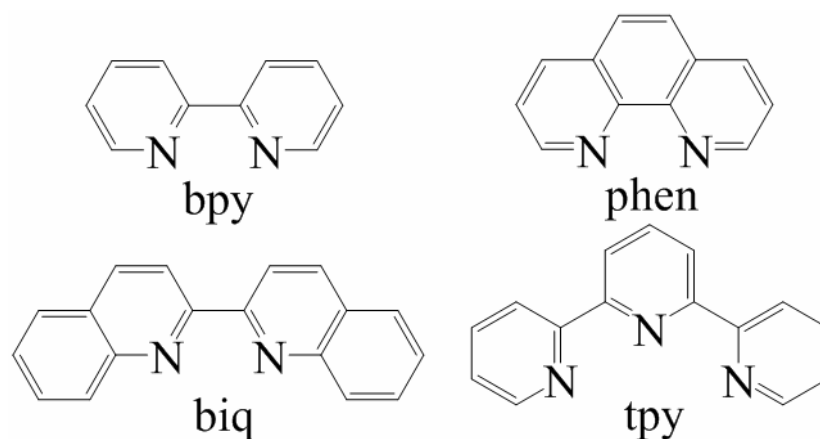


Figure 1.6 Structures of terminal ligands: bpy (2,2'-bipyridine), phen (1,10-phenanthroline), biq (2,2'-biquinoline) and tpy (2,2',6',2''-terpyridine).

1.3.2.3 Bridging Ligands

Bridging ligand (BL) simultaneously connects multiple metal centers through coordinative binding to multiple metals. Common bidentate bridging ligands include 2,3-bis(2-pyridyl)pyrazine (dpp), 2,3-bis(2-pyridyl)quinoxaline (dpq) and 2,3-bis(2-pyridyl)benzoquinoxaline (dpb) (Figure 1.7). Using dpp as the bridging ligand, a number of polynuclear complexes have been prepared whose corresponding spectroscopic and electrochemical properties have been thoroughly investigated.^{5, 11, 12, 51-54} With larger π conjugated systems, dpq and dpb have been shown to be better electron acceptors during electron transfer processes, compared with dpp.^{12, 55, 56}

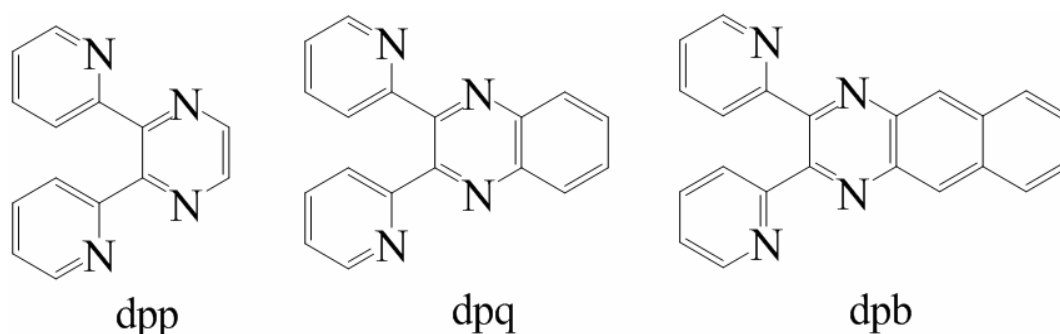


Figure 1.7 Structure of bridging ligands: dpp (2,3-bis(2-pyridyl)pyrazine), dpq (2,3-bis(2-pyridyl)quinoxaline) and dpb (2,3-bis(2-pyridyl)benzoquinoxaline).

1.3.2.4 Dendrimers

Dendrimers are repeatedly branched molecules. Dendritic Ru and Os supramolecular

complexes have been systematically studied (Figure 1.8).^{8, 11} Constructing dendrimers of Ru and Os polyazine complexes not only provides molecules with higher extinction coefficients, but also allows the possibility of designing predetermined energy or electron transfer after photoinitiation, when using various subunits with different energy states.

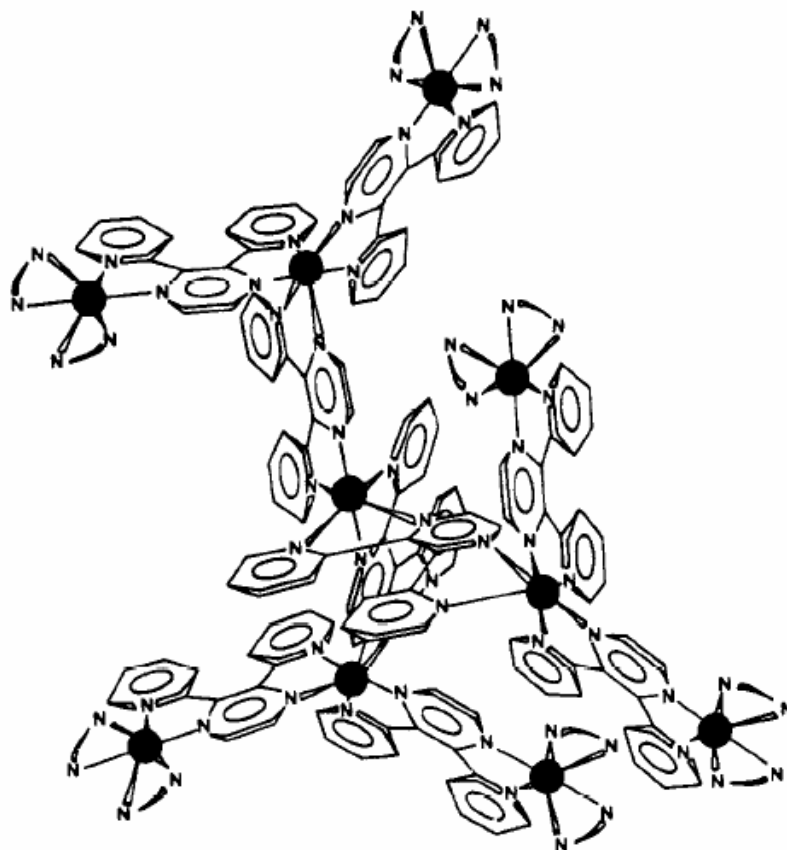


Figure 1.8 Structures of the decanuclear compounds. N-N stands for either bpy or biq (bpy = 2,2'-bipyridine, biq = 2,2'-biquinoline).⁵

A typical synthetic route for constructing a dendrimer is through the step-by-step “complexes as metals” or “complexes as ligands” strategies.^{5, 53} In order to obtain the desired molecule formation, stoichiometric ratio control is typically employed. Another synthetic method for preparing dendrimers is through methyl protection/deprotection, illustrated in Figure 1.9.^{11, 57-59} In this method, dpp is methylated to prevent bridge formation in the preparation of the monometallic intermediate. The methylated dpp is then demethylated and the chelating site is available for subsequent coordinative reaction. Through this protection/deprotection method, various metal centers can be added into a supramolecular

system.

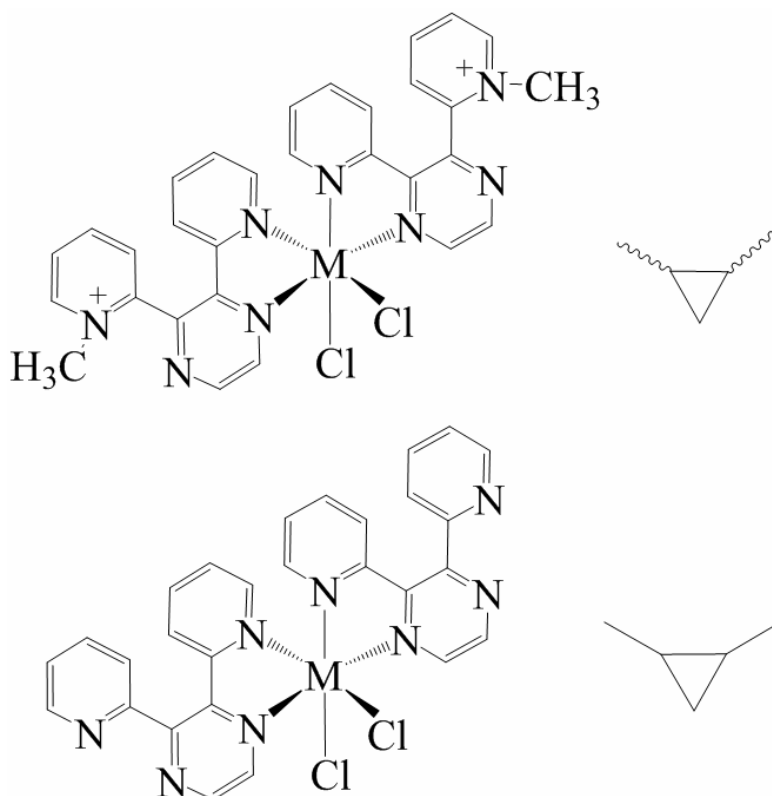
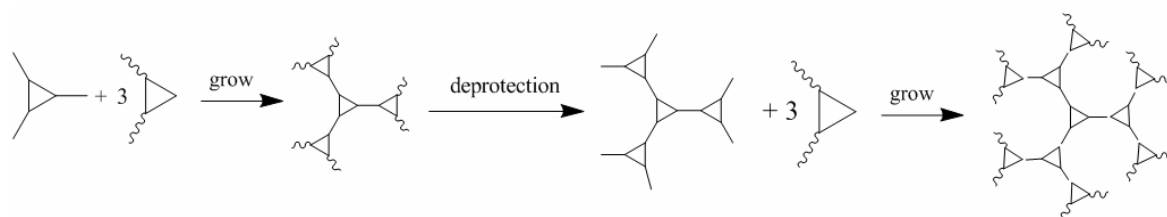


Figure 1.9 Synthetic pathway using protection/deprotection of bridging ligands, $M = \text{Ru}^{\text{II}}$ or Os^{II} .¹¹

1.3.3 Electrochemistry

Electrochemistry is typically used to study the redox properties of most supramolecular complexes. One commonly used electrochemical technique, cyclic voltammetry, is effective in probing ligand-based reduction and metal-based oxidations, especially for Ru or Os, the latter being more easily oxidized due to its higher d orbitals. Depending on the difference in π^* acceptor energies, different ligands display different redox potentials. For example, the reduction potential is less negative when the π accepting ability increases. Generally the more extended the π system, the lower energy the π^* orbitals. For

instance, dpb has the least negative reduction potential, follow sequentially by dpq, dpp and bpy. To illustrate, the reduction potential of dpp is -1.01 V and -0.64 V (vs. Ag/AgCl) in the monometallic complex $[(bpy)_2Ru(dpp)](PF_6)_4$ and in the bimetallic complex $[\{(bpy)_2Ru\}_2(dpp)](PF_6)_4$, respectively. In the monometallic complex $[(bpy)_2Ru(dpp)](PF_6)_4$, the dpp reduction displays more positive potential than do the bpy reductions, -1.01 V vs. -1.46 V, -1.67 V (Figure 1.10). With respect to dpp, dpq, and dpb, once they change from a monochelating state to a bischelating state, their redox potentials shift to less negative values due to the further lowering of the π^* orbitals. As a result of bridging, the $BL^{0/-}$ and $BL^{-/2-}$ usually occur prior to the $TL^{0/-}$ reduction.^{5, 12} Some typical electrochemical data for Ru or Os polyazine complexes are shown in Figure 1.10 and summarized in Table 1.1.

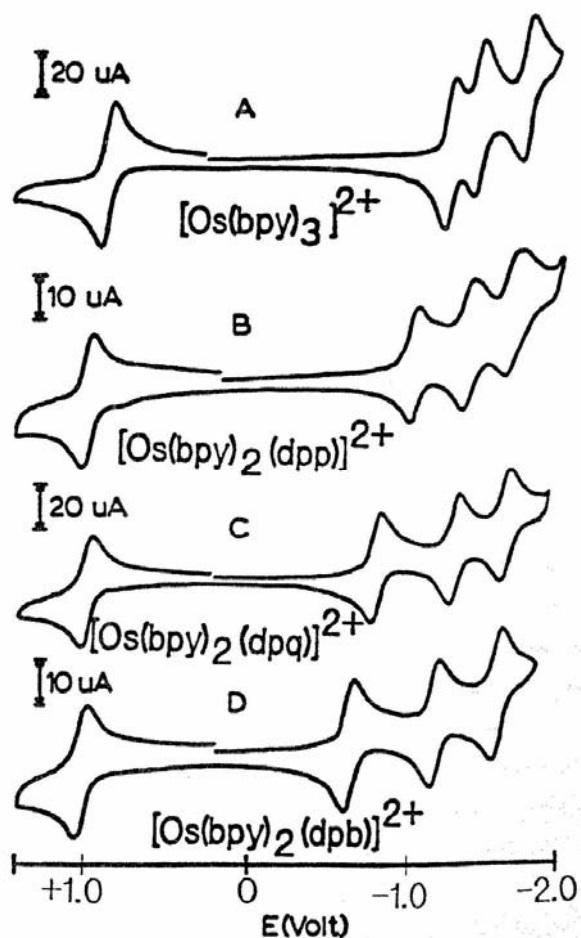


Figure 1.10 Cyclic voltammograms of $[Os(bpy)_2(L)](PF_6)_2$ complexes measured in a 0.1 M Bu_4NPF_6 in CH_3CN at room temperature ($L = bpy, dpp, dpq$ or dpb ; $bpy = 2,2$ -bipyridine; $dpp = 2,3$ -bis(2-pyridyl)pyrazine; $dpq = 2,3$ -bis(2-pyridyl)quinoxaline and $dpb = 2,3$ -bis(2-pyridyl)benzoquinoxaline; V vs. Ag/AgCl).²⁷

Table 1.1 Electrochemical data summary of selected Ru or Os polyazine complexes. ^{a,b} (bpy = 2,2'-bipyridine, dpp = 2,3-bis(2-pyridyl)pyrazine, dpq = 2,3-bis(2-pyridyl)quinoxaline, dpb = 2,3-bis(2-pyridyl)benzoquinoxaline).

Complex	E _{1/2} (V)	Assignment	Complex	E _{1/2} (V)	Assignment
[Ru(bpy) ₃](PF ₆) ₂ ^c	1.32	Ru ^{II/III}			
	-1.30	bpy ^{0/-}			
	-1.49	bpy ^{0/-}			
	-1.73	bpy ^{0/-}			
[(bpy) ₂ Ru(dpp)](PF ₆) ₂	1.38	Ru ^{II/III}	[{(bpy) ₂ Ru} ₂ (dpp)](PF ₆) ₄	1.64	Ru ^{II,III/III,III}
	-1.01	dpp ^{0/-}		1.46	Ru ^{II,II/II,III}
	-1.46	bpy ^{0/-}		-0.64	dpp ^{0/-}
	-1.67	bpy ^{0/-}		-1.14	dpp ^{-2/-}
[(bpy) ₂ Ru(dpq)](PF ₆) ₂	1.47	Ru ^{II/III}	[{(bpy) ₂ Ru} ₂ (dpq)](PF ₆) ₄	1.63	Ru ^{II,III/III,III}
	-0.72	dpq ^{0/-}		1.48	Ru ^{II,II/II,III}
	-1.40	bpy ^{0/-}		-0.40	dpq ^{0/-}
	-1.62	bpy ^{0/-}		-1.12	dpq ^{-2/-}
[(bpy) ₂ Ru(dpb)](PF ₆) ₂	1.48	Ru ^{II/III}	[{(bpy) ₂ Ru} ₂ (dpb)](PF ₆) ₄	1.63	Ru ^{II,III/III,III}
	-0.62	dpb ^{0/-}		1.45	Ru ^{II,II/II,III}
	-1.26	bpy ^{0/-}		-0.26	dpb ^{0/-}
	-1.60	bpy ^{0/-}		-0.90	dpb ^{-2/-}
[Os(bpy) ₃](PF ₆) ₂	0.82	Os ^{II/III}			
	-1.26	bpy ^{0/-}			
	-1.44	bpy ^{0/-}			
	-1.74	bpy ^{0/-}			
[(bpy) ₂ Os(dpp)](PF ₆) ₂	0.94	Os ^{II/III}	[{(bpy) ₂ Os} ₂ (dpp)](PF ₆) ₄	1.22	Os ^{II,III/III,III}
	-1.02	dpp ^{0/-}		0.91	Os ^{II,II/II,III}
	-1.38	bpy ^{0/-}		-0.68	dpp ^{0/-}
	-1.58	bpy ^{0/-}		-1.06	dpp ^{-2/-}
[(bpy) ₂ Os(dpq)](PF ₆) ₂	0.99	Os ^{II/III}	[{(bpy) ₂ Os} ₂ (dpq)](PF ₆) ₄	1.28	Os ^{II,III/III,III}
	-0.76	dpq ^{0/-}		0.98	Os ^{II,II/II,III}
	-1.26	bpy ^{0/-}		-0.44	dpq ^{0/-}
	-1.58	bpy ^{0/-}		-1.03	dpq ^{-2/-}
[(bpy) ₂ Os(dpb)](PF ₆) ₂	1.00	Os ^{II/III}	[{(bpy) ₂ Os} ₂ (dpb)](PF ₆) ₄	1.30	Os ^{II,III/III,III}
	-0.61	dpb ^{0/-}		0.98	Os ^{II,II/II,III}
	-1.16	bpy ^{0/-}		-0.33	dpb ^{0/-}
	-1.55	bpy ^{0/-}		-0.85	dpb ^{-2/-}

^a Data measured in 0.1 M Bu₄NPF₆ in CH₃CN, V vs. Ag/AgCl.

^b ref. 27 unless specified otherwise; ^c ref. 60.

1.3.4 Spectroscopic Properties of Ru and Os Polyazine Complexes

Most of the Ru and Os polyazine supramolecules have a O_h coordination environment and absorb in the ultraviolet (UV) and visible (Vis) regions of the spectrum and luminesce in the low energy visible or near-IR regions.⁵ The UV region is typically dominated by ligand $\pi \rightarrow \pi^*$ intraligand transitions and the visible region is dominated by the MLCT processes. Generally, the highest occupied molecular orbital (HOMO) is localized on a metal center, while the lowest unoccupied molecular orbital (LUMO) is localized on one of the ligands possessing the lowest π^* orbital. Complexes display red-shifted MLCT transitions when the incorporated ligands change from poorer π acceptors to stronger π acceptors as from bpy to dpp to dpq to dpb. For example, the $Ru(d\pi) \rightarrow bpy(\pi^*)$ ¹MLCT, $Ru(d\pi) \rightarrow dpp(\pi^*)$ ¹MLCT, $Ru(d\pi) \rightarrow dpq(\pi^*)$ ¹MLCT and $Ru(d\pi) \rightarrow dpb(\pi^*)$ ¹MLCT transitions have absorption maxima at ca. 452 nm, 470 nm, 515 nm and 550 nm in fluid CH_3CN at RT, respectively (Table 1.2).^{12, 13, 18, 19, 60-62} The π^* orbitals of ligands are further stabilized upon bridging by two or more metals. This results in lowering the corresponding ¹MLCT energy levels. For example, the $Ru(d\pi) \rightarrow dpp(\pi^*)$ ¹MLCT transition maximum is red-shifted from 470 nm to 525 nm from the monometallic complex $[(bpy)_2Ru(dpp)](PF_6)_2$ to the bimetallic complex $[\{(bpy)_2Ru\}_2(dpp)](PF_6)_4$.^{12, 13} It should be noted that a red-shifted ¹MLCT usually leads to a red-shifted ³MLCT. As a result, decreased emission quantum yields and shortened excited state lifetimes are typically observed, which is associated with an increased nonradiative processes rate (this effect will be further discussed in Section 1.3.6).⁶³⁻⁶⁶ Compared to Ru polyazine complex, Os analogues show ³MLCT absorptions lower in energy, which has typically been associated with higher energy $Os(d\pi)$ orbitals relative to $Ru(d\pi)$ orbitals.^{5, 16, 21, 27, 36, 67} For example, the maxima of $M(d\pi) \rightarrow dpp(\pi^*)$ ¹MLCT transitions of $[(bpy)_2M(dpp)]^{2+}$ ($M = Os^{II}$ or Ru^{II}) are approximately 486 nm for the Os complex and 470 nm for the Ru complex. Selected electronic absorption spectra of Os analogues are shown in Figure 1.11 and Figure 1.12, and related assignments are summarized in Table 1.2.

Table 1.2 Electronic absorption data summary for selected Ru or Os polyazine complexes (bpy = 2,2'-bipyridine, dpp = 2,3-bis(2-pyridyl)pyrazine, dpq = 2,3-bis(2-pyridyl)quinoxaline, dpb = 2,3-bis(2-pyridyl)benzoquinoxaline).^a

Complex	Wavelength (nm)	$\epsilon \times 10^3$ (M ⁻¹ cm ⁻¹)	Assignment
[Ru(bpy) ₃](PF ₆) ₂ ^b	452	14.6	Ru(d π) \rightarrow bpy(π^*) CT
[(bpy) ₂ Ru(dpp)](PF ₆) ₂ ^c	430	12.0	Ru(d π) \rightarrow bpy(π^*) CT
	470	10.2	Ru(d π) \rightarrow dpp(π^*) CT
[(bpy) ₂ Ru(dpq)](PF ₆) ₂ ^d	427	7.8	Ru(d π) \rightarrow bpy(π^*) CT
	515	8.1	Ru(d π) \rightarrow dpq(π^*) CT
[(bpy) ₂ Ru(dpb)](PF ₆) ₂ ^e	430	shoulder	Ru(d π) \rightarrow bpy(π^*) CT
			Ru(d π) \rightarrow dpb(π^*) CT
	550	8.3	Ru(d π) \rightarrow dpb(π^*) CT
[{(bpy) ₂ Ru} ₂ (dpp)](PF ₆) ₄ ^f	425	17.0	Ru(d π) \rightarrow bpy(π^*) CT
	525	21.0	Ru(d π) \rightarrow μ -dpp(π^*) CT
[{(bpy) ₂ Ru} ₂ (dpq)](PF ₆) ₄ ^d	423	8.1	Ru(d π) \rightarrow bpy(π^*) CT
	605	9.8	Ru(d π) \rightarrow μ -dpq(π^*) CT
[{(bpy) ₂ Ru} ₂ (dpb)](PF ₆) ₄ ^f	644	^h	Ru(d π) \rightarrow μ -dpb(π^*) CT
[(bpy) ₂ Os(dpp)](PF ₆) ₂ ^g	432	11.0	Os(d π) \rightarrow bpy(π^*) CT
	486	12.7	Os(d π) \rightarrow dpp(π^*) CT
[(bpy) ₂ Os(dpq)](PF ₆) ₂ ^g	428	11.0	Os(d π) \rightarrow bpy(π^*) CT
	536	13.4	Os(d π) \rightarrow dpq(π^*) CT
[(bpy) ₂ Os(dpb)](PF ₆) ₂ ^g	408	17.3	Os(d π) \rightarrow dpb(π^*) CT
	446	12.8	Os(d π) \rightarrow bpy(π^*) CT
	570	13.8	Os(d π) \rightarrow dpb(π^*) CT
[{(bpy) ₂ Os} ₂ (dpp)](PF ₆) ₄ ^g	432	19.8	Os(d π) \rightarrow bpy(π^*) CT
	552	25.2	Os(d π) \rightarrow μ -dpp(π^*) CT
[{(bpy) ₂ Os} ₂ (dpq)](PF ₆) ₄ ^g	398	19.6	Os(d π) \rightarrow μ -dpq(π^*) CT
	428	14.3	Os(d π) \rightarrow bpy(π^*) CT
	630	20.9	Os(d π) \rightarrow μ -dpq(π^*) CT
[{(bpy) ₂ Os} ₂ (dpb)](PF ₆) ₄ ^g	422	16.6	Os(d π) \rightarrow bpy(π^*) CT
	610	12.9	Os(d π) \rightarrow μ -dpb(π^*) CT
	670	16.8	Os(d π) \rightarrow μ -dpb(π^*) CT

^a Electronic absorption spectra are measured in CH₃CN at room temperature.

^b ref. 60 ; ^c ref. 13 ; ^d ref. 18 ; ^e ref. 61 ; ^f ref. 61 ; ^g ref. 27.

^h extinction coefficient not provided.

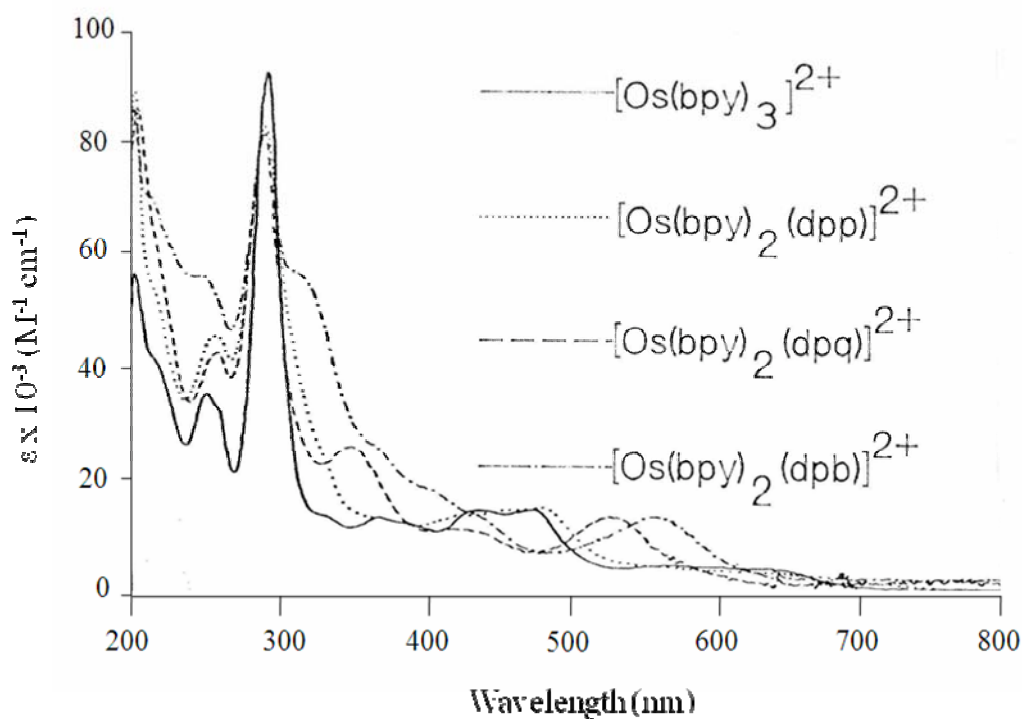


Figure 1.11 Electronic absorption spectra of $[\text{Os}(\text{bpy})_2(\text{L})](\text{PF}_6)_2$ complexes measured in CH_3CN solvent at room temperature. (L = bpy, dpp, dpq or dpb; bpy = 2,2-bipyridine; dpp = 2,3-bis(2-pyridyl)pyrazine; dpq = 2,3-bis(2-pyridyl)quinoxaline and dpb = 2,3-bis(2-pyridyl)benzoquinoxaline).²⁷

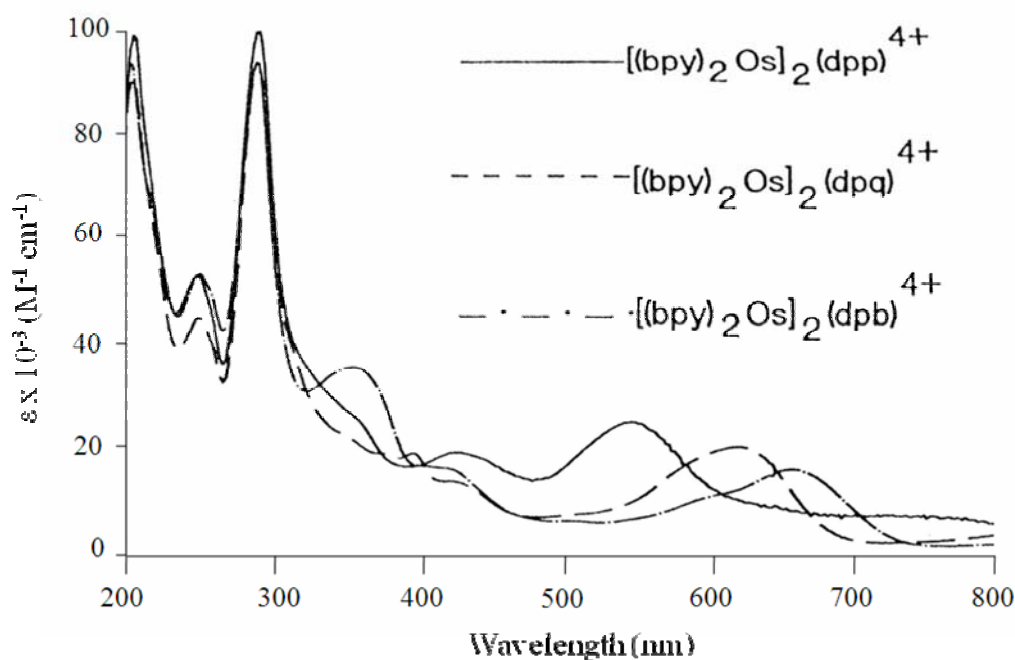


Figure 1.12 Electronic absorption spectra of $[\{(\text{bpy})_2\text{Os}\}_2(\text{L})](\text{PF}_6)_4$ complexes measured in CH_3CN solvent at room temperature. (L = dpp, dpq or dpb; dpp = 2,3-bis(2-pyridyl)pyrazine; dpq = 2,3-bis(2-pyridyl)quinoxaline and dpb = 2,3-bis(2-pyridyl)benzoquinoxaline).²⁷

1.3.5 Correlation Between Redox and Spectroscopic Properties

Since the ability of Ru or Os polyazine complexes to absorb visible light is due to metal to ligand charge transfer transitions, the energy of the absorbed light should correlate with the energy gap between the metal oxidation potentials and the ligand reduction potentials. In fact there is a linear relationship between the optical and electrochemical energy gaps.^{63, 68-75} An example of this relationship for [$\{(\text{bpy})_2\text{Os}\}_2(\text{L})\}(\text{PF}_6)_4$ (L = dpp, dpq or dpb) complexes is shown in Figure 1.13.

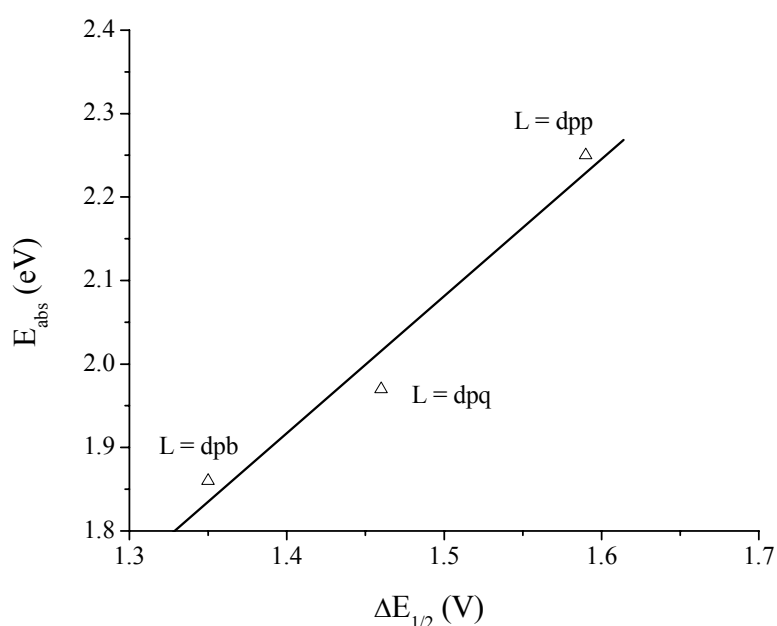


Figure 1.13 Correlation between the spectroscopic energy of $^1\text{MLCTs}$ and electrochemical potential of [$\{(\text{bpy})_2\text{Os}\}_2(\text{L})\}(\text{PF}_6)_4$ (L = dpp, dpq or dpb) complexes (bpy = 2,2'-bipyridine, dpp = 2,3-bis(2-pyridyl)pyrazine, dpq = 2,3-bis(2-pyridyl)quinoxaline, dpb = 2,3-bis(2-pyridyl)benzoquinoxaline).²⁷

As shown above, a linear relationship between the spectroscopic energy gap E_{abs} (eV) and the electrochemical potential gap $\Delta E_{1/2}$ can be observed, $E_{\text{abs}} = k \Delta E_{1/2} + C$ (eq 2), where the constant C usually depends on the degree of nuclear rearrangement to accommodate the excited electronic configuration and solvation.

Spectroelectrochemistry probes the electronic properties of multimetallic supramolecules.^{16, 17, 20, 67} In particular, the spectroelectrochemical approach enables one to

monitor an electronic absorption spectroscopy change when an electrochemical change occurs. Electrochemical oxidation of a metal center typically shifts the MLCT transitions out of the visible region of the spectrum. Reduction of a ligand typically changes the energy of the MLCT transitions as a result of the change of electron density on the ligand.²⁰ For example in $[\{(bpy)_2Ru\}_2(dpp)](PF_6)_4$ (Figure 1.14), the $Ru(d\pi) \rightarrow dpp(\pi^*)$ ¹MLCT transition is shifted out of the visible from 19000 cm^{-1} (525 nm). Following the second electron reduction leading to a two electron reduced dpp, the absorbance at ca. 475 nm is decreased and an increase of absorbance is observed at ca. 15000 cm^{-1} (660 nm). In $[\{(bpy)_2Ru\}_2(dpq)](PF_6)_4$ (Figure 1.15), the $Ru(d\pi) \rightarrow dpq(\pi^*)$ ¹MLCT absorbance at ca. 16500 cm^{-1} (605 nm) is lost after first electron reduction. At the same time, a maximum of the $Ru(d\pi) \rightarrow bpy(\pi^*)$ ¹MLCT appears at 475 nm. Followed by the second electron reduction, the absorbance at ca. 475 nm is increased.

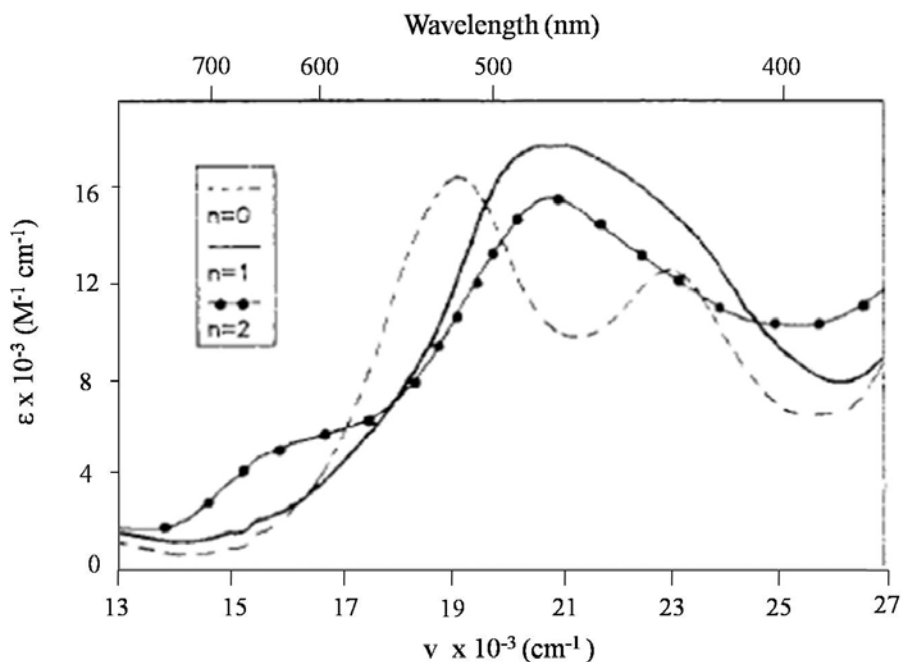


Figure 1.14 Visible region of the electronic spectra of $[\{(bpy)_2Ru\}_2(dpp)]^{(4-n)+}$ ($n = 0, 1, 2$), where n indicates the number of redox electrons added and ϵ is the extinction coefficient in $M^{-1}\text{ cm}^{-1}$ ($bpy = 2,2'$ -bipyridine and $dpp = 2,3$ -bis(2-pyridyl)pyrazine).²⁰

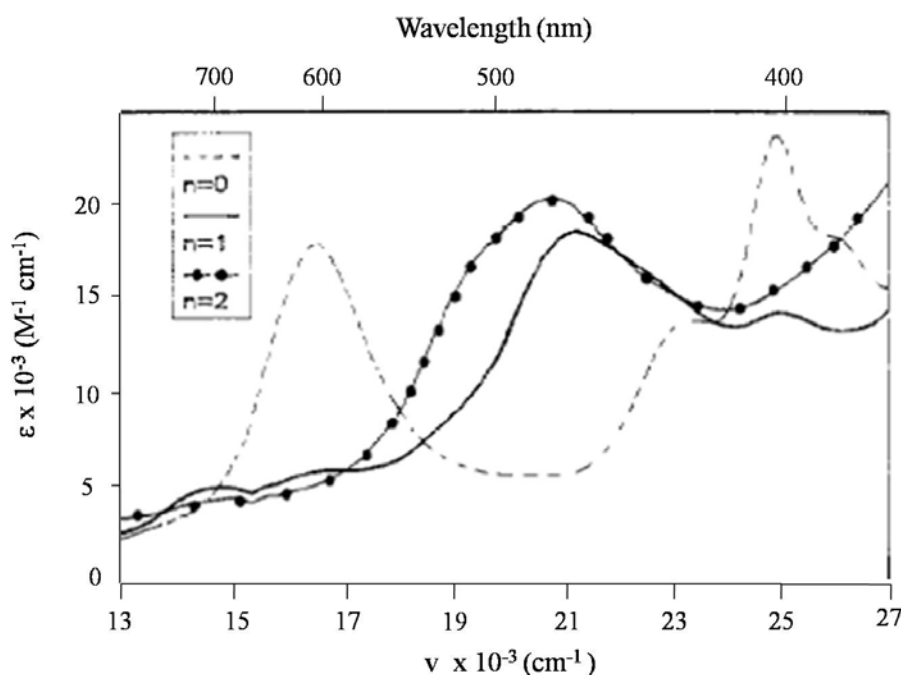


Figure 1.15 Visible region of the electronic spectra of $[\{(bpy)_2Ru\}_2(dpq)]^{(4-n)+}$ ($n = 0, 1, 2$), where n indicates the number of redox electrons added and ϵ is the extinction coefficient in $M^{-1} cm^{-1}$ ($bpy = 2,2'$ -bipyridine and $dpq = 2,3$ -bis(2-pyridyl)quinoxaline).²⁰

1.3.6 Excited State Properties

1.3.6.1 Excited State Properties of Ru and Os Polyazine Complexes

When a Ru or Os polyazine complex absorbs light, the excited state can then transfer that energy within different excited states according to their energy levels. Capturing this energy depends critically on understanding the properties of photochemically generated excited states – a set of properties often called “photophysics”. The photophysical properties of Ru and Os polyazine complexes can be studied in terms of excited state energy and excited state dynamics, both of which correlate to the electronic structure of these complexes. To help explain the photophysics of Ru or Os polyazine complexes, energy state diagrams are typically used. Figure 1.16 illustrates the energy state diagram for $[(bpy)_2Ru(dpq)Ru(bpy)_2]^{4+}$, which includes characteristic processes such as radiative decay (r) (straight lines), and nonradiative process (nr) (wavy lines). This figure depicts the conversion between states of different multiplicity, known as intersystem crossing (isc). Conversion between states of

the same multiplicity is internal conversion (ic). The emission occurring when converting between states of different multiplicity is phosphorescence while emission accompanying conversion between states of the same multiplicity is fluorescence.

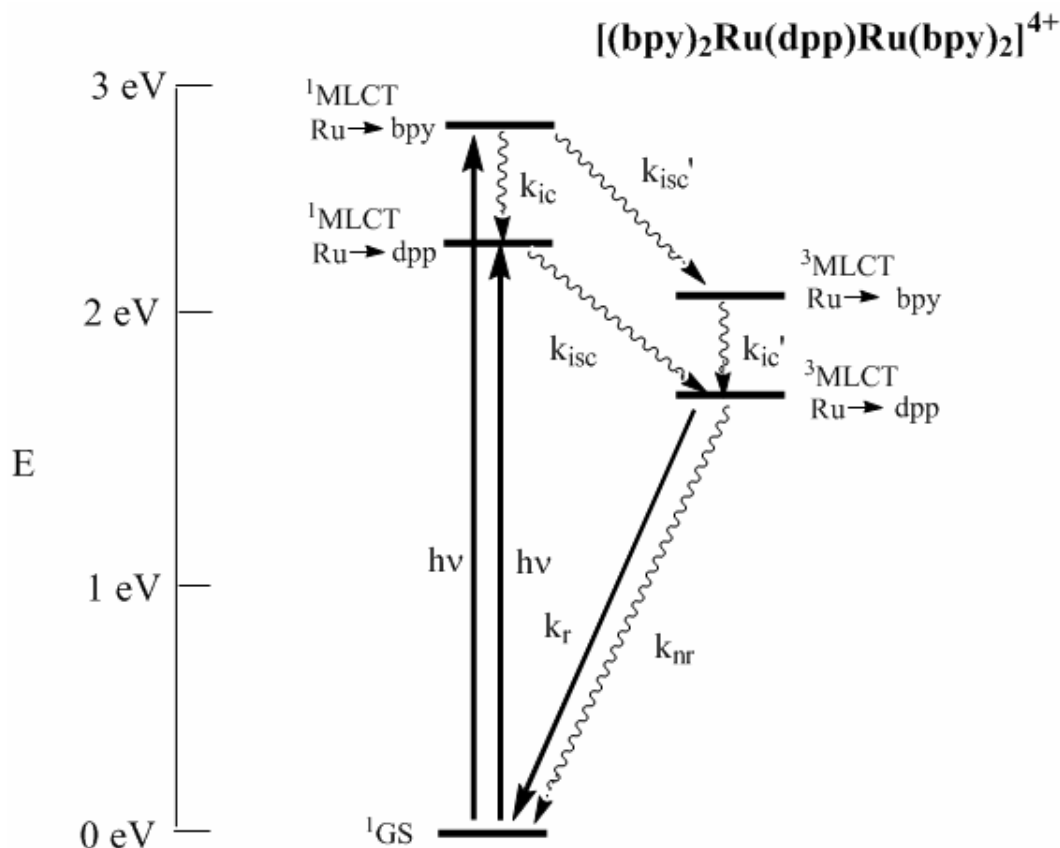


Figure 1.16 Energy state diagram of $[(bpy)_2Ru(dpp)Ru(bpy)_2]^{4+}$. GS = ground state; MLCT = metal to ligand charge transfer; isc = intersystem crossing; ic = internal conversion; r = radiative decay; nr = nonradiative decay (bpy = 2,2'-bipyridine, dpp = 2,3-bis(2-pyridyl)pyrazine).

Ru (and Os) polyazine complexes typically form a 1MLCT state upon visible light excitation. The excited electron retains its spin quantum number. The excited electron flips spin, resulting in a change from the singlet state (1MLCT) to the triplet state (3MLCT), which is lower in energy. For example, the bimetallic complex $[(bpy)_2Ru(dpp)Ru(bpy)_2]^{4+}$ has $Ru(d\pi) \rightarrow bpy(\pi^*)$ 1MLCT at ca. 425 nm and the $Ru(d\pi) \rightarrow dpp(\pi^*)$ 1MLCT at 525 nm. The excited triplet states are stabilized at 605 nm for the $Ru(d\pi) \rightarrow bpy(\pi^*)$ 3MLCT and at 725 nm for the $Ru(d\pi) \rightarrow dpp(\pi^*)$ 3MLCT . For $[(bpy)_2Ru(dpp)Ru(bpy)_2]^{4+}$, all of the excited state energy is transferred (k_{ic} or k_{ic}') to the lowest $Ru(d\pi) \rightarrow dpp(\pi^*)$ 3MLCT energy state with

unit efficiency. This ³MLCT state emits visible light with a rate constant of k_r . The lifetime of this emission τ is the reciprocal of all of the rate constants that deactivate that state:

$$\tau = 1/(k_r + k_{nr}) \quad (\text{eq 3})$$

The efficiency or quantum yield of the emission Φ^{em} , which is the efficiency of the emission, corresponds to the ratio of the radiative decay rate over the sum of all the rates at which various processes deactivate the emissive state:

$$\Phi^{\text{em}} = k_r/(k_r + k_{nr}) \quad (\text{eq 4})$$

The photophysical properties of some selected building blocks and supramolecular systems are summarized in Table 1.3.

Table 1.3 Photophysical properties of selected Ru or Os polyazine complexes. ^a

Complex	RT		77 K		
	$\lambda_{\text{max}}^{\text{em}}$ (nm)	τ (μs)	Φ^{em} $\times 10^3$	$\lambda_{\text{max}}^{\text{em}}$ (nm)	τ (μs)
$[(\text{bpy})_2\text{Ru}(\text{dpp})](\text{PF}_6)_2$ ^b	660	0.23			
^c	675	0.14	51		
^d	692	0.28		637	4.1
$[(\text{bpy})_2\text{Ru}(\text{dpq})](\text{PF}_6)_2$ ^e	760	< 0.02			
$[\{(\text{bpy})_2\text{Ru}\}_2(\text{dpp})](\text{PF}_6)_4$ ^f	790	0.14	25	702	2.38
^g	802	0.13	3		
$[\{(\text{bpy})_2\text{Ru}\}_2(\text{dpq})](\text{PF}_6)_4$ ^h	822	< 0.02			
$[(\text{bpy})_2\text{Os}(\text{dpp})](\text{PF}_6)_2$ ⁱ	1130	~ 0.005			
$[\{(\text{bpy})_2\text{Os}\}_2(\text{dpp})](\text{PF}_6)_4$ ^j				928	
$[\{(\text{bpy})_2\text{Ru}(\text{dpp})\}_3\text{Ru}](\text{PF}_6)_8$ ^k	811	0.06	1	727	1.38
$[\{(\text{bpy})_2\text{Ru}(\text{dpp})\}_2\text{Ru}_2\text{RuCl}_2](\text{PF}_6)_{12}$ ^l	895	< 0.01		880	

^a $\lambda_{\text{max}}^{\text{em}}$ is emission maximum, τ is emission lifetime in μs , Φ^{em} is emission quantum yield at room temperature. All experiments were performed in spectrograde CH_3CN unless otherwise specified; (bpy = 2,2'-bipyridine, dpp = 2,3-bis(2-pyridyl)pyrazine, dpq = 2,3-bis(2-pyridyl)quinoxaline).

^b ref. 76 ; ^c ref. 13 ; ^d ref. 56 ; ^e ref. 76 ; ^f ref. 77 ; ^g ref. 78 ; ^h ref. 76 ; ⁱ ref. 79 ;

^j ref. 80 and the experiment was carried at 90 K ; ^k ref. 78 ; ^l ref. 81.

Spectroscopic measurements provide information about the kinetics of interstate conversion after photoinitiation. For example, when dpp changes from monochelating in $[(\text{bpy})_2\text{Ru}(\text{dpp})](\text{PF}_6)_2$ to bischelating in $[\{(\text{bpy})_2\text{Ru}\}_2(\text{dpp})](\text{PF}_6)_4$, the stabilized π^* orbital lowers the energy of the $\text{Ru}(\text{d}\pi) \rightarrow \text{dpp}(\pi^*)$ $^3\text{MLCT}$ state emission from 660 nm to 760 nm. According to the energy gap law,⁶⁴⁻⁶⁶ the lower the energy of the emissive state, the higher the nonradiative decay rate k_{nr} . As a result of increased k_{nr} , the quantum yield and the lifetime of the emission from $\text{Ru}(\text{d}\pi) \rightarrow \text{dpp}(\pi^*)$ $^3\text{MLCT}$ state both decrease from $[(\text{bpy})_2\text{Ru}(\text{dpp})](\text{PF}_6)_2$ to $[\{(\text{bpy})_2\text{Ru}\}_2(\text{dpp})](\text{PF}_6)_4$. Comparing $[\{(\text{bpy})_2\text{Ru}\}_2(\text{dpp})](\text{PF}_6)_4$ and $[\{(\text{bpy})_2\text{Ru}(\text{dpp})\}_3\text{Ru}](\text{PF}_6)_8$, it is observed that they both display typical $\text{Ru}(\text{d}\pi) \rightarrow \mu\text{-dpp}(\pi^*)$ $^3\text{MLCT}$ emission with no bpy based emission observed, which suggests effective energy transfer within the molecules. However, a lower emission quantum yield and a decreased excited state lifetime are observed for $[\{(\text{bpy})_2\text{Ru}(\text{dpp})\}_3\text{Ru}](\text{PF}_6)_8$ vs. $[\{(\text{bpy})_2\text{Ru}\}_2(\text{dpp})](\text{PF}_6)_4$, indicative of more efficient nonradiative decay in the larger tetrametallic assembly.

1.3.6.2 Energy Transfer

Energy transfer is a common excited state quenching pathway. Figure 1.17 illustrates the typical energy transfer processes (also internal conversion processes: k_{ic} or k_{ic}') occurring in $[(\text{bpy})_2\text{Ru}(\text{dpp})\text{Os}(\text{bpy})_2]^{4+}$. Upon photoexcitation, the optically populated $\text{Ru}(\text{d}\pi) \rightarrow \text{dpp}(\pi^*)$ $^1\text{MLCT}$ state undergoes intersystem crossing (k_{isc}) to the $\text{Ru}(\text{d}\pi) \rightarrow \text{dpp}(\pi^*)$ $^3\text{MLCT}$ state followed by very rapid energy transfer (triplet-to-triplet) to the emissive $\text{Os}(\text{d}\pi) \rightarrow \text{dpp}(\pi^*)$ $^3\text{MLCT}$ state. It is also possible that the energy from $\text{Ru}(\text{d}\pi) \rightarrow \text{dpp}(\pi^*)$ $^1\text{MLCT}$ undergoes excited state energy transfer (singlet-to-singlet) to the $\text{Os}(\text{d}\pi) \rightarrow \text{dpp}(\pi^*)$ $^1\text{MLCT}$ state followed by intersystem crossing from $\text{Os}(\text{d}\pi) \rightarrow \text{dpp}(\pi^*)$ $^1\text{MLCT}$ to the emissive $\text{Os}(\text{d}\pi) \rightarrow \text{dpp}(\pi^*)$ $^3\text{MLCT}$ state. This energy transfer typically occurs with near unit efficiency and over a very short period of time. Using femtosecond transient absorption spectroscopy, Campagna *et al.* observed that the intercomponent energy transfer in $[(\text{bpy})_2\text{Ru}(\text{dpp})\text{Os}(\text{bpy})_2]^{4+}$ system happens within 200 fs.⁸²

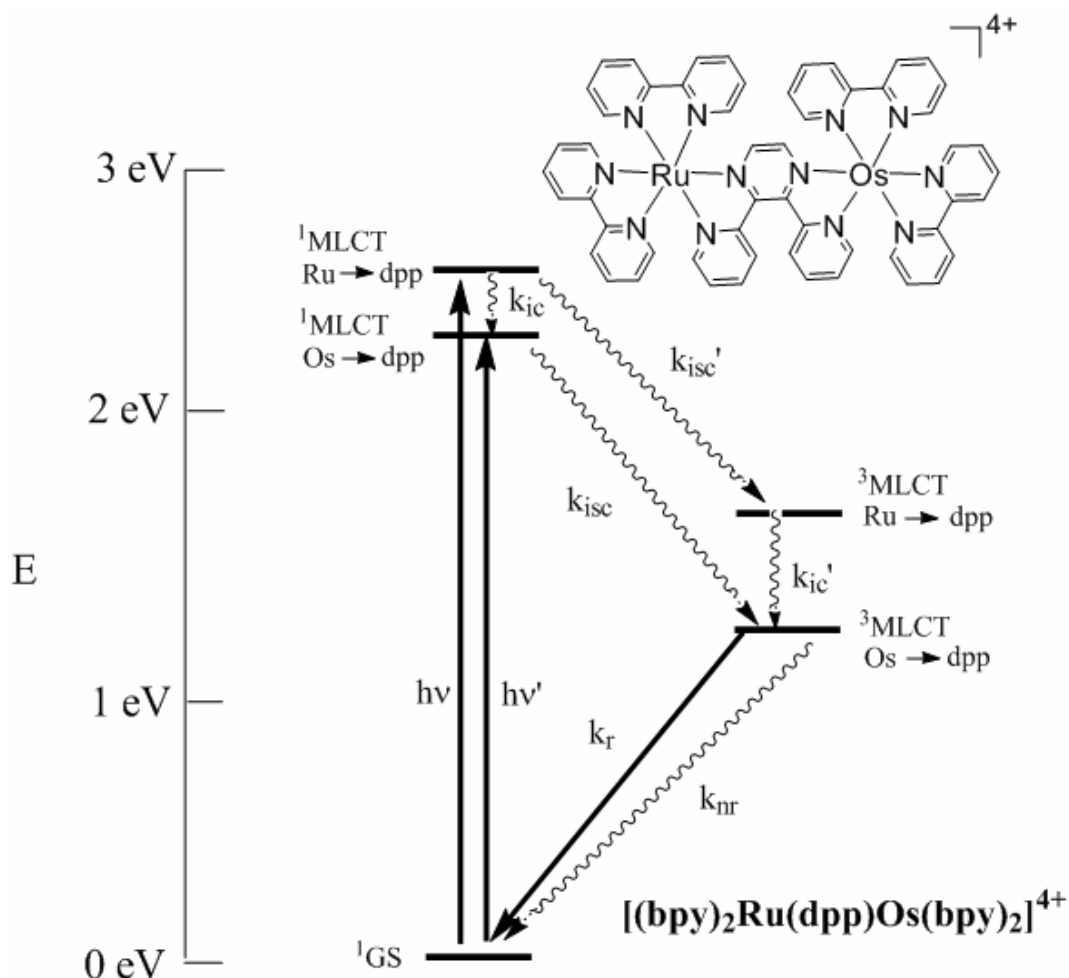


Figure 1.17 Energy state diagram of $[(bpy)_2Ru(dpp)Os(bpy)_2]^{4+}$. GS = ground state; MLCT = metal to ligand charge transfer; isc = intersystem crossing; ic = internal conversion; r = radiative decay; nr = nonradiative decay (bpy = 2,2'-bipyridine, dpp = 2,3-bis(2-pyridyl)pyrazine).

Balzani reported detailed studies of energy transfer within symmetric Ru/Os mixed-metal supramolecules (Figure 1.18 and 1.19), with dpp as the bridging ligands and bpy or biq as the terminal ligands. Based on the fact that only luminescence from the lowest energy level was observed for all of the multimetallic Ru/Os complexes, they concluded that rapid intercomponent energy transfer from all possible excited states to the lowest emissive energy state had occurred.^{5, 49, 53, 80, 83} The likely energy pathways for this phenomenon are shown in Figure 1.18, with arrows.⁵ The order of the energy of the moieties' lowest 3MLCT states is summarized as: $[Os(bpy)_2(\mu-dpp)]^{2+} < [Os(biq)_2(\mu-dpp)]^{2+} < [Os(\mu-dpp)_3]^{2+} < [Ru(bpy)_2(\mu-dpp)]^{2+} < [Ru(biq)_2(\mu-dpp)]^{2+} < [Ru(bpy)(\mu-dpp)_2]^{2+} < [Ru(\mu-dpp)_3]^{2+}$. The

researchers prepared various multimetallic Ru or Os polyazine complexes however no example containing mixed bridging ligands and mixed metals was ever reported.

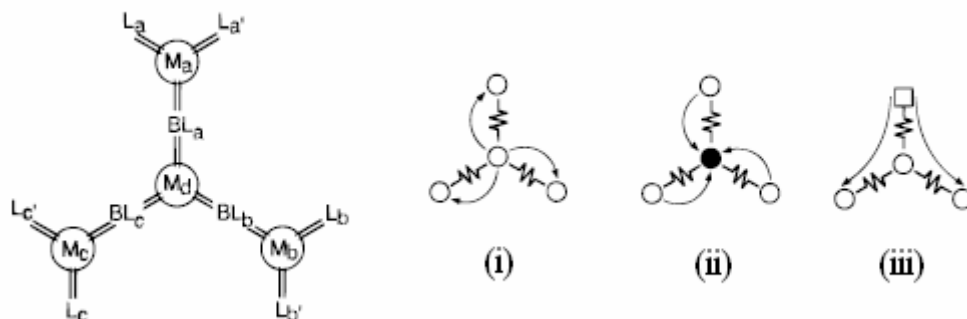


Figure 1.18 Energy migration patterns in tetranuclear compounds. The empty and shaded circles or squares indicate Ru^{2+} and Os^{2+} , respectively. In the peripheral positions, circles and squares indicate $\text{M}^{\text{II}}(\text{bpy})_2$ and $\text{M}^{\text{II}}(\text{biq})_2$ components, respectively. For the bridging ligand: wavy lines, dpp.⁵ (bpy = 2, 2'-bipyridine, biq = 2,2'-biquinoline, dpp = 2,3-bis(2-pyridyl)pyrazine).

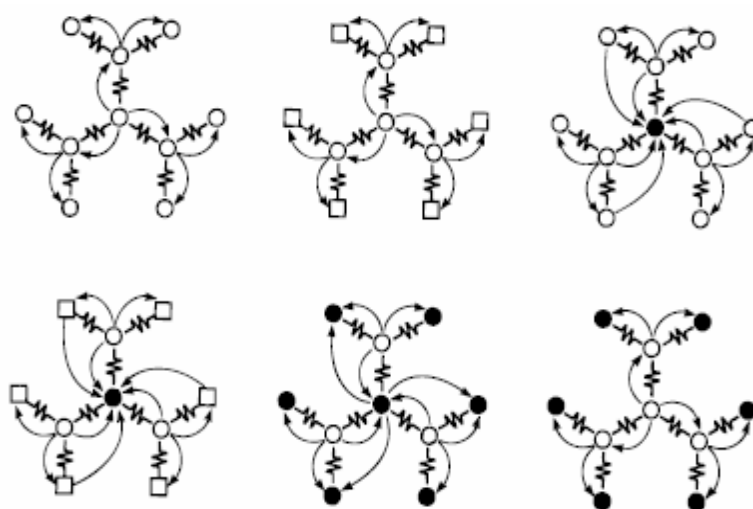


Figure 1.19 Energy migration patterns in decanuclear compounds. The empty and shaded circles or squares indicate Ru^{2+} and Os^{2+} , respectively. In the peripheral positions, circles and squares indicate $\text{M}^{\text{II}}(\text{bpy})_2$ and $\text{M}^{\text{II}}(\text{biq})_2$ components, respectively. For the bridging ligand: wavy lines, dpp.⁵ (bpy = 2, 2'-bipyridine, biq = 2,2'-biquinoline, dpp = 2,3-bis(2-pyridyl)pyrazine).

1.3.6.3 Electron Transfer

After absorbing the light, the excited electron may transfer between orbitals of different components, resulting a change of molecular energy state correspondingly.^{5, 60} For

example, if the electron transfers from the π^* orbital of bpy to the π^* orbital of μ -dpp, it corresponds to the internal conversion between $\text{Ru}(d\pi) \rightarrow \text{bpy}(\pi^*)$ $^1\text{MLCT}$ and $\text{Ru}(d\pi) \rightarrow \mu\text{-dpp}(\pi^*)$ $^1\text{MLCT}$, Figure 1.16.

MacDonnell and Campagna reported an interesting bimetallic Ru complex that photochemically collects two or more electrons.⁸⁴⁻⁸⁶ This system couples two Ru LA units through an extended aromatic BL, resulting in $[(\text{phen})_2\text{Ru}(\text{tatpp})\text{Ru}(\text{phen})_2]^{4+}$ (phen = 1,10-phenanthroline and tatpp = 9,11,20,22-Tetraazatetrapyrido[3,2-a:2'3'-c:3'',2''-1:2''',3'''-n]pentacene) (Figure 1.20). The extended nature of tatpp allows for the electronic isolation of the two Ru LA units. The LUMO of a ligand tatpp consists of a phen-like localized orbital that serves as the orbital for electron to be located at during the $^1\text{MLCT}$ state, as well as a central phenazine-like localized orbital that is involved in the ^3CS state, when the electron is further transferred to the phenazine. This complex functions by optical excitation of an electron into a phen-part orbital of tatpp followed by electron transfer to a lower lying secondary π^* acceptor orbital localized at the central phenazine-part of tatpp that collects the electron, with a lifetime of 1.3 μs in dichloromethane.⁸⁵ This process is depicted in Figure 1.20 and 1.21.

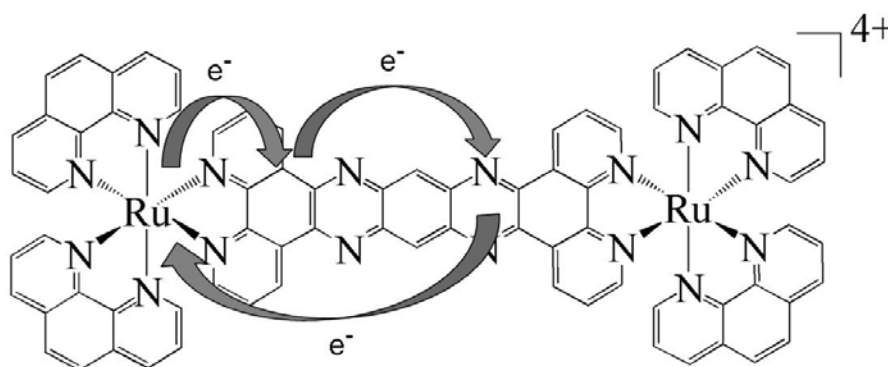


Figure 1.20 Structure of $[(\text{phen})_2\text{Ru}(\text{tatpp})\text{Ru}(\text{phen})_2]^{4+}$ (phen = 1,10-phenanthroline and tatpp = 9,11,20,22-Tetraazatetrapyrido[3,2-a:2'3'-c:3'',2''-1:2''',3'''-n]pentacene).⁸⁵

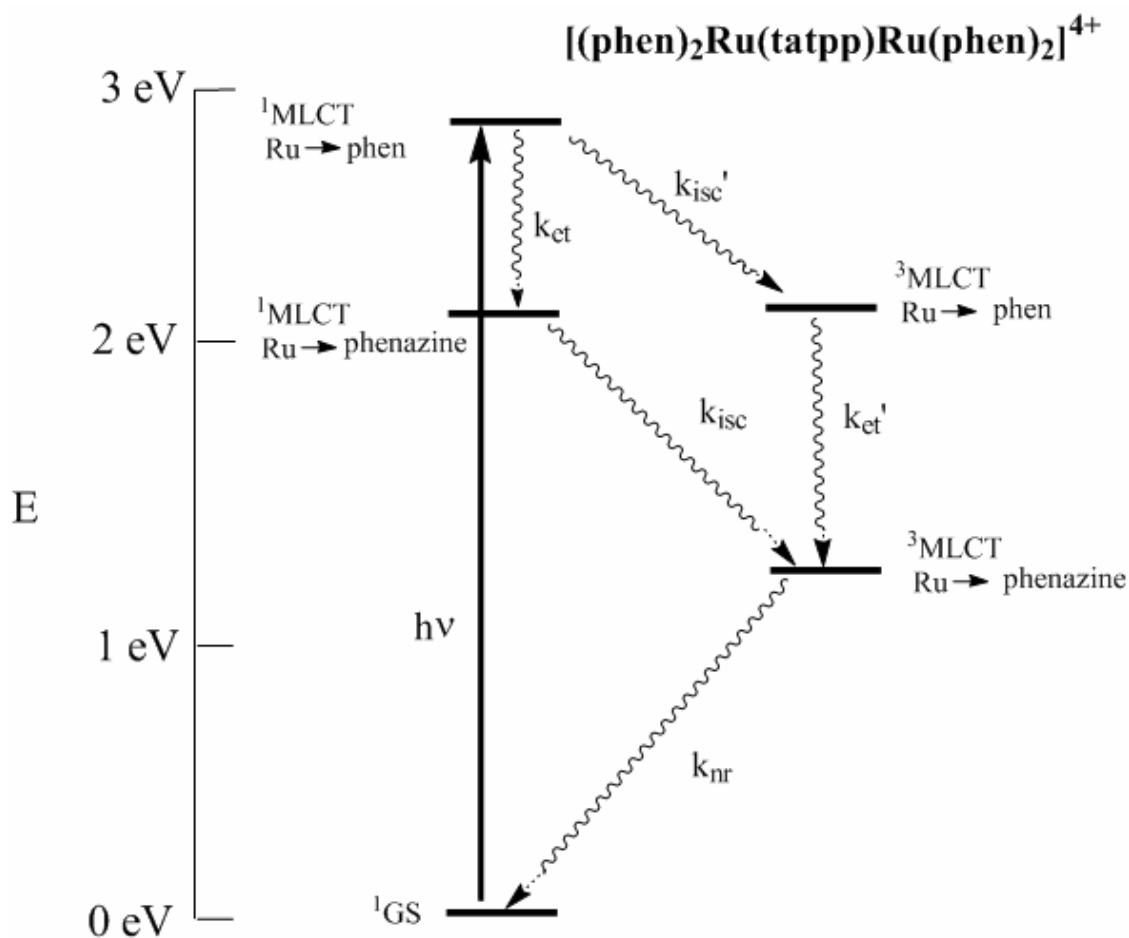


Figure 1.21 Energy state diagram of $[(\text{phen})_2\text{Ru}(\text{tatpp})\text{Ru}(\text{phen})_2]^{4+}$. GS = ground state; MLCT = metal to ligand charge transfer; isc = intersystem crossing; et = electron transfer; r = radiative decay; nr = nonradiative decay (phen = 1,10-phenanthroline, tatpp = 9,11,20,22-tetraazatetrapyrido[3,2-a:2'3'-c:3'',2''-l:2''',3'''-n]pentacene).⁸⁵

Transient absorption spectroscopy reveals a biexponential formation of an intense peak around 590 nm with characteristic decay times of 1ps and 35ps, corresponding to the state when the photoinduced electron is localized on the central phenazine-part orbital. The short 1 ps decay time frame corresponds to the direct excitation to the $\text{Ru}(d\pi) \rightarrow \text{phenazine-part}(\pi^*)$ $^1\text{MLCT}$, while 35 ps ($1/k_{\text{et}}$) decay time corresponds to rate at which the electron transfer from π^* orbital of phen-part of tatpp to the π^* orbital of phenazine-part of tatpp, resulting molecular energy state changing from $\text{Ru}(d\pi) \rightarrow \text{phen-part}(\pi^*)$ $^1\text{MLCT}$ to $\text{Ru}(d\pi) \rightarrow \text{phenazine-part}(\pi^*)$ $^1\text{MLCT}$. The charge separated state, $\text{Ru}(d\pi) \rightarrow \text{phenazine-part}(\pi^*)$ $^3\text{MLCT}$, undergoes back electron transfer to generate ground state within

4.8 ns ($1/k_{nr}$) in acetonitrile. Researchers have not been able to exclude the possibility of rapid intersystem crossing from the $Ru(d\pi) \rightarrow phen-part(\pi^*)^1MLCT$ state to the $Ru(d\pi) \rightarrow phen-part(\pi^*)^3MLCT$ state (k_{isc}), followed by energy transfer (k_{et}) from the $Ru(d\pi) \rightarrow phen-part(\pi^*)^3MLCT$ state to the $Ru(d\pi) \rightarrow phenazine-part(\pi^*)^3MLCT$ state. Nonetheless, researchers have favored this proposed mechanism, primarily based on their observation of the biexponential formation (1 and 35 ps) of an intense peak around 590 nm from transient absorption spectroscopy. Subsequent photolysis on $[(phen)_2Ru(tatpp)Ru(phen)_2]^{4+}$ in the presence of an electron donor, revealed the species as a two-electron reduced tatpp.⁸⁴

1.4 Applications of Ru and Os Polyazine Complexes

1.4.1 Charge Separation

Ru and Os polyazine complexes are excellent candidates for solar energy conversion, due to charge transfer nature of 1MLCT absorption in the visible regions. By carefully selecting the appropriate building blocks according to the relative energetics of various Ru and Os polyazine building blocks to separate the HOMO and LUMO by an energy barrier, mixed metal complexes can be synthesized that have the potential to generate effective charge separation.³⁵

Campagna *et al.* reported a Ru^{II} complex $[\{(bpy)_2Ru(\mu-dpp)\}_2Ru(bpy-TTF)](PF_6)_6$ (bpy-TTF = tetrathiafulvalene-substituted bipyridine), which demonstrated that bpy-TTF is a better electron donor than Ru^{II} . Capable of undergoing intramolecular electron transfer, these researchers showed that this complex was able to transfer the electron from bpy-TTF to the oxidized Ru^{III} after the $Ru^{II}(d\pi) \rightarrow bpy(\pi^*)^1MLCT$ excitation.⁸⁷ Introducing the central Ru energy barrier to separate the bpy-TTF HOMO and the $\mu-dpp$ LUMO, they observed a rate of $3 \times 10^9 s^{-1}$ for the electron transfer from the bpy-TTF to the peripheral Ru^{II} . However, they also showed that the back electron transfer to the ground state was faster than the forward electron transfer, $3 \times 10^9 s^{-1}$, suggesting that no effective charge separation existed in the excited state. However, the idea of introducing an energy barrier to separate the HOMO and the LUMO has been investigated, proving that remote electron transfer does occur.

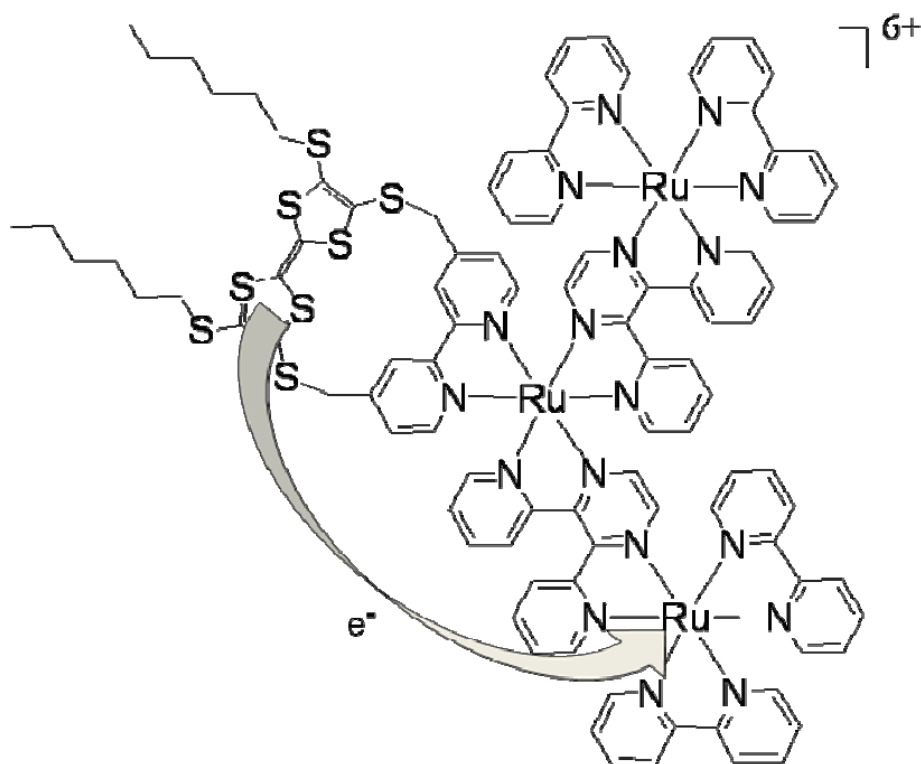


Figure 1.22 Electron transfer in $[\{(bpy)_2Ru(\mu-dpp)\}_2Ru(bpy-TTF)](PF_6)_6$ (bpy-TTF = tetrathiafulvalene-substituted polyazine, bpy = 2,2'-bipyridine, dpp = 2,3-bis(2-pyridyl)pyrazine).⁸⁷ (This picture is adapted from reference 87 but drawn by author).

Bignozzi *et al.* reported a $TiO_2-[RuCl(dcb)_2-bpa-OsCl(bpy)_2]-(PF_6)_2$ system (dcb = 4,4-(COOH)₂-2,2-bipyridine and bpa = 1,2-bis(4-pyridyl)ethane), utilizing the charge separation to increase the photoelectron injection efficiency, which is crucial to the operation of photovoltaic solar cells. After photoexcitation, the Ru^{II} moiety injects an electron into the TiO_2 conducting band, followed by an electron transfer from the Os^{II} moiety to the Ru^{III} , thereby generating the charge separated state. Selectively exciting the $Ru(d\pi) \rightarrow dcp(\pi^*)$ ¹MLCT band ($h\nu$) followed by an electron ejection from the dcp into the conducting band of the TiO_2 (1), shows that the forward electron transfer rate (2) is five times of that of back electron transfer rate, thereby enhancing the overall efficiency of a dye sensitized solar cell.³⁵

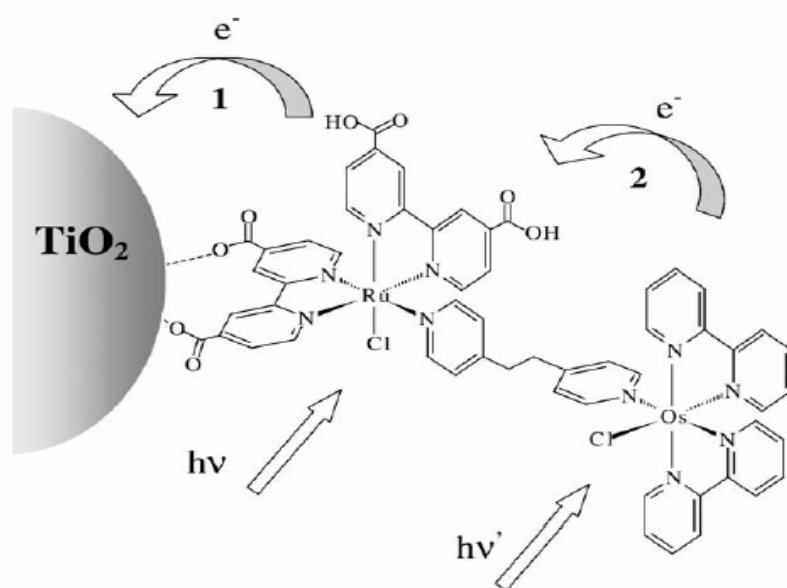


Figure 1.23 Interfacial and intramolecular electron transfer processes in $[\text{RuCl}(\text{dcb})_2\text{-bpa-OsCl}(\text{bpy})_2]^{2+}$ anchored on TiO_2 (dcb = 4,4-(COOH)₂-2,2-bipyridine and bpa = 1,2-bis(4-pyridyl)ethane).⁸⁸

1.4.2 Metal Complex Interactions with DNA and Photodynamic Therapy

In the 1960s, Rosenberg described the chemotherapeutic potential of cisplatin *cis*-[Pt(NH₃)₂Cl₂]. Substitution of the Cl ligands using appropriate solvents and DNA bases allows the Pt to crosslink with the DNA chain, which inhibits DNA replication. Since that time, the study of transition metal complexes and their interactions with DNA has continued, especially with respect to their application in photodynamic therapy.^{41, 89, 90}

Transition metal complexes typically interact with DNA via four possible mechanisms: covalent binding,^{41, 90, 91} electrostatic interaction,⁸⁹ groove binding^{89, 91, 92} or intercalation.^{89, 93} Because DNA is negatively charged, all cationic metal complexes undergo electrostatic interactions with DNA. Often the metal complexes with extended π conjugated rings intercalate into the DNA base pairs, and depending on the size and shape of those metal complexes, groove binding may occur. The complex $[\text{Ru}(\text{DIP})_3]^{2+}$ (DIP = 4,7-diphenyl-1,10-phenanthroline), Figure 1.24, has been shown to groove bind with double stranded DNA,⁹¹ while $[\text{Ru}(\text{phen})_3]^{2+}$ (phen = 1,10-phenanthroline) more weakly binds with the major groove of DNA⁹² and $[\text{Ru}(\text{bpy})_3]^{2+}$ (bpy = 2,2'-bipyridine) experiences only

electrostatic binding. In general, covalent binding between the labile metal complexes such as cisplatin, *cis*-[Pt(NH₃)₂Cl₂], is the strongest type of these four interactions.

Emission spectroscopy has also been used to detect interactions between metal complexes and DNA. For example, emissions from metal complexes may enhance (Figure 1.25), when DNA is present in the solution. This enhancement is somehow proportional to the concentration of DNA, which is associated with the solvation environment change upon the addition of the DNA species.^{92, 94}

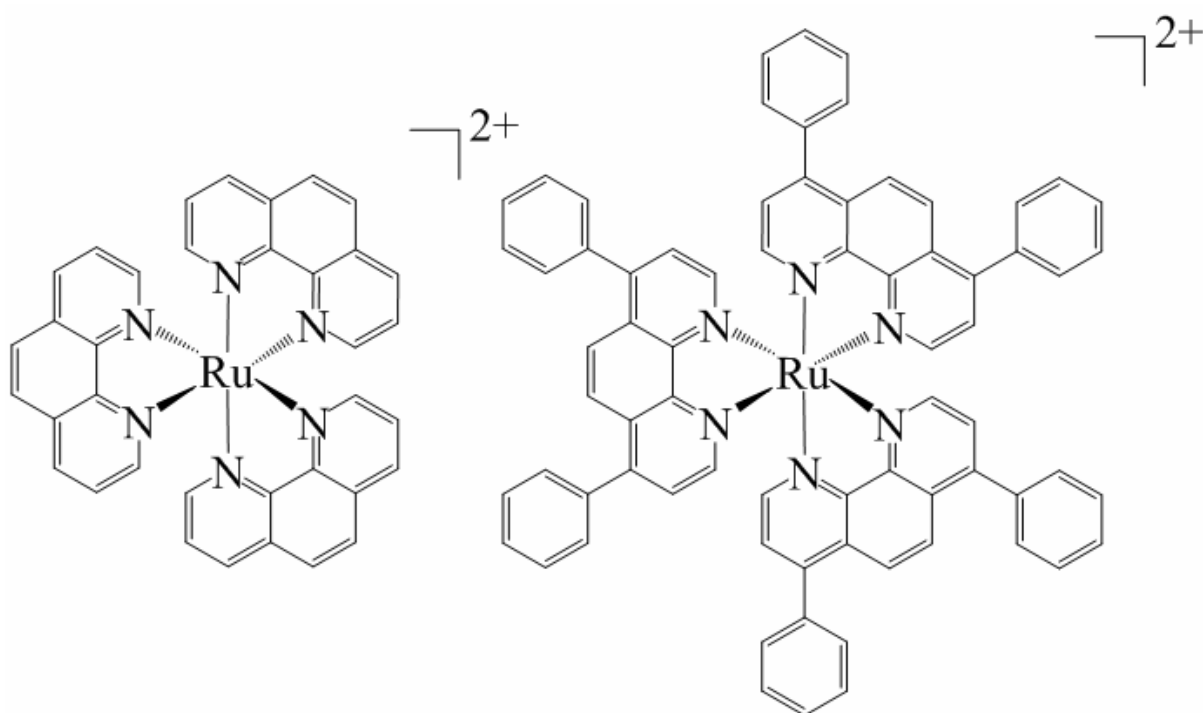


Figure 1.24 Structures of [Ru(phen)₃]²⁺ and [Ru(DIP)₃Cl₂]²⁺ (phen = 1,10-phenanthroline, DIP = 4,7-diphenyl-1,10-phenanthroline).⁹⁴

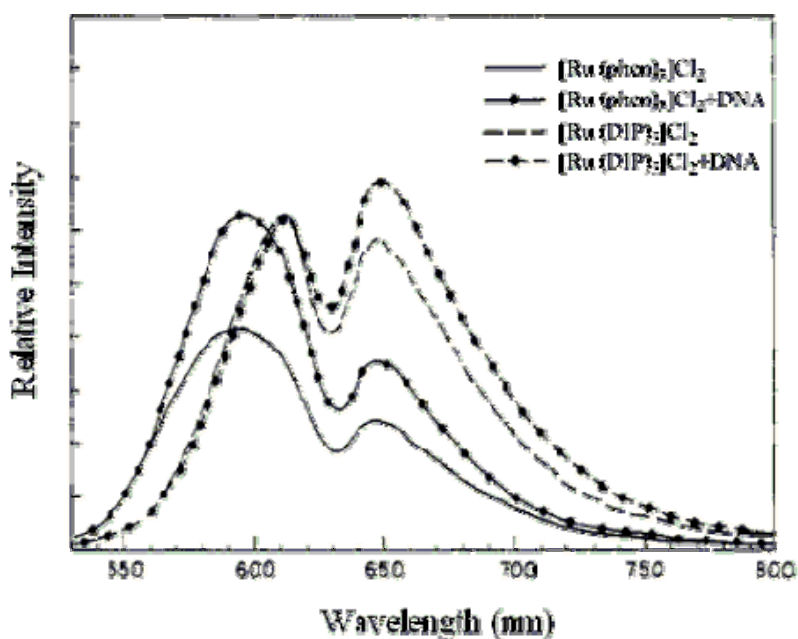


Figure 1.25 Emission spectra of $[\text{Ru}(\text{phen})_3]^{2+}$ and $[\text{Ru}(\text{DIP})_3]^{2+}$ in both the absence and presence of B-form calf thymus DNA (phen = 1,10-phenanthroline, DIP = 4,7-diphenyl-1,10-phenanthroline).⁹⁴

Ru polyazine complexes have been studied for their light activated interactions with DNA.^{41, 89, 90} The ³MLCT excited states of ruthenium polyazines can cleave DNA, typically through an oxygen mediated mechanism. For example, in the presence of oxygen, the optically populated ³MLCT state of ruthenium complexes such as $[\text{Ru}(\text{bpy})_3]^{2+}$ and $[\text{Ru}(\text{phen})_3]^{2+}$ can form a reactive oxygen species, ¹O₂,^{41, 89, 90, 95-97} that can then cause DNA strand scission.⁹⁸

The idea of combining the covalent binding capability of cisplatin with oxygen sensitizing Ru polyazine chromophore has been studied earlier.^{41-47, 99} The resulting $[(\text{tpy})\text{RuCl}(\text{dpp})\text{PtCl}_2](\text{PF}_6)$ did demonstrate covalent binding ability to DNA (Figure 1.27), similar to *cis*- $[\text{Pt}(\text{NH}_3)_2\text{Cl}_2]$.

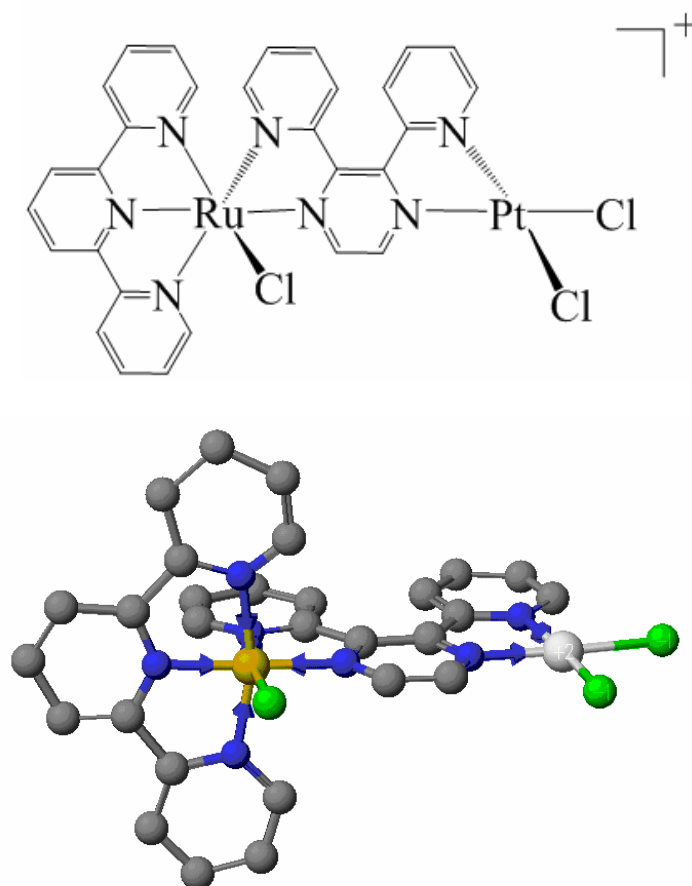


Figure 1.26 Structure of $[(\text{tpy})\text{RuCl}(\text{dpp})\text{PtCl}_2]^+$ (tpy = 2,2',6',2''-terpyridine, dpp = 2,3-bis(2-pyridyl)pyrazine).

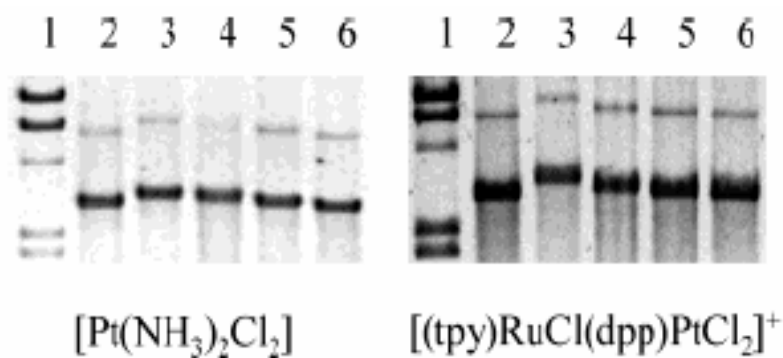


Figure 1.27 DNA binding studies for $[\text{Pt}(\text{NH}_3)_2\text{Cl}_2]$ and $[(\text{tpy})\text{RuCl}(\text{dpp})\text{PtCl}_2](\text{PF}_6)$ by agarose gel (electrophoresis using linearized pBluescript DNA; tpy = 2,2',6',2''-terpyridine, dpp = 2,3-bis(2-pyridyl)pyrazine). Lane 1 is the molecular weight standard 9.4, 6.6, 4.4, 2.3, and 2.0 kbp, lane 2 is the DNA control, lane 3 is the 5 : 1 base pairs (BP) : metal complex (MC) ratio, lane 4 is the 10 : 1 BP : MC ratio, lane 5 is the 20 : 1 BP : MC ratio, and lane 6 is the 100 : 1 BP : MC ratio.⁴³

Despite the relatively large number of Ru polyazine supramolecular assemblies that have been developed to date, few are able to couple reactive metals such as Pt to these LA units.^{28, 34, 43, 100-103} A variety of metal complexes, however, have shown promise with respect to their ability to target DNA. Many of these are, in fact, of interest as anti-cancer agents.^{22, 41, 43, 46, 47, 89, 95-98, 104-106} Moreover, because coordinated covalent binding of metal complexes to DNA can hinder transcription and/or replication, metal complexes are of interest as potential photodynamic therapy (PDT) agents, which inhibit cell function via light mediated processes such as DNA cleavage.^{41, 89, 96, 98, 105} A recent example coupling Ru polyazine chromophore and *cis*-PtCl₂ DNA binding unit has been reported by Sakai¹⁰³, which showed ability to photocleave DNA upon photoexcitation (Figure 1.28).

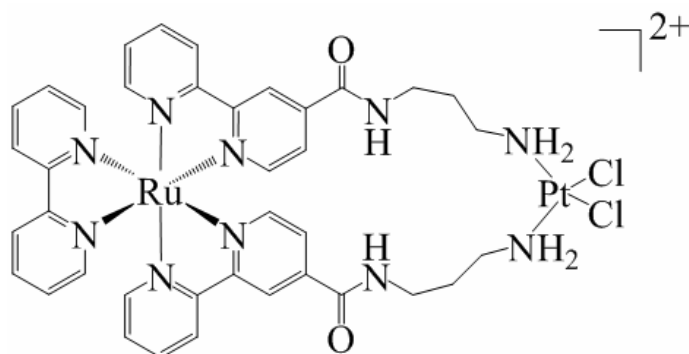
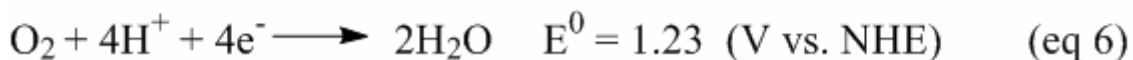
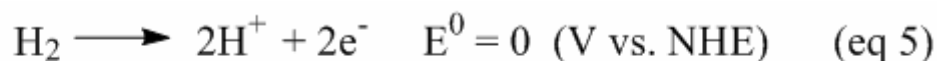


Figure 1.28 Structure of $[\text{Ru}(\text{bpy})_2\{\text{m-bpy}-(\text{CONH}-(\text{CH}_2)_3-\text{NH}_2)_2\}\text{PtCl}_2]^{2+}$ (bpy = 2,2'-bipyridine).¹⁰³

1.4.3 Photocatalyst for Hydrogen Production from Water

Using sunlight to convert solar energy into chemical energy or electricity is of great research interests worldwide – especially due to pressing environmental issues and the rising cost of fossil fuels. Splitting water into their elemental hydrogen and oxygen units using sunlight could contribute to cleaner and more effective alternative energy solutions due to the hydrogen combustion energy of 282 kJ/mol and its clean reaction product – water.¹⁰⁷⁻¹⁰⁹ It is well known that the two-electron water splitting reaction requires 1.23 eV, and most of the sunlight reaching the earth's surface from ultraviolet to visible region can provide enough energy to drive this reaction. However, sufficient direct absorption that would result in water splitting does not occur.



As noted earlier, the discovery of $[\text{Ru}(\text{bpy})_3]^{2+}$ led to photochemical studies exploring the use of metal to ligand charge transfer (MLCT) states in light-to-energy conversions. Importantly, $[\text{Ru}(\text{bpy})_3]^{2+}$ and related complexes do possess $^3\text{MLCT}$ excited states of sufficient energy to split water to H_2 and O_2 . Existing Ru systems produce H_2 using electron relays and heterogeneous metal catalysts. Upon MLCT excitation of $[\text{Ru}(\text{bpy})_3]^{2+}$, bimolecular electron transfer to $[\text{Rh}(\text{bpy})_3]^{3+}$ occurs, generating $[\text{Rh}(\text{bpy})_3]^{2+}$, which can disproportionate to both $[\text{Rh}(\text{bpy})_2]^+$ and $[\text{Rh}(\text{bpy})_3]^{3+}$. However, in the presence of a heterogeneous platinum catalyst, this system can generate hydrogen.

Recently Eisenberg *et al.* reported a platinum terpyridine chromophore that photocatalyzes hydrogen production from water utilizing a metallic Pt catalyst.¹¹⁰ Nocera *et al.* reported a homogenous H_2 production system wherein a dirhodium metal complex photocatalyzes hydrogen production from hydrohalic acids with 1% quantum efficiency.¹¹¹⁻¹¹³ Recently Sakai *et al.* reported a bimetallic Ru-Pt complex able to photocatalyze hydrogen evolution from the “visible-light-induced EDTA-reduction of water” with 1% conversion efficiency.^{114, 115} Using a Ru-Pd system, Rau *et al.* observed a production of hydrogen from triethylamine and a simultaneous hydrogenation of toluene to *cis*-stilbene.¹¹⁶ A recent communications in JACS showed these systems function through metallic Pd and Pt production.¹¹⁷ This system was proposed to collect two photoinduced electrons from electron donor triethylamine and reduce the H^+ into H_2 or it could catalyze the H_2 addition of toluene into *cis*-stilbene. Recently in our group, we designed a trimetallic Ru-Rh-Ru polypyridine complex embodying a similar design concept, which generates hydrogen from water with near 1% quantum efficiency (efficiency = 2 x moles of H_2 /moles of photon).¹¹⁸

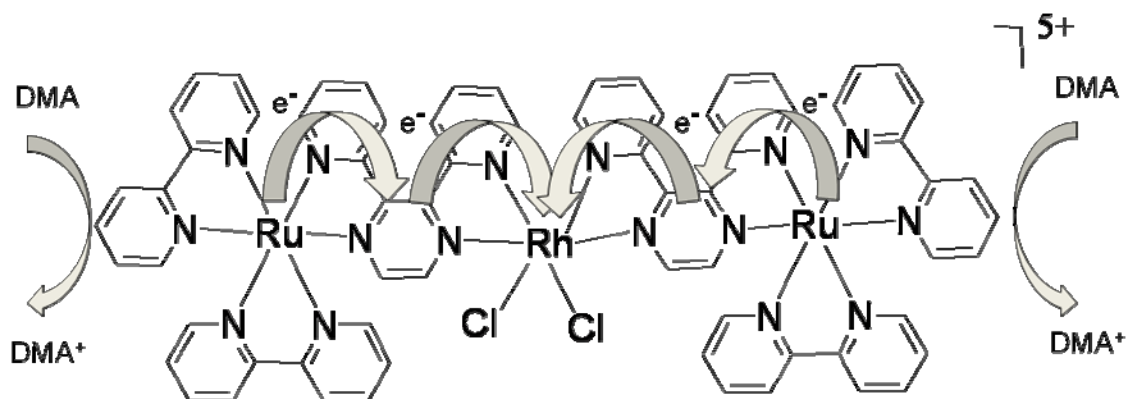


Figure 1.29 Structure of the trimetallic photocatalyst $[\{(bpy)_2Ru(dpp)\}_2Rh^{III}Cl_2]^{5+}$ (bpy = 2,2'-bipyridine, dpp = 2,3-bis(2-pyridyl)pyrazine and DMA = dimethylaniline).

1.5 Statement of Purpose

The goal of this research is to develop an understanding of how ruthenium and osmium polyazine building blocks function when incorporated within multimetallic supramolecular assemblies. That knowledge will then be used to couple appropriate Ru or Os light absorbers to a reactive Pt metal center into a supramolecular framework, which could subsequently be used for photodynamic therapy or photocatalysis of hydrogen generation from water.

As noted earlier, charge separation is one of the key aspects for solar energy conversion. For this study, we designed a hexametallc supramolecule $[\{[(bpy)_2Os(dpp)]_2Ru\}_2(dpq)](PF_6)_{12}$ (Figure 1.30 and 1.31) consisting of HOMO localizing in peripheral Os^{II} , LUMO localizing in μ -dpq and an Ru^{II} energy barrier separating the HOMO and the LUMO. This design would facilitate intramolecular charge separation.

In this study, we designed a series of tetrametallic complexes containing a trimetallic Ru (or Os) polyazine chromophore and a Pt^{II} moiety, $[\{(bpy)_2M(dpp)\}_2Ru(BL)PtCl_2](PF_6)_6$ ($M = Ru^{II}$ or Os^{II} , BL = dpp or dpq), in order to investigate the photocatalysis of hydrogen production from water in the presence of a sacrificial electron donor (Figure 1.32 and 1.33).

By combining the DNA photocleavage ability of Ru polypyridine complexes and the DNA covalent binding ability of *cis*-PtCl₂ moiety, we studied the DNA binding ability and photocleavage properties of the prototypical member of this series

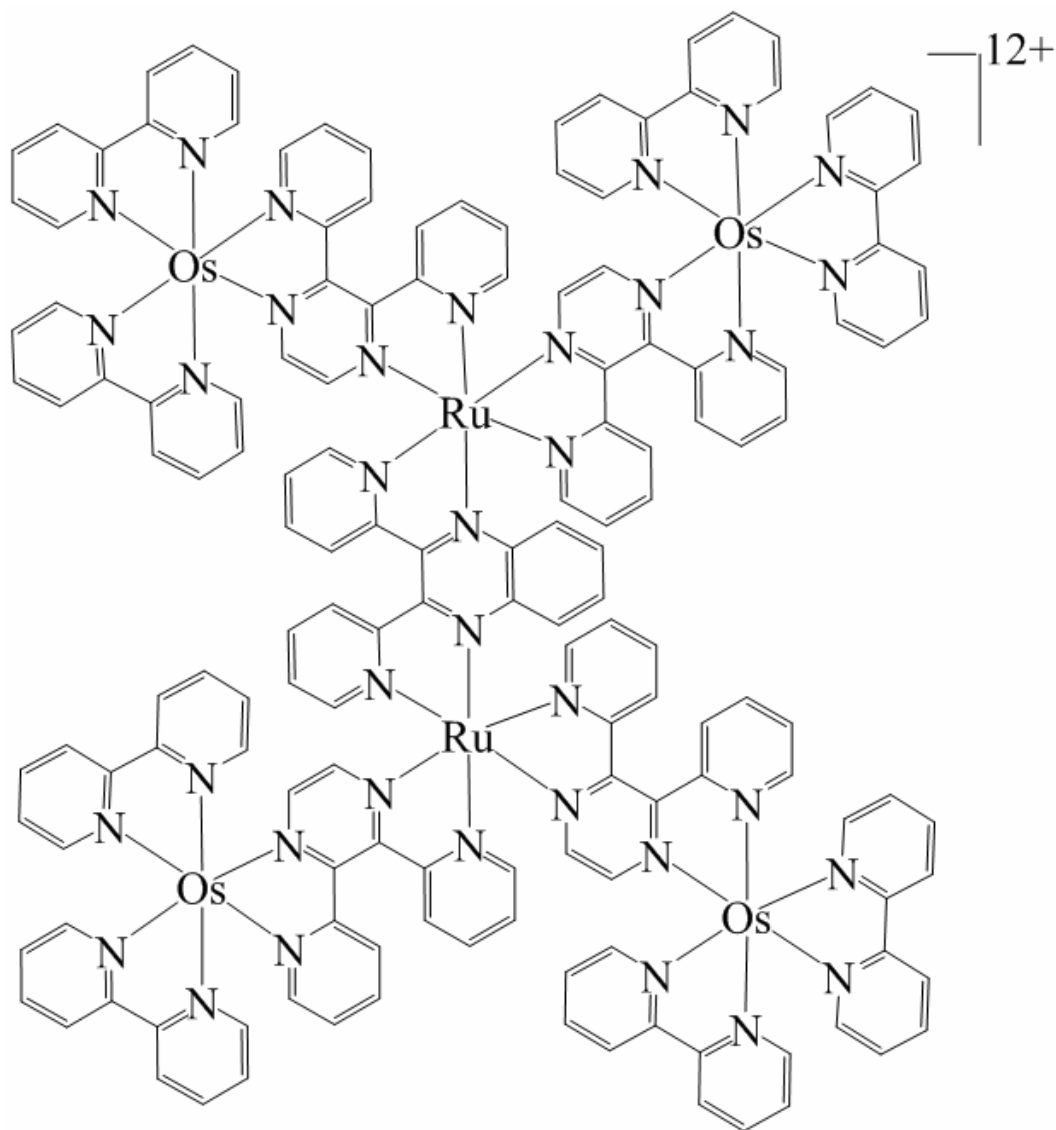


Figure 1.30 Schematic representation of a long-distance intramolecular charge separation device: $[\{[(bpy)_2Os(dpp)]_2Ru\}_2(dpq)](PF_6)_{12}$ (bpy = 2,2'-bipyridine, dpp = 2,3-bis(2-pyridyl)pyrazine and dpq = 2,3-bis(2-pyridyl)quinoxaline).

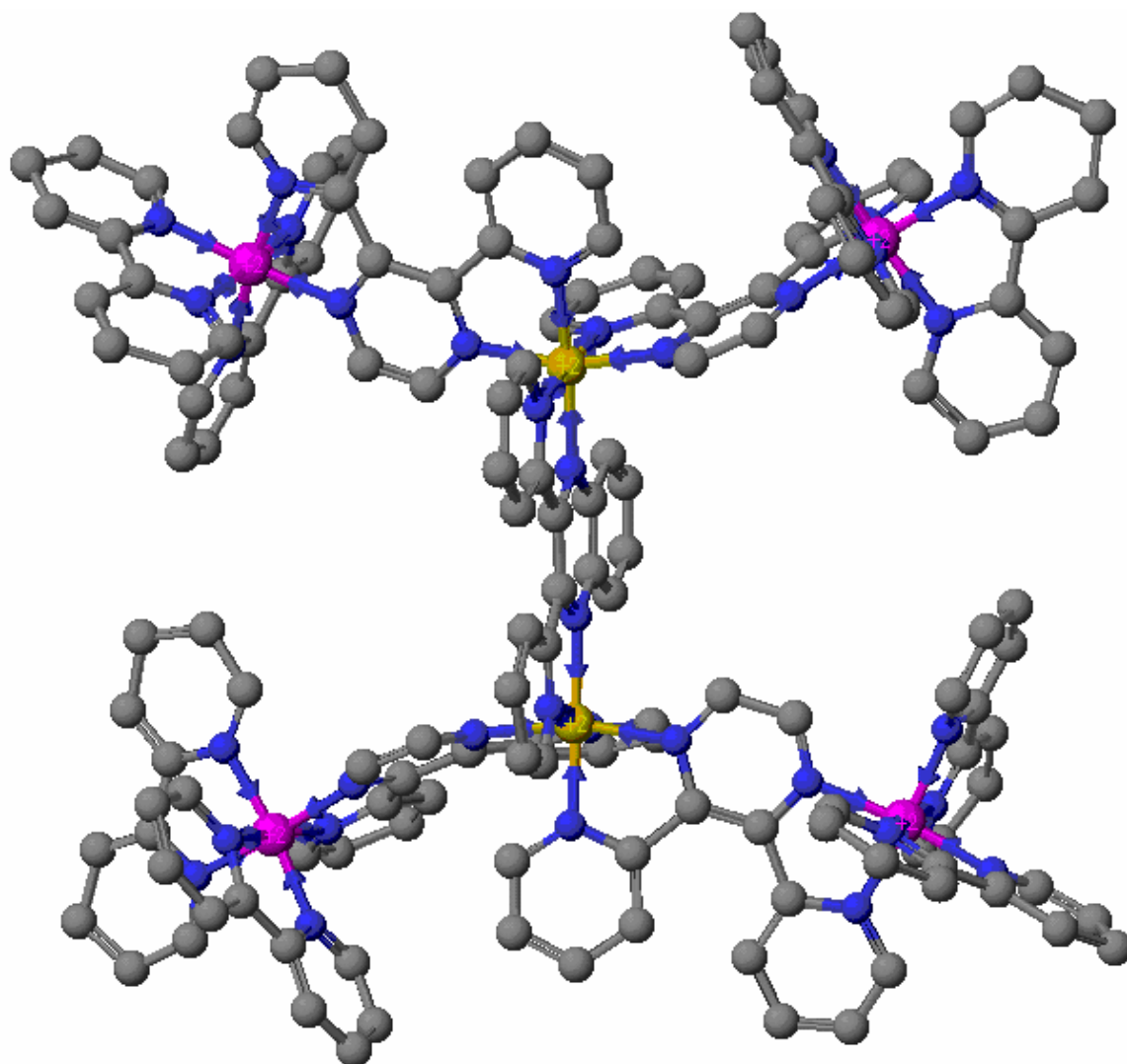


Figure 1.31 3-D representation of a long-distance intramolecular charge separation device: $[\{[(bpy)_2Os(dpp)]_2Ru\}_2(dpq)](PF_6)_{12}$ (bpy = 2,2'-bipyridine, dpp = 2,3-bis(2-pyridyl)pyrazine and dpq = 2,3-bis(2-pyridyl)quinoxaline).

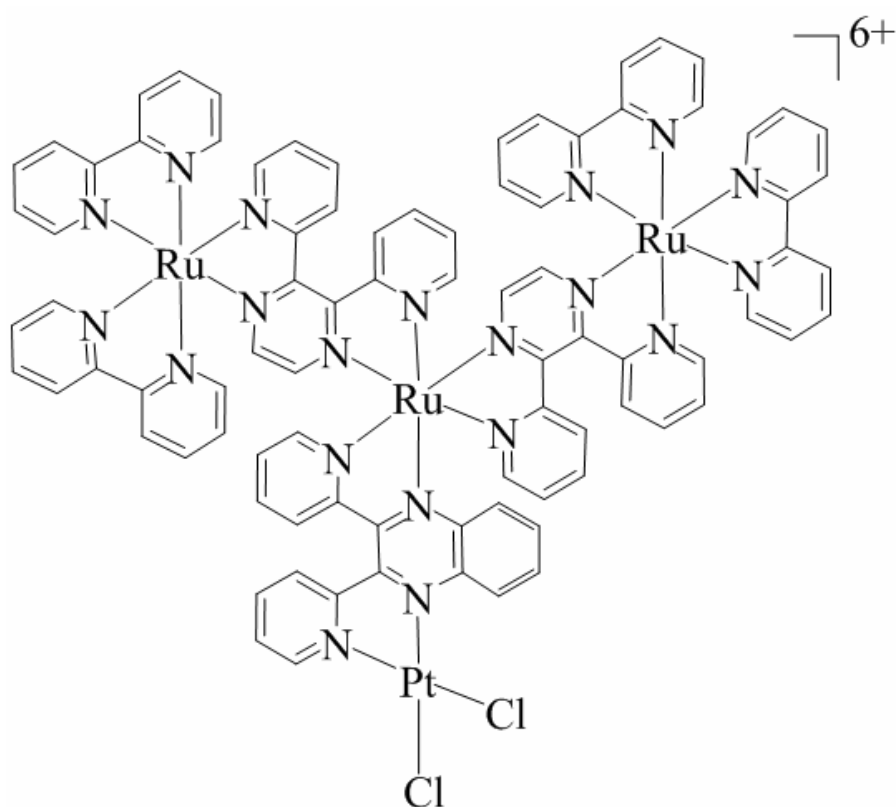


Figure 1.32 Schematic representation of $[\{ (bpy)_2Ru(dpp) \}_2Ru(dpq)PtCl_2] (PF_6)_6$ ($bpy = 2,2'$ -bipyridine and $dpq = 2,3$ -bis(2-pyridyl)quinoxaline).

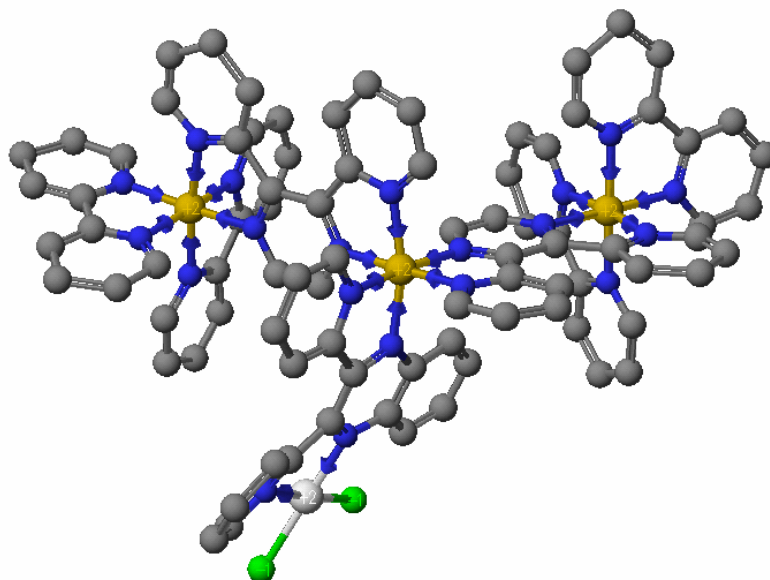


Figure 1.33 3-D representation of $[\{ (bpy)_2Ru(dpp) \}_2Ru(dpq)PtCl_2] (PF_6)_6$ ($bpy = 2,2'$ -bipyridine and $dpq = 2,3$ -bis(2-pyridyl)quinoxaline).

Chapter 2. Experiments

2.1 Materials and Solvents

Unless otherwise noted, all of the materials and solvents were reagent grade and used without further purification. The organic solvents used for synthesis were purchased from VWR in HPLC grade. For the photophysical experiments, spectral grade acetonitrile was purchased from Burdick and Jackson. Deionized water was used throughout this research. Ruthenium trichloride hydrate $\text{RuCl}_3 \cdot 3\text{H}_2\text{O}$ and osmium trichloride hydrate $\text{OsCl}_3 \cdot 3\text{H}_2\text{O}$ were purchased from Johnson Matthey. 2,2'-Bipyridine (bpy) and 2,3-bis(2-pyridyl)pyrazine (dpp) were purchased from Sigma-Aldrich. 2,3-Bis(2-pyridyl)quinoxaline (dpq) was synthesized according to the methodology described by Goodwin and Lions.¹¹⁹ The dpq ligand was purified via multiple recrystallizations and assayed by ^1H NMR spectroscopy. The $[\text{PtCl}_2(\text{DMSO})_2]$ was prepared as reported in the literature.¹²⁰ The 80-200 mesh adsorption alumina was purchased from Fisher. Sephadex LH-20 gel was purchased from Sigma-Aldrich. The supporting electrolyte tetrabutylammonium hexafluorophosphate (Bu_4NPF_6) was purchased from Fluka. For the hydrogen production experiments, high purity dimethylaniline (DMA) was purchased from Sigma-Aldrich and used without further purification. Triflic acid used in this study was purchased from Sigma-Aldrich, and ultra high purity Ar was purchased from Airgas Inc. (Radnor, PA). The LED array used for the photolysis was designed by Mr. Jared R. Brown from our research group.¹²¹ To determine the light flux of the LED array by actinometry, potassium tris(oxalato)ferrate(III) was purchased from Strem Chemicals, Inc. (Newburyport, MA) and used without further purification. Sulfuric acid, 1,10-phenanthroline (phen), and sodium acetate were purchased from Sigma-Aldrich, Inc. To determine the light flux by calorimetry, the power meter used was a Scientech, Inc. (Boulder, CO) Mentor MA10 with a MC 2501 calorimeter head unit.

For DNA experiments, dimethyl sulfoxide (DMSO, 99.6 %+) was purchased from Sigma-Aldrich. A λ DNA/*Hind*III molecular marker was purchased from Promega (Madison, WI). Dry calf thymus DNA was purchased from Rockland and dissolved into double deionized water to prepare the stock solution. The concentration of DNA was

determined by measuring the absorbance at 260 nm, then performing the calculations according to Beer's Law (extinction coefficient at 260 nm is $6600 \text{ M}^{-1} \text{ DNA base pairs cm}^{-1}$). Supercoiled, circular plasmid pUC18 DNA (P-101) was purchased from Bayou Biolabs. Electrophoresis grade agarose, boric acid, molecular biology grade N,N,N-tris(methylhydroxy)amine and monosodium phosphate were all purchased from Fisher. The control complex *cis*-[Pt(NH₃)₂Cl₂] was purchased from Alfa Aesar. Stock solutions of NaH₂PO₄ (0.1 M), 10 % w/v DMSO, 5x TBX (2.75% w/w boric acid, 5.4% w/w N(CH₂OH)₃) were made prior to beginning the DNA binding and photocleavage experiments.

2.2 Instrumentation

2.2.1 Elemental Analysis

Elemental analysis was performed by Galbraith Laboratories, Inc. (Knoxville, TN) and the samples were tested for C, H, and N percentages using a PerkinElmer Elemental Analyzer 240.

2.2.2 Mass Spectrometry

Fast-atom-bombardment mass spectrometry (FAB-MS) and matrix-assisted laser desorption/ionization mass spectrometry (MALDI-TOF MS) analyses were performed by M-Scan Inc. in West Chester, Pennsylvania. The FAB-MS was performed on a VG Analytical ZAB 2-SE high field mass spectrometer using m-nitrobenzyl alcohol as a matrix. MALDI-TOF MS was performed on an Applied Biosystems Voyager-DE Pro using 2,5-dihydroxybenzoic acid as a matrix (excited at 337 nm).

2.2.3 NMR Analysis

NMR spectra were obtained at ambient temperature in CD₃CN unless otherwise noted. ¹H NMR and COSY spectra were obtained at 400 MHz. Coupling constants J are given in Hz.

2.2.4 Electrochemical Analysis

All of the cyclic voltammetry (CV) and Osteryoung square wave voltammetry (OSWV) experiments were conducted using a one-compartment, three-electrode cell, controlled with a Bioanalytical Systems (BAS) 100B potentiostat. The working electrode was

a 1.9 mm diameter glassy carbon disk; the auxiliary electrode was a platinum wire; and the reference electrode was a Ag/AgCl electrode (0.29 V vs. NHE), which was calibrated against the FeCp₂/FeCp₂⁺ redox couple (0.67 V vs. NHE).³⁴ The supporting electrolyte was 0.1 M Bu₄NPF₆, and the measurements were carried out in Burdick and Jackson spectrograde acetonitrile under argon. Cyclic voltammetry applies a linearly varied potential upon scan time between the working electrode and reference electrode (Figure 2.1), monitoring the current change. The cyclic voltammetric measurements were made with an electro-window typically within -2 – +2 V vs. Ag/AgCl and at a scan rate of 200 mV/s unless specified otherwise. Square wave voltammetry applies pulsed potentials along with AC voltammetry techniques, providing better signal/noise ratio, lower detect limit and faster scan rate compared to cyclic voltammetry however losing the reversibility information.¹²² Compared to normal Barker square wave voltammetry (BSWV), which applies pulsed potentials on a rapidly changing potential ramp, Osteryoung square wave voltammetry (OSWV) applies pulsed potentials on a linearly increasing staircase potential-time waveform, lowers the capacity current and allows even faster scan rate (Figure 2.2). Specific parameters for OSWV were: sensitivity = 1 x 10⁻⁶ A/V, amplitude = 25 mV, frequency = 15 Hz, sampling points = 256, step E = 4 mV, quiet time = 2 sec. The measurements were carried out typically at a scan rate of 100 mV/s. For OSWV, the impurity detection limit was estimated at around +/- 15% by comparing the one electron process current and the background current. It was advised that more concentrated sample solutions should be used in future analyses to increase the signal-to-noise ratio. The working electrode was manually cleaned prior to each analysis.

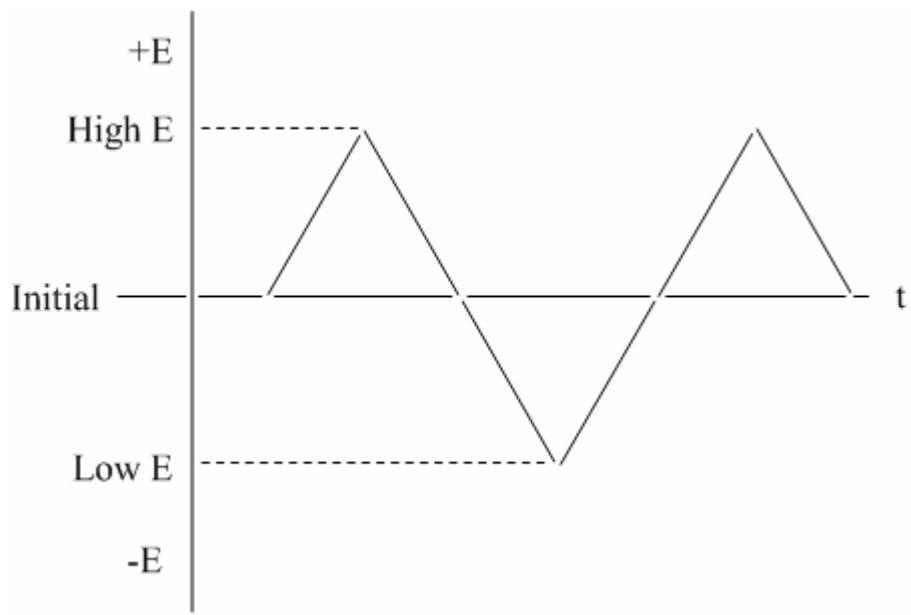


Figure 2.1 Potential waveform of cyclic voltammetry.

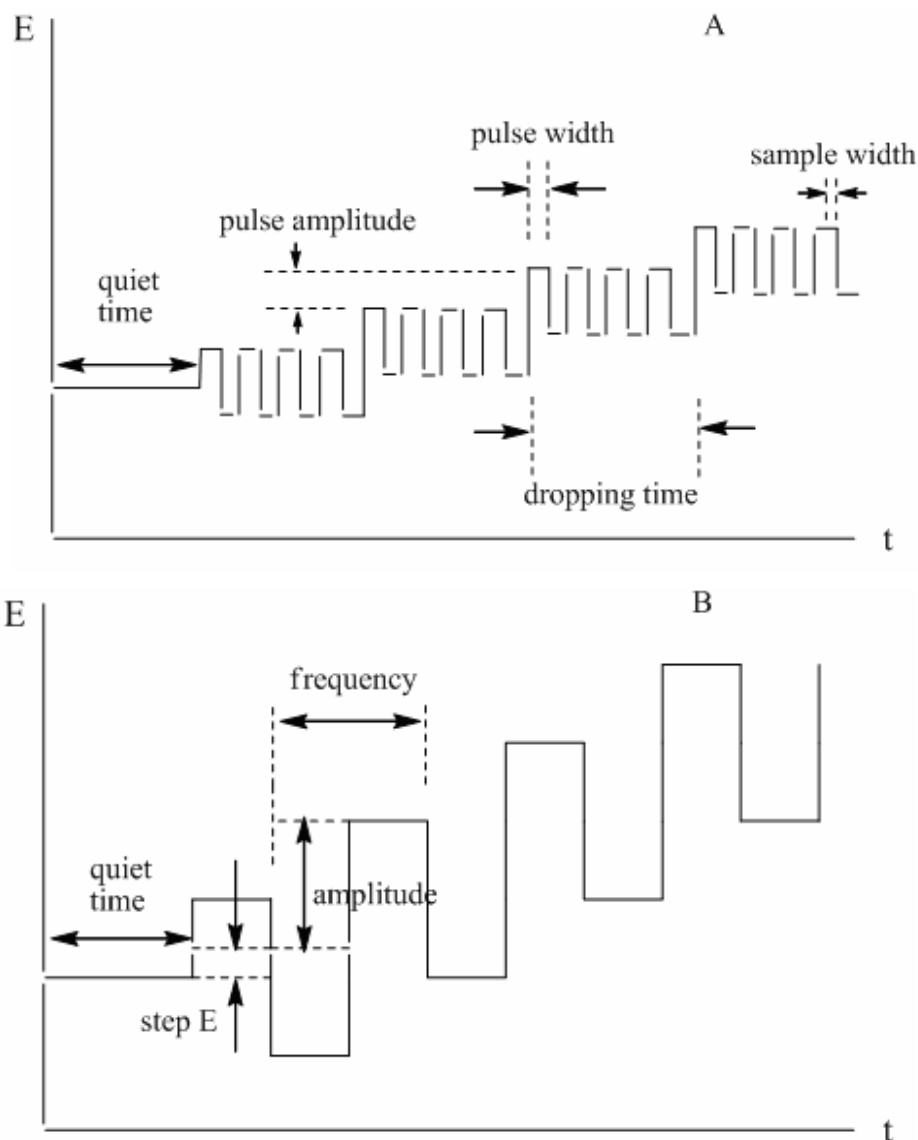


Figure 2.2 Potential waveform of Barker square wave voltammetry (A) and Osteryoung square wave voltammetry (B). (These pictures are adapted from BAS instrumental manual but drawn by author).

2.2.5 Electronic Absorption Spectroscopy

Electronic absorption spectra were recorded at room temperature using a Hewlett-Packard 8452 diode array spectrophotometer with 2 nm resolution and a 180 – 820 nm range. Spectra were collected in a 1 cm quartz cuvette after dissolving sample in UV-grade acetonitrile from Burdick and Jackson. For extinction coefficient measurements, solutions were prepared gravimetrically and the reported ϵ values represent the average of three measurements.

2.2.6 Spectroelectrochemistry

The necessary spectroelectrochemistry was performed using a HP-8452A diode array spectrophotometer H type cell of a local design, described as follows.³⁴ The cell uses a 1-cm quartz cuvette as the working compartment, Pt mesh as the working electrode, and carbon cloth as the auxiliary electrode. The Ag/AgCl reference electrode is housed in a separate compartment connected to the working compartment by a fine porosity glass frit. The Pt mesh and the Teflon tube for the Ar purge were integrated into a glass tube. Prior to the experiments, Ar gas was purged through the compartment containing the analyte so that the whole solution was fully mixed through convection and deoxygenated. When taking measurements, the integrated glass tube was lifted off the reservoir to avoid the spectrometer light beam. All electrolyses were continued until no further change in the electronic absorption spectrum was observed ($\pm 2\%$).

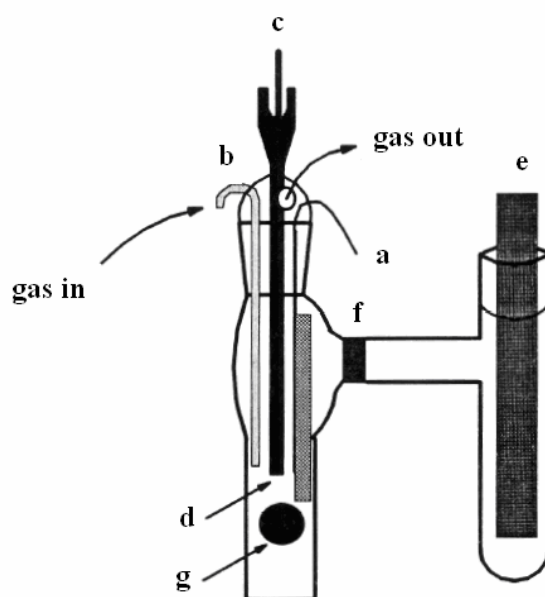


Figure 2.3 An H-type spectroelectrochemical cell. The left part is working compartment which contains 0.1 M TBAH in acetonitrile, the analyte and the following: [a] Pt mesh working electrode; [b] Teflon tube for Ar purge; [c] Ag/AgCl reference electrode; [d] integrated glass tube. The right compartment contains [e] carbon cloth auxiliary electrode and also 0.1 M TBAH in acetonitrile solution. The two compartments are bridged by a glass channel sealed by a porous glass fritted disk, which only allows passage of the electron and solvent. The [g] dark circle represents the position where the spectrometer light passes through during the measurement. All experiments were performed at room temperature.¹²³

2.2.7 Emission Spectroscopy

2.2.7.1 Emission Spectroscopy

Emission spectroscopy was performed on a modified QuantaMaster Model QM-200-45E fluorimeter from Photon Technology Inc. The system was modified to use a 150 W cooled xenon lamp excitation source, which was collected at a right angle by a thermoelectrically cooled Hamamatsu 1527 photomultiplier tube operating in photon counting mode with 0.25 nm resolution. Room temperature measurements were performed in spectrograde acetonitrile and the 77 K measurements were done using a 4:1 EtOH/MeOH glass. Since the photomultiplier response was not equal for the whole detection region, a correction file was used to obtain an accurate signal, especially for weakly emissive materials.

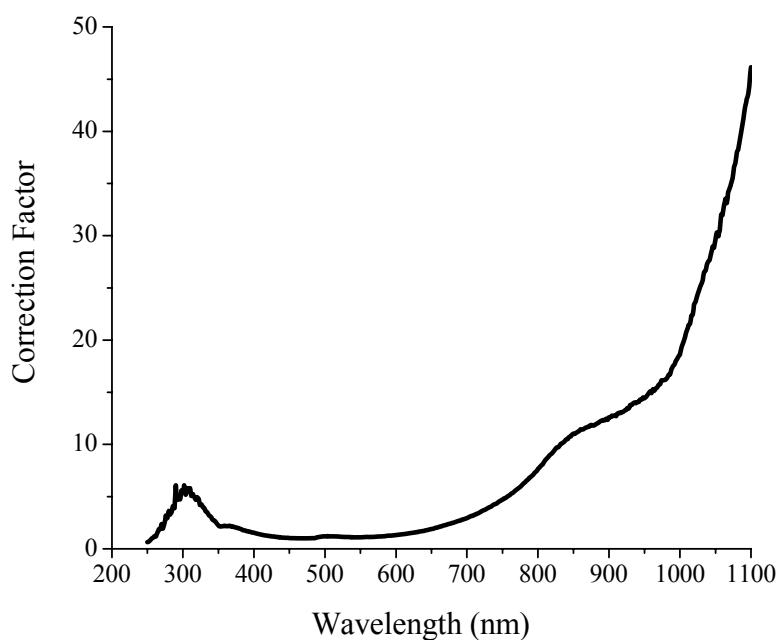


Figure 2.4 Correction file for Hamamatsu 1527 photomultiplier response.

2.2.7.2 Quantum Yield Measurement

Quantum yield is defined as the ratio of the number of photons emitted to the number of photons absorbed. The quantum yield of the complexes studied herein was typically

determined against standard emitter [(bpy)₂Os(dpp)](PF₆)₂ ($\Phi = 0.00462$ in deoxygenated CH₃CN at room temperature).^{64, 66} In order to identify the correct quantum yield standard, the electronic absorption spectrum and the emission profile should have reasonable overlap and similar efficiency of emission, to minimize the measuring error due to the instrumental response. During experimentation, the electronic absorption spectra of the studied complexes were compared to quantum yield standards at the particular wavelength where both the complexes were excited. The emission spectrum peak area of the analyte was then measured against the peak area of emission from the standard after correction for any PMT response. Since the quantum yield of the standards was known, the quantum yield of any studied complex can be calculated from the peak area ratio, as follows:

$$\Phi = \Phi_0 \times A/A_0 \quad (\text{eq 7})$$

where Φ is the quantum yield of the analyte, Φ_0 is the quantum yield of the standard, A is the area under the emission peak of the analyte, and A_0 is the area under the emission peak of the standard.

2.2.8 Excited State Emission Lifetime Measurement

Emission lifetime measurements were performed on a Photon Technology Inc. (PTI), PL2300 nitrogen laser pumping a PTI PL 201 continuously tunable dye laser as an excitation source (360 - 900 nm). This excitation source had an energy output of 240 μ J per pulse at 500 nm (average energy) and a pulse width of 500 ps. Prior to striking the sample holder, the laser pulse passed through the triggering system, which contained a beam splitter and a Motorola MK520 photodiode. To determine wavelength selection, the luminescence passed through a PTI 01-001 monochromator with gratings of 1200 lines/mm. In order to detect emissions, a Hamamatsu R928 red-sensitive photomultiplier tube was used. The PTI monochromator was at a right angle to the excitation beam. Overexposure of the PMT was prevented by slits on the monochromator, which were adjustable from 0-6 mm. These slit specifications permitted a band pass of 4 nm/mm. The signal was digitized and displayed on a LeCroy 9361 Dual 300 MHz oscilloscope (2.5 Gs/s). The acquired data represented the average of 200 scans. Fitting the acquired data to a single exponential function ($y = a+b[\exp(-kt)]$), where y is the PMT

response; a, b are scaling factors, t is time, and k is the rate constant), enabled the researcher to mathematically measure the rate constant associated with the decay of emission intensity. The noise data including $\tau \leq$ the laser pulse and the data points at the extreme end of the data collection window were removed prior to analyses. Once the rate constant, k, was determined, emission lifetime was calculated using the equation: $\tau = 1/k$.

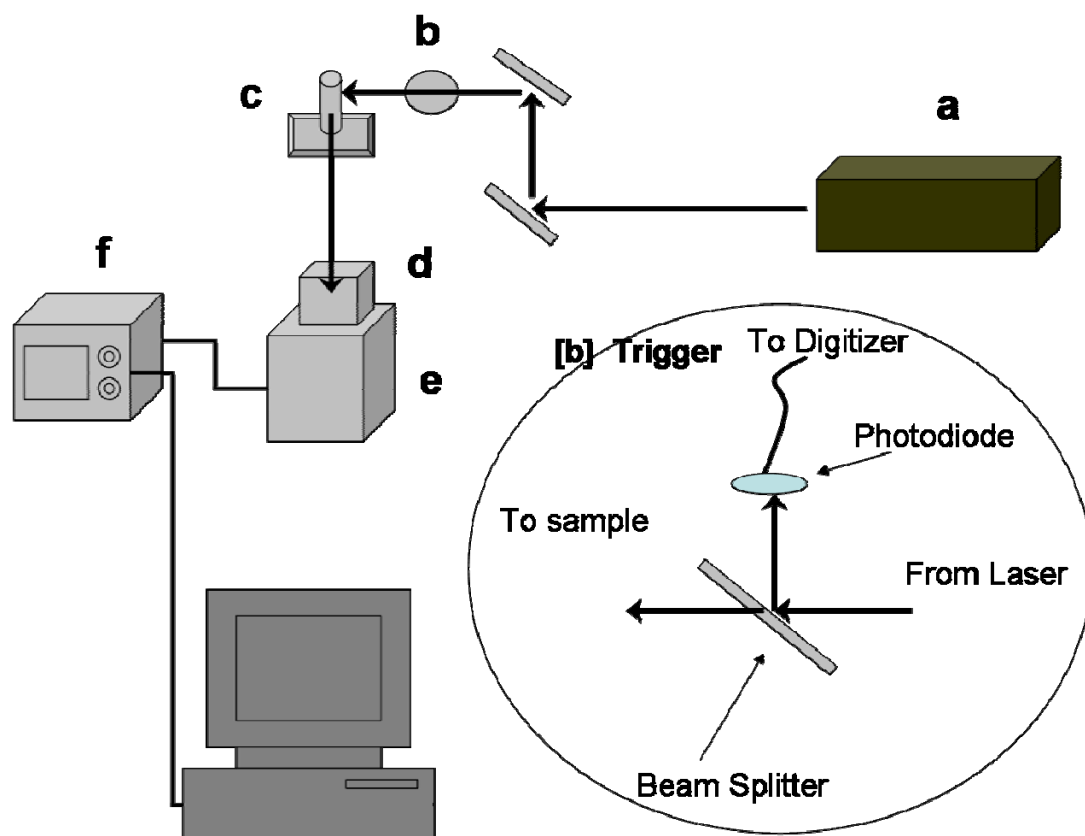


Figure 2.5 Emission lifetime measurement system: Photon Technology Inc. (PTI), PL2300 nitrogen laser. [a] a tunable nitrogen-pumped laser; [b] a series of single-face mirrors directing light pathway; [c] photochemical cell holder; [d] PTI 01-001 monochromator; [e] Hamamatsu R928 red-sensitive photomultiplier tube; [f] LeCroy 9361 Dual 300 MHz oscilloscope. An enlarged view of the triggering system [b] is provided.

2.2.9 Hydrogen Production

2.2.9.1 Photolysis

Hydrogen production photolysis was performed using an LED array of a local design as the light source (Figure 2.6B).¹²¹ Specifically, eight cell chambers were fabricated into a stainless steel box, thereby allowing eight photolysis experiments to be conducted

simultaneously. In Figure 2.6A, only the partial electrical circuit diagram is shown for the eight-LED array. The rheostats were tunable in order to achieve the desired output light flux for each LED. Prior to conducting the photolysis experiments, the LED array was calibrated by tuning the voltage input and the appropriate light flux was determined by calorimetry (6.1×10^{18} photons/min). The specific LED chosen was the Luxeon V star green LED with dominant wavelength at 530 nm and 35 nm half-width.

The complex to undergo photolysis were dissolved into spectrograde acetonitrile, then mixed with triflic acid and dimethylaniline at a predetermined ratio, after which the solvent mixture was placed in a septum topped screwable vial with an optical glass bottom. Prior to photolysis, the vial was purged with Ar and sonicated for 5 min then placed above the LED for irradiation. The samples were 22 mm in diameter and placed on the cell chamber during photolysis with LED irradiation from beneath through the optical glass. A typical photolysis experiment took approximately 3 h, but that varied depending on our specific experimental needs. The typical experimental conditions were mixing 1.5 mL of 6.3×10^{-5} M metal complex in acetonitrile, 0.50 mL of pH 2.0 H₂O acidified by CF₃SO₃H, 0.40 mL of dimethylaniline (DMA) and 1.0 mL acetonitrile. The final concentrations for each component were: ca. 2.8×10^{-5} M metal complex; 0.92 M DMA; 1.5×10^{-3} M CF₃SO₃H and 8.2 M H₂O. The pH of final solution was estimated at ca. 7.94.

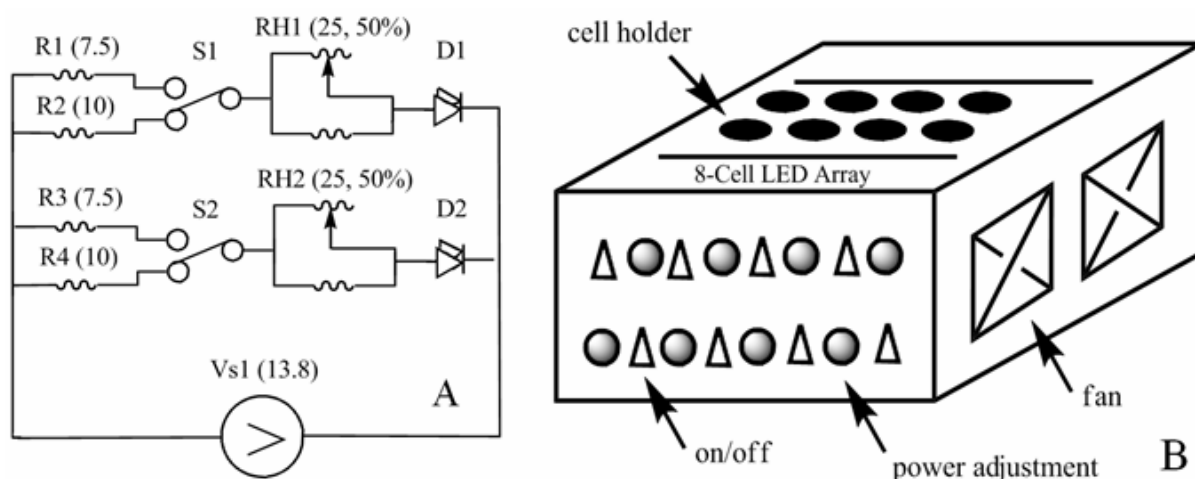


Figure 2.6 A 3rd generation eight-LED array: [A] Partial electrical circuit diagram for the eight-LED array, which shows only two of the eight LEDs. In this diagram, R1 and R3 refer to the 7.5 ohm resistors, R2 and R4 refer to the 10 ohm resistors, and R5 and R6 refer to the 5 ohm resistors. RH1 and RH2 refer to the 25 ohm rheostats which are tunable as needed. S1 and S2 are switches, D1 and D2 are LEDs, and Vs1 refers to the 13.8 V DC power supply. [B] Depiction of the eight-LED array for hydrogen production experiment. Each of the eight LEDs can be individually controlled. Eight cell chambers are housed in the stainless steel box, inside which LEDs are placed in the fashion of matching each optical glass for irradiation.¹²¹ (These pictures are adapted from reference 121 but drawn by the author).

2.2.9.2 Gas Chromatography to Quantify Hydrogen

The amount of photocatalytically generated hydrogen in the head space of the cell was quantified by using a Series 580 Gas Chromatograph (GOW-MAC instrument company), equipped with a 5 Å molecular sieves column and a rhenium tungsten thermal conductivity detector. The instrumental signal response vs. hydrogen amount was determined using a calibration curve, which was generated by plotting the injected hydrogen amount into GC vs. the peak area of hydrogen from the chromatogram (Figure 2.7).

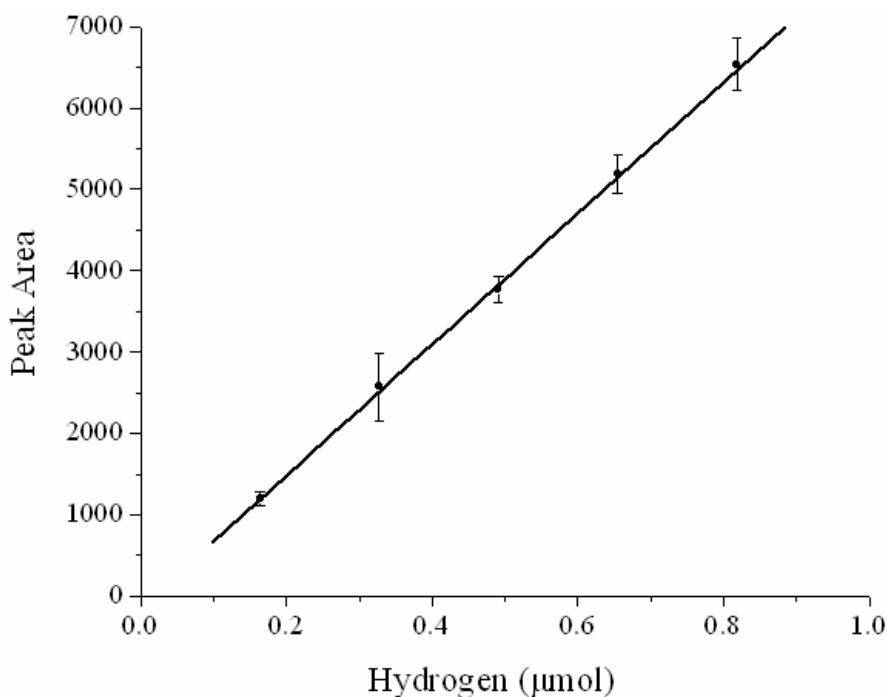


Figure 2.7 Calibration curve for hydrogen analysis using GC.

Ultra high purity Ar (Airgas) was used as the carrier gas and the experimental conditions were as follows: injection port temperature, 140 °C; column temperature 155 °C; detector temperature 170 °C; detection current 130 mA. The typical experimental conditions used for hydrogen photolysis required 1.5 mL of μM complex solution in acetonitrile, 0.50 mL of pH 2.0 H_2O with $\text{CF}_3\text{SO}_3\text{H}$, and 0.40 mL of dimethylaniline (DMA). The remaining head space was in the range of 2.3 mL. The final concentrations for each component were: ca. 2.8×10^{-5} M metal complex; 0.92 M DMA; 1.5×10^{-3} M $\text{CF}_3\text{SO}_3\text{H}$ and 8.2 M H_2O . The effective pH of the final solution was estimated at ca. 8.

Henry's Law (eq 8) was used to account for the hydrogen dissolved in the solution. The mole fraction of hydrogen at a saturated environment was used, per the literature: $\chi_{\text{H}_2} = 1.78 \times 10^{-4}$.¹²⁴ P_{H_2} refers to the partial pressure of hydrogen in the photolysis cell headspace; P_{sat} denotes the partial pressure of hydrogen in the hydrogen saturation experiment; K_{H} is the Henry's law constant; χ_{H_2} corresponds to the mole fraction of hydrogen in the photolysis cell solution; and χ_{sat} is the mole fraction of hydrogen in the hydrogen saturation experiment. In eq 8, P_{sat} is assumed to be 1 atm, since the amount of generated hydrogen is far less than the

Ar in the head space (at most 3%). The amount of hydrogen in the photolysis solution is then determined according to eq 10, where n_{sol} is the number of moles of solution, and n_{H_2} refers to the mole amount of hydrogen in the solution.

$$\frac{P_{H_2}}{P_{sat}} = \frac{(K_H)(\chi_{H_2})}{(K_H)(\chi_{sat})} \quad (\text{eq 8})$$

$$\chi_{H_2} = \frac{(P_{H_2})(\chi_{sat})}{(P_{sat})} = (P_{H_2})(\chi_{sat}) \quad (\text{eq 9})$$

$$n_{H_2} = (n_{sol})(\chi_{H_2}) \quad (\text{eq 10})$$

The total volume of hydrogen produced during photolysis is, therefore, the sum of the amount of hydrogen found in the headspace plus the amount of hydrogen found in the solution. Typically the contribution of dissolved hydrogen in solution amounts to ca. 10 % of the total volume of hydrogen.

2.2.10 DNA Photocleavage Assay (carried out by Mr. David F. Zigler)

Master solutions of the metal complexes were prepared prior to each of the photolysis experiments. Each complex was dissolved in 1% by volume aqueous DMSO : H₂O. The concentration of the master solutions containing [{(bpy)₂Ru(dpp)}₂Ru(dpp)](PF₆)₆ ($\epsilon = 34,500 \text{ M}^{-1}\text{cm}^{-1}$ at 542 nm) and [{(bpy)₂Ru(dpp)}₂Ru(dpp)PtCl₂](PF₆)₆ ($\epsilon = 34,000 \text{ M}^{-1}\text{cm}^{-1}$ at 540 nm) were determined spectrophotometrically after filtration through a 0.2 μm nylon syringe filter. The master solution of *cis*-[Pt(NH₃)₂Cl₂] was prepared with 1% by volume aqueous DMSO:H₂O using volumetric techniques. Analyte solutions for use in DNA binding and photocleavage studies were made simultaneously. Stock solutions (2 mL) containing ~1% DMSO, pUC18 DNA (15.3 μM in base pairs), 0.77 μM metal complex (20:1 BP : MC), and either 10 mM or 30 mM NaH₂PO₄. Aliquots of the stock solutions (50 μL) were incubated for 1 h in the dark at room temperature or at 37 °C in a Stable Therm incubator (Blue M Electric Company, Blue Island, IL). The remaining stock solution was then divided between two 2 mm path-length quartz cuvettes. One sample was purged by continuous flow of argon, while the other cell was left in gaseous equilibrium with the air. Both cuvettes were then illuminated with collimated 450 – 1000 nm light from a filtered 1000 W xenon arc-lamp.

During photolysis, 30 μL aliquots of the photolyzed solutions were removed at regular time intervals and stored in fresh microfuge tubes in the dark at room temperature for future analysis. The results of the DNA binding and photocleavage experiments were compared using agarose gel electrophoresis. All samples to be studied by electrophoresis were prepared according to standard protocol.²² The solutions loaded into the gel microwells (12 μL) contained 0.1 μg of DNA and 2 μL glycerin based gel loading buffer. The gels were made with 0.8 % w/w agarose, 0.55 % w/w boric acid and 1.08 % w/w $\text{N}(\text{CH}_2\text{OH})_3$. Electrophoresis was performed using an Owl Separation Systems, Inc. (Portsmouth, NH) Model B1A electrophoresis stage and an Owl Scientific Plastics OSP-105 VDC stable power supply with 1x TBX electrophoresis buffer. Gels were electrophoresed at 104 V (~ 35 mA) for ~ 90 min. Following electrophoresis, the gels were stained with ethidium bromide for 45 min followed by a 45 min soak in clean water. Gels were visualized on a Fisher Biotech UV transilluminator and photographed, using either an Olympus C-4000 Zoom or Olympus E-320 digital camera fitted with a Peca Products, Inc. (Beloit, WI) ethidium bromide filter and electrophoresis gel hood and stand.

2.2.11 Impact of DNA on Emission Spectroscopy

For the experiments studying the impact of DNA on the emission of the metal complexes, a 1.1 μM calf thymus solution was used. The metal complex was dissolved into a 1% DMSO, 10 mM Na_2HPO_4 aqueous solution, and the emission spectrum recorded. After the initial emission measurement of the original complex solution was collected, a series of solutions involving the addition of calf thymus DNA to the metal complex were analyzed. The experiments were performed at room temperature.

2.3 Synthesis and Characterization

2.3.1 Modified Preparations of Literature Complexes

$[(\text{bpy})_2\text{RuCl}_2]\cdot 2\text{H}_2\text{O}$

cis- $[\text{Ru}(\text{bpy})_2\text{Cl}_2]\cdot 2\text{H}_2\text{O}$ was prepared by a modification of the published method.⁷² Specifically, $\text{RuCl}_3\cdot 3\text{H}_2\text{O}$ (3.90 g, 14.9 mmol), 2,2'-bipyridine (4.68 g 30.0 mmol) and LiCl (4.20 g, 1.00 mmol) were added to 30 mL of DMF and heated at reflux for 8 h. The reaction

mixture was cooled to room temperature, and then 200 mL of acetone was added to the solution dropwise. The mixture was then stored in the refrigerator overnight. The solution was filtered and the red filtrate was separated from the dark green precipitate. The solid was washed with cool deionized water (3 x 30 mL), diethyl ether (3 x 30 mL) to remove excess LiCl, unreacted bipyridine, $\text{RuCl}_3 \cdot 3\text{H}_2\text{O}$, and the side product $[\text{Ru}(\text{bpy})_3]\text{Cl}_2$ and dried under vacuum. The reaction yielded 6.20 g (11.9 mmol) crude product (80%). Without further purification, the product was used to synthesize $[(\text{bpy})_2\text{Ru}(\text{dpp})](\text{PF}_6)_2$.

$[(\text{bpy})_2\text{OsCl}_2]$

cis- $[\text{Os}(\text{bpy})_2\text{Cl}_2]$ was synthesized by a modification of the published method.¹²⁵ Specifically, $\text{OsCl}_3 \cdot 3\text{H}_2\text{O}$ (2.00 g, 5.70 mmol) and 2,2'-bipyridine (2.21 g 14.3 mmol) were added to 30 mL of DMF and heated at reflux for 1 h. After the reaction mixture was cooled to room temperature, 100 mL of a solution of $\text{Na}_2\text{S}_2\text{O}_4$ (0.440 g, 2.53 mmol) was added to the mixture and the solution was placed in a 0 °C ice bath. After the cooling process, a resulting reddish-purple solid precipitate was collected by vacuum filtration. The solid was washed with deionized water (3 x 200 mL), acetone (3 x 200 mL) and diethyl ether (3 x 200 mL), and dried under vacuum. The reaction yielded 3.00 g (5.19 mmol) product (91%). Without further purification, the product was used to synthesize $[(\text{bpy})_2\text{Os}(\text{dpp})](\text{PF}_6)_2$.

$[(\text{bpy})_2\text{Ru}(\text{dpp})](\text{PF}_6)_2$

$[(\text{bpy})_2\text{Ru}(\text{dpp})](\text{PF}_6)_2$ was synthesized by a modification of the published method.¹³ Specifically, $[(\text{bpy})_2\text{RuCl}_2] \cdot 2\text{H}_2\text{O}$ (2.00 g, 3.84 mmol) and 2,3-bis(2-pyridyl)pyrazine (dpp) (1.40 g, 5.98 mmol) were added to 60 mL of 95% ethanol and heated to reflux for 2 h. The warm reaction mixture was then pipetted into a 500 mL of stirring saturated aqueous KPF_6 solution to precipitate the product. The solid was collected by vacuum filtration, after which the solid was purified by adsorption alumina column chromatography. The column was loaded with 2:1 toluene/acetonitrile. A typical stationary phase height in a 48 cm x 2.2 cm (I.D.) column was 30 cm. The first colored band (the product) that eluted following the colorless excess dpp ligand was red in color, which was subsequently collected and concentrated by evaporation under vacuum. The solid was dissolved in a minimal amount of

acetonitrile and pipetted into 200 mL of stirring diethyl ether to induce precipitation. The precipitate was collected by vacuum filtration, then washed by 100 mL of diethyl ether and dried under vacuum. Column chromatography was repeated 2 to 3 times to ensure the purity of final product. The reaction yielded 3.20 g (3.15 mmol) of a yellow product (82%). The purity of the product was ensured by matching the electronic absorption spectrum and cyclic voltammogram to standard literature values: MLCT maxima λ_{max} in CH₃CN at 470 nm ($\epsilon = 10.2 \times 10^3 \text{ M}^{-1} \text{ cm}^{-1}$) and $E_{1/2}$ values at 1.38 (Ru^{II/III}), -1.01 (dpp^{0/-}), -1.46 (bpy^{0/-}), -1.67 (bpy^{0/-}) (V vs. Ag/AgCl).^{12, 13} The matched extinction coefficient and the clean electrochemical data (no additional oxidation potential corresponding to Ru^{II/III} of unreacted [(bpy)₂RuCl₂]) helped to ensure the purity of the product. The product was also analyzed by ¹H NMR¹²⁶ (Figure A.1 in Appendix): 8.63 (d, $J = 6.0\text{Hz}$, 1H), 8.49 - 8.53 (overlap, 4H), 8.47 (d, $J = 3.2\text{Hz}$, 1H), 8.06 - 8.13 (overlap, 5H), 7.95 (d, $J = 8.0\text{Hz}$, 1H), 7.91 (d, $J = 5.6\text{Hz}$, 1H), 7.86 (d, $J = 3.2\text{Hz}$, 1H), 7.74 (d, $J = 5.6\text{Hz}$, 2H), 7.69 (d, $J = 5.6\text{Hz}$, 2H), 7.61 - 7.64 (overlap, 2H), 7.40 - 7.50 (overlap, 4H), 7.29 (t, $J = 6.4\text{Hz}$, 1H), 7.18 (d, $J = 8.4\text{Hz}$, 1H).

[(bpy)₂Os(dpp)](PF₆)₂

[(bpy)₂Os(dpp)](PF₆)₂ was synthesized by modification of published method.⁴ Specifically, [(bpy)₂OsCl₂] (1.04 g, 1.82 mmol) and 2,3-bis(2-pyridyl)pyrazine (dpp) (0.66 g, 2.7 mmol) were added to 30 mL of ethylene glycol and heated at reflux for 5 h. The warm reaction mixture was then pipetted into a 250 mL of stirring saturated aqueous KPF₆ solution to precipitate the product. The solid was collected by vacuum filtration, after which it was purified by adsorption alumina column chromatography. The column was loaded with 2:1 (vol./vol.) toluene/acetonitrile. A typical stationary phase height in a 48 cm x 2.2 cm (I.D.) column was 25 cm. The first colored dark brown band that eluted following the colorless excess dpp ligand. The product and was then collected, and the solvent was removed under vacuum. The resulting solid was then dissolved in a minimal amount of acetonitrile and pipetted into 200 mL of stirring diethyl ether to induce precipitation. The precipitate was collected by vacuum filtration, washed with 100 mL of diethyl ether, and dried under vacuum. Column chromatography was repeated 2 or 3 times to ensure the purity of final product. The

reaction yielded 1.53 g (1.49 mmol) product (82%). The purity of the product was ensured by matching the electronic absorption spectrum and cyclic voltammogram to standard literature values: MLCT maxima λ_{max} in CH₃CN at 486 nm ($\epsilon = 12.7 \times 10^3 \text{ M}^{-1}\text{cm}^{-1}$) and $E_{1/2}$ values at 0.94 (Os^{II/III}), -1.02 (dpp^{0/-}), -1.38 (bpy^{0/-}), -1.58 (bpy^{0/-}) (V vs. Ag/AgCl).¹⁶ The matched extinction coefficient and the clean electrochemical data (no additional oxidation potential corresponding to Os^{II/III} of unreacted [(bpy)₂OsCl₂]) helped to ensure the purity of the product. The product was also analyzed by ¹H NMR^{126, 127} (Figure A.2 in Appendix): 8.66 (d, $J = 4.8\text{Hz}$, 1H), 8.48 - 8.53 (overlap, 4H), 8.16 (d, $J = 3.6\text{Hz}$, 1H), 8.11 (t, $J = 7.8\text{Hz}$, 1H), 7.88 - 8.00 (overlap, 5H), 7.87 (d, $J = 4.0\text{Hz}$, 1H), 7.78 (d, $J = 6.0\text{Hz}$, 1H), 7.56 - 7.66 (overlap, 5H), 7.33 - 7.46 (overlap, 5H), 7.15 - 7.21 (overlap, 2H).

[{(bpy)₂Ru(dpp)}₂RuCl₂](PF₆)₄

[{(bpy)₂Ru(dpp)}₂RuCl₂](PF₆)₄ was synthesized by a modification of the published method.³⁶ Specifically, [(bpy)₂Ru(dpp)](PF₆)₂ (1.62 g, 1.73 mmol), RuCl₃•3H₂O (0.240 g, 0.921 mmol) and LiCl (0.400 g, 9.43 mmol) were added to 60 mL of 95% ethanol and heated at reflux for 24 h. The warm reaction mixture was then pipetted into a 250 mL of stirring saturated aqueous KPF₆ solution to precipitate the product. The product was collected by vacuum filtration and the solid was purified by adsorption alumina column chromatography. The column was loaded with 2:1 (vol./vol.) toluene/acetonitrile. A typical stationary phase height in a 48 cm x 2.2 cm (I.D.) column was 25 cm. The second colored band eluting after the red monometallic band was green in color. This product band was then collected, the solvent removed and the solid dried under vacuum. The solid was dissolved in a minimal amount of acetonitrile and pipetted into 200 mL of stirring diethyl ether to form the precipitate. The precipitate was collected under vacuum and washed with 100 mL of diethyl ether and dried. Column chromatography was repeated 2 to 3 times to ensure the purity of the final product. The reaction yielded 1.33 g (0.650 mmol) of purple product (75%). The purity of the product was ensured by matching the electronic absorption spectrum and cyclic voltammograms (only the peaks of the product were observed) to standard literature values: MLCT maxima at 625 nm ($\epsilon = 2.6 \times 10^4 \text{ M}^{-1}\text{cm}^{-1}$) and $E_{1/2}$ values at 0.83 (Ru^{II/III}), 1.60

($2\text{Ru}^{\text{II/III}}$), -0.71 ($\text{dpp}^{0\cdot-}$), -0.88 ($\text{dpp}^{0\cdot-}$), -1.43 ($\text{dpp}^{-2\cdot-}$), -1.52 ($\text{dpp}^{-2\cdot-}$) (V vs. Ag/AgCl).^{15, 128}

[{(bpy)₂Os(dpp)}₂RuCl₂](PF₆)₄

[{(bpy)₂Os(dpp)}₂RuCl₂](PF₆)₄ was synthesized by a modification of the published method.³⁶ Specifically, [(bpy)₂Os(dpp)](PF₆)₂ (1.36 g, 1.33 mmol), RuCl₃•3H₂O (0.17 g, 0.66 mmol) and LiCl (0.19 g, 4.48 mmol) were added to 60 mL of 95% ethanol and heated at reflux for 48 h. The warm reaction mixture was then pipetted into 250 mL of a stirred saturated aqueous KPF₆ solution to precipitate the product. The solid was collected by vacuum filtration and purified by adsorption alumina column chromatography. The column was loaded with 2:1 (vol./vol.) toluene/acetonitrile. A typical stationary phase height in a 48 cm x 2.2 cm (I.D.) column was 25 cm. The second colored band eluting after the brown monometallic band was dark purple in color. This product band was then collected, the solvent removed and the solid dried under vacuum. The resulting solid was then dissolved in a minimal amount of acetonitrile and pipetted into 200 mL of stirring diethyl ether to form the precipitate. The precipitate was collected by vacuum filtration, washed by 100 mL of diethyl ether and dried under vacuum. Column chromatography was repeated 2 to 3 times to ensure the purity of the final product. The reaction yielded 1.03 g (0.460 mmol) of purple product (70%). The purity of the product was ensured by matching the electronic absorption spectrum and cyclic voltammogram (only the peaks of the product were observed) to standard literature values: MLCT maxima at 586 nm ($\epsilon = 3.9 \times 10^4 \text{ M}^{-1} \text{ cm}^{-1}$) and $E_{1/2}$ values at 0.78 ($\text{Ru}^{\text{II/III}}$), 1.21 ($2\text{Os}^{\text{II/III}}$), -0.70 ($\text{dpp}^{0\cdot-}$), -0.84 ($\text{dpp}^{0\cdot-}$), -1.30 ($\text{dpp}^{-2\cdot-}$), -1.40 ($\text{bpy}^{0\cdot-}$) (V vs. Ag/AgCl).^{15, 128}

[{(bpy)₂Os(dpp)}₂Ru(dpq)](PF₆)₆

[{(bpy)₂Os(dpp)}₂Ru(dpq)](PF₆)₆ was synthesized by a modification of the literature method.³⁶ Specifically, the terminal [(bpy)₂Os(dpp)](PF₆)₂ light absorber was assembled first and then coupled to the central Ru to produce [(bpy)₂Os(dpp)]₂RuCl₂(PF₆)₄.³⁶ The dichloro precursor [(bpy)₂Os(dpp)]₂RuCl₂(PF₆)₄ (0.19 g, 0.084 mmol) and AgSO₃CF₃ (0.071 g, 0.35 mmol) were heated at reflux in 30 mL of 95% ethanol for 4 h, under Ar. In another flask,

excess dpq (0.040 g, 0.14 mmol) was heated at reflux in 15 mL of ethylene glycol. The dichloro precursor solution was added in three aliquots to the refluxing dpq solution to maintain an excess of dpq during the reaction, favoring trimetallic formation. This mixture was heated at reflux for an additional 36 h. The reaction mixture was cooled to room temperature and added to 500 mL of saturated aqueous KPF₆ to precipitate the product. The crude product was collected by vacuum filtration, dissolved in minimal acetonitrile (ca. 2 mL), and reprecipitated in 200 mL of diethyl ether. Purification was achieved by size exclusion chromatography using a Sephadex LH-20 column (120 cm (height) x 2.2 cm (I.D.)) eluted with 2:1/v:v ethanol:acetonitrile solvent mixture. The red band that eluted first, followed by unreacted excess dpq, was collected and dried under vacuum. The reaction yielded 0.20 g (0.076 mmol) of purple product (90%). (Found C, 36.55; H, 2.53; N, 9.72. Calc. for [{(bpy)₂Os(dpp)}₂Ru(dpq)](PF₆)₆•6H₂O: C, 36.41; H, 2.70; N, 9.88.) ¹H NMR confirmed the presence of six H₂O solvent crystals in one molecule (Appendix Figure A.3). FAB-MS: m/z [relative abundance, ion]: 2583.4 [76, (M-PF₆)⁺]; 2438.6 [100, (M-2PF₆)⁺]; 2293.7 [36, (M-3PF₆)⁺] (Appendix Figure A.11). MALDI-TOF MS: m/z [relative abundance, ion]: 2441 [18, (M-2PF₆+2H)⁺]; 2297 [81, (M-3PF₆+3H)⁺]; 2150 [100, (M-4PF₆+H)⁺]; 2005 [32, (M-5PF₆+H)⁺]; 954 [100, (M-6PF₆-4bpy-dpq+4H)⁺] (Appendix Figure A.12).

[{(bpy)₂Ru(dpp)}₂Ru(dpp)](PF₆)₆

[{(bpy)₂Ru(dpp)}₂Ru(dpp)](PF₆)₆ was synthesized by a modification of the published methods.^{15, 36, 81} In the literature, this complex is usually reported as a synthetic precursor without full characterization.⁸¹ The terminal [(bpy)₂Ru(dpp)](PF₆)₂ light absorber was assembled first and then coupled to the central Ru to produce [{(bpy)₂Ru(dpp)}₂RuCl₂](PF₆)₄.³⁶ The dichloro precursor [{(bpy)₂Ru(dpp)}₂RuCl₂](PF₆)₄ (1.21 g, 0.591 mmol) and AgSO₃CF₃ (0.820 g, 4.04 mmol) were heated at reflux in 30 mL of 95% ethanol for 2 h, under Ar. In another flask, excess dpp (0.820 g, 3.50 mmol) was heated at reflux in 20 mL of 95% ethanol. After filtration to remove the AgCl solid, the dichloro precursor solution was added slowly in four aliquots to the refluxing dpp solution to maintain an excess of dpp during the reaction, favoring trimetallic formation. This mixture was heated

at reflux for 24 h. The reaction mixture was cooled to room temperature and added to 150 mL of saturated aqueous KPF_6 to precipitate the product. The crude product was collected by vacuum filtration, dissolved in minimal acetonitrile (ca. 2 mL), and reprecipitated in 200 mL of diethyl ether. Purification was achieved by size exclusion chromatography using a Sephadex LH-20 column (120 cm (height) x 2.2 cm (I.D.)) developed with 2:1/v:v ethanol:acetonitrile solvent mixture. The very first portion of the purple-colored band was discarded and the predominant rosy red band was collected. The product was flash precipitated into 200 mL of diethyl ether and dried under vacuum. The reaction yielded 1.18 g (0.472 mmol) product (80%). (Found C, 38.31; H, 2.74; N, 10.98. Calc. for $[\{(\text{bpy})_2\text{Ru}(\text{dpp})\}_2\text{Ru}(\text{dpp})](\text{PF}_6)_6 \cdot 5\text{H}_2\text{O}$: C, 38.01; H, 2.80; N, 10.81.) ^1H NMR confirmed the presence of five H_2O solvent crystals in one molecule (Appendix Figure A.4). FAB-MS: m/z [relative abundance, ion]: 2209 [53, $(\text{M}-\text{PF}_6+\text{H})^+$]; 2067 [100, $(\text{M}-2\text{PF}_6+2\text{H})^+$]; 1923 [57, $(\text{M}-3\text{PF}_6+3\text{H})^+$]. (Appendix Figure A.13).

$[\{(\text{bpy})_2\text{Ru}(\text{dpp})\}_2\text{Ru}(\text{dpq})](\text{PF}_6)_6$

$[\{(\text{bpy})_2\text{Ru}(\text{dpp})\}_2\text{Ru}(\text{dpq})](\text{PF}_6)_6$ was synthesized by a modification of the published methods.^{15, 36, 81} The terminal $[(\text{bpy})_2\text{Ru}(\text{dpp})](\text{PF}_6)_2$ light absorber was assembled first and then coupled to the central Ru to produce the dichloro precursor, $[\{(\text{bpy})_2\text{Ru}(\text{dpp})\}_2\text{RuCl}_2](\text{PF}_6)_4$.³⁶ The dichloro precursor $[\{(\text{bpy})_2\text{Ru}(\text{dpp})\}_2\text{RuCl}_2](\text{PF}_6)_4$ (0.344 g, 0.168 mmol) and AgSO_3CF_3 (0.187 g, 0.921 mmol) were heated at reflux in 20 mL of 95% ethanol for 2 h, under Ar. In another flask, excess dpq (0.160 g, 0.563 mmol) was heated at reflux in 20 mL of 95% ethylene glycol. After filtration to remove the AgCl, the dichloro precursor solution was slowly added in 3 aliquots to the refluxing dpp solution to maintain an excess of dpp during the reaction, favoring trimetallic formation. This mixture was heated at reflux for an additional 24 h. The reaction mixture was cooled to room temperature and added to 150 mL of saturated aqueous KPF_6 to precipitate the product. The crude product was collected by vacuum filtration, dissolved in minimal acetonitrile (ca. 2 mL), and reprecipitated in 200 mL of diethyl ether. Purification was achieved by size exclusion chromatography using a Sephadex LH-20 column (120 cm (height) x 2.2 cm (I.D.))

developed with 2:1/v:v ethanol:acetonitrile solvent mixture. The very first portion of color band was discarded and the predominant rosy red band was collected. The product was flash precipitated from 200 mL of diethyl ether and dried under vacuum. The reaction yielded 0.385 g (0.151 mmol) product (90%). FAB-MS: m/z [relative abundance, ion]: 2403 [31, (M-PF₆-2H)⁺]; 2258 [100, (M-2PF₆-2H)⁺]; 2117 [75, (M-3PF₆+2H)⁺]; 1973 [22, (M-4PF₆+3H)⁺]. (Appendix Figure A.14).

2.3.2 Preparations of New Supramolecular Complexes

[{[(bpy)₂Os(dpp)]₂Ru}₂(dpq)](PF₆)₁₂

[{[(bpy)₂Os(dpp)]₂Ru}₂(dpq)](PF₆)₁₂ was synthesized by a building block method (Figure 2.8). The [(bpy)₂Os(dpp)](PF₆)₂ light absorber was assembled first, then coupled to the central Ru to produce the dichloro precursor [{(bpy)₂Os(dpp)}₂RuCl₂](PF₆)₄.³⁶ During the hexametallc synthesis, careful stoichiometric control was needed. The dichloro precursor [{(bpy)₂Os(dpp)}₂RuCl₂](PF₆)₄ (0.27 g, 0.12 mmol) and AgSO₃CF₃ (0.10 g, 0.49 mmol) were heated at reflux in 20 mL of 95% ethanol for 4 h, under Ar. In another flask, dpq (0.017 g, 0.060 mmol) was heated at reflux in 7.5 mL of 1:4/v:v ethanol : ethylene glycol solvent. The dpq solution was slowly injected in three aliquots into the refluxing dichloro precursor solution to maintain an excess of the dichloro precursor, favoring hexametallc formation. The reaction was then heated at reflux for an additional 48 h. The reaction mixture was cooled to room temperature and added to 500 mL of saturated aqueous KPF₆ to precipitate the product. The crude product was collected by vacuum filtration, dissolved in minimal acetonitrile (ca. 2 mL), and reprecipitated in 200 mL of diethyl ether. Purification was achieved by size exclusion chromatography using a Sephadex LH-20 column (120 cm (height) x 2.2 cm (I.D.)) developed with a 2:1/v:v ethanol:acetonitrile solvent mixture. The violet product band that eluted first (prior to a small amount of a violet red band) was collected and dried under vacuum. The reaction yielded 0.28 g (0.054 mmol) product (90%). (Found C, 37.14; H, 2.71; N, 10.64. Calc. for [{[(bpy)₂Os(dpp)]₂Ru}₂(dpq)](PF₆)₁₂•8CH₃CN•4H₂O: C, 36.63; H, 2.68; N, 11.06.) ¹H NMR confirmed the presence of nine H₂O and two CH₃CN solvent crystals in one molecule which accounted for

[{[(bpy)₂Os(dpp)]₂Ru}₂(dpq)](PF₆)₁₂•2CH₃CN•9H₂O: C, 35.02; H, 2.60; N, 9.83.) (Appendix Figure A.5A). (Note: the samples submitted for elemental analysis and ¹H NMR were not from the same batch due to practical reason. Varied numbers of solvent crystals had been experimentally observed for different batches of same molecule, Figure A.5 – A: 2 CH₃CN, 9 H₂O; B: less than 1 CH₃CN, 7 H₂O, 1 CH₂Cl₂. Due to the availability of samples from different batches and the broad-peak pattern for aromatic Hs of the complex, the signal-to-noise ratios of Hs of the complex were not so good. Thus the integration of solvent peaks contained certain error, depending on the intergration of Hs of the complex. However apparent difference was observed for combinations of associated solvent crystals in varied samples.) FAB-MS: m/z [relative abundance, ion]: 3326 [32, (M-4PF₆-8bpy-F+H)⁺]; 3181 [100, (M-5PF₆-8bpy-F+H)⁺]; 2439 [67, (M-8PF₆-{(bpy)₂Os(dpp)}₂Ru)⁺]; 1518 [100*,(M-6PF₆-8bpy-F+H)²⁺] (* denotes relative abundance measured from separate scan window) (Appendix Figure A.15). MALDI-TOF MS: m/z [relative abundance, ion]: 3039 [14, (M-6PF₆-8bpy-F+4H)⁺]; 2892 [32, (M-7PF₆-8bpy-F+2H)⁺]; 2748 [21, (M-8PF₆-8bpy-F+3H)⁺]; 2440 [24, (M-8PF₆-{(bpy)₂Os(dpp)}₂Ru+H)⁺]; 2295 [79, (M-9PF₆-{(bpy)₂Os(dpp)}₂Ru+H)⁺]; 2150 [100, (M-10PF₆-{(bpy)₂Os(dpp)}₂Ru+H)⁺]; 2005 [43, (M-11PF₆-{(bpy)₂Os(dpp)}₂Ru+H)⁺]; 923 [23, (M-12PF₆-4{(bpy)₂Os(dpp)}+2H)⁺] (Appendix Figure A.16).

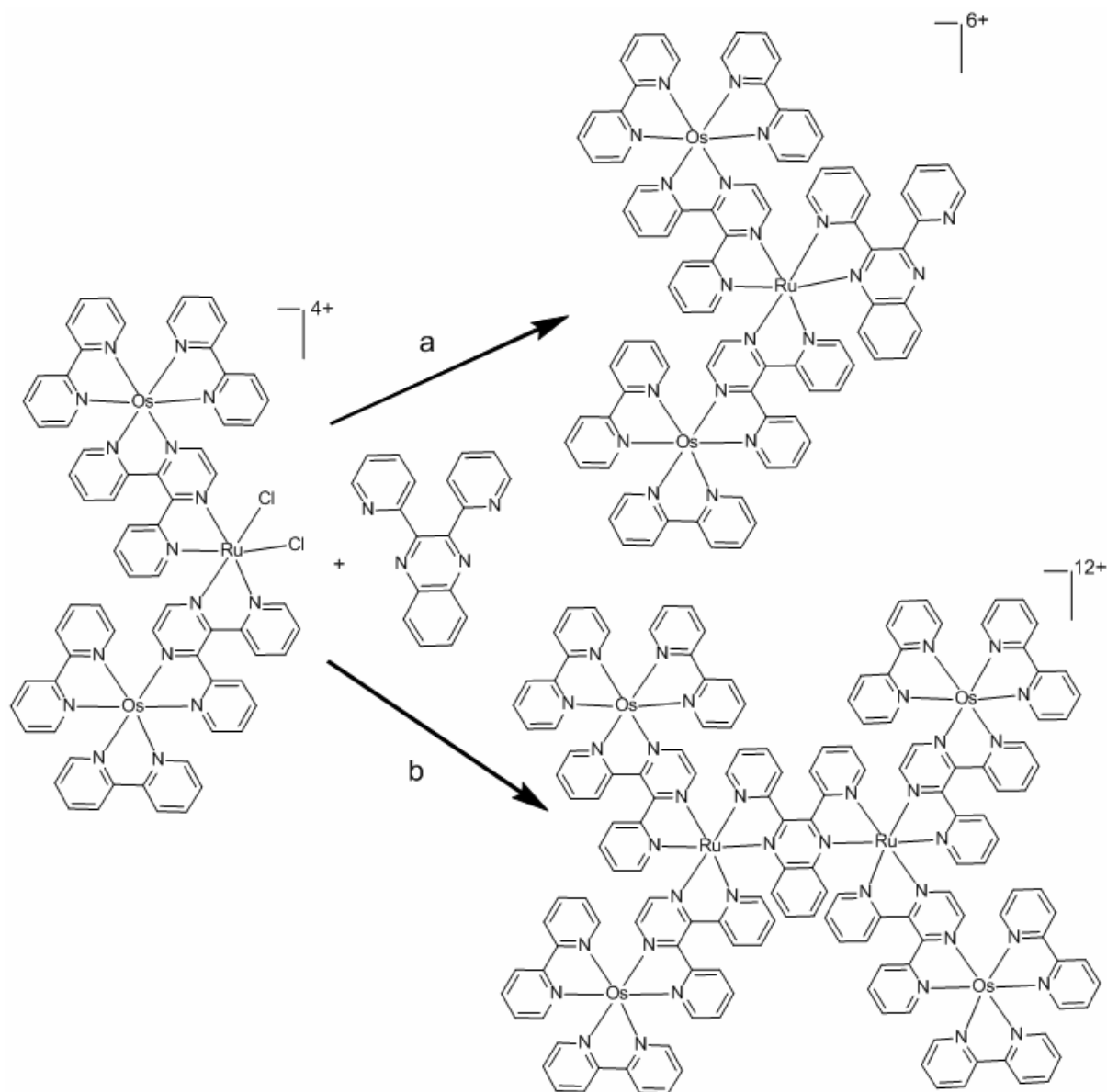


Figure 2.8 Stoichiometric control of supramolecular synthesis producing $[\{(\text{bpy})_2\text{Os}(\text{dpp})\}_2\text{Ru}(\text{dpq})](\text{PF}_6)_6$ or $[\{[(\text{bpy})_2\text{Os}(\text{dpp})]_2\text{Ru}\}_2(\text{dpq})](\text{PF}_6)_{12}$ (bpy = 2,2'-bipyridine, dpp = 2,3-bis(2-pyridyl)pyrazine, dpq = 2,3-bis(2-pyridyl)quinoxaline). Condition a: An excess amount of dpq, 95% ethanol; trimetallic precursor was added to refluxing dpq in 3 aliquots and refluxed for 36 h. Condition b: trimetallic precursor : dpq = 2 : 1, 95% ethanol; dpq was added to refluxing trimetallic precursor in 3 aliquots and refluxed for 48 h.



$[\{(\text{bpy})_2\text{Ru}(\text{dpp})\}_2\text{Ru}(\text{dpp})\text{PtCl}_2](\text{PF}_6)_6$ was synthesized by reacting the trimetallic complex $[\{(\text{bpy})_2\text{Ru}(\text{dpp})\}_2\text{Ru}(\text{dpp})](\text{PF}_6)_6$ with excess $[\text{PtCl}_2(\text{DMSO})_2]$ (DMSO = dimethyl

sulfoxide) (Figure 2.9).⁷² [$\{(bpy)_2Ru(dpp)\}_2Ru(dpp)PtCl_2](PF_6)_6$ (150 mg, 0.060 mmol) and $[PtCl_2(DMSO)_2]$ (47 mg, 0.10 mmol) were mixed in 25 mL of 95% ethanol and heated at reflux for 40 h. The addition of a saturated KPF_6 solution induced precipitation and the resulting product was collected by vacuum filtration. The product was then dissolved in a minimal amount of CH_3CN (ca. 2 mL), flash precipitated in 200 mL of diethyl ether, collected by vacuum filtration, rinsed with 100 mL of diethyl ether and dried under vacuum. Further purification was accomplished by recrystallization from (ca. 50 mL) hot ethanol. This process was repeated three times. The reaction yielded 0.10 g (0.036 mmol) product (60%). FAB-MS: m/z [relative abundance, ion]: 2623 [36, $(M-PF_6+H)^+$]; 2477 [100, $(M-2PF_6+H)^+$]; 2331 [57, $(M-3PF_6)^+$] (Appendix Figure A.17). MALDI-TOF MS: m/z [relative abundance, ion]: 2478 [20, $(M-2PF_6+H)^+$]; 2332 [55, $(M-3PF_6)^+$]; 2297 [55, $(M-3PF_6-Cl+H)^+$]; 2266 [23, $(M-3PF_6-2Cl+5H)^+$]; 2189 [73, $(M-4PF_6+2H)^+$]; 2153 [100, $(M-4PF_6-Cl+2H)^+$]; 2117 [38, $(M-4PF_6-2Cl+H)^+$]; 2046 [23, $(M-5PF_6+4H)^+$] (Appendix Figure A.18).

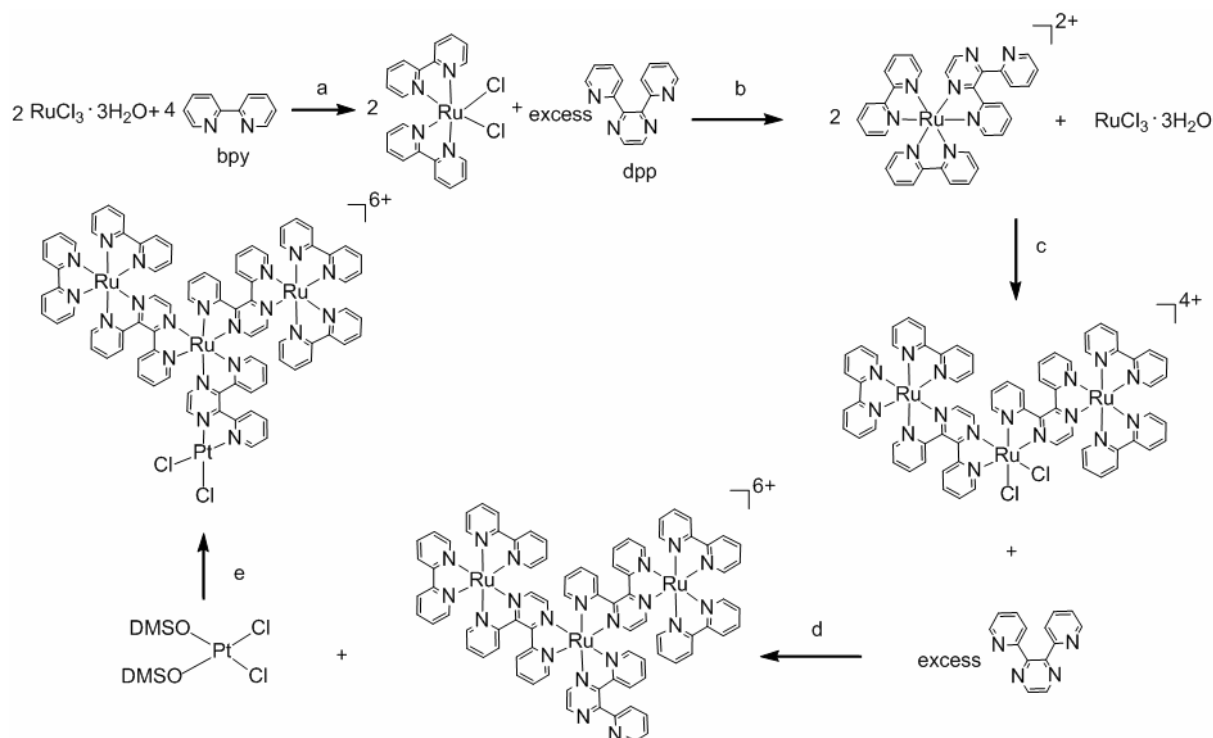


Figure 2.9 Synthetic scheme of preparing $[\{(bpy)_2Ru(dpp)\}_2Ru(dpp)PtCl_2](PF_6)_6$ where $bpy = 2,2'$ -bipyridine, $dpp = 2,3$ -bis(2-pyridyl)pyrazine. a. ref 13; b. ref 36; c. ref 81; d. ref 120; e. excess $[PtCl_2(DMSO)_2]$, 95% ethanol, heated at reflux for 40 h.

[{(bpy)₂Ru(dpp)}₂Ru(dpq)PtCl₂](PF₆)₆

Similar to the [{(bpy)₂Ru(dpp)}₂Ru(dpq)PtCl₂](PF₆)₆, the complex [{(bpy)₂Ru(dpp)}₂Ru(dpq)PtCl₂](PF₆)₆ was synthesized by reacting the trimetallic complex [{(bpy)₂Ru(dpp)}₂Ru(dpq)](PF₆)₆ with excess [PtCl₂(DMSO)₂] (DMSO = dimethyl sulfoxide).¹²⁰ [{(bpy)₂Ru(dpp)}₂Ru(dpq)](PF₆)₆ (147 mg, 0.0576 mmol) and [PtCl₂(DMSO)₂] (39 mg, 0.086 mmol) were mixed in 50 mL of 95% ethanol and heated at reflux for 40 h. The addition of a saturated KPF₆ solution induced precipitation and the resulting product was collected by vacuum filtration. The product was dissolved in a minimal amount of CH₃CN (ca. 2 mL), flash precipitated in 200 mL of diethyl ether, collected by vacuum filtration, rinsed with diethyl ether and dried under vacuum. Further purification was accomplished by recrystallization from ca. 50 mL of hot ethanol. This process was repeated three times. The reaction yielded 0.098 g (0.035 mmol) product (60%). FAB-MS: m/z [relative abundance, ion]: 2673 [17, (M-PF₆+H)⁺]; 2527 [33, (M-2PF₆)⁺]; 2405 [82, (M-PF₆-PtCl₂)⁺]; 2260 [100, (M-2PF₆-PtCl₂)⁺]; 2116 [33, (M-3PF₆-PtCl₂)⁺] (Appendix Figure A.19).

[{(bpy)₂Os(dpp)}₂Ru(dpq)PtCl₂](PF₆)₆

Similar to the [{(bpy)₂Ru(dpp)}₂Ru(dpq)PtCl₂](PF₆)₆, the complex [{(bpy)₂Os(dpp)}₂Ru(dpq)PtCl₂](PF₆)₆ was synthesized by reacting the trimetallic complex [{(bpy)₂Os(dpp)}₂Ru(dpq)](PF₆)₆ with excess [PtCl₂(DMSO)₂] (DMSO = dimethyl sulfoxide).¹⁵ [{(bpy)₂Os(dpp)}₂Ru(dpq)](PF₆)₆ (100. mg, 0.0366 mmol) and [PtCl₂(DMSO)₂] (37 mg, 0.081 mmol) were mixed in 50 mL of 95% ethanol and heated at reflux for 40 h. The addition of a saturated KPF₆ solution induced precipitation and the resulting product was collected by vacuum filtration. The product was dissolved in a minimal amount (ca. 2 mL) of CH₃CN, flash precipitated in 200 mL of diethyl ether, collected by vacuum filtration, rinsed with 100 mL of diethyl ether and dried under vacuum. Further purification was accomplished by recrystallization from ca. 50 mL of hot ethanol. The process was repeated three times. The reaction yielded 0.066 g (0.022 mmol) product (60%). FAB-MS: m/z [relative abundance, ion]: 2852 [23, (M-PF₆+2H)⁺]; 2705 [47, (M-2PF₆)⁺]; 2583 [69, (M-PF₆-PtCl₂)⁺]; 2439 [100, (M-2PF₆-PtCl₂)⁺]; 2294 [42, (M-3PF₆-PtCl₂)⁺] (Appendix Figure A.20).

Chapter 3. Results and Discussion

Based on understandings of the electronic properties of Ru, Os polyazine building blocks, several molecular photodevices were designed and are described herein. The hexametallic complex $[\{[(bpy)_2Os(dpp)]_2Ru\}_2(dpq)](PF_6)_{12}$, designed to induce a long distance intramolecular charge separation state, was successfully prepared and characterized. The electronic properties were investigated, which revealed that the HOMO was localized on the peripheral Os metals; while the LUMO was localized on the central μ -dpq ligand. By coupling a reactive metal center Pt^{II} into a Ru or Os polyazine chromophore, a series of tetrametallic complexes $[\{(bpy)_2M(dpp)\}_2Ru(BL)PtCl_2](PF_6)_6$ ($M = Ru^{II}$ or Os^{II} , $BL = dpp$ or dpq), were prepared and investigated for applications in photocatalysis of hydrogen generation from water and photodynamic therapy.

3.1 Synthesis

As has been shown, supramolecular complexes can be assembled in high yield using a building block synthetic method. To prepare the hexametallic complex $[\{[(bpy)_2Os(dpp)]_2Ru\}_2(dpq)](PF_6)_{12}$, the terminal ligand bpy was bound to an Os metal, followed by the incorporation of a bridging ligand into the supramolecular assembly. The purity of products of each step was crucial to the product yield and purity of the following synthetic step. Pure precursor limits the variety of product formation and helps the analysis during the purification step. The modified preparation of the trimetallic compound $[\{(bpy)_2Os(dpp)\}_2Ru(dpq)](PF_6)_{129-132}$ generally enhanced yield compared to the literature method and simplified purification through the sequential addition of the dichloro metal complex precursor $[\{(bpy)_2Os(dpp)\}_2RuCl_2](PF_6)_4$ into a refluxing dpq solution. This method used an excess of dpq in solution, which was then available to bind to the dichloro precursor immediately upon chloride loss. Conversely, the slow addition of dpq into a refluxing solution of $[\{(bpy)_2Os(dpp)\}_2RuCl_2](PF_6)_4$ maintained a limited amount of available dpq ligand, thereby producing the desired hexametallic compound $[\{[(bpy)_2Os(dpp)]_2Ru\}_2(dpq)](PF_6)_{12}$ in good yield. In both cases, Ag^+ was added to scavenge free chloride anion.

Techniques used to control the stoichiometric ratio of reactants can also play an important role in preparing the tetrametallic Ru/Os-Pt series. For example, excess dpp was used when preparing the trimetallic chromophore $[\{(bpy)_2Ru(dpp)\}_2Ru(dpp)](PF_6)_6$ from $[\{(bpy)_2Ru(dpp)\}_2RuCl_2](PF_6)_4$, ensuring that the dpp bound to the central Ru was monochelating. Excess $[PtCl_2(DMSO)_2]$ was also used in the final step of connecting the trimetallic chromophore and the *cis*-PtCl₂ subunit.

Metathesis, column chromatography, and recrystallization were typically used for purification purposes. Due to the adsorption behavioral change between reactants and products, alumina column chromatography was used. However size exclusion chromatography was routinely used with complexes containing 3 - 6 metal centers, because of the similar polarity between the reactants and products. For Pt complexes, however, optimized synthetic procedures and multiple recrystallizations from ethanol must be employed due to the strong interaction between the Pt complexes and the stationary phase during adsorption chromatography.^{22, 100}

3.2 Discussion of the Isomers

The multimetallic complexes synthesized in this work contain many geometric isomers due to the variation of ligand coordination, as well as stereoisomers due to the chirality of octahedral Ru or Os. However these stereoisomers have very similar photophysical properties as well as redox properties, as described by MacDonnell and Campagna *et al.*^{133, 134} In one of their work, they discussed the possible number of isomers for complex $[(phen)_2Ru(\mu\text{-}tpphz))_3Ru](PF_6)_8$ (*tpphz* = tetrapyrido[3,2-a:2',3'-c:3'',2''-h:2''',3''-j]phenazine) and differentiated the stereochemistry by labeling each metal center of particular complex (Figure 3.1). Similarly, the complexes studied in this work are mixtures of stereoisomers, and the discussion of numbers of isomers is briefly given.

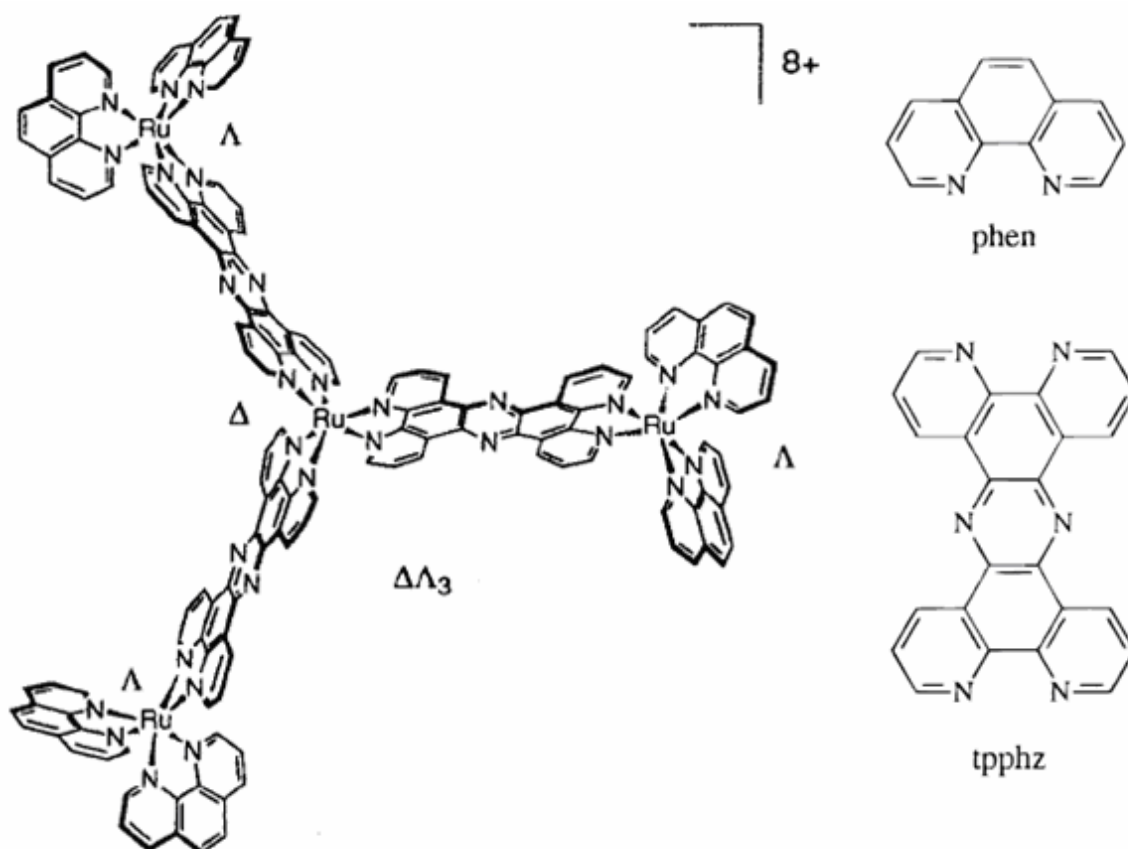


Figure 3.1 Stereoisomer of $[(\text{phen})_2\text{Ru}(\mu\text{-tpphz})_3\text{Ru}](\text{PF}_6)_8$: $[(\Lambda\text{-}(\text{phen})_2\text{Ru}(\mu\text{-tpphz}))_3\text{-}\Delta\text{-Ru}](\text{PF}_6)_8 (\Delta\Lambda_3)$.¹³³

Some representative isomers for complex $[\{(\text{bpy})_2\text{Ru}(\text{dpp})\}_2\text{Ru}(\text{dpq})\text{PtCl}_2](\text{PF}_6)_6$ are shown in Figure 3.2. The left $[(\text{bpy})_2\text{Ru}(\text{dpp})]$ unit switches from Λ to Δ formation when the molecule changes from structure A to structure B. The central $[(\text{dpp})\text{Ru}(\text{dpp})(\text{dpq})]$ unit has a pyrazine-trans-pyridine geometry in structure B while a pyrazine-trans-pyrazine geometry in structure C.

The number of isomers of $[\{(\text{bpy})_2\text{Ru}(\text{dpp})\}_2\text{Ru}(\text{dpq})\text{PtCl}_2](\text{PF}_6)_6$ can be calculated as in Figure 3.2. (1) Since the dpp and dpq both have a “AB” chelating fashion: pyridine (py) or pyrazine (pz) for dpp and pyridine (py’) or quinoxaline (qn) for dpq, there are 4 Δ isomers (i – iv) and 4 Λ isomer (v – viii) for A. (2) From A to B, the 2 peripheral $[(\text{bpy})_2\text{Ru}]$ units introduce 4 more stereoisomer combinations for each isomer of A: $\Lambda\Delta$, $\Lambda\Lambda$, $\Delta\Delta$ and $\Delta\Lambda$. So the factor is “x 4” and the number of isomers of $[\{(\text{bpy})_2\text{Ru}(\text{dpp})\}_2\text{Ru}(\text{dpq})\text{PtCl}_2](\text{PF}_6)_6$ is

calculated as: $8 \times 4 = 32$. In Figure 3.3, the particularly shown A has a “vii” Λ structure and the B has a “ $\Delta\Lambda\Lambda$ ” structure. For $[\{[(bpy)_2Os(dpp)]_2Ru\}_2(dpq)](PF_6)_{12}$, the number of isomers can also be estimated similarly (Figure 3.4). (1) For A, it contains 2 $[(dpp)_2Ru(dpq)]$ units, each of which has 8 isomers as discussed for structure A in Figure 3.3. However, the structure A for $[\{[(bpy)_2Os(dpp)]_2Ru\}_2(dpq)](PF_6)_{12}$ may contain a C_2 symmetry for certain structure, as shown in Figure 3.4. The particular shown structure A has a “ $\Lambda\Lambda$ ” structure for both of the Ru centers. So the total number of isomers of A is less than: $8 + 8 = 16$. (2) From A to B, there are Δ and Λ formations for each peripheral $[(bpy)_2Ru]$ unit as discussed for the tetrametallic complex in Figure 3.3. However some equivalent structures may exist when A has a C_2 symmetry, such as the shown structure B in Figure 3.4 (“ $\Lambda\Lambda\Lambda\Lambda\Lambda\Lambda$ ”). So the factor N is less than $2^4 = 16$ and the total number of isomers is calculated to be less than: $16 \times 16 = 256$.

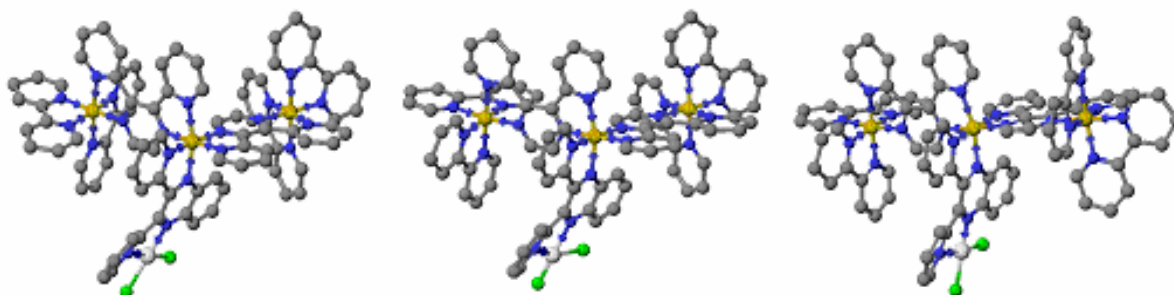


Figure 3.2 Representative isomers of $[\{[(bpy)_2Ru(dpp)]_2Ru(dpq)PtCl_2\}](PF_6)_6$ (bpy = 2,2'-bipyridine and dpq = 2,3-bis(2-pyridyl)quinoxaline).

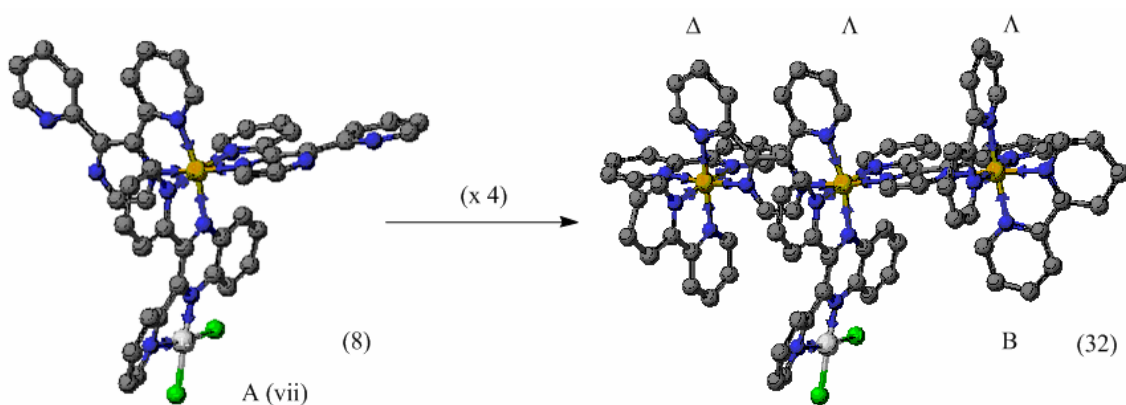


Figure 3.3 Number of isomers of $[\{(\text{bpy})_2\text{Ru}(\text{dpp})\}_2\text{Ru}(\text{dpq})\text{PtCl}_2](\text{PF}_6)_6$ (bpy = 2,2'-bipyridine and dpq = 2,3-bis(2-pyridyl)quinoxaline).

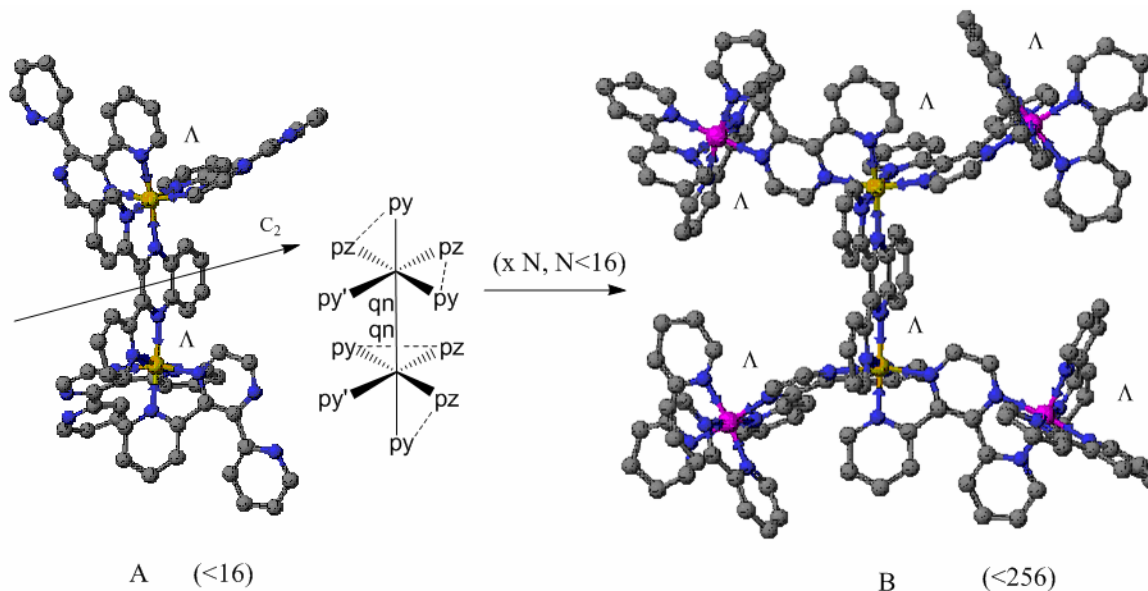


Figure 3.4 Number of isomers of $[\{[(\text{bpy})_2\text{Os}(\text{dpp})]_2\text{Ru}\}_2(\text{dpq})](\text{PF}_6)_{12}$ (pz = pyrazine, py = pyridine; bpy = 2,2'-bipyridine, dpp = 2,3-bis(2-pyridyl)pyrazine and dpq = 2,3-bis(2-pyridyl)quinoxaline).

3.3 Characterization

3.3.1 Mass Spectrometry

Fast atom bombardment mass spectrometry (FAB-MS) and matrix-assisted laser desorption/ionization time of flight mass spectrometry (MALDI-TOF-MS) were used to characterize our compounds. Typically, distinct singly charged fragments corresponding to molecular ions minus several counterions (such as PF_6^- or halides) are observed.^{129, 131, 132} The higher m/z peaks provide valuable information with respect to molecular composition. The major m/z peaks for the trimetallic chromophores $[\{(\text{bpy})_2\text{Os}(\text{dpp})\}_2\text{Ru}(\text{dpq})](\text{PF}_6)_6$, $[\{(\text{bpy})_2\text{Ru}(\text{dpp})\}_2\text{Ru}(\text{dpp})](\text{PF}_6)_6$ and $[\{(\text{bpy})_2\text{Ru}(\text{dpp})\}_2\text{Ru}(\text{dpq})](\text{PF}_6)_6$, the hexametallic complex $[(\{(\text{bpy})_2\text{Os}(\text{dpp})\}_2\text{Ru})_2(\text{dpq})](\text{PF}_6)_{12}$ and the tetrametallic complexes $[\{(\text{bpy})_2\text{Ru}(\text{dpp})\}_2\text{Ru}(\text{dpp})\text{PtCl}_2](\text{PF}_6)_6$ (Figure 3.5), $[\{(\text{bpy})_2\text{Ru}(\text{dpp})\}_2\text{Ru}(\text{dpq})\text{PtCl}_2](\text{PF}_6)_6$ and $[\{(\text{bpy})_2\text{Os}(\text{dpp})\}_2\text{Ru}(\text{dpq})\text{PtCl}_2](\text{PF}_6)_6$ are consistent with their formulation.

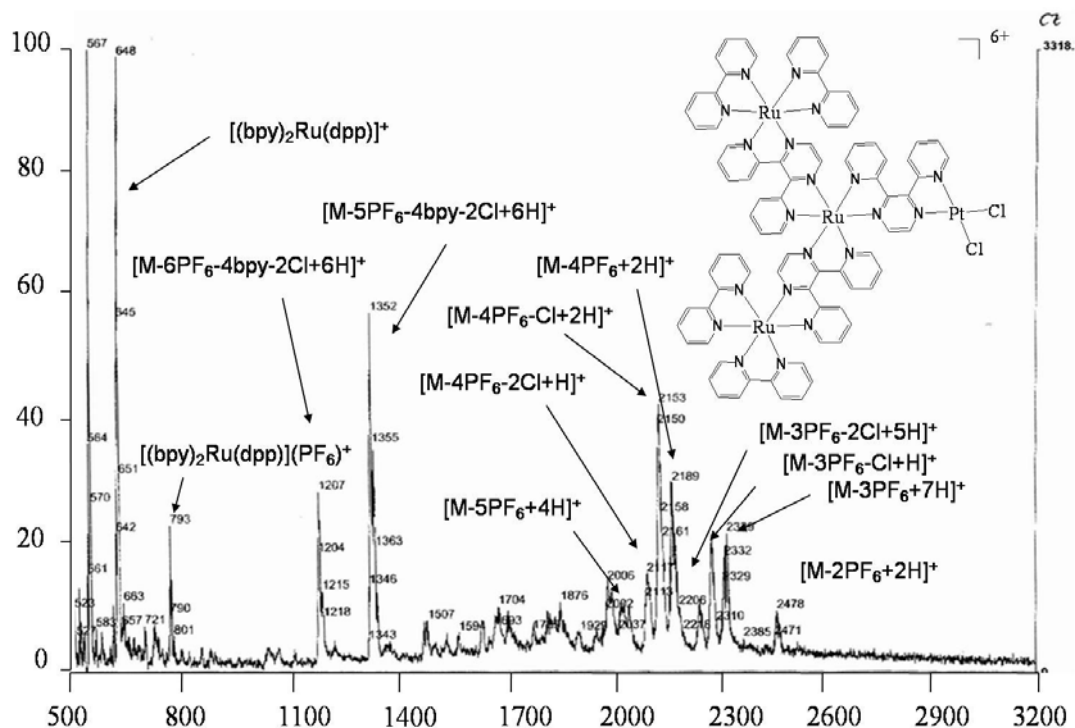


Figure 3.5 MALDI-TOF-MS of $[\{(\text{bpy})_2\text{Ru}(\text{dpp})\}_2\text{Ru}(\text{dpp})\text{PtCl}_2](\text{PF}_6)_6$ ($\text{bpy} = 2,2'$ -bipyridine, $\text{dpp} = 2,3$ -bis(2-pyridyl)pyrazine) (MALDI-TOF-MS = matrix-assisted laser desorption/ionization time of flight mass spectrometry; MALDI-TOF MS was performed on an Applied Biosystems Voyager-DE Pro using 2,5-dihydroxybenzoic acid as a matrix and 337 nm as the excitation wavelength).

The fragmentations of these supramolecular complexes have characteristic patterns, including loss of counterions or intact ligands (MS spectra are provided in the Appendix). The displayed m/z peaks often display H addition from the matrix, 2,5-dihydroxybenzoic acid, during the ionization process.¹²⁹ On occasion, F transfer from one fragment to another fragment will occur during the fragmentation process.¹³¹ Those fragments, corresponding to molecular ions minus terminal ligands such as bpy or half of the structure,^{5, 10-12, 51, 52} $[M-\{(bpy)_2Os(dpp)\}_2Ru]^+$ ($M = [(\{(bpy)_2Os(dpp)\}_2Ru)_2(dpq)](PF_6)_{12}$), are also typically observed. For example, in $[\{(bpy)_2Os(dpp)\}_2Ru(dpq)](PF_6)_6$ (Table 3.1), the m/z peak at 954 corresponds to $(M-6PF_6-4bpy-dpq+4H)^+$, which is the result of the molecular ion minus all the terminal ligands, including the 4 bpy ligands, the 1 dpq ligand, and the PF_6^- counterions. In addition, in the case of $[(\{(bpy)_2Os(dpp)\}_2Ru)_2(dpq)](PF_6)_{12}$ (Table 3.2), the m/z peaks at 3039, 2892 and 2748 correspond to the fragments of molecular ions minus all the 8 terminal bpy ligands. Similar effects were also observed for $[\{(bpy)_2Ru(dpp)\}_2Ru(dpp)PtCl_2](PF_6)_6$ (Table 3.3), in which the peak at 1352 corresponds to the fragment of molecular ion minus all the terminal bpy ligand and two chlorides. For the $[(\{(bpy)_2Os(dpp)\}_2Ru)_2(dpq)](PF_6)_{12}$, the m/z peaks at 2440, 2295, 2150 and 2005 were observed, corresponding to the $[(M-nPF_6-\{(bpy)_2Os(dpp)\}_2Ru)]^+$ series ($n = 8, 9, 10$ and 11). The m/z peak at 923 corresponds to $[Ru(\mu-dpq)Ru-2H]^+$, the central part of the hexametalllic complex.

Table 3.1 Mass spectral data of $[\{(bpy)_2Os(dpp)\}_2Ru(dpq)](PF_6)_6$.^a (bpy = 2,2'-bipyridine, dpp = 2,3-bis(2-pyridyl)pyrazine, dpq = 2,3-bis(2-pyridyl)quinoxaline)

MS DATA	Peak (m/z)	Abundance (%)	Fragment
FAB	2583	76	$[M-PF_6]^+$
	2439	100	$[M-2PF_6]^+$
	2294	36	$[M-3PF_6]^+$
MALDI-TOF	2441	18	$[M-2PF_6+2H]^+$
	2297	81	$[M-3PF_6+3H]^+$
	2150	100	$[M-4PF_6+H]^+$
	2005	32	$[M-5PF_6+H]^+$
	954	100	$[M-6PF_6-4bpy-dpq+4H]^+$

^a The FAB-MS was performed on a VG Analytical ZAB 2-SE high field mass spectrometer using m-nitrobenzyl alcohol as a matrix. The MALDI-TOF-MS was performed on an Applied Biosystems Voyager-DE Pro using 2,5-dihydroxybenzoic acid as a matrix (excited at 337 nm).

Table 3.2 Mass spectral data of $[(\{(bpy)_2Os(dpp)\}_2Ru)_2(dpq)](PF_6)_{12}$.^a (bpy = 2,2'-bipyridine, dpp = 2,3-bis(2-pyridyl)pyrazine, dpq = 2,3-bis(2-pyridyl)quinoxaline)

MS DATA	Peak (m/z)	Abundance (%)	Fragment
FAB	3326	32	$(M-4PF_6-8bpy-F+H)^+$
	3181	100	$(M-5PF_6-8bpy-F+H)^+$
	3036	96	$(M-6PF_6-8bpy-F+H)^+$
	2892	38	$(M-7PF_6-8bpy-F+2H)^+$
	2583	28	$(M-7PF_6-\{(bpy)_2Os(dpp)\}_2Ru-H)^+$
	2439	67	$(M-8PF_6-\{(bpy)_2Os(dpp)\}_2Ru)^+$
	2295	33*	$(M-9PF_6-\{(bpy)_2Os(dpp)\}_2Ru +H)^+$
	1591	82*	$(M-5PF_6-8bpy-F+2H)^{2+}$
	1518	100*	$(M-6PF_6-8bpy-F+H)^{2+}$
	1446	42*	$(M-7PF_6-8bpy-F+2H)^{2+}$
	MALDI-TOF	3039	14
2892		32	$[M-7PF_6-8bpy-F+2H]^+$
2748		21	$[M-8PF_6-8bpy-F+3H]^+$
2440		24	$[M-8PF_6-\{(bpy)_2Os(dpp)\}_2Ru+H]^+$
2295		79	$[M-9PF_6-\{(bpy)_2Os(dpp)\}_2Ru +H]^+$
2150		100	$[M-10PF_6-\{(bpy)_2Os(dpp)\}_2Ru +H]^+$
2005		43	$[M-11PF_6-\{(bpy)_2Os(dpp)\}_2Ru +H]^+$
923		23	$[M-12PF_6-4\{(bpy)_2Os(dpp)\}+2H]^+$

^a The FAB-MS was performed on a VG Analytical ZAB 2-SE high field mass spectrometer using m-nitrobenzyl alcohol as a matrix. The MALDI-TOF-MS was performed on an Applied Biosystems Voyager-DE Pro using 2,5-dihydroxybenzoic acid as a matrix (excited at 337 nm).

* denotes abundance measured from separate scan window

Table 3.3 Mass spectral data of $[\{(bpy)_2Ru(dpp)\}_2Ru(dpp)PtCl_2](PF_6)_6^a$ (bpy = 2,2'-bipyridine, dpp = 2,3-bis(2-pyridyl)pyrazine).

MS DATA	Peak (m/z)	Abundance (%)	Fragment
FAB	2623	36	$(M-PF_6+H)^+$
	2477	100	$(M-2PF_6+H)^+$
	2332	57	$(M-3PF_6)^+$
	2184	18	$(M-4PF_6-3H)^+$
MALDI-TOF	2478	8	$[M-2PF_6+2H]^+$
	2339	22	$[M-3PF_6+7H]^+$
	2297	22	$[M-3PF_6-Cl+H]^+$
	2266	9	$[M-3PF_6-2Cl+5H]^+$
	2189	29	$[M-4PF_6+2H]^+$
	2153	40	$[M-4PF_6-Cl+2H]^+$
	2117	15	$[M-4PF_6-2Cl+H]^+$
	2046	9	$[M-5PF_6+4H]^+$
	1352	58	$[M-5PF_6-4bpy-2Cl+6H]^+$
	1207	29	$[M-6PF_6-4bpy-2Cl+6H]^+$
	793	24	$[\{(bpy)_2Ru(dpp)\}(PF_6)]^+$
	648	99	$[(bpy)_2Ru(dpp)]^+$

^a The FAB-MS was performed on a VG Analytical ZAB 2-SE high field mass spectrometer using m-nitrobenzyl alcohol as a matrix. The MALDI-TOF-MS was performed on an Applied Biosystems Voyager-DE Pro using 2,5-dihydroxybenzoic acid as a matrix (excited at 337 nm).

3.3.2 Electrochemical Analysis

3.3.2.1 General Electrochemical Considerations

Cyclic voltammetry (CV) and square wave voltammetry (SWV) are widely used to study the redox properties and orbital energetics of supramolecular metal complexes of

polyazine ligands.^{10, 17, 20} Since both the metals and ligands are electroactive, electrochemical analysis can be a valuable tool in ascertaining the components of a supramolecular complex as well as purity with respect to electroactive impurities. The detection limit for impurities was estimated at ca. 15% by comparing the one electron process current and the background current. Due to the limited amount of available analyte through multiple-step synthesis, the quantity used for electrochemical analysis was limited and the purity was oftenly assayed combining with spectroscopy and elemental analysis. To get a better signal-to-noise ratio, it was advised that more analyte should be consumed in the future analyses. However under such experimental conditions, the difference between the synthetic synthons and target supramolecules were significant enough to probe the quality difference associated with the structural variation. For the complexes studied, oxidations are typically metal based while reductions are usually ligand based processes. The potentials of metal based processes are indicative of the metals present and their coordination environment. The potentials of ligand reductions are characteristic of the ligands' identities and their coordination modes, terminal vs. bridging. For ligands in these supramolecular complexes, dpq reduces at the least negative potential followed by dpp and then bpy. This trend is consistent with the relative energies of their π^* acceptor orbitals.⁵² Coordination to both bidentate sites to produce μ -dpp or μ -dpq results in a dramatic stabilization of the π^* orbitals and a shift of the ligand based reductions to more positive potentials by ca. 0.4 V.¹⁵ This cathodic shift is so significant that the μ -dpp⁻²⁻ or μ -dpq⁻²⁻ couples now occur prior to terminal ligand, bpy^{0/-}, couples. The presence of low potential couple of dpp^{0/-} or dpq^{0/-} is often used to establish the bridging coordination of these ligands.^{5, 14, 18, 19, 56, 135, 136}

3.3.2.2 Electrochemistry of $[(\{(\text{bpy})_2\text{Os}(\text{dpp})\}_2\text{Ru})_2(\text{dpq})](\text{PF}_6)_{12}$ and $\{(\text{bpy})_2\text{Os}(\text{dpp})\}_2\text{Ru}(\text{dpq})](\text{PF}_6)_6$

The electrochemical properties of the hexametalllic complex $[(\{(\text{bpy})_2\text{Os}(\text{dpp})\}_2\text{Ru})_2(\text{dpq})](\text{PF}_6)_{12}$ and the trimetallic complex $\{(\text{bpy})_2\text{Os}(\text{dpp})\}_2\text{Ru}(\text{dpq})](\text{PF}_6)_6$ ⁶⁷ are summarized in Table 3.4 with cyclic voltammograms shown in Figure 3.6 and reductive square wave voltammograms shown in Figure 3.7. One

reversible couple (cathodic current similar to anodic current) is observed by CV in the oxidative region for the hexametallic complex, corresponding to the simultaneous oxidation of the four peripheral Os centers, 4 Os^{II/III}. Several overlapping redox couples are observed in the reduction region for [$\{(\text{bpy})_2\text{Os}(\text{dpp})\}_2\text{Ru}_2(\text{dpq})\}(\text{PF}_6)_{12}$ and [$\{(\text{bpy})_2\text{Os}(\text{dpp})\}_2\text{Ru}(\text{dpq})\}(\text{PF}_6)_6$.

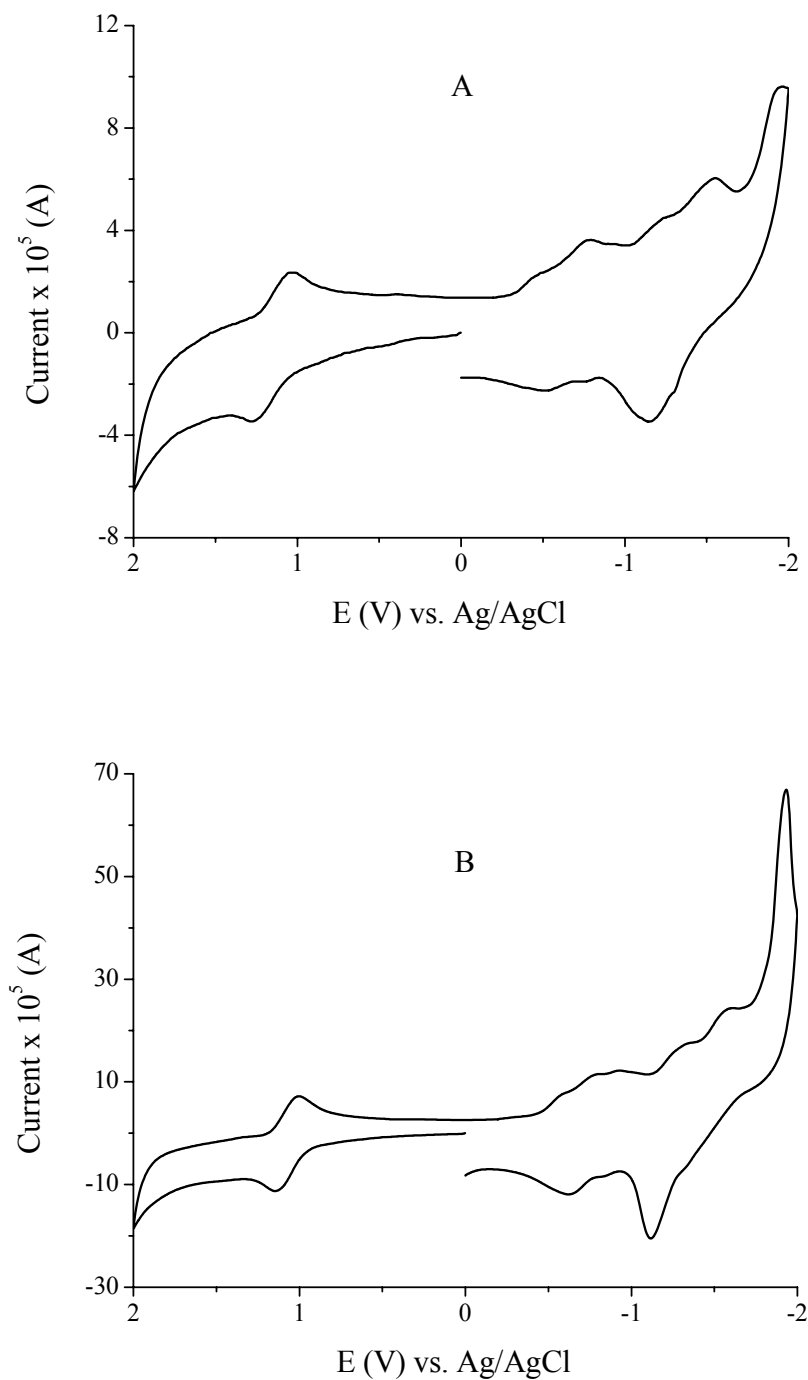


Figure 3.6 Cyclic voltammograms of [$\{(\text{bpy})_2\text{Os}(\text{dpp})\}_2\text{Ru}_2(\text{dpq})\}(\text{PF}_6)_{12}$ (A) and [$\{(\text{bpy})_2\text{Os}(\text{dpp})\}_2\text{Ru}(\text{dpq})\}(\text{PF}_6)_6$ (B) measured in 0.1 M Bu_4NPF_6 in CH_3CN solution at room temperature at a scan rate 200 mV/s (potential reported vs. Ag/AgCl; bpy = 2,2'-bipyridine, dpp = 2,3-bis(2-pyridyl)pyrazine, dpq = 2,3-bis(2-pyridyl)quinoxaline).

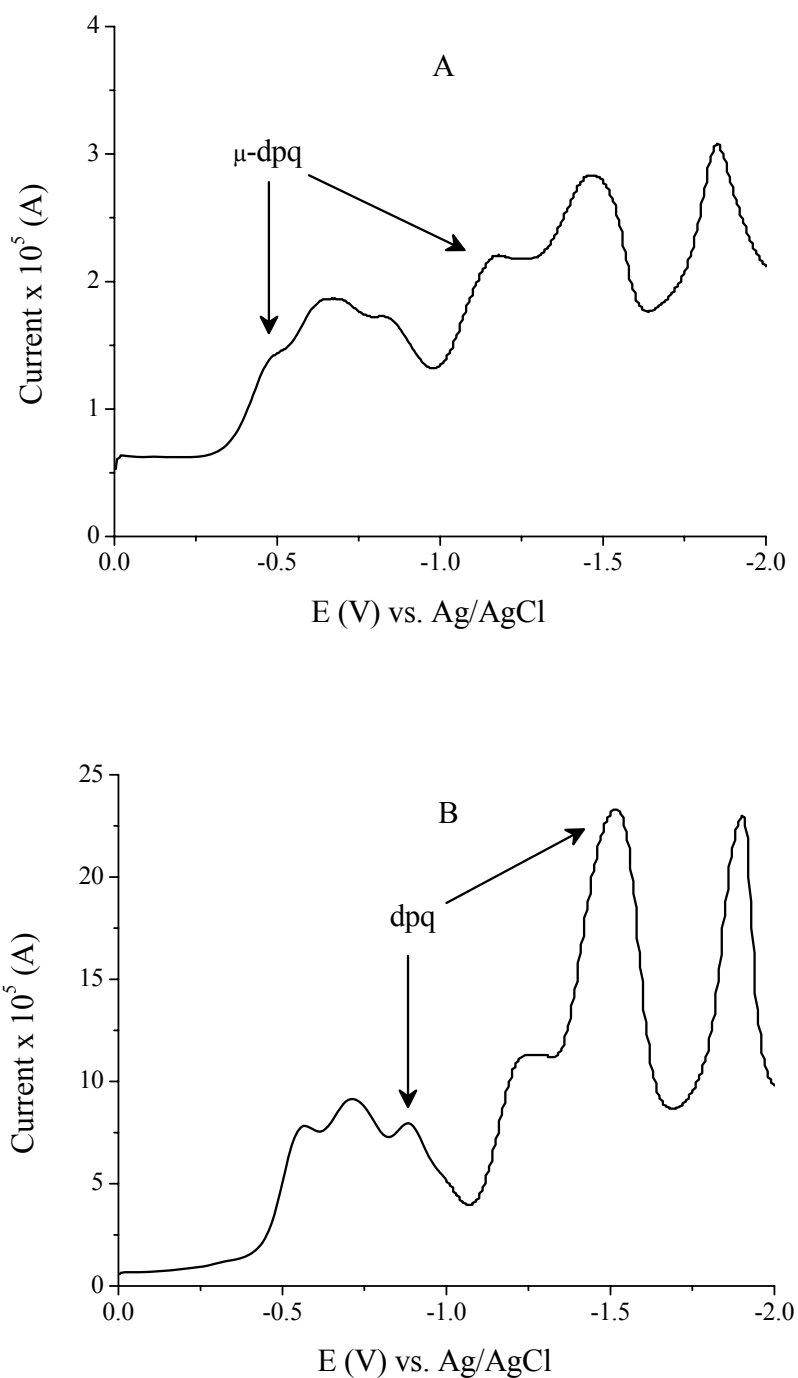


Figure 3.7 Square wave voltammograms of $[({(bpy)_2Os(dpp)}_2Ru)_2(dpq)](PF_6)_{12}$ (A) and $[({(bpy)_2Os(dpp)}_2Ru(dpq)](PF_6)_6$ (B) measured in 0.1 M Bu_4NPF_6 in CH_3CN solution at room temperature at a scan rate 200 mV/s (potential reported vs. Ag/AgCl; bpy = 2,2'-bipyridine, dpp = 2,3-bis(2-pyridyl)pyrazine, dpq = 2,3-bis(2-pyridyl)quinoxaline).

Table 3.4 Electrochemical properties of [$\{(\text{bpy})_2\text{Os}(\text{dpp})\}_2\text{Ru}_2(\text{dpq})\}(\text{PF}_6)_{12}$, [$\{(\text{bpy})_2\text{Os}(\text{dpp})\}_2\text{Ru}(\text{dpq})\}(\text{PF}_6)_6$ and related systems. ^a (bpy = 2,2'-bipyridine, dpp = 2,3-bis(2-pyridyl)pyrazine, dpq = 2,3-bis(2-pyridyl)quinoxaline)

Complex	$E_{1/2}$ (V)			
	Oxidations		Reductions	
$[(\text{bpy})_2\text{Ru}(\text{dpq})\text{Ru}(\text{bpy})_2](\text{PF}_6)_4$ ^b	1.57	$\text{Ru}^{\text{II,III/III,III}}$	-0.42	$\text{dpq}^{0/-}$
	1.42	$\text{Ru}^{\text{II,II/II,III}}$	-1.15	$\text{dpq}^{-/2-}$
$[(\text{bpy})_2\text{Ru}(\text{dpq})](\text{PF}_6)_2$ ^b	1.36	$\text{Ru}^{\text{II/III}}$	-0.83	$\text{dpq}^{0/-}$
			-1.46	$\text{bpy}^{0/-}$
$[\{(\text{bpy})_2\text{Os}(\text{dpp})\}_2\text{Ru}_2(\text{dpq})\}(\text{PF}_6)_{12}$	1.17	$4\text{Os}^{\text{II/III}}$	-0.48	$\text{dpq}^{0/-}$
			-0.66	$2\text{dpp}^{0/-}$
			-0.84	$2\text{dpp}^{0/-}$
			-1.20	$\text{dpq}^{-/2-}$
				$2\text{dpp}^{-/2-}$
			-1.41	$2\text{dpp}^{-/2-}$
			-1.81	$4\text{bpy}^{0/-}$
$[\{(\text{bpy})_2\text{Os}(\text{dpp})\}_2\text{Ru}(\text{dpq})\}(\text{PF}_6)_6$	1.07	$2\text{Os}^{\text{II/III}}$	-0.56	$\text{dpp}^{0/-}$
			-0.71	$\text{dpp}^{0/-}$
			-0.88	$\text{dpq}^{0/-}$
			-1.22	$2\text{dpp}^{-/2-}$
			-1.42	$2\text{bpy}^{0/-}$
				$\text{dpq}^{-/2-}$
		-1.83	$2\text{bpy}^{0/-}$	

^a Electrochemistry was measured in 0.1 M Bu_4NPF_6 in CH_3CN solution at room temperature at a scan rate 200 mV/s (potential reported vs. Ag/AgCl, 0.286 V vs. NHE), except for other specified experimental conditions.

^b ref. 33. Data is converted to the value vs. Ag/AgCl electrode. The experiment was performed in 0.1 M Et_4NClO_4 CH_3CN at room temperature vs. saturated sodium calomel electrode (SSCE).

The hexametalllic complex $[(\{(bpy)_2Os(dpp)\}_2Ru)_2(dpq)](PF_6)_{12}$ and the trimetalllic complex $[\{(bpy)_2Os(dpp)\}_2Ru(dpq)](PF_6)_6$ have similar electroactive units, except for the fact that the hexametalllic complex possesses a μ -dpq ligand, compared to the terminal dpq in the trimetalllic complex. The trimetalllic complex $[\{(bpy)_2Os(dpp)\}_2Ru(dpq)](PF_6)_6$ displays two μ -dpp^{0/-} couples prior to the terminal dpq^{0/-} couple, consistent with a bridging dpp and terminal dpq ligand. The redox properties of the hexametalllic complex $[(\{(bpy)_2Os(dpp)\}_2Ru)_2(dpq)](PF_6)_{12}$ are consistent with its formulation. The first reduction of dpq occurs at -0.48 V for the hexametalllic complex, which is in a more positive range than observed for the first reduction at -0.56 V for the trimetalllic complex. This is consistent with a bridging dpq in the hexametalllic complex. The μ -dpq^{0/-} couple is followed closely by a set of two μ -dpp^{0/-} couples at -0.66 and -0.84 V (Figure 3.8). This electrochemical data demonstrates the peripheral Os($d\pi$) based nature of highest-occupied molecular orbital (HOMO), as well as the μ -dpq(π^*) nature of the lowest-unoccupied molecular orbital (LUMO) for the hexametalllic complex vs. the μ -dpp(π^*) LUMO in the trimetalllic system. This orbital arrangement for the hexametalllic complex illustrates the thermodynamic possibility of generating a charge separated excited state for the hexametalllic complex between the terminal Os and central dpq, separated by the intervening Ru metal center. This large spatial separation between the localization site of the HOMO and LUMO in $[(\{(bpy)_2Os(dpp)\}_2Ru)_2(dpq)](PF_6)_{12}$ makes this structural moiety of interest. Specifically, when the excited state kinetics are studied, it could lead to information about the factors that govern light initiated charge separation and charge recombination within a metal based framework.^{34, 49, 54, 78}

Square wave voltammetry of both the trimetallic complex $[\{(bpy)_2Ru(dpp)\}_2Ru(\mathbf{dpp})](PF_6)_6$ and the tetrametallic complex $[\{(bpy)_2Ru(dpp)\}_2Ru(\mathbf{dpp})PtCl_2](PF_6)_6$ display complicated electrochemistry, which is consistent with the number of electroactive subunits in these complexes. Ruthenium polyazine complexes display Ru based oxidations in positive potential regions, and ligand based reductions in negative potential regions. The tetrametallic complex $[\{(bpy)_2Ru(dpp)\}_2Ru(\mathbf{dpp})PtCl_2](PF_6)_6$ displays only the peripheral $Ru^{II/III}$ oxidative redox couples in the electrochemical window, which is consistent with previously reported results for similar molecular architectures.³⁶ Generally, a central Ru bound to three μ -dpp ligands is more electron deficient, which leads to a shift of the $Ru^{II/III}$ couple outside the -2 to +2 V vs. Ag/AgCl potential window. The $Ru^{II/III}$ couple at 1.58 V vs. Ag/AgCl is identified as the point at which oxidation occurs for both terminal Ru centers. This is consistent with a multimetallic complex where Ru is coordinated to two bpy and one μ -dpp ligand.^{28, 43} The reductive region of $[\{(bpy)_2Ru(dpp)\}_2Ru(\mathbf{dpp})](PF_6)_6$ is consistent with its subunit composition. Typically μ -dpp is reduced in two one-electron steps prior to bpy reduction in this structural motif. $[\{(bpy)_2Ru(dpp)\}_2Ru(\mathbf{dpp})](PF_6)_6$ displays the expected μ -dpp^{0/-} couples at -0.50 and -0.64 V vs. Ag/AgCl, prior to the $\mathbf{dpp}^{0/-}$ couple at -1.08 V. $[\{(bpy)_2Ru(dpp)\}_2Ru(\mathbf{dpp})](PF_6)_6$ further displays the μ -dpp⁻²⁻ couples at -1.21 and -1.36 V vs. Ag/AgCl also prior to the \mathbf{dpp}^{-2-} couple at -1.52 V. Coordination of the terminal \mathbf{dpp} to Pt to form $[\{(bpy)_2Ru(dpp)\}_2Ru(\mathbf{dpp})PtCl_2](PF_6)_6$, leads to a significant shift of the $\mathbf{dpp}^{0/-}$ couple in $[\{(bpy)_2Ru(dpp)\}_2Ru(\mathbf{dpp})PtCl_2](PF_6)_6$. $[\{(bpy)_2Ru(dpp)\}_2Ru(\mathbf{dpp})PtCl_2](PF_6)_6$ displays three low potential dpp^{0/-} couples at -0.40 -0.60, and -0.71 V vs. Ag/AgCl with μ - \mathbf{dpp} bridging the Ru and Pt center being reduced first. This is consistent with the more easily reducible μ -dpp in $[(bpy)_2Ru(dpp)PtCl_2]^{2+}$ vs. $[(bpy)_2Ru(dpp)Ru(bpy)_2]^{4+}$ (Table 3.5).²⁸ The μ -dpp^{0/-} couples in the tetrametallic complex are followed by three μ -dpp⁻²⁻ couples prior to the bpy^{0/-} reductive couples (Figure 3.9 and Figure 3.10). The observed redox potential shift of dpp^{0/-} from -1.08 V (when dpp is a terminal ligand) to -0.40 V (when dpp connects Pt and Ru) identified the structure of tetrametallic complex and also helped to assign other similar

complex systems. The electrochemistry indicates that the LUMO of $[\{(bpy)_2Ru(dpp)\}_2Ru(dpp)](PF_6)_6$ is localized on the μ -dpp connecting two terminal Ru centers, while the LUMO of $[\{(bpy)_2Ru(dpp)\}_2Ru(dpp)PtCl_2](PF_6)_6$ is localized at the central μ -dpp connecting the central Ru and Pt. The greater degree of stabilization of a μ -dpp (π^*) bound to a Ru and Pt metals, in comparison to μ -dpp (π^*) bound to two Ru, is consistent with previously reported results (Table 3.5).^{12, 13} These orbitals provide spatial separation of these frontier orbitals to generate a charge separated state between the terminal Ru and the μ -dpp bridging the Ru and Pt centers in $[\{(bpy)_2Ru(dpp)\}_2Ru(dpp)PtCl_2](PF_6)_6$.

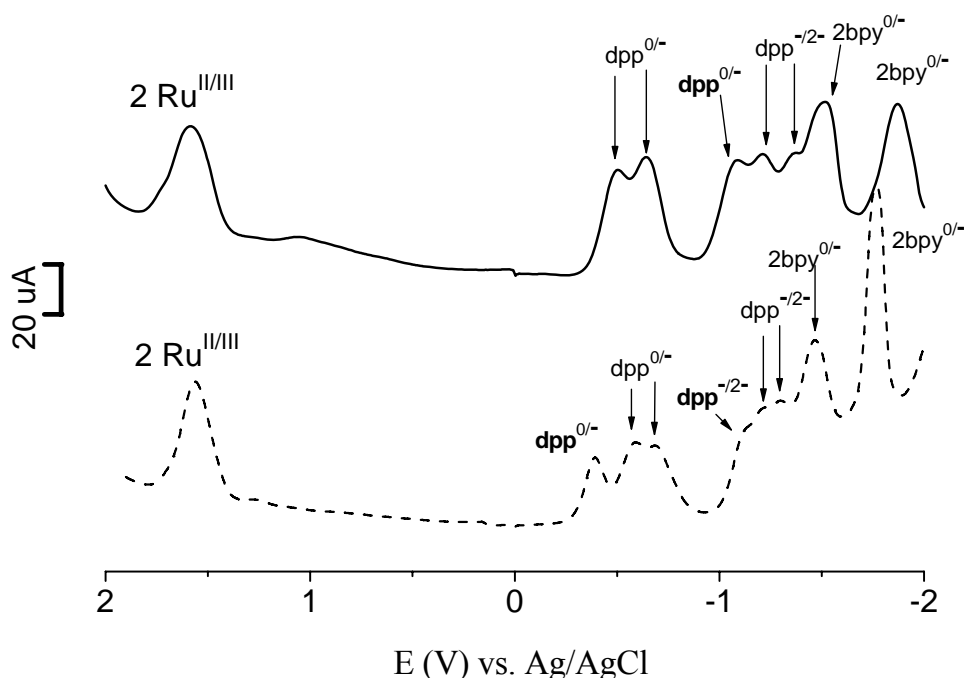


Figure 3.9 Square wave voltammograms of $[\{(bpy)_2Ru(dpp)\}_2Ru(dpp)](PF_6)_6$ (—) and $[\{(bpy)_2Ru(dpp)\}_2Ru(dpp)PtCl_2](PF_6)_6$ (---) measured in 0.1 M Bu_4NPF_6 in CH_3CN solution at room temperature at a scan rate 200 mV/s (V vs. Ag/AgCl; bpy = 2,2'-bipyridine, dpp = 2,3-bis(2-pyridyl)pyrazine, dpq = 2,3-bis(2-pyridyl)quinoxaline).

Table 3.5 Electrochemical properties for [$\{(bpy)_2Ru(dpp)\}_2Ru(dpp)PtCl_2\}(PF_6)_6$ and related systems. ^{a,b}

Complex	$E_{1/2}$ (V)			
	Oxidations		Reductions	
$[(bpy)_2Ru(dpp)](PF_6)_2^c$	1.38	$Ru^{II/III}$	-1.16	$dpp^{0/-}$
$[(bpy)_2Ru(dpp)Ru(bpy)_2](PF_6)_4^d$	1.57	$Ru^{II,III/III,III}$	-1.55	$bpy^{0/-}$
	1.38	$Ru^{II,II/II,III}$	-1.76	$bpy^{0/-}$
$[(bpy)_2Ru(dpp)PtCl_2](PF_6)_2^e$	1.62	$Ru^{II/III}$	-0.66	$dpp^{0/-}$
			-1.13	dpp^{-2-}
$[\{(bpy)_2Ru(dpp)\}_3Ru](PF_6)_8^f$	1.45	$3Ru^{II/III}$	-1.50	$2bpy^{0/-}$
			-0.49	$dpp^{0/-}$
			-1.06	dpp^{-2-}
			-1.44	$bpy^{0/-}$
			-0.61	$dpp^{0/-}$
$[\{(bpy)_2Ru(dpp)\}_2Ru(dpp)](PF_6)_6$	1.58	$2Ru^{II/III}$	-0.79	$dpp^{0/-}$
			-0.94	$dpp^{0/-}$
			-1.17	dpp^{-2-}
			-1.27	dpp^{-2-}
			-1.42	dpp^{-2-}
			-0.50	$dpp^{0/-}$
			-0.64	$dpp^{0/-}$
			-1.08	$dpp^{0/-}$
			-1.21	dpp^{-2-}
			-1.36	dpp^{-2-}
$[\{(bpy)_2Ru(dpp)\}_2Ru(dpp)PtCl_2](PF_6)_6$	1.58	$2Ru^{II/III}$	-1.52	dpp^{-2-}
			-0.40	$dpp^{0/-}$
			-0.60	$dpp^{0/-}$
			-0.71	$dpp^{0/-}$
			-1.12	dpp^{-2-}
			-1.22	dpp^{-2-}
			-1.30	dpp^{-2-}

^a Data measured in 0.1 M Bu_4NPF_6 in CH_3CN , V vs. $Ag/AgCl$.

^b bpy = 2,2'-bipyridine and dpp = 2,3-bis(2-pyridyl)pyrazine.

^c ref. 12.

^d ref. 12, converted from V vs. SCE.

^e ref. 28, converted from V vs. SCE.

^f ref. 136, converted from V vs. SCE.

Synthesized Oxidative State

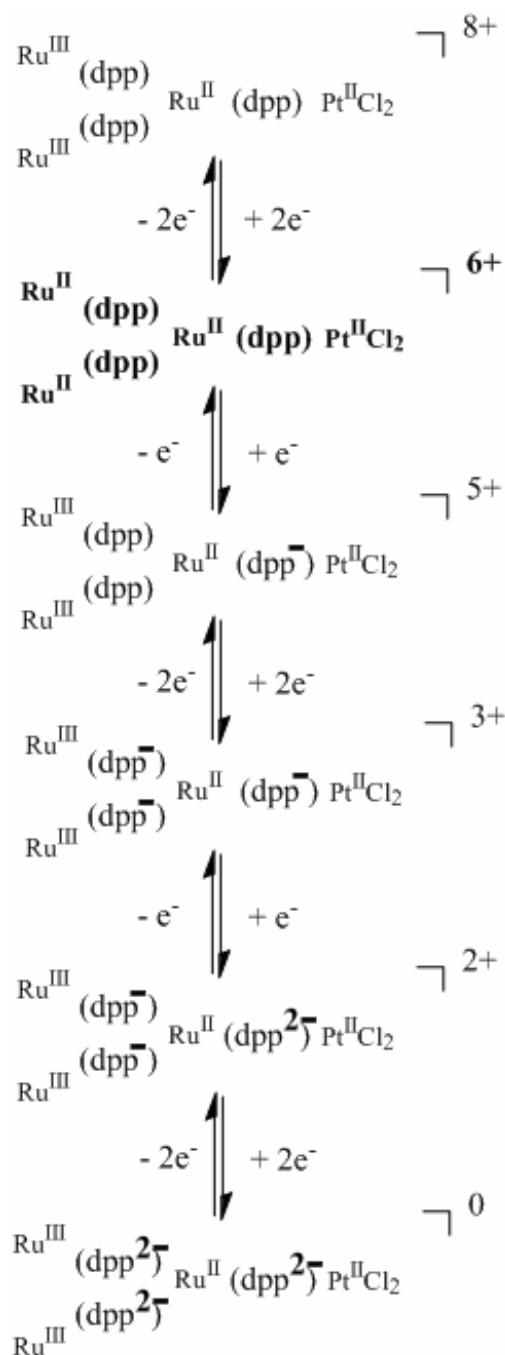


Figure 3.10 Electrochemical mechanism for $[\{(bpy)_2Ru(dpp)\}_2Ru(dpp)PtCl_2](PF_6)_6$ with the bpy ligands omitted for clarity (bpy = 2,2'-bipyridine, dpp = 2,3-bis(2-pyridyl)pyrazine).

The electrochemical properties of the trimetallic complexes

$[\{(bpy)_2Ru(dpp)\}_2Ru(dpp)](PF_6)_6$, $[\{(bpy)_2Ru(dpp)\}_2Ru(dpq)](PF_6)_6$ and

$[\{(bpy)_2Os(dpp)\}_2Ru(dpq)](PF_6)_6$, as well as the tetrametallic complexes

$[\{(bpy)_2Ru(dpp)\}_2Ru(dpp)PtCl_2](PF_6)_6$, $[\{(bpy)_2Ru(dpp)\}_2Ru(dpq)PtCl_2](PF_6)_6$ and

$[\{(bpy)_2Os(dpp)\}_2Ru(dpq)PtCl_2](PF_6)_6$ are shown in Figure 3.11 and summarized in Table 3.6.

As discussed previously, $Os^{II/III}$ oxidation (~ 1.1 V vs. Ag/AgCl) typically occurs at less positive potentials compared to $Ru^{II/III}$ (~ 1.6 V vs. Ag/AgCl). The less positive potential of $Os^{II/III}$ oxidation is consistent with the higher energy $d\pi$ orbitals of Os compared to Ru. The reductive region is typically dominated by ligand based redox couples, depending on each ligand's electron accepting ability. As has been shown, dpq is a better electron acceptor than dpp, primarily due to the enlarged π conjugated system in dpq.²⁸ For the trimetallic complexes, the terminal $dpp^{0/-}$ is at -1.08 V vs. Ag/AgCl, while the terminal $dpq^{0/-}$ is at -0.82 V or -0.88 V vs. Ag/AgCl. For the tetrametallic complexes, the π^* orbital of the bridging ligands connecting central Ru and Pt are significantly stabilized. In fact, their first reductions are shifted to the least negative values in each tetrametallic complex, -0.40 V for the μ -dpp^{0/-} and -0.08 V for the μ -dpq^{0/-} (V vs. Ag/AgCl).

From this electrochemical data, we can conclude that (1) the HOMO of all the complexes is localized on the peripheral $[(bpy)_2M(dpp)]^{2+}$ ($M = Ru^{II}$ or Os^{II}), (2) the LUMO of all the trimetallic complexes is localized on the μ -dpp, and (3) the LUMO of all the tetrametallic complexes is localized on the bridging ligand connecting central Ru and Pt.

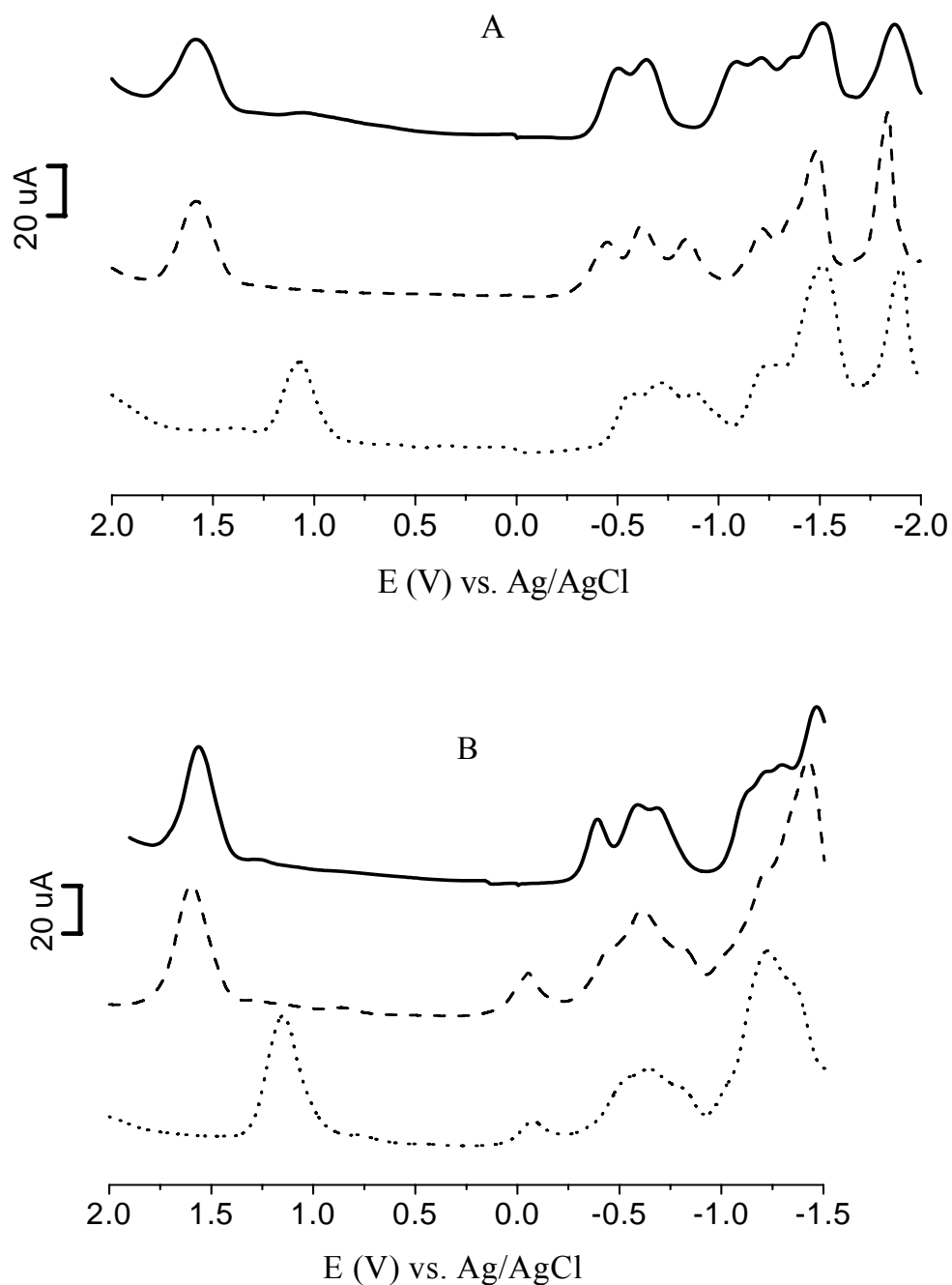


Figure 3.11 Square wave voltammograms of the trimetallic complexes (A) including $[\{(bpy)_2Ru(dpp)\}_2Ru(dpp)](PF_6)_6$ (—), $[\{(bpy)_2Ru(dpp)\}_2Ru(dpq)](PF_6)_6$ (---), and $[\{(bpy)_2Os(dpp)\}_2Ru(dpq)](PF_6)_6$ (•••); as well as the tetrametallic complexes (B) including $[\{(bpy)_2Ru(dpp)\}_2Ru(dpp)PtCl_2](PF_6)_6$ (—), $[\{(bpy)_2Ru(dpp)\}_2Ru(dpq)PtCl_2](PF_6)_6$ (---), and $[\{(bpy)_2Os(dpp)\}_2Ru(dpq)PtCl_2](PF_6)_6$ (•••) measured in 0.1 M Bu_4NPF_6 CH_3CN solution at room temperature at a scan rate 200 mV/s (V vs. Ag/AgCl; bpy = 2,2'-bipyridine, dpp = 2,3-bis(2-pyridyl)pyrazine, dpq = 2,3-bis(2-pyridyl)quinoxaline).

Table 3.6 Electrochemical properties of trimetallic and tetrametallic complexes. ^{a,b}

Complex	$E_{1/2}$ (V)			
	Oxidations		Reductions	
[{(bpy) ₂ Ru(dpp)} ₂ Ru(dpp)](PF ₆) ₆	1.58	2Ru ^{II/III}	-0.50	dpp ^{0/-}
			-0.64	dpp ^{0/-}
			-1.08	dpp ^{0/-}
			-1.21	dpp ^{-2/-}
			-1.36	dpp ^{-2/-}
			-1.52	dpp ^{-2/-}
[{(bpy) ₂ Ru(dpp)} ₂ Ru(dpq)](PF ₆) ₆	1.58	2Ru ^{II/III}	-0.42	dpp ^{0/-}
			-0.62	dpp ^{0/-}
			-0.82	dpq ^{0/-}
			-1.24	dpp ^{-2/-}
			-1.37	dpp ^{-2/-}
			-1.50	dpq ^{-2/-}
[{(bpy) ₂ Os(dpp)} ₂ Ru(dpq)](PF ₆) ₆	1.07	2Os ^{II/III}	-0.56	dpp ^{0/-}
			-0.71	dpp ^{0/-}
			-0.88	dpq ^{0/-}
			-1.22	2dpp ^{-2/-}
			-1.42	2bpy ^{0/-}
				dpq ^{-2/-}

Complex	$E_{1/2}$ (V)			
	Oxidations		Reductions	
[$\{(\text{bpy})_2\text{Ru}(\text{dpp})\}_2\text{Ru}(\text{dpp})\text{PtCl}_2](\text{PF}_6)_6$]	1.58	$2\text{Ru}^{\text{II/III}}$	-0.40	$\text{dpp}^{0/-}$
			-0.60	$\text{dpp}^{0/-}$
			-0.71	$\text{dpp}^{0/-}$
			-1.12	dpp^{-2-}
			-1.22	dpp^{-2-}
			-1.30	dpp^{-2-}
[$\{(\text{bpy})_2\text{Ru}(\text{dpp})\}_2\text{Ru}(\text{dpq})\text{PtCl}_2](\text{PF}_6)_6$]	1.59	$2\text{Ru}^{\text{II/III}}$	-0.08	$\text{dpq}^{0/-}$
			-0.44	$\text{dpp}^{0/-}$
			-0.64	$\text{dpp}^{0/-}$
			-0.84	dpq^{-2-}
			-1.04	dpp^{-2-}
			-1.22	dpp^{-2-}
[$\{(\text{bpy})_2\text{Os}(\text{dpp})\}_2\text{Ru}(\text{dpq})\text{PtCl}_2](\text{PF}_6)_6$]	1.10	$2\text{Os}^{\text{II/III}}$	-0.08	$\text{dpq}^{0/-}$
			-0.52	$\text{dpp}^{0/-}$
			-0.65	$\text{dpp}^{0/-}$
			-0.83	dpq^{-2-}
			-1.24	2dpp^{-2-}
			-1.36	$2\text{bpy}^{0/-}$

^a Data measured in 0.1 M Bu_4NPF_6 in CH_3CN , V vs. Ag/AgCl .

^b bpy = 2,2'-bipyridine, dpp = 2,3-bis(2-pyridyl)pyrazine and dpq = 2,3-bis(2-pyridyl)quinoxaline.

3.3.3 Electronic Absorption Spectroscopy of [$\{(\text{bpy})_2\text{Os}(\text{dpp})\}_2\text{Ru}\}_2(\text{dpq})](\text{PF}_6)_{12}$ and [$\{(\text{bpy})_2\text{Os}(\text{dpp})\}_2\text{Ru}(\text{dpq})](\text{PF}_6)_6$

The electronic absorption spectra of [$\{(\text{bpy})_2\text{Os}(\text{dpp})\}_2\text{Ru}\}_2(\text{dpq})](\text{PF}_6)_{12}$ and [$\{(\text{bpy})_2\text{Os}(\text{dpp})\}_2\text{Ru}(\text{dpq})](\text{PF}_6)_6$ ^{5, 10, 137} are shown in Figure 3.12. Both complexes show

similar spectroscopy, which results from their comparable chromophoric units. The hexametallic $[(\{(bpy)_2Os(dpp)\}_2Ru)_2(dpq)](PF_6)_{12}$ and related trimetallic $[(\{(bpy)_2Os(dpp)\}_2Ru(dpq)](PF_6)_6$ are efficient light absorbers with absorbance throughout the UV and visible regions. The extinction coefficient of the hexametallic complex is roughly twice as much as that of the trimetallic complex, displaying additivity of the absorbance.

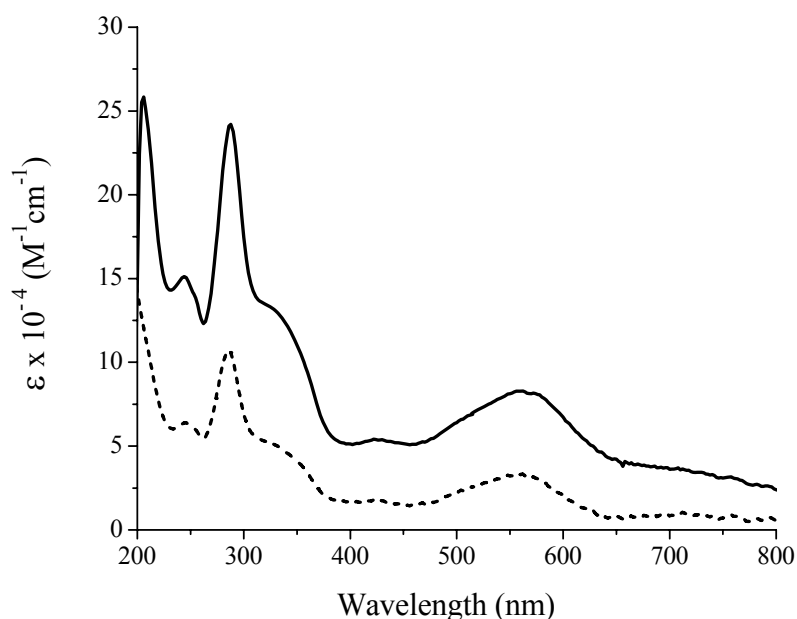


Figure 3.12 Electronic absorption spectra of $[(\{(bpy)_2Os(dpp)\}_2Ru)_2(dpq)](PF_6)_{12}$ (—) and $[(\{(bpy)_2Os(dpp)\}_2Ru(dpq)](PF_6)_6$ (---), measured in CH_3CN solvent at room temperature (bpy = 2,2'-bipyridine, dpp = 2,3-bis(2-pyridyl)pyrazine, dpq = 2,3-bis(2-pyridyl)quinoxaline).

Polyazine complexes of Ru and Os display intense transitions in the UV region dominated by intraligand $\pi \rightarrow \pi^*$ transitions for each ligand and a series of absorptions in the visible region, which can be attributed to metal to ligand charge transfer (1MLCT) transitions from each metal to each acceptor ligand.¹⁵ The lowest energy bands in the visible region typically correspond to MLCT transitions to the bridging ligands. Osmium polyazine complexes display low energy tails, along with their 1MLCT transitions, which is associated with 3MLCT transitions due to the strong spin orbit coupling of the Os complexes. Table 3.7 summarizes the spectroscopic data for $[(\{(bpy)_2Os(dpp)\}_2Ru)_2(dpq)](PF_6)_{12}$,

$[\{(bpy)_2Os(dpp)\}_2Ru(dpq)](PF_6)_6$ ¹³ and related model systems. Both the hexametalllic and trimetalllic complexes display peaks in the UV region characteristic of each polypyridine ligand. Peaks occurring at 290 nm is characteristic of bpy $\pi \rightarrow \pi^*$ transitions, and scale relative to the number of bpy ligands.⁵ Additional intraligand bands are observed as low energy shoulders on the bpy based transition, which is characteristic of μ -dpp $\pi \rightarrow \pi^*$ transitions. This shoulder extends to lower energy regions in the hexametalllic complex relative to the trimetalllic complex, which is consistent with the terminal dpq $\pi \rightarrow \pi^*$ transition shifted to lower energy consistent with the μ -dpq $\pi \rightarrow \pi^*$ transition.¹⁸ The ¹MLCT transitions for $Ru(d\pi) \rightarrow bpy(\pi^*)$, $Os(d\pi) \rightarrow bpy(\pi^*)$, $Os(d\pi) \rightarrow \mu$ -dpp(π^*), $Ru(d\pi) \rightarrow \mu$ -dpp(π^*) and $Ru(d\pi) \rightarrow \mu$ -dpq(π^*) ¹MLCT are all expected to occur in the visible region of the spectrum. The ³MLCT for $Os(d\pi) \rightarrow bpy(\pi^*)$ and $Os(d\pi) \rightarrow \mu$ -dpp(π^*) CT occur in the low energy visible and near-IR regions. Based on the model systems and our observed electrochemical data, the $Os(d\pi) \rightarrow bpy(\pi^*)$ ¹MLCT is estimated at 430 nm, $Ru(d\pi) \rightarrow \mu$ -dpp(π^*) ¹MLCT transition at 525 nm,^{4, 16, 36} the $Os(d\pi) \rightarrow \mu$ -dpp(π^*) ¹MLCT transition at 550 nm,^{18, 19} and the $Ru(d\pi) \rightarrow \mu$ -dpq(π^*) ¹MLCT at 605 nm.¹³ Due to the overlapping MLCT transitions present in these supramolecules, it is difficult to make the assignments. Some of the MLCT transitions were assigned combining the difference spectrum and the spectroelectrochemistry, as well as synthetic variations.

As this research demonstrated, a careful analysis of the spectrum of the hexametalllic vs. the trimetalllic complexes is possible through the process of spectral subtraction, see Figure 3.13. For this study, the spectra were normalized at a bpy $\pi \rightarrow \pi^*$ of 290 nm (Figure 3.13A) and at 562 nm corresponding to overlapping various ¹MLCT bands (Figure 3.13B) prior to the subtraction. As shown in the normalized difference spectrum, there was a dip at 554 nm and a peak at 610 nm. The 554 nm is where the $Ru(d\pi) \rightarrow dpq(\pi^*)$ (terminal) ¹MLCT transition in the trimetalllic complex $[\{(bpy)_2Os(dpp)\}_2Ru(dpq)](PF_6)_6$ is, and the peak at 610 nm matches the $Ru(d\pi) \rightarrow \mu$ -dpq(π^*) ¹MLCT transition, consistent with the previously reported 605 nm $Ru(d\pi) \rightarrow \mu$ -dpq(π^*) ¹MLCT band in the $[(bpy)_2Ru(dpq)Ru(bpy)_2](PF_6)_4$.⁵ This dip and peak shape in the difference spectrum may be explained by the change of dpq from terminal ligand in the trimetalllic complex to bridging ligand in the hexametalllic

complex, which was consistent with the proposed hexametallic structural formation. The electronic absorption spectral analysis is consistent with the dpq (π^*) based LUMO in the $[(\{(\text{bpy})_2\text{Os}(\text{dpp})\}_2\text{Ru})_2(\text{dpq})](\text{PF}_6)_{12}$.

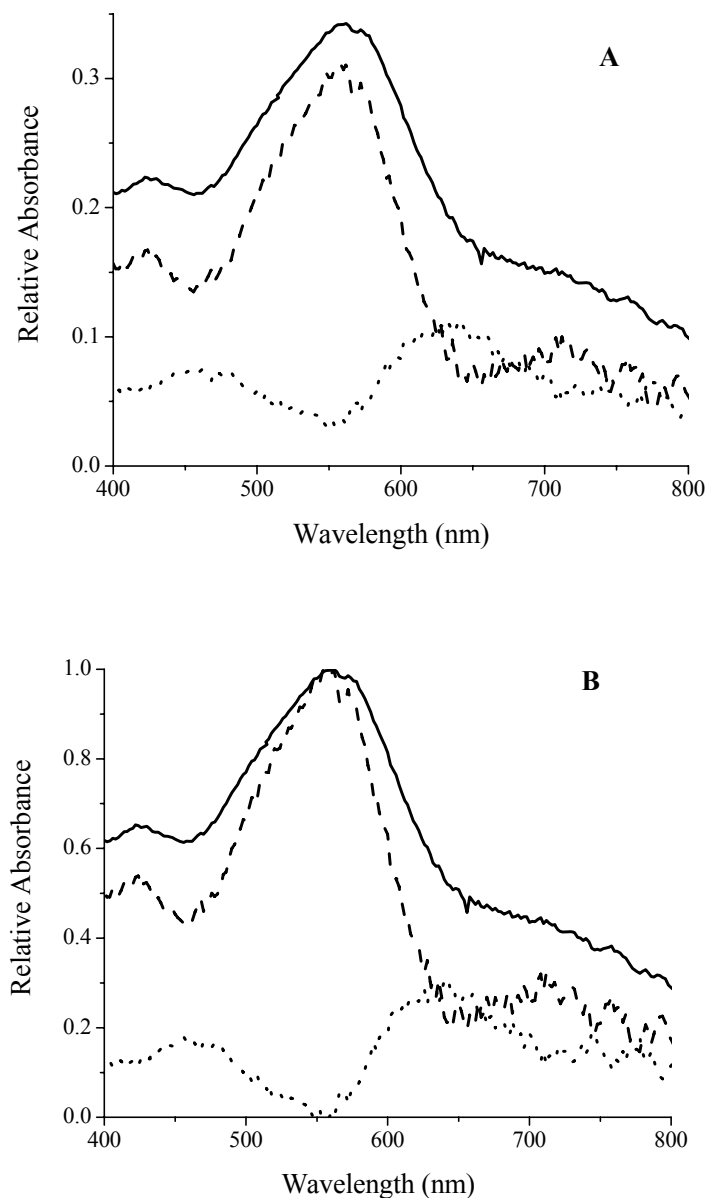


Figure 3.13 Normalized electronic absorption spectra (A at 290 nm and B at 562 nm) of $[(\{(\text{bpy})_2\text{Os}(\text{dpp})\}_2\text{Ru})_2(\text{dpq})](\text{PF}_6)_{12}$ (—), $[(\{(\text{bpy})_2\text{Os}(\text{dpp})\}_2\text{Ru}(\text{dpq})](\text{PF}_6)_6$ (---) and the subtraction of trimetallic from hexametallic complex (•••) measured in CH_3CN at room temperature (bpy = 2,2'-bipyridine, dpp = 2,3-bis(2-pyridyl)pyrazine, dpq = 2,3-bis(2-pyridyl)quinoxaline).

Table 3.7 Electronic absorption spectra data summary of $[(\{\text{bpy}\}_2\text{Os}(\text{dpp})\}_2\text{Ru})_2(\text{dpq})](\text{PF}_6)_{12}$, $[(\{\text{bpy}\}_2\text{Os}(\text{dpp})\}_2\text{Ru}(\text{dpq}))(\text{PF}_6)_6$ and related systems. ^a(bpy = 2,2'-bipyridine, dpp = 2,3-bis(2-pyridyl)pyrazine, dpq = 2,3-bis(2-pyridyl)quinoxaline).

Complex	Wavelength (nm)	$\epsilon \times 10^{-4}$ ($\text{M}^{-1}\text{cm}^{-1}$)	Assignments
$[(\text{bpy})_2\text{Ru}(\text{dpp})\text{Ru}(\text{bpy})_2](\text{PF}_6)_4^{\text{b}}$	425	1.7	$\text{Ru}(\text{d}\pi) \rightarrow \text{bpy}(\pi^*)$ CT
	525	2.1	$\text{Ru}(\text{d}\pi) \rightarrow \mu\text{-dpp}(\pi^*)$ CT
$[(\text{bpy})_2\text{Os}(\text{dpp})\text{Os}(\text{bpy})_2](\text{PF}_6)_4^{\text{c}}$	432	2.0	$\text{Os}(\text{d}\pi) \rightarrow \text{bpy}(\pi^*)$ CT
	552	2.5	$\text{Os}(\text{d}\pi) \rightarrow \mu\text{-dpp}(\pi^*)$ CT
$[(\text{bpy})_2\text{Ru}(\text{dpp})\text{Os}(\text{bpy})_2](\text{PF}_6)_4^{\text{d}}$	430	2.2	$\text{Ru}(\text{d}\pi) \rightarrow \text{bpy}(\pi^*)$ CT
			$\text{Os}(\text{d}\pi) \rightarrow \text{bpy}(\pi^*)$ CT
	542	2.9	$\text{Os}(\text{d}\pi) \rightarrow \mu\text{-dpp}(\pi^*)$ CT
$[(\text{bpy})_2\text{Ru}(\text{dpp})\text{Os}(\text{bpy})_2](\text{PF}_6)_4^{\text{d}}$			$\text{Ru}(\text{d}\pi) \rightarrow \mu\text{-dpp}(\pi^*)$ CT
	542	2.9	$\text{Os}(\text{d}\pi) \rightarrow \mu\text{-dpp}(\pi^*)$ CT
$[(\text{bpy})_2\text{Ru}(\text{dpq})\text{Ru}(\text{bpy})_2](\text{PF}_6)_4^{\text{e}}$	423	^f	$\text{Ru}(\text{d}\pi) \rightarrow \text{bpy}(\pi^*)$ CT
	605	0.98	$\text{Ru}(\text{d}\pi) \rightarrow \mu\text{-dpq}(\pi^*)$ CT
$[(\text{bpy})_2\text{Ru}(\text{dpq})](\text{PF}_6)_2^{\text{e}}$	515	0.81	$\text{Ru}(\text{d}\pi) \rightarrow \text{dpq}(\pi^*)$ CT
$[(\{\text{bpy}\}_2\text{Os}(\text{dpp})\}_2\text{Ru})_2(\text{dpq})](\text{PF}_6)_{12}$	430	5.4	$\text{Ru}(\text{d}\pi) \rightarrow \text{bpy}(\pi^*)$ CT
			$\text{Os}(\text{d}\pi) \rightarrow \text{bpy}(\pi^*)$ CT
	560	8.3	$\text{Os}(\text{d}\pi) \rightarrow \mu\text{-dpp}(\pi^*)$ CT
			$\text{Ru}(\text{d}\pi) \rightarrow \mu\text{-dpp}(\pi^*)$ CT
	720	3.5	$^3\text{Os}(\text{d}\pi) \rightarrow \mu\text{-dpp}(\pi^*)$ CT

$[\{(\text{bpy})_2\text{Os}(\text{dpp})\}_2\text{Ru}(\text{dpq})](\text{PF}_6)_6$	430	1.8	$\text{Ru}(\text{d}\pi) \rightarrow \text{bpy}(\pi^*)$ CT
			$\text{Os}(\text{d}\pi) \rightarrow \text{bpy}(\pi^*)$ CT
	560	3.3	$\text{Os}(\text{d}\pi) \rightarrow \mu\text{-dpp}(\pi^*)$ CT
			$\text{Ru}(\text{d}\pi) \rightarrow \mu\text{-dpp}(\pi^*)$ CT
	720	0.89	$^3\text{Os}(\text{d}\pi) \rightarrow \mu\text{-dpp}(\pi^*)$ CT

^a Electronic absorption spectroscopy measured in CH_3CN solvent at room temperature.

^b ref. 13 ; ^c ref. 4 ; ^d ref. 67 ; ^e ref. 18.

^f extinction coefficient not provided in the ref. 18.

3.3.4 Spectroelectrochemistry of $[\{(\text{bpy})_2\text{Os}(\text{dpp})\}_2\text{Ru}(\text{dpq})](\text{PF}_6)_{12}$ and

$[\{(\text{bpy})_2\text{Os}(\text{dpp})\}_2\text{Ru}(\text{dpq})](\text{PF}_6)_6$

The nature and behavior of these complex assemblies can be further clarified through the use of spectroelectrochemistry. For example, the hexametalllic compound $[\{(\text{bpy})_2\text{Os}(\text{dpp})\}_2\text{Ru}(\text{dpq})](\text{PF}_6)_{12}$ and the trimetalllic compound $[\{(\text{bpy})_2\text{Os}(\text{dpp})\}_2\text{Ru}(\text{dpq})](\text{PF}_6)_6$ ^{5, 12} can be reversibly oxidized and their spectroscopy studied in detail using spectroelectrochemistry (Figure 3.14). Oxidation at 1.30 V vs. Ag/AgCl , which is more positive than the $\text{Os}^{\text{II/III}}$ couple at 1.17 V vs. Ag/AgCl , leads to the generation of the Os^{III} form of these complexes. Oxidation also leads to a shift out of the visible region of the spectrum for all osmium based MLCT transitions, such as the $\text{Os}(\text{d}\pi) \rightarrow \mu\text{-dpp}(\pi^*)$ ¹MLCT transition at 552 nm and the $\text{Os}(\text{d}\pi) \rightarrow \text{bpy}(\pi^*)$ ¹MLCT at 432 nm. This shift of the osmium based MLCT transitions reveal the Ru based MLCT transitions in this region. The oxidation of the Os decreases the electron density on the $\mu\text{-dpp}$ ligand, slightly red-shifting the Ru based MLCT transitions. The $\text{Ru}(\text{d}\pi) \rightarrow \mu\text{-dpp}(\pi^*)$ ¹MLCT band occurs at 515 nm for the oxidized trimetalllic $[\{(\text{bpy})_2\text{Os}^{\text{III}}(\text{dpp})\}_2\text{Ru}^{\text{II}}(\text{dpq})]^{8+}$, and at 523 nm for oxidized hexametalllic $[\{(\text{bpy})_2\text{Os}^{\text{III}}(\text{dpp})\}_2\text{Ru}^{\text{II}}(\text{dpq})]^{16+}$. This is consistent with the band at 525 nm $\text{Ru}(\text{d}\pi) \rightarrow \mu\text{-dpp}(\pi^*)$ ¹MLCT transition for the symmetric $[(\text{bpy})_2\text{Ru}(\text{dpp})\text{Ru}(\text{bpy})_2](\text{PF}_6)_2$ system.^{15, 21} It should also be noted that the low energy tails

shown at 650 nm to 800 nm are lost upon oxidation of the osmium centers, consistent with their Os based $^3\text{MLCT}$ assignments.¹³⁸ Comparison of the spectroscopy of the Os^{III} forms of the trimetallic and hexametallic compounds by spectral subtraction uncovers an additional peak at 570 nm for the hexametallic $[\{(\text{bpy})_2\text{Os}(\text{dpp})\}_2\text{Ru}_2(\text{dpq})](\text{PF}_6)_{12}$, which is shown in Figure 3.15. This 570 nm peak corresponds to the $\text{Ru}(\text{d}\pi) \rightarrow \mu\text{-dpq}(\pi^*)$ $^1\text{MLCT}$ in $[\{(\text{bpy})_2\text{Os}(\text{dpp})\}_2\text{Ru}_2(\text{dpq})](\text{PF}_6)_{12}$. The reversibility of the oxidative spectroelectrochemistry of both the $[\{(\text{bpy})_2\text{Os}(\text{dpp})\}_2\text{Ru}(\text{dpq})](\text{PF}_6)_6$ and the $[\{(\text{bpy})_2\text{Os}(\text{dpp})\}_2\text{Ru}_2(\text{dpq})](\text{PF}_6)_{12}$ was also studied, which showed that > 95% retain their original spectrum upon reduction to Os^{II} at 0 V.

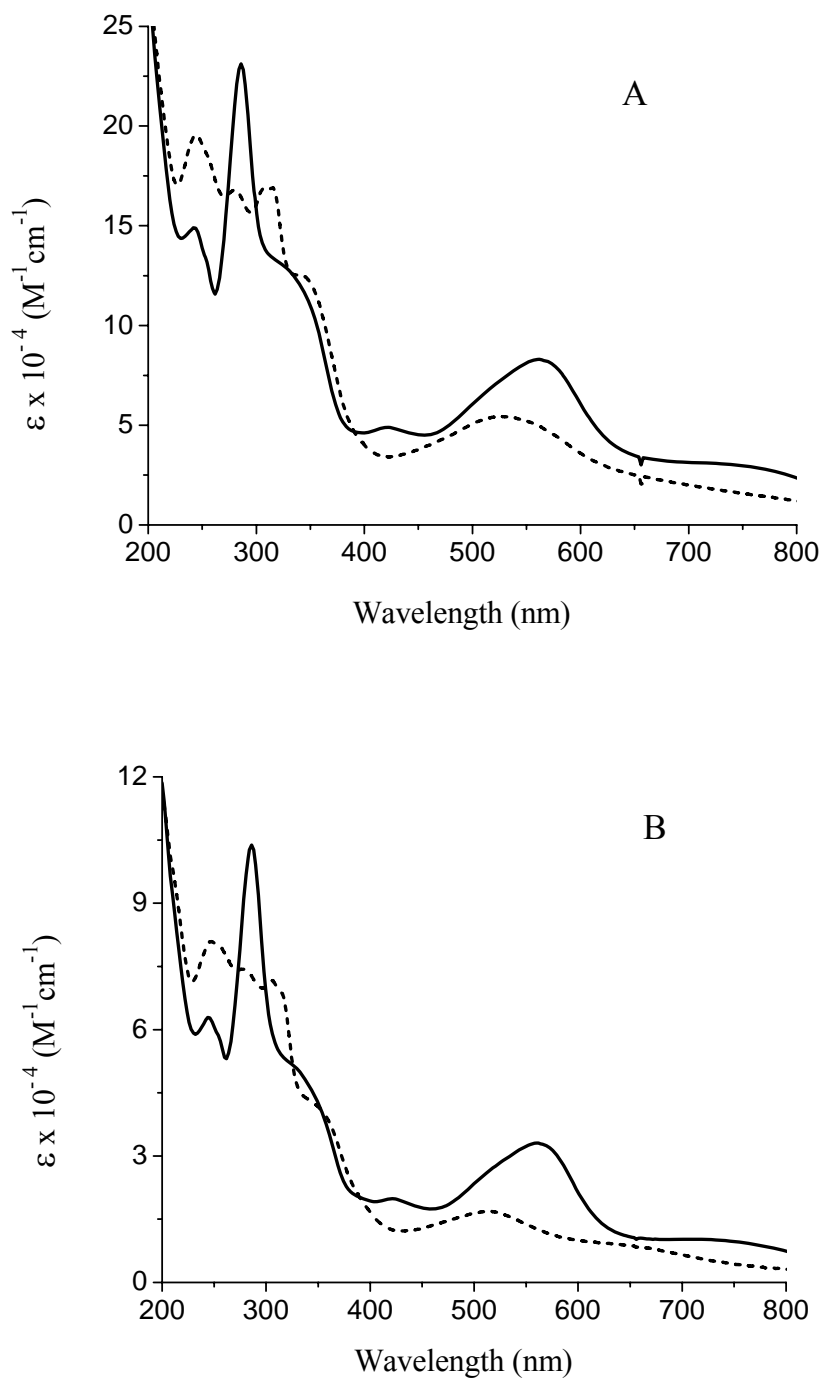


Figure 3.14 Oxidative spectroelectrochemistry of [$\{(\text{bpy})_2\text{Os}(\text{dpp})\}_2\text{Ru}_2(\text{dpq})\}(\text{PF}_6)_{12}$ (A) (— Os^{II}, --- Os^{III}) and [$\{(\text{bpy})_2\text{Os}(\text{dpp})\}_2\text{Ru}(\text{dpq})\}(\text{PF}_6)_6$ (B) (— Os^{II}, --- Os^{III}) measured in CH₃CN at room temperature with 0.1 M Bu₄NPF₆ in CH₃CN. The oxidative potential was set at 1.30 V vs. Ag/AgCl (bpy = 2,2'-bipyridine, dpp = 2,3-bis(2-pyridyl)pyrazine, dpq = 2,3-bis(2-pyridyl)quinoxaline).

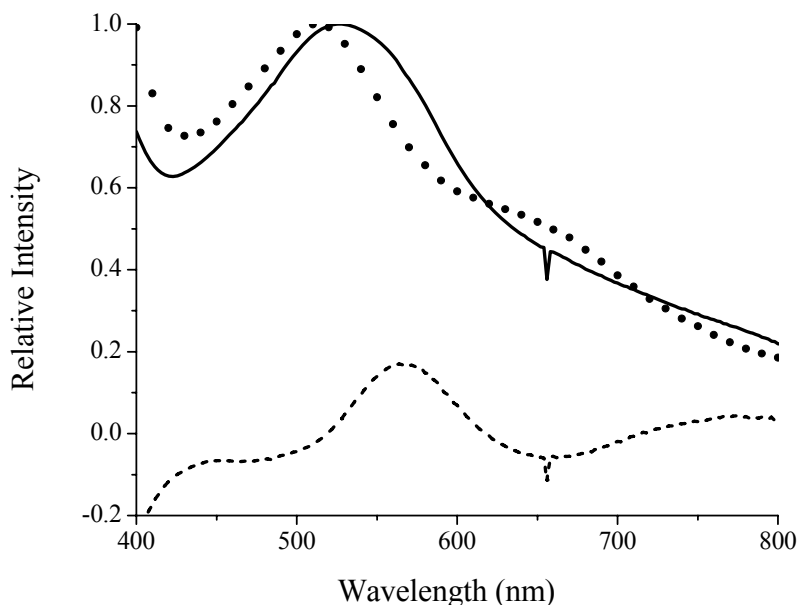


Figure 3.15 Difference spectra of the Os^{III} forms of $[(\{\text{(bpy)}_2\text{Os}^{\text{III}}(\text{dpp})\}_2\text{Ru}^{\text{II}})_2(\text{dpq})]^{16+}$ (—), $[\{\text{(bpy)}_2\text{Os}^{\text{III}}(\text{dpp})\}_2\text{Ru}^{\text{II}}(\text{dpq})]^{8+}$ (•••) and the subtraction of oxidized trimetallic spectrum from oxidized hexametallc spectrum (---), measured in CH₃CN at room temperature with 0.1 M Bu₄NPF₆ in CH₃CN (bpy = 2,2'-bipyridine, dpp = 2,3-bis(2-pyridyl)pyrazine, dpq = 2,3-bis(2-pyridyl)quinoxaline).

3.3.5 Electronic Absorption Spectroscopy of the Tetrametallic Complexes

Electronic absorption spectra of the trimetallic complex

$[\{\text{(bpy)}_2\text{Ru}(\text{dpp})\}_2\text{Ru}(\text{dpp})](\text{PF}_6)_6$ and the tetrametallic complex

$[\{\text{(bpy)}_2\text{Ru}(\text{dpp})\}_2\text{Ru}(\text{dpp})\text{PtCl}_2](\text{PF}_6)_6$ are shown in Figure 3.16. The spectra of

$[\{\text{(bpy)}_2\text{Ru}(\text{dpp})\}_2\text{Ru}(\text{dpp})](\text{PF}_6)_6$ and $[\{\text{(bpy)}_2\text{Ru}(\text{dpp})\}_2\text{Ru}(\text{dpp})\text{PtCl}_2](\text{PF}_6)_6$ show similar transitions throughout the UV and visible regions because they both contain structurally similar chromophores within the molecular formation. In addition the different unit between the trimetallic and the tetrametallic complex is actually *cis*-PtCl₂ which does not significantly contribute to the light absorbing ability of the molecule. The peak at approximately 415 nm is characteristic of the Ru(dπ) → bpy(π*) ¹MLCT transition, while the peak at approximately 540 nm is characteristic of Ru(dπ) → μ-dpp(π*) ¹MLCT transition.

The stabilization of the dpp π* orbital in the $[\{\text{(bpy)}_2\text{Ru}(\text{dpp})\}_2\text{Ru}(\text{dpp})\text{PtCl}_2](\text{PF}_6)_6$ as compared to the $[\{\text{(bpy)}_2\text{Ru}(\text{dpp})\}_2\text{Ru}(\text{dpp})](\text{PF}_6)_6$ is reflected in a minor change in the

visible region of the spectra. This slight decrease in the 400-450 nm region and increase in the 500-560 nm region for the $[\{(\text{bpy})_2\text{Ru}(\text{dpp})\}_2\text{Ru}(\text{dpp})\text{PtCl}_2](\text{PF}_6)_6$ relative to the $[\{(\text{bpy})_2\text{Ru}(\text{dpp})\}_2\text{Ru}(\text{dpp})](\text{PF}_6)_6$ is consistent with a $\text{Ru}(\text{d}\pi) \rightarrow \text{terminal dpp}(\pi^*)$ $^1\text{MLCT}$ transition shift to lower energy in the $[\{(\text{bpy})_2\text{Ru}(\text{dpp})\}_2\text{Ru}(\text{dpp})\text{PtCl}_2](\text{PF}_6)_6$.

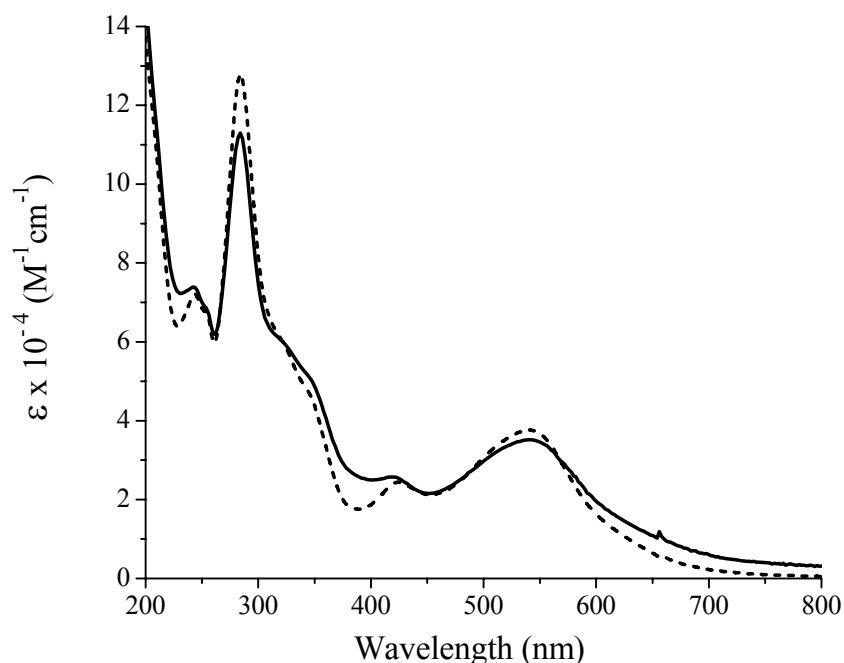


Figure 3.16 Electronic absorption spectra of $[\{(\text{bpy})_2\text{Ru}(\text{dpp})\}_2\text{Ru}(\text{dpp})\text{PtCl}_2](\text{PF}_6)_6$ (—) and $[\{(\text{bpy})_2\text{Ru}(\text{dpp})\}_2\text{Ru}(\text{dpp})](\text{PF}_6)_6$ (---), measured in CH_3CN solvent at room temperature (bpy = 2,2'-bipyridine, dpp = 2,3-bis(2-pyridyl)pyrazine).

The overlapping electronic absorption spectra of the tetrametallic complexes $[\{(\text{bpy})_2\text{Ru}(\text{dpp})\}_2\text{Ru}(\text{dpp})\text{PtCl}_2](\text{PF}_6)_6$, $[\{(\text{bpy})_2\text{Ru}(\text{dpp})\}_2\text{Ru}(\text{dpq})\text{PtCl}_2](\text{PF}_6)_6$ and $[\{(\text{bpy})_2\text{Os}(\text{dpp})\}_2\text{Ru}(\text{dpq})\text{PtCl}_2](\text{PF}_6)_6$ are shown in Figure 3.17, and their assignments are summarized in Table 3.8.

Due to the relative complexity of the metals and ligands incorporated into tetrametallic systems, various MLCT transitions are expected to appear in the visible region. There are typically associated with the stronger absorption capabilities of these complexes. As shown in Figure 3.17, the UV region is dominated by intraligand $\pi \rightarrow \pi^*$ transitions, while the visible region is dominated by overlapping MLCT transitions such as $\text{Ru}(\text{d}\pi) \rightarrow$

bpy(π^*) 1 MLCT and Os($d\pi$) \rightarrow bpy(π^*) 1 MLCT at around 420 nm; Ru($d\pi$) \rightarrow μ -dpp(π^*) 1 MLCT at around 540 nm, and Os($d\pi$) \rightarrow μ -dpp(π^*) 1 MLCT at approximately 560 nm. Another important difference between Os analogues and Ru analogues is the stronger direct 3 MLCT absorption capability of the Os analogues, shown in Figure 3.17 for the $[\{(\text{bpy})_2\text{Os}(\text{dpp})\}_2\text{Ru}(\text{dpq})\text{PtCl}_2](\text{PF}_6)_6$ complex in the 650-800 nm range. This particular property of the Os analogues, i.e., a possible excitation window ranging from 600 – 1000 nm, makes them potential candidates for applications in photodynamic therapy.¹⁵

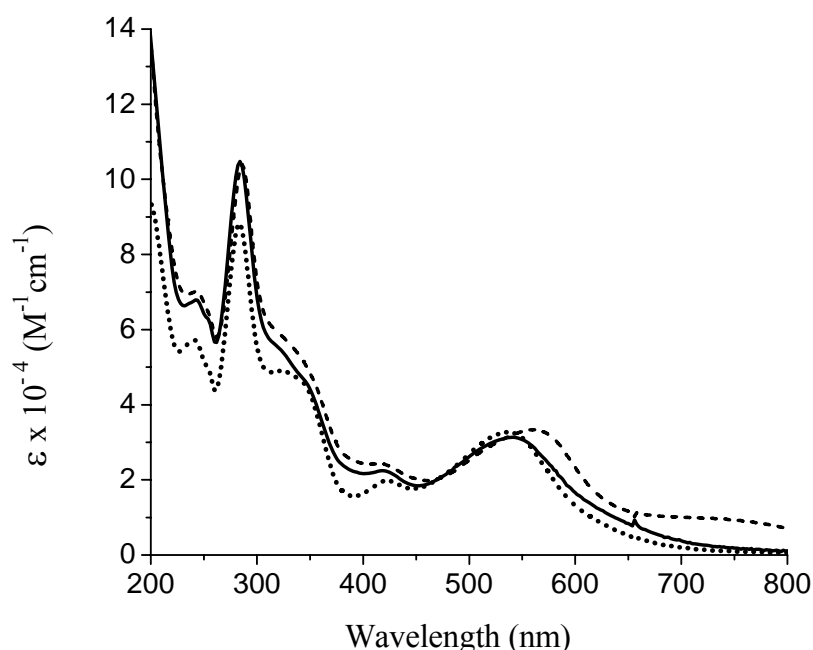


Figure 3.17 Electronic absorption spectra of the trimetallic complexes: $[\{(\text{bpy})_2\text{Ru}(\text{dpp})\}_2\text{Ru}(\text{dpp})\text{PtCl}_2](\text{PF}_6)_6$ (—), $[\{(\text{bpy})_2\text{Ru}(\text{dpp})\}_2\text{Ru}(\text{dpq})\text{PtCl}_2](\text{PF}_6)_6$ (•••), $[\{(\text{bpy})_2\text{Os}(\text{dpp})\}_2\text{Ru}(\text{dpq})\text{PtCl}_2](\text{PF}_6)_6$ (---), measured in CH_3CN solvent at room temperature (bpy = 2,2'-bipyridine, dpp = 2,3-bis(2-pyridyl)pyrazine and dpq = 2,3-bis(2-pyridyl)quinoxaline).

Table 3.8 Electronic absorption spectra data summary of $[\{(bpy)_2Ru(dpp)\}_2Ru(dpp)](PF_6)_6$, $[\{(bpy)_2Ru(dpp)\}_2Ru(dpp)PtCl_2](PF_6)_6$, $[\{(bpy)_2Ru(dpp)\}_2Ru(dpq)PtCl_2](PF_6)_6$ and $[\{(bpy)_2Os(dpp)\}_2Ru(dpq)PtCl_2](PF_6)_6$.^a (bpy = 2,2'-bipyridine, dpp = 2,3-bis(2-pyridyl)pyrazine, dpq = 2,3-bis(2-pyridyl)quinoxaline).

Complex	Wavelength (nm)	$\epsilon \times 10^{-4}$ ($M^{-1}cm^{-1}$)	Assignments
$[\{(bpy)_2Ru(dpp)\}_2Ru(dpp)](PF_6)_6$	420	2.8	$Ru(d\pi) \rightarrow bpy(\pi^*)$ CT
	540	3.4	$Ru(d\pi) \rightarrow \mu-dpp(\pi^*)$ CT
$[\{(bpy)_2Ru(dpp)\}_2Ru(dpp)PtCl_2](PF_6)_6$	420	2.8	$Ru(d\pi) \rightarrow bpy(\pi^*)$ CT
	540	3.4	$Ru(d\pi) \rightarrow \mu-dpp(\pi^*)$ CT
$[\{(bpy)_2Ru(dpp)\}_2Ru(dpq)PtCl_2](PF_6)_6$	420	2.7	$Ru(d\pi) \rightarrow bpy(\pi^*)$ CT
	540	3.3	$Ru(d\pi) \rightarrow \mu-dpp(\pi^*)$ CT
$[\{(bpy)_2Os(dpp)\}_2Ru(dpq)PtCl_2](PF_6)_6$	420	2.7	$Ru(d\pi) \rightarrow bpy(\pi^*)$ CT
	540	3.3	$Ru(d\pi) \rightarrow \mu-dpp(\pi^*)$ CT
	556	3.5	$Os(d\pi) \rightarrow \mu-dpp(\pi^*)$ CT
	650-800	~1.5	${}^3Os(d\pi) \rightarrow \mu-dpp(\pi^*)$ CT

^a Electronic absorption spectroscopy measured in CH_3CN solvent at room temperature.

3.3.6 Spectroelectrochemistry of $[\{(bpy)_2Ru(dpp)\}_2Ru(dpp)](PF_6)_6$ and $[\{(bpy)_2Ru(dpp)\}_2Ru(dpp)PtCl_2](PF_6)_6$

The spectroelectrochemistry revealed the MLCT nature of the light absorbing properties of these multimetallic complexes. When the metals were oxidized or the ligands were reduced, the corresponding metal to ligand charge transfer previously existing in the molecules had been shifted out the original spectral window. The study of oxidative and reductive spectroelectrochemistry both helped to verify our assignment of MLCTs in the complex multimetallic supramolecules. Spectroelectrochemistry correlates the electrochemical properties and the spectroscopic properties of complexes and reveals the MLCT nature of light absorption. Upon oxidation of peripheral metal centers in multimetallic complexes, the MLCT transitions of the central metals can be observed and the relative

energy levels can be estimated.

For the tetrametallic complex $[\{(bpy)_2Ru(dpp)\}_2Ru(dpp)PtCl_2](PF_6)_6$, both oxidative spectroelectrochemistry (Figure 3.18) and reductive spectroelectrochemistry (Figure 3.19) were performed. The tetrametallic complex $[\{(bpy)_2Ru(dpp)\}_2Ru(dpp)PtCl_2](PF_6)_6$ was oxidized at a potential 1.70 V to generate $[\{(bpy)_2Ru^{III}(dpp)\}_2Ru^{II}(dpp)PtCl_2]^{8+}$, and its electronic absorption spectrum was monitored. Decrease in absorbance was observed for $Ru(d\pi) \rightarrow bpy(\pi^*)$ 1MLCT at ca. 415 nm and $Ru(d\pi) \rightarrow \mu-dpp(\pi^*)$ 1MLCT at ca. 520-540 nm, after the oxidation of the peripheral Ru centers. At the same time, absorbance in the region attributed to the dpp ligand based $\pi \rightarrow \pi^*$ transitions at around 360 nm slightly increased. The oxidation of Ru^{II} to Ru^{III} typically results in a shift to a region outside the visible region of the spectrum of MLCT transitions.^{15, 21} For the electrogenerated $[\{(bpy)_2Ru^{III}(dpp)\}_2Ru^{II}(dpp)PtCl_2]^{8+}$, both the $Ru(d\pi) \rightarrow bpy(\pi^*)$ 1MLCT , and the $Ru(d\pi) \rightarrow dpp(\pi^*)$ 1MLCT transitions for these terminal metals shift out of the visible region. As a result of this change, an anticipated decrease in absorbance to 420-550 nm is observed, which is typically associated with Ru oxidation. An increase in absorbance to the 625-750 nm region has been observed, which has been associated with LMCT transitions from $\mu-dpp(\pi) \rightarrow Ru^{III}(d\pi)$, consistent with a $[(bpy)_2Ru^{III}(\mu-dpp)]$ sub-unit.^{5, 12, 18} The increase in absorbance in the 300-320 nm region upon metal oxidation is characteristic of a $[(bpy)_2Ru^{III}(\mu-dpp)]$ sub-unit, reflecting the stabilization of a ligand π^* acceptor orbital shifting from a $\pi \rightarrow \pi^*$ transition to lower energy upon Ru oxidation. The presence of a remaining Ru^{II} center in the oxidized complex leads to retention of $Ru(d\pi) \rightarrow \mu-dpp(\pi^*)$ 1MLCT transitions in the 450-550 nm region, with a shift to higher energy which is consistent with lower energy $d\pi$ orbitals of the Ru bound to three $\mu-dpp$ ligands. The reversibility of the oxidative spectroelectrochemistry of the compound $[\{(bpy)_2Ru(dpp)\}_2Ru(dpp)PtCl_2](PF_6)_6$ was also studied, which showed a > 95% return to the original spectrum upon regeneration of Ru^{II} at 0 V.

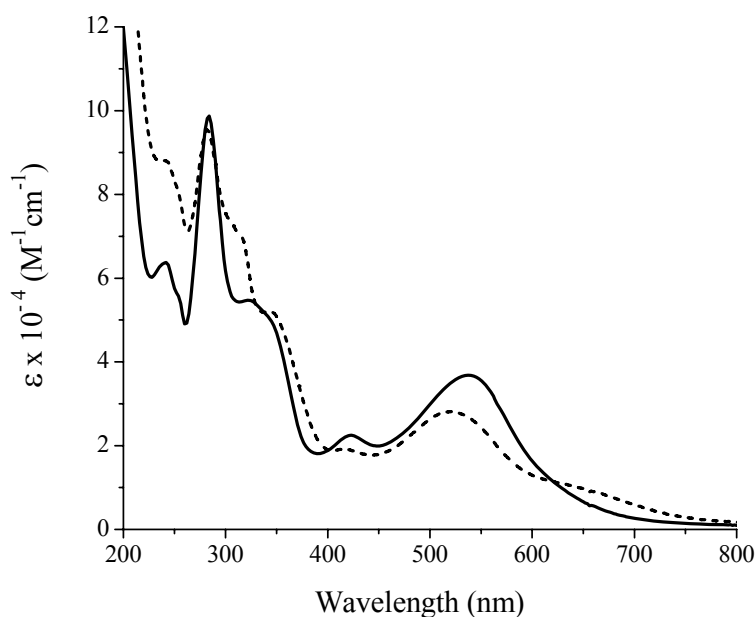


Figure 3.18 Oxidative spectroelectrochemistry of $[\{(bpy)_2Ru(dpp)\}_2Ru(dpp)PtCl_2](PF_6)_6$ measured in CH_3CN at room temperature with 0.1 M Bu_4NPF_6 in CH_3CN . Original $[\{(bpy)_2Ru^{II}(dpp)\}_2Ru^{II}(dpp)PtCl_2]^{6+}$ (—) and electrogenerated $[\{(bpy)_2Ru^{III}(dpp)\}_2Ru^{II}(dpp)PtCl_2]^{8+}$ (---) The oxidative potential was set at 1.70 V vs. Ag/AgCl (bpy = 2,2'-bipyridine, dpp = 2,3-bis(2-pyridyl)pyrazine).

The reductive spectroelectrochemistry of $[\{(bpy)_2Ru(dpp)\}_2Ru(dpp)PtCl_2](PF_6)_6$ was also studied, which is illustrated in Figure 3.19. Electrolysis was conducted by applying a potential at -0.50 V vs. Ag/AgCl (slightly more negative than the $E_{1/2}$ of the first reduction of μ -dpp connecting the central Ru and Pt) in order to generate $[\{(bpy)_2Ru(dpp)\}_2Ru(dpp^-)PtCl_2]^{5+}$. It should be noted that a certain level of reduction of the other μ -dpp cannot be ruled out under these conditions. The absorbance at approximately 415 nm, which is attributed to the $Ru(d\pi) \rightarrow bpy(\pi^*)$ 1MLCT , does not appear to be impacted by the μ -dpp reduction. In fact, the reduction of the μ -dpp results in a shift out of the visible of the $Ru(d\pi) \rightarrow \mu$ -dpp(π^*) 1MLCT transition for this dpp ligand. A decrease in the dpp based $\pi \rightarrow \pi^*$ transition is also observed in the 320-340 nm region, which is consistent with the population of the μ -dpp π^* orbital upon reduction. The reoxidation of this reduced species is possible with > 90% regeneration of the spectroscopy observed.

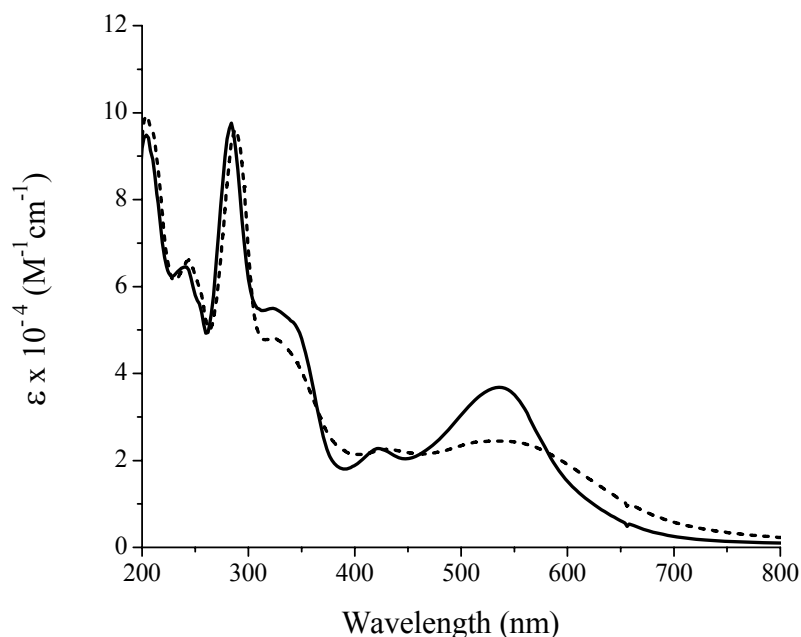


Figure 3.19 Reductive spectroelectrochemistry of $[(\text{bpy})_2\text{Ru}(\text{dpp})]_2\text{Ru}(\text{dpp})\text{PtCl}_2(\text{PF}_6)_6$ measured in CH_3CN at room temperature with 0.1 M Bu_4NPF_6 in CH_3CN . Original $[(\text{bpy})_2\text{Ru}(\text{dpp})]_2\text{Ru}(\text{dpp})\text{PtCl}_2^{6+}$ (—), reduced $[(\text{bpy})_2\text{Ru}(\text{dpp})]_2\text{Ru}(\text{dpp}^-)\text{PtCl}_2^{5+}$ (---) The oxidative potential was set at -0.50 V vs. Ag/AgCl (bpy = 2,2'-bipyridine, dpp = 2,3-bis(2-pyridyl)pyrazine).

3.3.7 Emission Spectroscopy

Room temperature emission spectra of the tetrametallic complex $[(\text{bpy})_2\text{Ru}(\text{dpp})]_2\text{Ru}(\text{dpp})\text{PtCl}_2(\text{PF}_6)_6$, the trimetallic synthon complex $[(\text{bpy})_2\text{Ru}(\text{dpp})]_2\text{Ru}(\text{dpp})(\text{PF}_6)_6$, and the model bimetallic complex $[(\text{bpy})_2\text{Ru}(\text{dpp})\text{Ru}(\text{bpy})_2](\text{PF}_6)_4$ are all shown in Figure 3.20. The wavelength of excitation for all three complexes was 524 nm, corresponding to the $\text{Ru}(\text{d}\pi) \rightarrow \mu\text{-dpp}(\pi^*)^1\text{MLCT}$ absorption.^{5, 81} All the complexes displayed typical $\text{Ru}(\text{d}\pi) \rightarrow \mu\text{-dpp}(\pi^*)^3\text{MLCT}$ emissions centered at close to 750 nm^{64, 66}, with decrease in the quantum yields from the bimetallic, to the trimetallic, and then to the tetrametallic. Other possible emissive energy states such as $\text{Ru}(\text{d}\pi) \rightarrow \mu\text{-dpp}(\pi^*)$ (when dpp was a terminal ligand in $[(\text{bpy})_2\text{Ru}(\text{dpp})]_2\text{Ru}(\text{dpp})(\text{PF}_6)_6$) $^3\text{MLCT}$ were not observed, indicating effective energy or electron transfer within the molecule. Quantum yields for emissions were determined using the standard reference

[Os(bpy)₃](PF₆)₂, $\Phi^{\text{em}} = 0.0050$, and $\Phi = \Phi_0 \times A/A_0$, where Φ is the quantum yield of the analyte, Φ_0 is the quantum yield of the standard (0.0050), A is the area under the emission peak of the analyte, and A_0 is the area under the emission peak of the standard.^{11, 53, 139} At room temperature, the quantum yield for emission the tetrametallic complex was reduced by 48% from that of the trimetallic complex, suggesting the emission quenching by a lower lying Ru(d π) \rightarrow μ -dpp(π^*) ³CT charge separated state, in which the μ -dpp was the one connecting Ru and Pt. At 77 K, the emission of the tetrametallic complex [{(bpy)₂Ru(dpp)}₂Ru(dpp)PtCl₂](PF₆)₆ was centered at 712 nm, compared to 698 nm for the [{(bpy)₂Ru(dpp)}₂Ru(dpp)](PF₆)₆ system (Figure 3.21). The broader emission profile for the tetrametallic complex than the trimetallic complex in 77 K may be due to additional emission from other close energy state involving various μ -dpp ligands. Both the room temperature and 77 K emission data are summarized in Table 3.9.

The trimetallic complex [{(bpy)₂Ru(dpp)}₂Ru(dpq)](PF₆)₆ and the tetrametallic complex [{(bpy)₂Ru(dpp)}₂Ru(dpq)PtCl₂](PF₆)₆ both display emissions from the Ru(d π) \rightarrow μ -dpp(π^*) ³MLCT excited state at room temperature and at 77 K. The lowest emissive states in [{(bpy)₂Ru(dpp)}₂Ru(dpp)](PF₆)₆ and [{(bpy)₂Ru(dpp)}₂Ru(dpq)](PF₆)₆ are both the Ru(d π) \rightarrow μ -dpp(π^*) ³MLCT state, with almost identical quantum yields and excited state lifetimes (described later). Consequently, the population of the Ru(d π) \rightarrow t-dpp(π^*) ³MLCT (t-dpp is terminal dpp) in [{(bpy)₂Ru(dpp)}₂Ru(dpp)](PF₆)₆ and Ru(d π) \rightarrow t-dpq(π^*) ³MLCT states in [{(bpy)₂Ru(dpp)}₂Ru(dpq)](PF₆)₆ are effectively quenched by energy transfer to the lowest emissive Ru(d π) \rightarrow μ -dpp(π^*) ³MLCT state. This is a typical process in Ru and Os polyazine complexes containing bpy, dpp and dpq.^{140, 141}

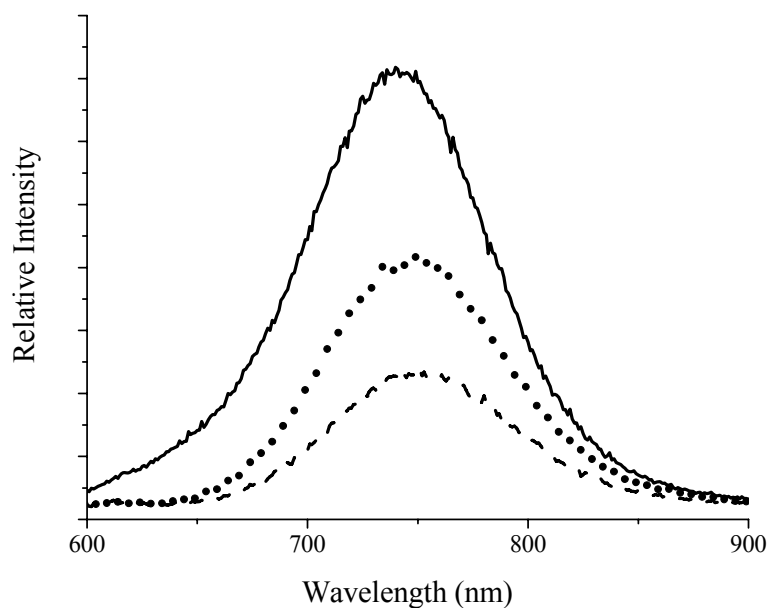


Figure 3.20 Uncorrected room temperature emission spectra of $[(bpy)_2Ru(dpp)Ru(bpy)_2](PF_6)_4$ (—), $[\{(bpy)_2Ru(dpp)\}_2Ru(dpp)](PF_6)_6$ (•••) and $[\{(bpy)_2Ru(dpp)\}_2Ru(dpp)PtCl_2](PF_6)_6$ (---) measured in spectrograde CH_3CN , absorbance matched at 524 nm. (bpy = 2,2'-bipyridine, dpp = 2,3-bis(2-pyridyl)pyrazine).

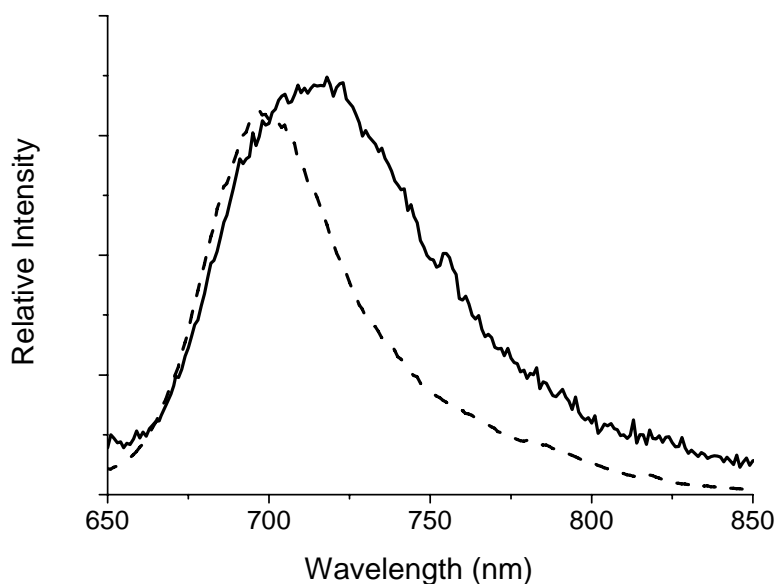


Figure 3.21 Uncorrected 77 K emission spectra of the tetrametallic complex $[\{(bpy)_2Ru(dpp)\}_2Ru(dpp)PtCl_2](PF_6)_6$ (—) and the trimetallic complex $[\{(bpy)_2Ru(dpp)\}_2Ru(dpp)](PF_6)_6$ (---) measured in 4:1 EtOH/MeOH glass (bpy = 2,2'-bipyridine, dpp = 2,3-bis(2-pyridyl)pyrazine).

3.3.8 Excited State Emission Lifetime Measurement

Room temperature and 77 K emission lifetime measurements were performed on the bimetallic complex $[(\text{bpy})_2\text{Ru}(\text{dpp})\text{Ru}(\text{bpy})_2](\text{PF}_6)_4$, the trimetallic complexes $[\{(\text{bpy})_2\text{Ru}(\text{dpp})\}_2\text{Ru}(\text{dpp})](\text{PF}_6)_6$ and $[\{(\text{bpy})_2\text{Ru}(\text{dpp})\}_2\text{Ru}(\text{dpq})](\text{PF}_6)_6$, and the tetrametallic complexes $[\{(\text{bpy})_2\text{Ru}(\text{dpp})\}_2\text{Ru}(\text{dpp})\text{PtCl}_2](\text{PF}_6)_6$ and $[\{(\text{bpy})_2\text{Ru}(\text{dpp})\}_2\text{Ru}(\text{dpq})\text{PtCl}_2](\text{PF}_6)_6$. The excited state lifetimes for all five complexes under scrutiny were different when measured at room temperature, but identical at 77 K (within experimental error) (Table 3.9). All the complexes displayed typical $\text{Ru}(\text{d}\pi) \rightarrow \mu\text{-dpp}(\pi^*)$ $^3\text{MLCT}$ emissions at ca. 745 nm at room temperature, and at ca. 700 nm at 77 K. However, the trimetallic chromophores and the tetrametallic complexes displayed a decrease in quantum yields and emission lifetime for both the dpp and dpq complexes. The decrease in both quantum yield and emission lifetime suggests the existence of a long-range intramolecular charge separation state where the peripheral Ru is oxidized and the $\mu\text{-dpp}$ and $\mu\text{-dpq}$ bridged by central Ru and Pt are reduced. Considering that dpq possesses a more stabilized π^* orbital than dpp, the process of electron transfer quenching to the charge separation state is presumably more effective for $[\{(\text{bpy})_2\text{Ru}(\text{dpp})\}_2\text{Ru}(\text{dpq})\text{PtCl}_2](\text{PF}_6)_6$ vs. $[\{(\text{bpy})_2\text{Ru}(\text{dpp})\}_2\text{Ru}(\text{dpp})\text{PtCl}_2](\text{PF}_6)_6$.

Table 3.9 Photophysical properties of [(bpy)₂Ru(dpp)Ru(bpy)₂](PF₆)₄, [{(bpy)₂Ru(dpp)}₂Ru(dpp)](PF₆)₆, [{(bpy)₂Ru(dpp)}₂Ru(dpq)](PF₆)₆, [{(bpy)₂Ru(dpp)}₂Ru(dpp)PtCl₂](PF₆)₆ and [{(bpy)₂Ru(dpp)}₂Ru(dpq)PtCl₂](PF₆)₆.^{a,b}

Complex	RT			77 K	
	$\lambda_{\max}^{\text{em}}$	τ	Φ^{em}	$\lambda_{\max}^{\text{em}}$	τ
	(nm)	(μs)	$\times 10^3$	(nm)	(μs)
[(bpy) ₂ Ru(dpp)Ru(bpy) ₂](PF ₆) ₄	740	0.13	1.21	700	2.0
[{(bpy) ₂ Ru(dpp)} ₂ Ru(dpp)](PF ₆) ₆	747	0.13	0.61	698	1.7
[{(bpy) ₂ Ru(dpp)} ₂ Ru(dpp)PtCl ₂](PF ₆) ₆	750	0.10	0.32	712	1.7
[{(bpy) ₂ Ru(dpp)} ₂ Ru(dpq)](PF ₆) ₆	745	0.13	0.60	710	1.7
[{(bpy) ₂ Ru(dpp)} ₂ Ru(dpq)PtCl ₂](PF ₆) ₆	745	0.09	0.25	703	1.7

^a $\lambda_{\max}^{\text{em}}$ is emission maximum, τ is emission lifetime in μs , Φ^{em} is emission quantum yield at room temperature measured relative to [Os(bpy)₃](PF₆)₂: $\Phi^{\text{em}} = 0.0050$. All room temperature experiments were performed in spectrograde CH₃CN and 77 K measurements were performed in 4 : 1 EtOH/MeOH glass.

^b (bpy = 2,2'-bipyridine, dpp = 2,3-bis(2-pyridyl)pyrazine, dpq = 2,3-bis(2-pyridyl)quinoxaline)

3.3.9 Energy Diagram

Based on all available spectroscopic, electrochemical and photophysical data, energy level diagrams of the trimetallic complex [{(bpy)₂Ru(dpp)}₂Ru(**dpp**)](PF₆)₆ and the tetrametallic complex [{(bpy)₂Ru(dpp)}₂Ru(**dpp**)PtCl₂](PF₆)₆ are shown in Figure 3.22. For the trimetallic complex [{(bpy)₂Ru(dpp)}₂Ru(**dpp**)](PF₆)₆, only the emission corresponding to the Ru($d\pi$) \rightarrow μ -dpp(π^*) ³MLCT excited state was observed. This is indicative of efficient internal conversion and intersystem crossing, which facilitates the population of the emissive, lowest lying Ru($d\pi$) \rightarrow μ -dpp(π^*) ³MLCT state typical of polymetallic dpp bridged complexes.

For the tetrametallic complex [{(bpy)₂Ru(dpp)}₂Ru(**dpp**)PtCl₂](PF₆)₆, only the emission from the Ru($d\pi$) \rightarrow μ -dpp(π^*) ³MLCT state was observed. The quantum yield for the emission of [{(bpy)₂Ru(dpp)}₂Ru(**dpp**)PtCl₂](PF₆)₆ was 50% of the emission for the [{(bpy)₂Ru(dpp)}₂Ru(**dpp**)](PF₆)₆. With respect to [{(bpy)₂Ru(dpp)}₂Ru(**dpp**)PtCl₂](PF₆)₆,

the peripheral Ru centers are the sites of localization for the HOMO, while the central μ -dpp ligand bridging the Ru and Pt centers is the site of localization for the LUMO. This spatial separation of HOMO and LUMO in $[\{(\text{bpy})_2\text{Ru}(\text{dpp})\}_2\text{Ru}(\mathbf{dpp})\text{PtCl}_2](\text{PF}_6)_6$ allows for the generation of a non-emissive charge separated state, in which the positive charge is localized on a $\text{Ru}(\text{d}\pi)$ orbital on the terminal $(\text{bpy})_2\text{Ru}(\mu\text{-dpp})$ subunit, with the promoted electron in the $\mu\text{-dpp}(\pi^*)$ bridging the central Ru and Pt. The population of this charge separated state acts to quench the emission of the $\text{Ru}(\text{d}\pi) \rightarrow \mu\text{-dpp}(\pi^*)$ $^3\text{MLCT}$ emissive state. With respect to the compound, $[\{(\text{bpy})_2\text{Ru}(\text{dpp})\}_2\text{Ru}(\mathbf{dpp})](\text{PF}_6)_6$, the k_{nr} and k_{r} were calculated to be $7.7 \times 10^6 \text{ s}^{-1}$ and $4.7 \times 10^3 \text{ s}^{-1}$, respectively (using $k_{\text{r}} = \Phi^{\text{em}}/\tau$ and $k_{\text{nr}} = 1/\tau - k_{\text{r}}$). The large reduction in Φ^{em} for $[\{(\text{bpy})_2\text{Ru}(\text{dpp})\}_2\text{Ru}(\mathbf{dpp})\text{PtCl}_2](\text{PF}_6)_6$ vs. $[\{(\text{bpy})_2\text{Ru}(\text{dpp})\}_2\text{Ru}(\mathbf{dpp})](\text{PF}_6)_6$ (from 0.61×10^{-3} to 0.32×10^{-3}) with a smaller reduction in the τ of the $^3\text{MLCT}$ state (from $0.13 \mu\text{s}$ to $0.10 \mu\text{s}$) implies that there are two pathways to populate the CS state: k_{cs} and k_{isc} , or $[\{(\text{bpy})_2\text{Ru}(\text{dpp})\}_2\text{Ru}(\mathbf{dpp})](\text{PF}_6)_6$ has varied k_{r} and k_{nr} compared to $[\{(\text{bpy})_2\text{Ru}(\text{dpp})\}_2\text{Ru}(\mathbf{dpp})\text{PtCl}_2](\text{PF}_6)_6$. Typically, one would expect the trimetallic complex to serve as a good predictive model, suggesting the k_{isc} as a viable operative pathway. In frozen glass at 77 K, the charge separation quenching is typically inhibited. Thus the tetrametallic complex shows similar lifetimes as the model trimetallic complex.

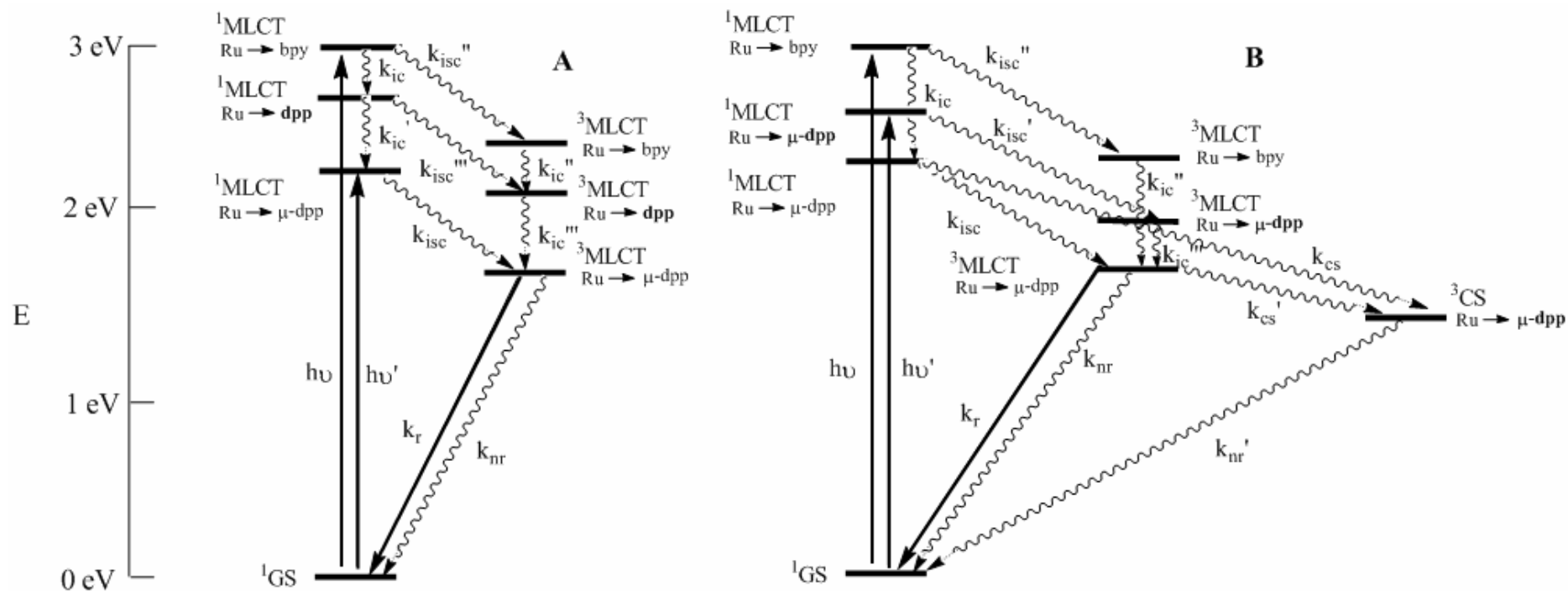


Figure 3.22 Energy state diagrams of $[\{(bpy)_2Ru(dpp)\}_2Ru(dpp)](PF_6)_6$ (A) and $[\{(bpy)_2Ru(dpp)\}_2Ru(dpp)PtCl_2](PF_6)_6$ (B) ($bpy = 2,2'$ -bipyridine, $dpp = 2,3$ -bis(2-pyridyl)pyrazine). 1GS corresponds to the ground state, while CS refers to the excited charge separation state with oxidized terminal Ru centers and a reduced **dpp** ligand. k_{ic} , k_{ic}' , k_{ic}'' and k_{ic}''' are the rate constants for internal conversion, k_{isc} , k_{isc}' and k_{isc}'' are the rate constants for intersystem crossing; k_r refers to the rate constant for radiative decay; k_{nr} and k_{nr}' are the rate constants for nonradiative decay and k_{cs} and k_{cs}' are the rate constants for the quenching pathway to the charge separation state. The intraligand transitions for terminal bpy ligands are omitted for better clarification.

Simplified energy state diagrams of the trimetallic complex

$[\{(bpy)_2Ru(dpp)\}_2Ru(dpq)](PF_6)_6$ and the tetrametallic complex

$[\{(bpy)_2Ru(dpp)\}_2Ru(dpq)PtCl_2](PF_6)_6$ are shown in Figure 3.23. Similar to

$[\{(bpy)_2Ru(dpp)\}_2Ru(dpp)](PF_6)_6$, the emission displayed from compound

$[\{(bpy)_2Ru(dpp)\}_2Ru(dpq)](PF_6)_6$ corresponds only to the $Ru(d\pi) \rightarrow \mu-dpp(\pi^*)$ 3MLCT excited state with almost identical quantum yields. This is indicative of efficient internal conversion and intersystem crossing which populates the emissive, lowest lying $Ru(d\pi) \rightarrow \mu-dpp(\pi^*)$ 3MLCT state.

Conversely, for the tetrametallic complex $[\{(bpy)_2Ru(dpp)\}_2Ru(dpq)PtCl_2](PF_6)_6$, only the emission from the $Ru \rightarrow \mu-dpp$ 3MLCT state was observed; however, the possibility of an $Ru(d\pi) \rightarrow \mu-dpq(\pi^*)$ 3MLCT emission can't be excluded. The quantum yield for emission from the $Ru(d\pi) \rightarrow \mu-dpp(\pi^*)$ 3MLCT state of $[\{(bpy)_2Ru(dpp)\}_2Ru(dpq)PtCl_2](PF_6)_6$ was about 40% that of the $[\{(bpy)_2Ru(dpp)\}_2Ru(dpq)](PF_6)_6$, which shows more quenching of the $Ru \rightarrow \mu-dpp$ 3MLCT state than was observed for the $[\{(bpy)_2Ru(dpp)\}_2Ru(\mathbf{dpp})PtCl_2](PF_6)_6$ system. It seems likely that the internal conversion from $Ru(d\pi) \rightarrow \mu-dpp(\pi^*)$ 1MLCT to $Ru(d\pi) \rightarrow \mu-dpp(\pi^*)$ 3MLCT transfer resulted in further decreasing the quantum yield from the emissive $Ru(d\pi) \rightarrow \mu-dpp(\pi^*)$ 3MLCT energy state (Figure 3.23).

Similar to $[\{(bpy)_2Ru(dpp)\}_2Ru(\mathbf{dpp})PtCl_2](PF_6)_6$, the peripheral Ru centers of $[\{(bpy)_2Ru(dpp)\}_2Ru(dpq)PtCl_2](PF_6)_6$ serve as the position of the HOMO, while the $\mu-dpq$ that bridges the central Ru and Pt centers is the position of the LUMO. This spatial separation of HOMO and LUMO in $[\{(bpy)_2Ru(dpp)\}_2Ru(dpq)PtCl_2](PF_6)_6$ allows for the generation of a non-emissive charge separated state, in which the positive charge is localized on an $Ru(d\pi)$ orbital on the terminal $(bpy)_2Ru(\mu-dpp)$ subunits with the promoted electron in the $\mu-dpq(\pi^*)$. As shown in Figure 3.23, the population of the charge separated state (k_{cs}) and energy transfer from the $Ru(d\pi) \rightarrow \mu-dpp(\pi^*)$ 3MLCT to the $Ru(d\pi) \rightarrow \mu-dpq(\pi^*)$ 3MLCT would quench the emission of the $Ru(d\pi) \rightarrow \mu-dpp(\pi^*)$ 3MLCT emissive state. The k_{nr} and k_r were determined as $7.7 \times 10^6 \text{ s}^{-1}$ and $4.7 \times 10^3 \text{ s}^{-1}$ for $[\{(bpy)_2Ru(dpp)\}_2Ru(dpq)](PF_6)_6$, and assumed to have similar values in $[\{(bpy)_2Ru(dpp)\}_2Ru(dpq)PtCl_2](PF_6)_6$. The large reduction in Φ^{em} for $[\{(bpy)_2Ru(dpp)\}_2Ru(dpq)PtCl_2](PF_6)_6$ vs. $[\{(bpy)_2Ru(dpp)\}_2Ru(dpq)](PF_6)_6$ (0.60×10^{-3} vs. 0.25×10^{-3}) with a smaller reduction in τ of the 3MLCT state ($0.13 \mu\text{s}$ vs. $0.09 \mu\text{s}$) implies that there are two possible pathways to quenching the $Ru(d\pi) \rightarrow \mu-dpp(\pi^*)$ 1MLCT , namely, k_{cs} and k_{isc} , or a significant difference in the values of k_r and k_{nr} between $[\{(bpy)_2Ru(dpp)\}_2Ru(dpq)](PF_6)_6$ and $[\{(bpy)_2Ru(dpp)\}_2Ru(dpq)PtCl_2](PF_6)_6$. Typically, one

would expect the trimetallic complex to serve as a good model for the tetrametallic complex, suggesting k_{isc} is a likely operative pathway. The lifetime difference of $Ru(d\pi) \rightarrow \mu\text{-dpp}(\pi^*)$ $^3\text{MLCT}$ between $[\{(bpy)_2Ru(dpp)\}_2Ru(dpp)PtCl_2](PF_6)_6$ (0.10 μs) and $[\{(bpy)_2Ru(dpp)\}_2Ru(dpq)PtCl_2](PF_6)_6$ (0.09 μs) could be due to the greater driving force for k_{cs} in the dpq analogue than in the dpp analogue. In a frozen glass (4 : 1 ethanol : methanol) at 77 K, the charge separation quenching is typically inhibited. Therefore, it was determined that the tetrametallic complex shows a similar lifetime to the trimetallic model.

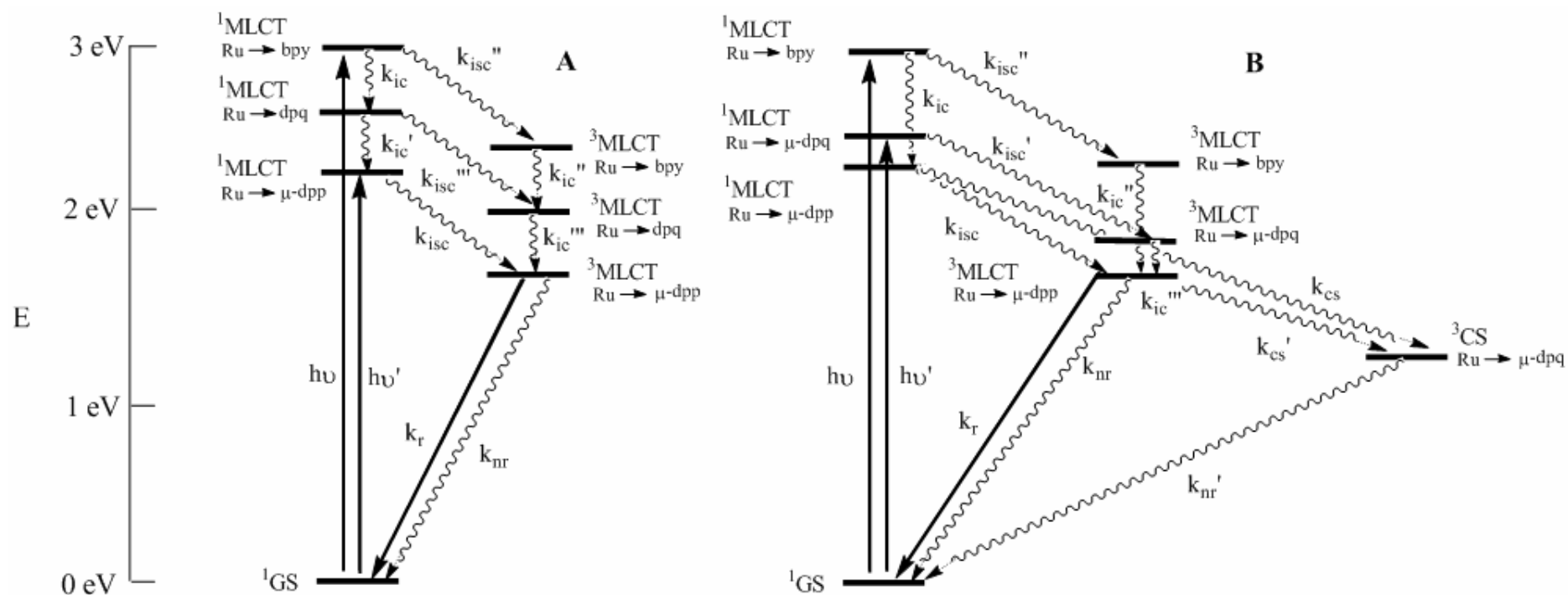
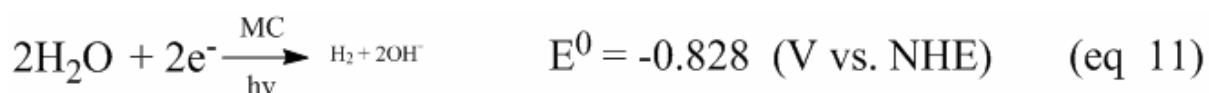


Figure 3.23 Energy state diagrams of $[(bpy)_2Ru(dpp)]_2Ru(dpq)(PF_6)_6$ and $[(bpy)_2Ru(dpp)]_2Ru(dpq)PtCl_2(PF_6)_6$ (bpy = 2,2'-bipyridine, dpp = 2,3-bis(2-pyridyl)pyrazine, dpq = 2,3-bis(2-pyridyl)quinoxaline). 1GS refers to the ground state; CS corresponds to the excited charge separation state; k_{ic} , k_{ic}' , k_{ic}'' and k_{ic}''' are the rate constants for internal conversion, k_{isc} , k_{isc}' and k_{isc}'' are the rate constants for intersystem crossing; k_r refers to the rate constant for radiative decay; k_{nr} and k_{nr}' are the rate constants for nonradiative decay and k_{cs} and k_{cs}' are the rate constants for the quenching pathway to the charge separation state. The intraligand transitions for terminal bpy ligands are omitted for better clarification.

3.3.10 Preliminary Investigation of the Photochemical Properties

3.3.10.1 Stern-Volmer Emission Quenching Analysis

Potentially, the tetrametallic complexes [{(bpy)₂Ru(dpp)}₂Ru(dpp)PtCl₂](PF₆)₆ and [{(bpy)₂Ru(dpp)}₂Ru(dpq)PtCl₂](PF₆)₆ both have the ability to collect multiple electrons on their bridging ligands when photolyzed in the presence of a sacrificial electron donor. The photoreduced complexes are capable of reducing water to produce hydrogen, thereby enabling them to function as photocatalysts for the hydrogen production (eq 11).



However it is also possible that the hydrogen comes from the electron donor DMA, which will form a dimer after dehydrogenation (eq 17, Figure 3.24). Adams *et al.* studied the electrochemical oxidation product of dimethylaniline and found several possible products due to the rearrangement of resonance structure. The most likely product is the tetramethylbenzidine (DMB or TMB, Figure 3.24).^{142, 143}

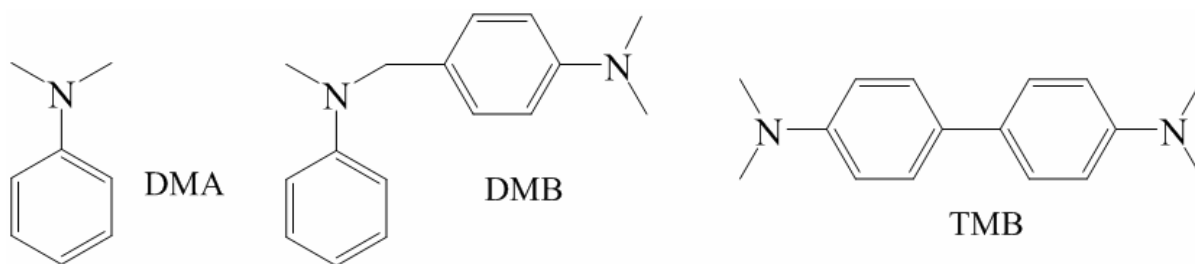
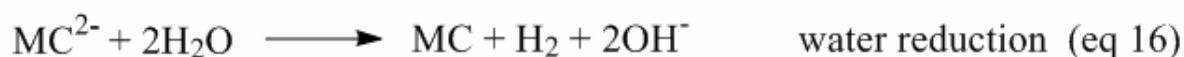


Figure 3.24 Possible mechanism for the photocatalysis of hydrogen production with $[\{(bpy)_2Ru(dpp)\}_2Ru(dpp)PtCl_2](PF_6)_6$ and $[\{(bpy)_2Ru(dpp)\}_2Ru(dpq)PtCl_2](PF_6)_6$ (bpy = 2,2'-bipyridine, dpp = 2,3-bis(2-pyridyl)pyrazine, dpq = 2,3-bis(2-pyridyl)quinoxaline, MC = metal complex).

The driving force of the overall reaction (eq 18) can not be calculated using ΔG_f^0 as G_f^0 are not reported for DMB or TMB. However the driving force was estimated by the associated bond energies of the broken bonds (C-H) and bonds formed (C-C and H-H). The bond energy for H-H, C-C (single bond), C-H (estimated from C_6H_5-H) and C-H (estimated from $C_6H_5N(CH_2CH_3)_2$) are 435.8, 347, 472.2 and 383.3 kJ/mol.¹⁴⁴ The ΔH_{rxn} for formation of DMB is estimated as: $(472.2 + 383.3) - (435.8 + 347) = 72.7$ kJ/mol of DMB and the ΔH_{rxn} for formation of TMB is estimated as: $2 \times 472.2 - (435.8 + 347) = 161.6$ kJ/mol of TMB. The chemical storage efficiency η can be calculated by:

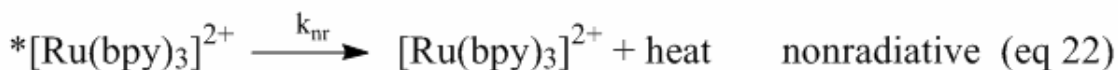
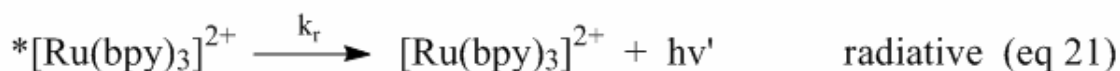
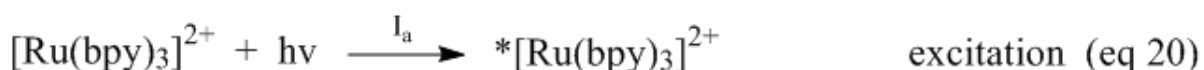
$$\eta = (\text{energy stored to drive chemical reaction}) \times 100 \% / (\text{light energy input}) \quad (\text{eq 19})$$

$$= (\text{moles of product}) \times \Delta H_{rxn} \times 100 \% / (\text{light flux} \times \text{time} \times \text{light energy})$$

For 3 h photolysis, complex $[\{(bpy)_2Ru(dpp)\}_2Ru(dpq)PtCl_2](PF_6)_6$ generated 3.3 $\mu\text{mol H}_2$ (Table 3.10). The $\eta_{(TMB)}$ for production of TMB is calculated as 0.13 % and $\eta_{(DMB)}$ for production of DMB is 0.057 % (light flux = 6.1×10^{18} photons/sec, average photon wavelength = 520 nm). It should be noted that the quantum yield Φ (defined as: 2 x number of moles of hydrogen / number of moles of input photons) for hydrogen generation under the same condition was calculated as 0.0036 (Table 3.10). However the actual chemical storage efficiency η (light energy to chemical energy conversion efficiency), dependent on the chemical reaction driven, is smaller than the quantum yield.

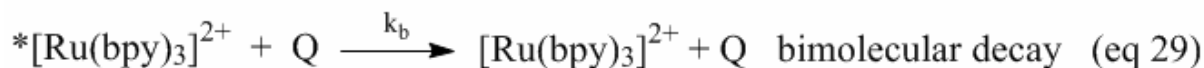
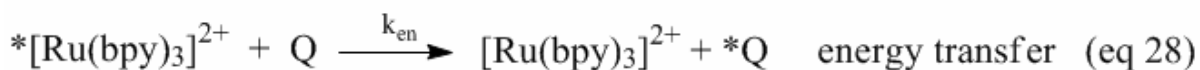
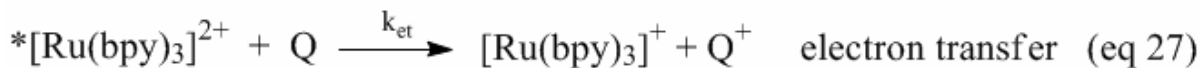
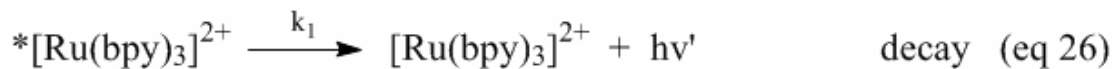
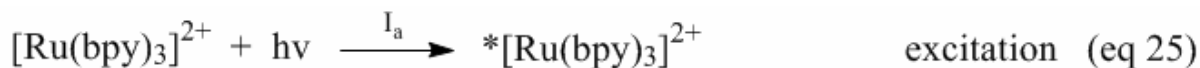
The interactions between an excited state of a metal complex and a dimethylaniline electron donor can be studied by Stern-Volmer emission quenching analysis.¹¹⁸ For this research, a metal complex was dissolved in spectrograde acetonitrile, deoxygenated by Ar purge, and the resulting emission was measured at room temperature. This was repeated with a series of DMA concentrations. The quantum yield quenching ratio, Φ_0^{em}/Φ^{em} , was determined using the emission peak area (Φ_0^{em} refers to the quantum yield of a metal complex without DMA, while Φ^{em} is the quantum yield of a metal complex when DMA is present). The plot using Φ_0^{em}/Φ^{em} vs. [DMA] generates a straight line, from which the quenching rate constant k_q can be evaluated. Typical Stern-Volmer emission quenching analyses are illustrated below using a prototypical $[Ru(bpy)_3]^{2+}$ MLCT light absorber:

When no quencher was present, the following processes occur:



where $k_1 = k_r + k_{nr}$ (eq 23) and $\tau_0 = 1/(k_r+k_{nr})$ (eq 24) where k_r and k_{nr} refer to radiative decay and nonradiative decay rate constants. The luminescence can be quenched by both energy or electron transfers as well as bimolecular deactivation.

When a quencher was present, however, the following processes occur:



where $k_q = k_{\text{et}} + k_{\text{en}} + k_b$ (eq 30) and $\tau = 1/(k_r + k_{\text{nr}} + k_q[\text{Q}])$ (eq 31) and k_q refers to quenching rate constants. In general, the quenching rate constant, k_q , can be determined from the following Stern-Volmer relationship: ¹¹⁸

$$\tau_o / \tau = 1 + \tau_o k_q [\text{Q}] \quad (\text{eq 32}) \quad \text{or} \quad \Phi_o^{\text{em}} / \Phi^{\text{em}} = 1 + t_o k_q [\text{Q}] \quad (\text{eq 33})$$

where Φ^{em} and Φ_o^{em} are the quantum yields of $[\text{Ru}(\text{bpy})_3]^{2+}$ in the presence or absence of a quencher and k_q is the overall rate constant for electron transfer, energy transfer and all other bimetallic deactivation pathways associated with DMA. The equations above suggest that k_q may be obtained experimentally when the luminescence lifetime or the luminescence intensity of $[\text{Ru}(\text{bpy})_3]^{2+}$ are measured at different quencher concentrations.

The results of a Stern-Volmer analysis of emission quenching by DMA on the complexes $[\{(\text{bpy})_2\text{Ru}(\text{dpp})\}_2\text{Ru}(\text{dpp})\text{PtCl}_2](\text{PF}_6)_6$ and $[\{(\text{bpy})_2\text{Ru}(\text{dpp})\}_2\text{Ru}(\text{dpq})\text{PtCl}_2](\text{PF}_6)_6$ are shown in Figure 3.25. The quantum yield for the emission from the $\text{Ru}(\text{d}\pi) \rightarrow \text{dpp}(\pi^*)^3\text{MLCT}$ state was quenched in a linear manner with an increased concentration of DMA, resulting in the following Stern-Volmer relationship:

$$\Phi_o^{\text{em}} / \Phi^{\text{em}} = 1 + \tau_o k_q [\text{DMA}] \quad (\text{eq 34})$$

$\tau_o (\text{dpq}) = 92 \text{ ns}$; so $k_q (\text{dpq}) = 5.1 \times 10^9 (\pm 0.1) \text{ M}^{-1} \text{ s}^{-1}$ for

$[\{(\text{bpy})_2\text{Ru}(\text{dpp})\}_2\text{Ru}(\text{dpq})\text{PtCl}_2](\text{PF}_6)_6$; and

$\tau_o (\text{dpp}) = 127 \text{ ns}$; so $k_q (\text{dpp}) = 1.6 \times 10^9 (\pm 0.03) \text{ M}^{-1} \text{ s}^{-1}$ for

$[\{(\text{bpy})_2\text{Ru}(\text{dpp})\}_2\text{Ru}(\text{dpp})\text{PtCl}_2](\text{PF}_6)_6$.

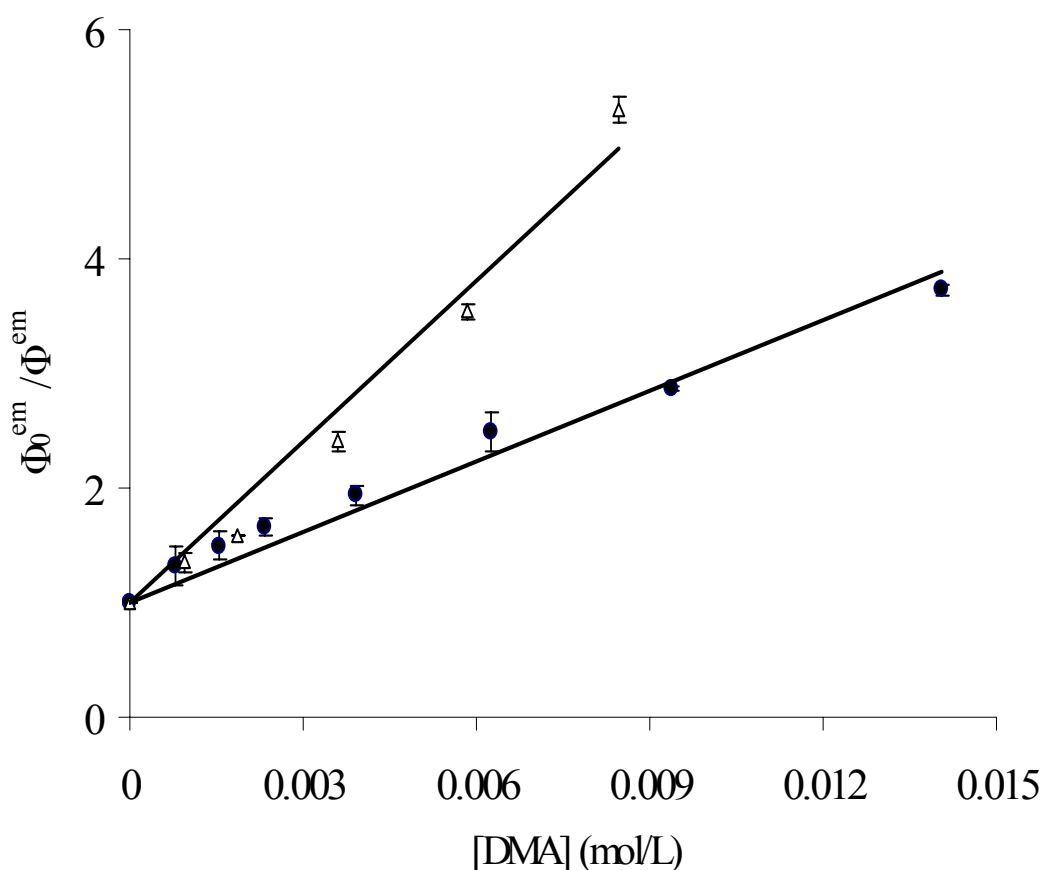


Figure 3.25 Stern-Volmer plots for DMA emission quenching on $[\{(bpy)_2Ru(dpp)\}_2Ru(dpp)PtCl_2](PF_6)_6$ (●) and $[\{(bpy)_2Ru(dpp)\}_2Ru(dpq)PtCl_2](PF_6)_6$ (Δ) in CH_3CN ($bpy = 2,2'$ -bipyridine, $dpp = 2,3$ -bis(2-pyridyl)pyrazine, $dpq = 2,3$ -bis(2-pyridyl)quinoxaline).

The Stern-Volmer study verified a larger quenching rate for the $[\{(bpy)_2Ru(dpp)\}_2Ru(dpq)PtCl_2](PF_6)_6$ than for the $[\{(bpy)_2Ru(dpp)\}_2Ru(dpp)PtCl_2](PF_6)_6$, which suggests more efficient interaction between the dpq analogue and the DMA than between the dpp analogue and the DMA.

3.3.10.2 Hydrogen Production

Quite recently, our group designed a Ru polyazine complexes able to collect electrons photochemically and transfer them to reactive metal centers, a process instrumental in catalyzing hydrogen production from water.^{118, 145} These complexes possess both the light absorber Ru polyazine moiety and catalytically active Pt site.¹⁴⁶⁻¹⁵⁰ Both the tetrametallic complexes $[\{(bpy)_2Ru(dpp)\}_2Ru(dpp)PtCl_2](PF_6)_6$ and $[\{(bpy)_2Ru(dpp)\}_2Ru(dpq)PtCl_2](PF_6)_6$ have been shown to be able to produce H_2

photocatalytically from H₂O in mixed CH₃CN/H₂O solution in the presence of the electron donor DMA. These metal complexes possess ³MLCT excited states that are quenched by DMA, leading to the production of reduced complexes.

Preliminary photocatalytic experiments tested the applicability of these complexes as candidates for visible light induced H₂O reduction for producing H₂. A summary of the results is provided in Table 3.10. Both these tetrametallic complexes produced H₂ when photolyzed with 530 nm light. The final concentrations for each component were: ca. 2.8 x 10⁻⁵ M metal complex; 0.92 M DMA; 1.5 x 10⁻³ M CF₃SO₃H and 8.2 M H₂O. The effective pH of the final solution was estimated at ca. 8, using pH = pK_a + log [A⁻]/[HA] (eq 35). For the tetrametallic complexes [{(bpy)₂Ru(dpp)}₂Ru(dpp)PtCl₂](PF₆)₆ and [{(bpy)₂Ru(dpp)}₂Ru(dpq)PtCl₂](PF₆)₆, the dpq analogue produced almost twice as much hydrogen after undergoing 3 h of photolysis than the dpp analogue. For [{(bpy)₂Ru(dpp)}₂Ru(dpq)PtCl₂](PF₆)₆, 3.5 μmol of H₂ were produced, which represents 36 turnovers of the tetrametallic catalyst after 4 h of photolysis. This difference is likely because the μ-dpq is a better electron collector than μ-dpp, which facilitates the electron transfer from the μ-dpp to the μ-dpq and results higher efficiency.

Systems with coordinated Pt could lead to the decomposition of the Pt followed by the formation of the colloidal Pt for H₂ production. To better understand this process, several control experiments were performed. First, the trimetallic synthon give a formular either alone or with [PtCl₂(DMSO)₂] was photolyzed under these conditions for 3 h, which did not lead to any measurable H₂ production, thereby indicating the importance of the tetrametallic assembly in the observed photochemistry. Second, the addition of a colloidal Pt to the trimetallic [{(bpy)₂Ru(dpp)}₂Ru(dpq)](PF₆)₆ with DMA did lead to H₂ production, but at a rate of only 50% of that of the tetrametallic complex. Third, an excess of metallic Hg was added to the cell containing the tetrametallic complex [{(bpy)₂Ru(dpp)}₂Ru(dpq)PtCl₂](PF₆)₆ to capture and inactivate Pt⁰, which could have been generated following photoreduction.¹⁴⁶⁻¹⁵⁰ The hydrogen conversion efficiency was observed to be 75 % of that of the tetrametallic complex without the Hg present, which suggests that “Pt^{II} to Pt⁰” may not be the only mechanism for photocatalysis. Last, when the trimetallic complex was mixed with equimolar colloidal Pt and excess amount of metallic Hg, no measurable H₂ was detected by

GC analysis, which supported the necessity of tetrametallic complex during the hydrogen generation process. The results of these control studies suggest that tetrametallic complex formation is crucial for the catalytic cycle.

The Os analogues, trimetallic complex $[\{(bpy)_2Os(dpp)\}_2Ru(dpq)](PF_6)_6$, and tetrametallic complex $[\{(bpy)_2Os(dpp)\}_2Ru(dpq)PtCl_2](PF_6)_6$ were also assessed for their role in hydrogen production. However, none resulted in any observable generated hydrogen. This was possibly due to the fact that the lower energy $Os(d\pi) \rightarrow \mu-dpp(\pi^*)^3MLCT$ is not efficiently reduced by DMA (0.80 V vs. Ag/AgCl), given the excited state reduction potential 0.90 V vs. Ag/AgCl for the Os tetrametallic complex. Thus the metal complex won't be able to transfer the electrons to the water. Another possible factor leading to no photocatalytic activity is possibly due to the very low lifetime of the $Os(d\pi) \rightarrow \mu-dpp(\pi^*)^3MLCT$ state (< 5 ns), which doesn't allow efficiency electron transfer from the metal complex to the water. However further study on these mechanisms would be of interest for future research.

Table 3.10 Photocatalytic studies of H₂ production using tetrametallic complexes, trimetallic complexes and some related controls. ^a

Complex	[H ₂ O] (mL)	[DMA] (mL)	Photolysis Time (hr)	H ₂ (μmol)	Turnover	Φ x 10 ²
Ru ₃ Ptdpq ^b	0.50	0.40	1	1.6	17	0.53
	0.50	0.40	2	2.8	28	0.45
	0.50	0.40	3	3.3	34	0.36
	0.50	0.40	4	3.9	41	0.33
	0.50	0	3	<0.01	n/a	n/a
Ru ₃ dpq + PtCl ₂ (DMSO) ₂	0.50	0.40	3	<0.01	n/a	n/a
Ru ₃ dpq + Pt ^c	0.50	0.40	3	1.8	18	0.19
Ru ₃ Ptdpq + Hg ^d	0.50	0.40	3	2.5	26	0.27
Ru ₃ Ptdpq + Pt + Hg ^e	0.50	0.40	3	<0.01	n/a	n/a
Ru ₃ dpq ^f	0.50	0.40	3	<0.01	n/a	n/a
Ru ₃ Ptdpp ^g	0.50	0.40	3	1.7	17	0.18
Ru ₃ dpp ^h	0.50	0.40	3	<0.01	n/a	n/a
Os ₂ RuPtdpq ⁱ	0.50	0.40	3	<0.01	n/a	n/a
Os ₂ Rudpq ^j	0.50	0.40	3	<0.01	n/a	n/a

^a Photochemical generation of H₂ as determined by GC using 1.5 mL of 6.3 x 10⁻⁵ M metal complex in acetonitrile, 0.50 mL of pH 2.0 H₂O acidified by CF₃SO₃H, 0.40 mL of dimethylaniline (DMA) and 1.0 mL acetonitrile. The final concentrations for each component were: ca. 2.8 x 10⁻⁵ M metal complex; 0.92 M DMA; 1.5 x 10⁻³ M CF₃SO₃H and 8.2 M H₂O. The effective pH of final solution was estimated at ca. 8. (bpy = 2,2'-bipyridine, dpp = 2,3-bis(2-pyridyl)pyrazine and dpq = 2,3-bis(2-pyridyl)quinoxaline).

^b Ru₃Ptdpq = [{(bpy)₂Ru(dpp)}₂Ru(dpq)PtCl₂](PF₆)₆.

^c Ru₃dpq + Pt = equimolar amount of [{(bpy)₂Ru(dpp)}₂Ru(dpq)PtCl₂](PF₆)₆ and colloidal Pt.

^d Ru₃Ptdpq + Hg = [{(bpy)₂Ru(dpp)}₂Ru(dpq)PtCl₂](PF₆)₆ and excess amount (100 times) of metallic Hg.

^e Ru₃Ptdpq + Pt + Hg = [{(bpy)₂Ru(dpp)}₂Ru(dpq)PtCl₂](PF₆)₆, equimolar amount of colloidal Pt and excess amount (100 times) of metallic Hg.

^f Ru₃dpq = [{(bpy)₂Ru(dpp)}₂Ru(dpq)PtCl₂](PF₆)₆.

^g Ru₃Ptdpp = [{(bpy)₂Ru(dpp)}₂Ru(dpp)PtCl₂](PF₆)₆.

^h Ru₃dpp = [{(bpy)₂Ru(dpp)}₂Ru(dpp)PtCl₂](PF₆)₆.

ⁱ Os₂RuPtdpq = [{(bpy)₂Ru(dpp)}₂Ru(dpq)PtCl₂](PF₆)₆.

^j Os₂Rudpq = [{(bpy)₂Ru(dpp)}₂Ru(dpq)PtCl₂](PF₆)₆.

Our study of the generation of hydrogen as a function of time of photolysis, using the tetrametallic complex $[\{(bpy)_2Ru(dpp)\}_2Ru(dpq)PtCl_2](PF_6)_6$ as the photocatalyst, is shown in Figure 3.26. As documented, the amount of hydrogen generated increased in relation to duration of photolysis, with hydrogen production occurring faster at the beginning of the experiment, which suggests certain non-Pt(solid) mechanism during the photocatalysis.

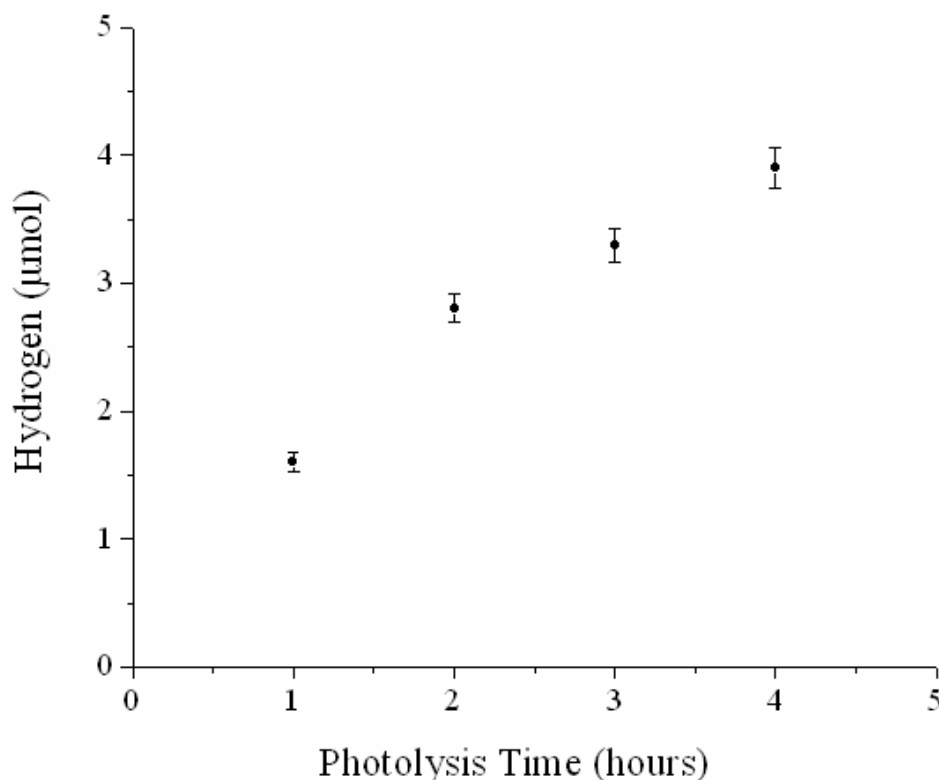


Figure 3.26 Hydrogen generated vs. photolysis time for $[\{(bpy)_2Ru(dpp)\}_2Ru(dpq)PtCl_2](PF_6)_6$. (bpy = 2,2'-bipyridine, dpp = 2,3-bis(2-pyridyl)pyrazine, dpq = 2,3-bis(2-pyridyl)quinoxaline). Each time a 100 µL of gas sample was syringed into the GC and the total amount of hydrogen was calculated based on the ratio between the head space volume and the sample volume (100 µL). Each data point was an average of 3 measurements.

The sustainability of the catalyst is supported by the high turnover number and the electronic absorption spectroscopy. Comparisons of the electronic absorption spectroscopy of the $[\{(bpy)_2Ru(dpp)\}_2Ru(dpq)PtCl_2](PF_6)_6$ system before and after photocatalysis did not indicate either any significant decomposition of the Pt to form $[\{(bpy)_2Ru(dpp)\}_2Ru(dpq)](PF_6)_6$, or any significant decomposition of the catalyst (Figure 3.27). Thus, H₂ production by the $[\{(bpy)_2Ru(dpp)\}_2Ru(dpq)PtCl_2](PF_6)_6$ system is a promising result for converting solar energy into chemical energy.

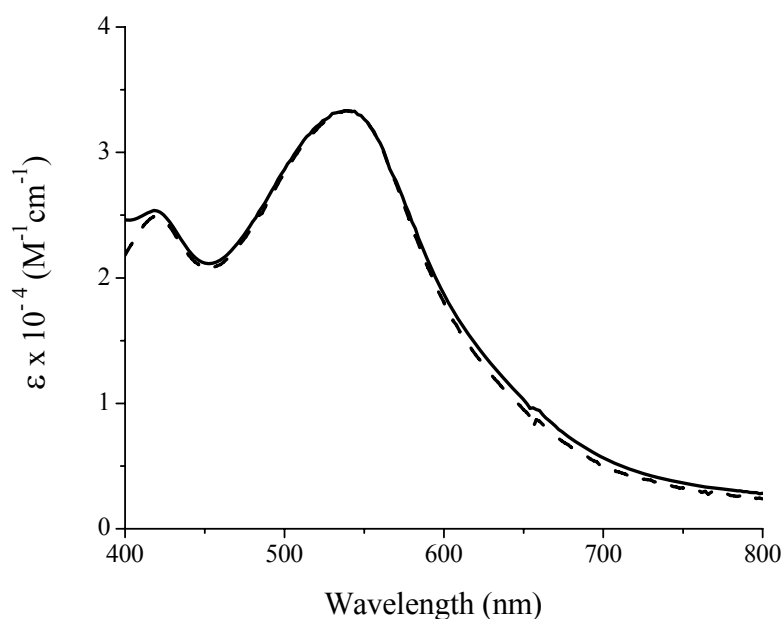


Figure 3.27 Comparison of electronic absorption spectra prior to (—) and after (---) the photocatalytic production of H₂ for [{(bpy)₂Ru(dpp)}₂Ru(dpq)PtCl₂](PF₆)₆ (bpy = 2,2'-bipyridine, dpp = 2,3-bis(2-pyridyl)pyrazine, dpq = 2,3-bis(2-pyridyl)quinoxaline).

3.4 DNA Photocleavage Assay

3.4.1 DNA Photocleavage Study (This work is carried out by Mr. David F. Zigler using complexes prepared as described in Chapter 3.1)

DNA binding and photocleavage experiments were performed using a protocol adapted from previous work.³⁴ Standard agarose gels compared samples of DNA and metal stored in the dark to those that were photolyzed in air or under an argon atmosphere at 1000 nm > λ > 450 nm with a light flux of 10¹⁹ photons/min. Experiments were performed to examine the impact of buffer ionic strength and photolysis time on the binding and photocleavage properties of [{(bpy)₂Ru(dpp)}₂Ru(dpp)](PF₆)₆ and [{(bpy)₂Ru(dpp)}₂Ru(dpp)PtCl₂](PF₆)₆. Figure 3.28 shows the assay of DNA binding and photocleavage for [{(bpy)₂Ru(dpp)}₂Ru(dpp)PtCl₂](PF₆)₆, [{(bpy)₂Ru(dpp)}₂Ru(dpp)](PF₆)₆ and standard cisplatin. In each gel lane, λ served as the molecular weight standard with bands at 23.1, 9.4, 6.6, 4.4, 2.3 and 2.0 k base pairs. Lane C was used as the pUC18 DNA control, which contained primarily supercoiled Form I DNA with minor amounts of relaxed, Form II, DNA. pUC18 DNA was a closed circular plasmid DNA of 2686 bp with approximately 85-90 % GC content. Samples of pUC18 DNA were also mixed with metal at a ratio of 20 : 1

[DNA base pairs (BP) : metal complex (MC)] in 10 mM phosphate buffer. These were then incubated at 20°C for 1 h (MC), 37 °C for 1 h (MC*) or photolyzed at 1000 nm > λ > 450 nm for 1 h under atmospheric conditions (Lane O₂), or under Ar (Lane Ar).

DNA binding study shows that the interaction between the tetrametallic complex [{(bpy)₂Ru(dpp)}₂Ru(dpp)PtCl₂](PF₆)₆ and DNA is mainly covalent. The impact on DNA migration of the pUC18 DNA after incubation with cisplatin, a known DNA binder, was studied under our conditions (Figure 3.28A), which produced results consistent with the literature.⁴³ The results of the DNA binding experiments (Figure 3.28B) indicate that under the 20 : 1 ratio tested, [{(bpy)₂Ru(dpp)}₂Ru(dpp)PtCl₂](PF₆)₆ formed coordinate covalent bonds with DNA, while the trimetallic complex [{(bpy)₂Ru(dpp)}₂Ru(dpp)](PF₆)₆ did not (Figure 3.28C). Moreover, these results showed that the coordinate covalent binding of [{(bpy)₂Ru(dpp)}₂Ru(dpp)PtCl₂](PF₆)₆ occurred independent of light.^{45, 151, 152}

It has been shown that binding [Pt(NH₃)₂Cl₂] (cisplatin) to DNA results in a change in the topology of the DNA polymer around the point of binding. The reduced rate of migration of DNA incubated with [{(bpy)₂Ru(dpp)}₂Ru(dpp)PtCl₂](PF₆)₆, therefore, reflects either a change in the topology of the supercoiled circular pUC18, or a change in the metal complex DNA adduct charge or size, or possibly a combination of these factors.⁴³ Binding the larger [{(bpy)₂Ru(dpp)}₂Ru(dpp)PtCl₂](PF₆)₆ metal complex will likely have a greater impact on topology than will binding of the cisplatin, as we have observed in other related Ru/Pt complexes.^{92, 94, 153-155} The slower migration of supercoiled DNA treated with [{(bpy)₂Ru(dpp)}₂Ru(dpp)PtCl₂](PF₆)₆, relative to DNA treated with cisplatin, may also reflect the higher cationic charge of the [{(bpy)₂Ru(dpp)}₂Ru(dpp)PtCl₂](PF₆)₆, thereby reducing the overall negative charge density of DNA or a greater degree of unwinding of the DNA by [{(bpy)₂Ru(dpp)}₂Ru(dpp)PtCl₂](PF₆)₆ binding.

The photolysis experiments conducted also revealed that pUC18 treated with either [{(bpy)₂Ru(dpp)}₂Ru(dpp)](PF₆)₆ or [{(bpy)₂Ru(dpp)}₂Ru(dpp)PtCl₂](PF₆)₆ and photolyzed in air resulted in DNA cleavage. This photocleavage was documented by the reduced migration of the pUC18 in the gel, since it converted from the supercoiled form (Form I) to the open circular topoisomer form (Form II), as shown in Figure 3.28, lane O₂. The fact that molecular oxygen is required for photochemical activity of either metal complex indicates

that each indirectly acts on the DNA through photosensitization of molecular oxygen.

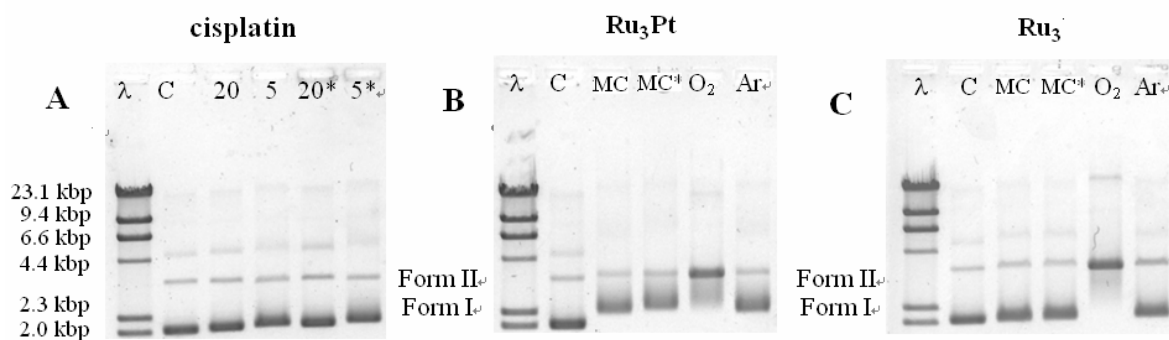


Figure 3.28 DNA interaction studies of $[\{(bpy)_2Ru(dpp)\}_2Ru(dpp)PtCl_2](PF_6)_6$, *cis*- $[Pt(NH_3)_2Cl_2]$ and $[\{(bpy)_2Ru(dpp)\}_2Ru(dpp)](PF_6)_6$. Experiments used 0.8% agarose gels and metal complexes were dissolved in 10 mM NaH_2PO_4 buffer with ~1% DMSO. Gel (A) *cis*- $[Pt(NH_3)_2Cl_2]$, (B) $[\{(bpy)_2Ru(dpp)\}_2Ru(dpp)PtCl_2](PF_6)_6$ (**Ru₃Pt**) and (C) $[\{(bpy)_2Ru(dpp)\}_2Ru(dpp)](PF_6)_6$ (**Ru₃**). Samples were stored in the dark for 1 h. Lanes corresponding to photolyzed samples were illuminated using light from a 1000 W xenon arc lamp, filtered to give $1000\text{ nm} > \lambda > 450\text{ nm}$ light. Base pair (BP) to metal complex (MC) ratios were 20 : 1. Form I = supercoiled pUC18, Form II = Nicked, relaxed pUC18, λ = Lamda molecular weight standard, C = native pUC18 control and lanes with an asterisks (*) were samples incubated at 37 °C in the dark with unstarred lanes being stored at 20 °C. In gels A and C, MC is the 20 : 1 BP : MC ratio control, O₂ is the aerated, photolyzed sample and Ar is the photolyzed sample purged under argon. In gel B, 20 indicates that the base pair to metal complex ratio was 20 : 1 and 5 indicates a BP to MC ratio of 5 : 1

The method of pre-association of each complex with DNA was studied by changing the ionic strength of the buffer solution containing DNA and metal complex. Specifically, DNA binding and photocleavage studies were performed using either 10 mM or 30 mM NaH_2PO_4 buffer. DNA is a polyanion and each of the metal complexes has a +6 charge. Increasing the ionic strength of the analyte solutions did not change in the observed DNA binding or photochemistry of $[\{(bpy)_2Ru(dpp)\}_2Ru(dpp)PtCl_2](PF_6)_6$. The amount of pUC18 being converted from supercoiled to open circular form following photolysis was the same for either the 10 mM or the 30 mM NaH_2PO_4 , as shown in Figures 3.29A and 3.29B. The trimetallic complex $[\{(bpy)_2Ru(dpp)\}_2Ru(dpp)](PF_6)_6$, however, exhibited reduced photochemical activity with pUC18 when the NaH_2PO_4 buffer concentration was increased from 10 mM to 30 mM, as documented in Figures 3.29C and 3.29D. Therefore, the ionic strength independence of the photochemical action on the pUC18 of $[\{(bpy)_2Ru(dpp)\}_2Ru(dpp)PtCl_2](PF_6)_6$ indicates that the mode of binding of the metal

complex is primarily covalent and not electrostatic, as is the case for the metal complex lacking the bioactive Pt metal center. The bioactive Pt site, therefore, enhances the DNA activity of this complex, giving it multifunctional (DNA binding and photocleavage) capabilities. The dependence of the photocleavage by the trimetallic on ionic strength implies the association of this complex with DNA is largely ionic in nature. Thus, by combining the *cis*-Pt^{II}Cl₂ covalent binding ability with the Ru polypyridine chromophore photosensitizing ability, this complex is a promising candidate as a photodynamic therapy drug for the treatment of cancer.

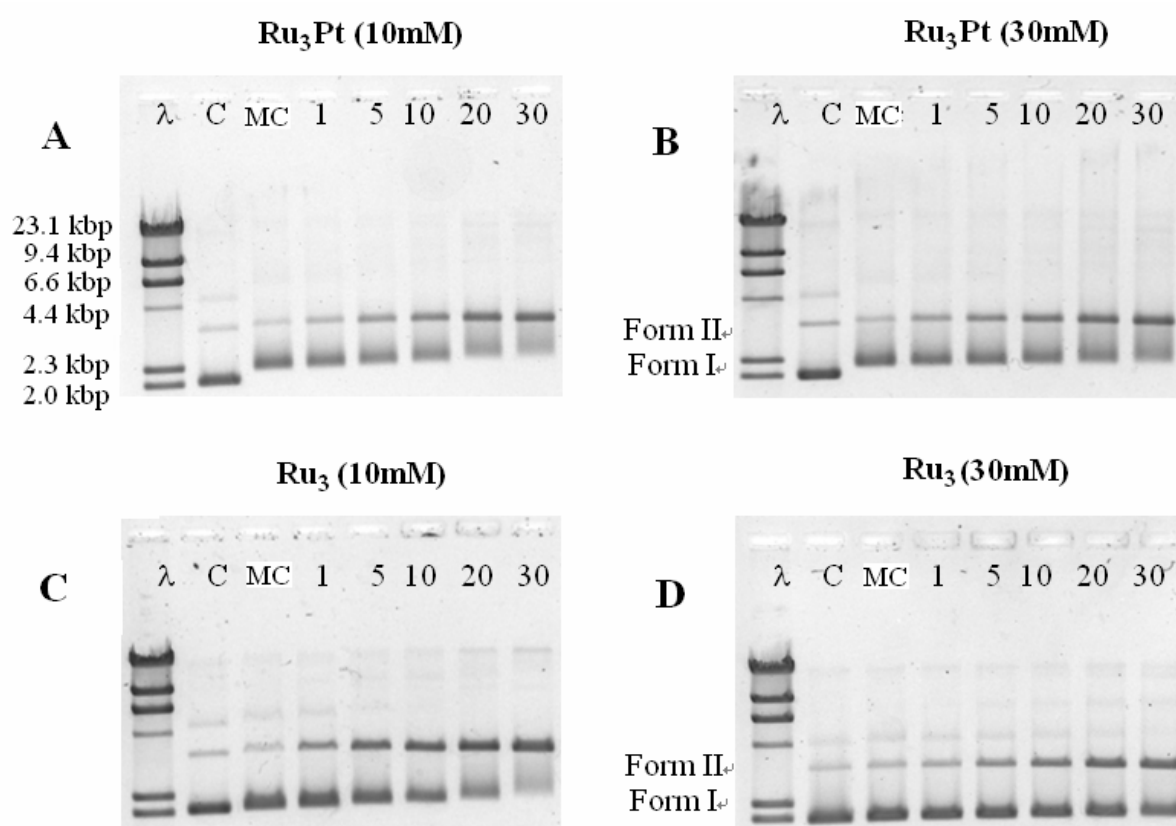


Figure 3.29 Ionic strength effect on the interaction of DNA with $[\{(bpy)_2Ru(dpp)\}_2Ru(dpp)PtCl_2](PF_6)_6$ (**Ru₃Pt**) (A, B) or $[\{(bpy)_2Ru(dpp)\}_2Ru(dpp)](PF_6)_6$ (**Ru₃**) (C, D) in 10 mM (A, C) or 30 mM (B, D) NaH₂PO₄ buffer with ~1% DMSO. Photolyzed samples were illuminated using light from a 1000 W xenon arc lamp, filtered to give 1000 nm > λ > 450 nm light. Base pair to metal complex ratios were 20:1. Form I = supercoiled pUC18, Form II = open circular pUC18, λ = Lamda molecular weight standard, C = pUC18 control, MC = metal complex/DNA control, numbers = min of photolysis.

3.4.2 Emission Quenching Experiment

The emission properties of the $[\{(bpy)_2Ru(dpp)\}_2Ru(dpp)](PF_6)_6$ and

$[\{(bpy)_2Ru(dpp)\}_2Ru(dpp)PtCl_2](PF_6)_6$ complex were studied in aqueous solution in both the presence and absence of DNA and molecular oxygen. These complexes were also studied in the presence and absence of DNA to probe the impact of DNA on their 3MLCT states. The emission of $[\{(bpy)_2Ru(dpp)\}_2Ru(dpp)](PF_6)_6$ and $[\{(bpy)_2Ru(dpp)\}_2Ru(dpp)PtCl_2](PF_6)_6$ was quenched by 11% and 13%, respectively, under atmospheric conditions vs. under an Ar atmosphere (Table 3.11). This indicated energy or electron transfer quenching by O_2 of these complexes to produce a reactive oxygen species, which supported the hypothesis of an oxygen mediated pathway during the DNA photocleavage experiments. An overall emission enhancement was observed upon adding DNA to an aqueous solution of $[\{(bpy)_2Ru(dpp)\}_2Ru(dpp)](PF_6)_6$ or $[\{(bpy)_2Ru(dpp)\}_2Ru(dpp)PtCl_2](PF_6)_6$. “DNA light switch” effects for similar complexes are known. The emission increased by 55% for $[\{(bpy)_2Ru(dpp)\}_2Ru(dpp)](PF_6)_6$ in the presence of a 4 : 1 BP : MC ratio and by 38% for the $[\{(bpy)_2Ru(dpp)\}_2Ru(dpp)PtCl_2](PF_6)_6$ system.

Table 3.11 Comparative DNA quenching experiments on $[\{(bpy)_2Ru(dpp)\}_2Ru(dpp)](PF_6)_6$ and $[\{(bpy)_2Ru(dpp)\}_2Ru(dpp)PtCl_2](PF_6)_6$.^{a, b}

Experimental Condition	Ratio of Emission Intensity under Various Conditions over That under Deoxygenation and No DNA	
	$[\{(bpy)_2Ru(dpp)\}_2Ru(dpp)](PF_6)_6$	$[\{(bpy)_2Ru(dpp)\}_2Ru(dpp)PtCl_2](PF_6)_6$
	deoxygenated, no DNA	1.00
oxygenated, no DNA	0.87	0.89
MC : BP = 2 : 1	1.10	1.18
MC : BP = 1 : 2	1.29	1.38
MC : BP = 1 : 4	1.55	1.38

^a Experiments were performed in 1% DMSO, 10 mM Na_2HPO_4 solution at RT. The DNA used is a 1.14×10^{-3} M calf thymus solution. Experiments were performed by adding calf thymus DNA into the metal complex solution to reach a molar ratio of MC : BP (metal complex to DNA base pair) = 2 : 1, 1 : 2, 1 : 4. The mixture of metal complex and DNA was shaken vigorously and kept for 2 mins prior to collecting the data.

^b bpy = 2,2'-bipyridine and dpp = 2,3-bis(2-pyridyl)pyrazine.

Chapter 4. Conclusions and Future Work

4.1 Conclusions

Assembling two metals and two bridging ligands into a hexametalllic supramolecule, it is possible to generate an efficient light absorber that possesses a spatially separated HOMO and LUMO generating a long-distance intramolecular charge separation state that is lowest in energy. The hexametalllic complex $[\{[(bpy)_2Os(dpp)]_2Ru\}_2(dpq)](PF_6)_{12}$ contains four light absorbing osmium metal centers, coupled to two ruthenium metal centers, linked by two different bridging ligands capped by bpy terminal ligands, thereby making it a structurally diverse supramolecule. Electrochemistry showed the least negative redox potential of the complex was at -0.48 V for the central $\mu\text{-dpq}^{0/-}$ (LUMO) and the least positive potential was 1.17 V for peripheral $Os^{II/III}$ (HOMO) (vs. Ag/AgCl). The comparative electronic absorption spectroscopy of $[\{[(bpy)_2Os(dpp)]_2Ru\}_2(dpq)](PF_6)_{12}$ and $[\{(bpy)_2Os(dpp)\}_2Ru(dpq)](PF_6)_6$ revealed a peak at 590 nm in the difference spectrum for

$[\{[(bpy)_2Os(dpp)]_2Ru\}_2(dpq)](PF_6)_{12}$ corresponding to the $Ru(d\pi) \rightarrow \mu\text{-dpq}(\pi^*)$ 1MLCT transition, which was consistent with the previously reported 605 nm $Ru(d\pi) \rightarrow \mu\text{-dpq}(\pi^*)$ 1MLCT band in $[(bpy)_2Ru(dpq)Ru(bpy)_2](PF_6)_4$.⁵ Similarly, a peak at 570 nm in the difference spectrum, comparing the oxidized hexametalllic and the oxidized trimetalllic complexes, was also attributed to the $Ru(d\pi) \rightarrow \mu\text{-dpq}(\pi^*)$ 1MLCT . The consistency in electrochemistry, electronic absorption spectroscopy and spectroelectrochemistry revealed the $\mu\text{-dpq}$ based LUMO in $[\{[(bpy)_2Os(dpp)]_2Ru\}_2(dpq)](PF_6)_{12}$. Prior to this research, a few multimetalllic Ru/Os polyazine dendrimers have been synthesized by Balzani et al.^{5, 11, 83} However when constructing the molecules, either a single-type bridging ligand was used,^{5, 11, 83} or single-type metal center was used.⁸³ Due to the lack of variation of the ligands in literature examples, no significant difference in electron accepting ability exists within the bridging ligands, which leads to no significant charge separation. The excited state kinetics was dominated by energy transfer from higher energy levels to the lowest energy level. The hexametalllic complex represents the first example incorporating metals with different d orbital energy and bridging ligands with different π^* orbital energy to allow possible generation of long distance intramolecular charge separation. The comparative studies on

electronic absorption spectroscopy and spectroelectrochemistry shed light on identification of fingerprint difference between structurally similar complexes.

In large supramolecular systems, the π^* orbitals of bridging ligands bound to Pt is further stabilized compared to those bound to Ru or Os while at the same time, the energetics of the moieties away from Pt is relatively retained though perturbed by the incorporation of Pt. The potential of $\text{dpp}^{0/-}$ bound to Pt and Ru in $[\{(\text{bpy})_2\text{Ru}(\text{dpp})\}_2\text{Ru}(\text{dpp})\text{PtCl}_2](\text{PF}_6)_6$ was at -0.40 V and the other two $\text{dpp}^{0/-}$ potentials were at -0.60 and -0.71 V, which were comparable to -0.50 V and -0.64 V for $\text{dpp}^{0/-}$ in $[\{(\text{bpy})_2\text{Ru}(\text{dpp})\}_2\text{Ru}(\text{dpp})](\text{PF}_6)_6$ (vs. Ag/AgCl). The potential of $\text{dpq}^{0/-}$ in tetrametallic complexes was at -0.08 V, more negative than the -0.42 V for $\text{dpq}^{0/-}$ in the bimetallic complex $[(\text{bpy})_2\text{Ru}(\text{dpq})\text{Ru}(\text{bpy})_2](\text{PF}_6)_4$ (vs. Ag/AgCl). However the potentials of $\text{dpp}^{0/-}$ were at -0.44 V and -0.65 V, similarly to -0.42 V and -0.62 V in $[\{(\text{bpy})_2\text{Ru}(\text{dpp})\}_2\text{Ru}(\text{dpq})](\text{PF}_6)_6$ (vs. Ag/AgCl).

$[\{(\text{bpy})_2\text{Ru}(\text{dpp})\}_2\text{Ru}(\text{dpp})\text{PtCl}_2](\text{PF}_6)_6$ displayed emission from the $\text{Ru} \rightarrow \mu\text{-dpp}^3\text{MLCT}$ state at the typical 750 nm but with a reduced lifetime as well as quantum yield for emission ($\Phi^{\text{em}} = 3.2 \times 10^{-4}$; $\tau = 0.10 \mu\text{s}$) compared to model bimetallic complex $[(\text{bpy})_2\text{Ru}(\text{dpp})\text{Ru}(\text{bpy})_2](\text{PF}_6)_4$ ($\Phi^{\text{em}} = 1.2 \times 10^{-3}$; $\tau = 0.13 \mu\text{s}$). The reduction in the lifetime and quantum yield could be explained by the quenching of emissive state through charge separation state involving the dpp bound to Pt. Prior to this work, there were a few examples coupling Pt to Ru polyazine chromophores,^{28, 43, 100-103} however there were no reported examples using multimetallic Ru polyazine complex as chromophores and accordingly no fundamental study for such complex system have been carried out. The study carried out by this research sets examples about how to tune the energy level by incorporation of different metals and how this change affects the photophysical properties of the complex, which is useful to design molecular devices for certain photophysical/photochemical applications, such as photocatalysis of hydrogen production from water.

$[\{(\text{bpy})_2\text{Ru}(\text{dpp})\}_2\text{Ru}(\text{dpq})\text{PtCl}_2](\text{PF}_6)_6$ is able to photocatalyze hydrogen generation from water. The complex $[\{(\text{bpy})_2\text{Ru}(\text{dpp})\}_2\text{Ru}(\text{dpq})\text{PtCl}_2](\text{PF}_6)_6$ has been studied for its catalytic ability in generating hydrogen and was found to have 34 product turnovers after 3 h photolysis. The generated hydrogen amount (3.3 μmol in 3 h) increased with the photolysis time and had a relatively faster rate in the beginning of the experiment. The

$[\{(bpy)_2Ru(dpp)\}_2Ru(dpp)PtCl_2](PF_6)_6$ is also observed to have photocatalytic ability in generating hydrogen from water but with lower efficiency under the same experimental conditions, which was possibly due to poorer electron collection by dpp than that by dpq. The Ru trimetallic chromophores themselves or mixed with $[PtCl_2(DMSO)_2]$ at the stoichiometric ratio under same conditions showed no hydrogen generated, which indicates the necessity of the catalytic center Pt in the composition of tetrametallic complexes. The Ru trimetallic chromophores mixed with colloidal Pt at stoichiometric ratio under same conditions showed less hydrogen generated (1.8 μ mol in 3 h), which identified the contribution from tetrametallic complex although this could not exclude the possibility of decomposition of the supramolecules followed by catalysis through Pt^0 reduced from Pt^{II} . However, when the Ru trimetallic chromophores mixed with excess amount of metallic Hg, forming an alloy with Pt^0 , significant amount of hydrogen was still observed, suggesting some photocatalytic ability comes from the intact tetrametallic complex. Prior to this work, there was only one reported molecular photoinitiated electron collector able to convert light to chemical fuel, incorporating both the light absorber and electron collector into one single molecule.¹⁵⁶ Recently Sakai *et al.* reported a bimetallic Ru-Pt complex able to photocatalyze hydrogen evolution from the “visible-light-induced EDTA-reduction of water” with 1% conversion efficiency.^{114, 115} Using a Ru-Pd system, Rau *et al.* observed a production of hydrogen from triethylamine and a simultaneous hydrogenation of toluene to *cis*-stilbene.¹¹⁶ A recent communications in JACS showed these systems function through metallic Pd and Pt production.¹¹⁷ Elvington from our group recently reported a trimetallic Ru-Rh-Ru system able to collect multiple electrons into central Rh center and perform the photocatalysis of hydrogen generation.¹⁵⁶ The described research herein identified the catalytic ability of supramolecules containing Ru polyazine chromophores and reactive Pt within single molecule. And it also established the importance of incorporating an efficient electron collector bound to reactive metal center. Although the detailed information about how this catalyst works is still unclear, it suggests the idea that coupling light absorbers with reactive metal centers fashioned by a controllable electron flow can effectively utilize solar energy.

Incorporating *cis*- $PtCl_2$ DNA binding moiety and Ru polyazine chromophore into a supramolecule allows the supramolecule to covalently bind to DNA through *cis*- $PtCl_2$ and

photocleave the DNA by the reactive oxygen sensitized by the long enough excited state of Ru polyazine chromophore. By gel electrophoresis, we observed covalent binding ability of this complex as well as DNA photocleavage effect through oxygen mediated mechanism. Emission quenching experiment showed oxygen quenched the $\text{Ru} \rightarrow \mu\text{-dpp}^3\text{MLCT}$ emission by ca. 10 %, consistent with proposed mechanism. The independence of ionic strength variation when $[\{(\text{bpy})_2\text{Ru}(\text{dpp})\}_2\text{Ru}(\text{dpp})\text{PtCl}_2](\text{PF}_6)_6$ interacted with DNA, suggested the covalent interaction nature of the complex. Prior to this research, Ru polyazine complexes have been studied for their light activated interactions with DNA.^{41, 89, 90} Despite the relatively large number of Ru polyazine supramolecular assemblies that have been developed to date, few were able to couple reactive metals such as Pt to Ru chromophores.^{28, 43, 100-102} Although some of these Ru-Pt complexes showed covalent binding ability to DNA,^{43, 100} none of them was capable of covalent binding to DNA and photocleaving DNA. Importantly, this is the first time that a multifunctional Ru-Pt complex has been shown to bind to and photocleave DNA. Following our report, Sakai *et al.* designed a Ru-Pt bimetallic system that displayed similar properties.¹⁰³ Aided by this research, future design of photodynamic therapy drug with tunable therapeutic window, through variation of Ru/Os polyazine chromophores, can be proposed, as long as the excited state lifetime is long enough and able to sensitize the molecular oxygen.

4.2 Future Work

Future work can be carried in the following areas:

- For the hexametallic complex $[\{[(\text{bpy})_2\text{Os}(\text{dpp})]_2\text{Ru}\}_2(\text{dpq})](\text{PF}_6)_{12}$, transient absorption spectroscopy should be carried out to identify the formation of reduced $\mu\text{-dpq}$ in the excited state prior to electron back transfer to the ground state. The lifetime of the excited state reduced $\mu\text{-dpq}$ will indicate the lifetime of the long distance intramolecular charge separation state.
- For hydrogen generation project, the photochemical product of water and DMA should be examined and the fate of each reactant should also be tracked, based on which more clear mechanism in terms of photocatalysis of hydrogen production will be elaborated. Hydrogen generation from all these tetrametallic complexes should be examined with respect to a number of important factors, such as

concentration of the electron donor DMA, concentration of water, concentration of metal complexes, pH values, photolysis time, etc. Comparison studies should also be undertaken that investigate the amount of hydrogen generated under certain fixed conditions using all the candidates in the tetrametallic series. Correlations between the excited state properties and the hydrogen conversion efficiency for all the examined complexes should also be studied. In addition, new systems with varied bridging ligands, such as stronger electron acceptor dpb (2,3-bis(2-pyridyl)benzoquinoxaline), can be used to prepare tetrametallic analogue such as $[\{(bpy)_2Ru(dpp)\}_2Ru(dpb)PtCl_2](PF_6)_6$, with μ -dpb connecting the central Ru and the reactive Pt, with potentially better hydrogen conversion rates.

- With respect to potential photodynamic therapies, the tetrametallic Os analogue should be further investigated as a candidate for DNA binding and photocleavage studies within the ideal therapeutic wavelength window (600 – 1000 nm) due to its stronger absorption of $Os(d\pi) \rightarrow BL(\pi^*)^3MLCT$. Moreover, studies on the DNA photocleavage properties of other complexes, under varied factors such as photolysis time and oxygen dependence, should also be carried out.
- Based on a thorough understanding of the properties of building blocks once they have been incorporated into multimetallic systems, it is possible to design new complexes with increased light harvesting ability throughout the entire spectrum. By selecting the appropriate building block for every part of the spectrum, it is possible to design a complex that is able to absorb light evenly through the whole spectrum. This could have important applications for the generation of dye sensitized solar cells or photochemical cells.

References

1. http://www1.eere.energy.gov/solar/pv_cell_light.html.
2. Lehn, J. M. *Science* **1993**, *260*, 1762.
3. Balzani, V.; Moggi, L.; Scandola, F. *Supramolecular Photochemistry, Ed. NATO ASI Series 214, Reidel, Dordrecht, The Netherlands* **1987**, 1.
4. Kalyanasundaram, K.; Nazeeruddin, M. K. *Chem. Phys. Lett.* **1989**, *158*, 45.
5. Balzani, V.; Juris, A.; Venturi, M.; Campagna, S.; Serroni, S. *Chem. Rev.* **1996**, *96*, 759.
6. Steel, P. J. *Coord. Chem. Rev.* **1990**, *106*, 227.
7. Ballardini, R.; Balzani, V.; Credi, A.; Gandolfi, M. T.; Venturi, M. *Acc. Chem. Res.* **2001**, *34*, 445.
8. Balzani, V.; Ceroni, P.; Juris, A.; Venturi, M.; Campagna, S.; Puntoriero, F.; Serroni, S. *Coord. Chem. Rev.* **2001**, *219*, 545.
9. Burstall, F. H. *J. Chem. Soc.* **1936**, 173.
10. Juris, A.; Balzani, V.; Barigelletti, F.; Campagna, S.; Belser, P.; Von Zelewsky, A. *Coord. Chem. Rev.* **1988**, *84*, 85.
11. Balzani, V.; Campagna, S.; Denti, G.; Juris, A.; Serroni, S.; Venturi, M. *Acc. Chem. Res.* **1998**, *31*, 26.
12. Fuchs, Y.; Lofters, S.; Dieter, T.; Shi, W.; Morgan, R.; Streckas, T. C.; Gafney, H. D.; Baker, A. D. *J. Am. Chem. Soc.* **1987**, *109*, 2691.
13. Braunstein, C. H.; Baker, A. D.; Streckas, T. C.; Gafney, H. D. *Inorg. Chem.* **1984**, *23*, 857.
14. Brewer, K. J.; Murphy, W. R.; Spurlin, S. R.; Petersen, J. D. *Inorg. Chem.* **1986**, *25*, 882.
15. Brauns, E.; Jones, S. W.; Clark, J. A.; Molnar, S. M.; Kawanishi, Y.; Brewer, K. J. *Inorg. Chem.* **1997**, *36*, 2861.
16. Richter, M. M.; Brewer, K. J. *Inorg. Chim. Acta* **1991**, *180*, 125.
17. Berger, R. M. *Inorg. Chem.* **1990**, *29*, 1920.
18. Rillema, D. P.; Mack, K. B. *Inorg. Chem.* **1982**, *21*, 3849.
19. Rillema, D. P.; Taghdiri, D. G.; Jones, D. S.; Keller, C. D.; Worl, L. A.; Meyer, T. J.; Levy, H. A. *Inorg. Chem.* **1987**, *26*, 578.
20. Cooper, J. B.; MacQueen, D. B.; Petersen, J. D.; Wertz, D. W. *Inorg. Chem.* **1990**, *29*, 3701.
21. Richter, M. M.; Brewer, K. J. *Inorg. Chem.* **1993**, *32*, 2827.
22. Milkevitch, M.; Storrie, H.; Brauns, E.; Brewer, K. J.; Shirley, B. W. *Inorg. Chem.* **1997**, *36*, 4534.
23. Yam, V. W. W.; Lee, W. K.; Cheung, K. K.; Lee, H. J.; Leung, W. P. *J. Chem. Soc., Dalton Trans.* **1996**, 2889.
24. Yam, V. W. W.; Lee, W. K.; Cheung, K. K. *J. Chem. Soc., Dalton Trans.* **1996**, 2335.
25. Yam, V. W. W.; Wong, K. M. C.; Lee, V. W. M.; Lo, K. K. W.; Cheung, K. K. *Organometallics* **1995**, *14*, 4034.
26. Yam, V. W. W.; Lee, V. W. M.; Cheung, K. K. *J. Chem. Soc., Chem. Commun.* **1995**, 801.
27. Richter, M. M. *Ph.D. Thesis: Spectroscopic, electrochemical and spectroelectrochemical investigations of mono-, bi- and tri-metallic Os(II)/Ru(II) and Os(II)/Os(II) complexes incorporating polyazine bridging ligands; Virginia Tech: Blacksburg* **1993**.
28. Yam, V. W. W.; Lee, V. W. M.; Cheung, K. K. *Organometallics* **1997**, *16*, 2833.
29. Yam, V. W. W.; Lee, V. W. M.; Cheung, K. K. *J. Chem. Soc., Dalton Trans.* **1997**, 2335.
30. Zigler, D. F.; Mongelli, M. T.; Jeletic, M.; Brewer, K. J. *Inorg. Chem. Commun.* **2007**, *10*, 295.
31. Miao, R.; Zigler, D. F.; Mongelli, M. T.; Winkel, B. S. J.; Brewer, K. J. *submitted to Inorganic Chemistry*

2007.

32. Miao, R.; Zigler, D. F.; Brewer, K. J. *Submitted to Inorganic Chemistry* **2007**.
33. Miao, R.; Brewer, K. J. *Inorg. Chem. Commun.* **2007**, *10*, 307.
34. Miao, R.; Mongelli, M. T.; Zigler, D. F.; Winkel, B. S. J.; Brewer, K. J. *Inorg. Chem.* **2006**, *45*, 10413.
35. Argazzi, R.; Iha, N. Y. M.; Zabri, H.; Odobel, F.; Bignozzi, C. A. *Coord. Chem. Rev.* **2004**, *248*, 1299.
36. Richter, M. M.; Brewer, K. J. *Inorg. Chem.* **1993**, *32*, 5762.
37. Armaroli, N. *Chem. Soc. Rev.* **2001**, *30*, 113.
38. Olenyuk, B.; Whiteford, J. A.; Fechtenkotter, A.; Stang, P. J. *Nature* **1999**, *398*, 796.
39. Seidel, S. R.; Stang, P. J. *Acc. Chem. Res.* **2002**, *35*, 972.
40. Stang, P. J.; Olenyuk, B. *Acc. Chem. Res.* **1997**, *30*, 502.
41. Clarke, M. J. *Coord. Chem. Rev.* **2002**, *232*, 69.
42. Avijita, J.; Winkel, B. S. J.; Brewer, K. J. *Inorg. Biochem.* **2007**, *101*, 1525.
43. Williams, R. L.; Toft, H. N.; Winkel, B.; Brewer, K. J. *Inorg. Chem.* **2003**, *42*, 4394.
44. Cohen, G. L.; Ledner, J. A.; Bauer, W. R.; Ushay, H. M.; Caravana, C.; Lippard, S. J. *J. Am. Chem. Soc.* **1980**, *102*, 2487.
45. Cohen, G. L.; Bauer, W. R.; Barton, J. K.; Lippard, S. J. *Science* **1979**, *203*, 1014.
46. Lippard, S. J.; Bond, P. J.; Wu, K. C.; Bauer, W. R. *Science* **1976**, *194*, 726.
47. Howe-Grant, M.; Wu, K. C.; Bauer, W. R.; Lippard, S. J. *Biochemistry* **1976**, *15*, 4339.
48. Roecker, L.; Kutner, W.; Gilbert, J. A.; Simmons, M.; Murray, R. W.; Meyer, T. J. *Inorg. Chem.* **1985**, *24*, 3784.
49. Denti, G.; Serroni, S.; Campagna, S.; Ricevuto, V.; Juris, A.; Ciano, M.; Balzani, V. *Inorg. Chim. Acta* **1992**, *200*, 507.
50. Winkler, J. R.; Netzel, T. L.; Creutz, C.; Sutin, N. *J. Am. Chem. Soc.* **1987**, *109*, 2381.
51. Marcaccio, M.; Paolucci, F.; Paradisi, C.; Carano, M.; Roffia, S.; Fontanesi, C.; Yellowlees, L. J.; Serroni, S.; Campagna, S.; Balzani, V. *J. Electroanal. Chem.* **2002**, *532*, 99.
52. Marcaccio, M.; Paolucci, F.; Paradisi, C.; Roffia, S.; Fontanesi, C.; Yellowlees, L. J.; Serroni, S.; Campagna, S.; Denti, G.; Balzani, V. *J. Am. Chem. Soc.* **1999**, *121*, 10081.
53. Denti, G.; Campagna, S.; Serroni, S.; Ciano, M.; Balzani, V. *J. Am. Chem. Soc.* **1992**, *114*, 2944.
54. Serroni, S.; Juris, A.; Campagna, S.; Venturi, M.; Denti, G.; Balzani, V. *J. Am. Chem. Soc.* **1994**, *116*, 9086.
55. Rasmussen, S. C.; Richter, M. M.; Yi, E.; Place, H.; Brewer, K. J. *Inorg. Chem.* **1990**, *29*, 3926.
56. Campagna, S.; Denti, G.; Sabatino, L.; Serroni, S.; Ciano, M.; Balzani, V. *J. Chem. Soc., Chem. Commun.* **1989**, 1500.
57. Serroni, S.; Denti, G.; Campagna, S.; Juris, A.; Ciano, M.; Balzani, V. *Angew Chem Int Edit* **1992**, *31*, 1493.
58. Campagna, S.; Denti, G.; Serroni, S.; Juris, A.; Venturi, M.; Ricevuto, V.; Balzani, V. *Chem. Eur. J.* **1995**, *1*, 211.
59. Serroni, S.; Denti, G. *Inorg. Chem.* **1992**, *31*, 4251.
60. Kalyanasundaram, K. *Coord. Chem. Rev.* **1982**, *46*, 159.
61. Molnar, S. M.; Neville, K. R.; Jensen, G. E.; Brewer, K. J. *Inorg. Chim. Acta* **1993**, *206*, 69.
62. Sherborne, J.; Scott, S. M.; Gordon, K. C. *Inorg. Chim. Acta* **1997**, *260*, 199.
63. Allen, G. H.; White, R. P.; Rillema, D. P.; Meyer, T. J. *J. Am. Chem. Soc.* **1984**, *106*, 2613.
64. Caspar, J. V.; Kober, E. M.; Sullivan, B. P.; Meyer, T. J. *J. Am. Chem. Soc.* **1982**, *104*, 630.
65. Caspar, J. V.; Meyer, T. J. *Inorg. Chem.* **1983**, *22*, 2444.
66. Caspar, J. V.; Meyer, T. J. *J. Am. Chem. Soc.* **1983**, *105*, 5583.
67. Richter, M. M.; Brewer, K. J. *Inorg. Chem.* **1992**, *31*, 1594.

68. Anderson, P. A.; Keene, F. R.; Meyer, T. J.; Moss, J. A.; Strouse, G. F.; Treadway, J. A. *J. Chem. Soc., Dalton Trans.* **2002**, 3820.
69. Kober, E. M.; Marshall, J. L.; Dressick, W. J.; Sullivan, B. P.; Caspar, J. V.; Meyer, T. J. *Inorg. Chem.* **1985**, *24*, 2755.
70. Rillema, D. P.; Allen, G.; Meyer, T. J.; Conrad, D. *Inorg. Chem.* **1983**, *22*, 1617.
71. Caspar, J. V.; Sullivan, B. P.; Meyer, T. J. *Inorg. Chem.* **1984**, *23*, 2104.
72. Sullivan, B. P.; Salmon, D. J.; Meyer, T. J. *Inorg. Chem.* **1978**, *17*, 3334.
73. Vlcek, A. A.; Dodsworth, E. S.; Pietro, W. J.; Lever, A. B. P. *Inorg. Chem.* **1995**, *34*, 1906.
74. Dodsworth, E. S.; Lever, A. B. P. *Chem. Phys. Lett.* **1984**, *112*, 567.
75. Curtis, J. C.; Sullivan, B. P.; Meyer, T. J. *Inorg. Chem.* **1983**, *22*, 224.
76. Wallace, A. W.; Murphy, W. R.; Petersen, J. D. *Inorg. Chim. Acta* **1989**, *166*, 47.
77. Kalyanasundaram, K.; Nazeeruddin, M. K. *Inorg. Chem.* **1990**, *29*, 1888.
78. Denti, G.; Campagna, S.; Sabatino, L.; Serrni, S.; Ciano, M.; Balzani, V. *Inorg. Chem.* **1990**, *29*, 4750.
79. Treadway, J. A.; Strouse, G. F.; Ruminski, R. R.; Meyer, T. J. *Inorg. Chem.* **2001**, *40*, 4508.
80. Juris, A.; Balzani, V.; Campagna, S.; Denti, G.; Serroni, S.; Frei, G.; Gudel, H. U. *Inorg. Chem.* **1994**, *33*, 1491.
81. Puntoriero, F.; Serroni, S.; Galletta, M.; Juris, A.; Licciardello, A.; Chiorboli, C.; Campagna, S.; Scandola, F. *ChemPhysChem* **2005**, *6*, 129.
82. Baudin, H. B.; Davidsson, J.; Serroni, S.; Juris, A.; Balzani, V.; Campagna, S.; Hammarstrom, L. *J. Phys. Chem. A* **2002**, *106*, 4312.
83. Campagna, S.; Denti, G.; Serroni, S.; Ciano, M.; Balzani, V. *Inorg. Chem.* **1991**, *30*, 3728.
84. Chiorboli, C.; Fracasso, S.; Ravaglia, M.; Scandola, F.; Campagna, S.; Wouters, K. L.; Konduri, R.; MacDonnell, F. M. *Inorg. Chem.* **2005**, *44*, 8368.
85. Chiorboli, C.; Fracasso, S.; Scandola, F.; Campagna, S.; Serroni, S.; Konduri, R.; MacDonnell, F. M. *Chem. Commun.* **2003**, 1658.
86. Konduri, R.; Ye, H. W.; MacDonnell, F. M.; Serroni, S.; Campagna, S.; Rajeshwar, K. *Angew. Chem. Int. Ed. Engl.* **2002**, *41*, 3185.
87. Campagna, S.; Serroni, S.; Puntoriero, F.; Loiseau, F.; De Cola, L.; Kleverlaan, C. L.; Becher, J.; Sorensen, A. P.; Hascoat, P.; Thorup, N. *Chem. Eur. J.* **2002**, *8*, 4461.
88. Kleverlaan, C.; Alebbi, M.; Argazzi, R.; Bignozzi, C. A.; Hasselmann, G. N.; Meyer, G. J. *Inorg. Chem.* **2000**, *39*, 1342.
89. Boerner, L. J. K.; Zaleski, J. M. *Curr. Opin. Chem. Biol.* **2005**, *9*, 135.
90. Zhang, C. X.; Lippard, S. J. *Curr. Opin. Chem. Biol.* **2003**, *7*, 481.
91. Goldstein, B. M.; Barton, J. K.; Berman, H. M. *Inorg. Chem.* **1986**, *25*, 842.
92. Barton, J. K.; Kumar, C. V.; Turro, N. J. *J. Am. Chem. Soc.* **1986**, *108*, 6391.
93. Delaney, S.; Pascaly, M.; Bhattacharya, P. K.; Han, K.; Barton, J. K. *Inorg. Chem.* **2002**, *41*, 1966.
94. Kumar, C. V.; Barton, J. K.; Turro, N. J. *J. Am. Chem. Soc.* **1985**, *107*, 5518.
95. Demas, J. N.; Harris, E. W.; Flynn, C. M.; Diemente, D. *J. Am. Chem. Soc.* **1975**, *97*, 3838.
96. Hergueta-Bravo, A.; Jimenez-Hernandez, M. E.; Montero, F.; Oliveros, E.; Orellana, G. J. *Phys. Chem. B* **2002**, *106*, 4010.
97. Erkkila, K. E.; Odom, D. T.; Barton, J. K. *Chem. Rev.* **1999**, *99*, 2777.
98. Fleisher, M. B.; Waterman, K. C.; Turro, N. J.; Barton, J. K. *Inorg. Chem.* **1986**, *25*, 3549.
99. Rosenberg, B.; Van Camp, L.; Krigas, T. *Nature* **1965**, *205*, 698.
100. Milkevitch, M.; Brauns, E.; Brewer, K. J. *Inorg. Chem.* **1996**, *35*, 1737.

101. Yam, V. W. W.; Lee, V. W. M.; Cheung, K. K. *J. Chem. Soc., Chem. Commun.* **1994**, 2075.
102. Sommovigo, M.; Denti, G.; Serroni, S.; Campagna, S.; Mingazzini, C.; Mariotti, C.; Juris, A. *Inorg. Chem.* **2001**, *40*, 3318.
103. Sakai, K.; Ozawa, H.; Yamada, H.; Tsubomura, T.; Hara, M.; Higuchi, A.; Haga, A. *Dalton Trans.* **2006**, 3300.
104. Jamieson, E. R.; Lippard, S. J. *Chem. Rev.* **1999**, *99*, 2467.
105. Sharman, W. M.; Allen, C. M.; van Lier, J. E. *Drug Discov. Today* **1999**, *4*, 507.
106. Yavin, E.; Stemp, E. D. A.; Weiner, L.; Sagi, I.; Arad-Yellin, R.; Shanzer, A. *J. Inorg. Biochem.* **2004**, *98*, 1750.
107. Dempsey, J. L.; Esswein, A. J.; Manke, D. R.; Rosenthal, J.; Soper, J. D.; Nocera, D. G. *Inorg. Chem.* **2005**, *44*, 6879.
108. Rosenthal, J.; Bachman, J.; Dempsey, J. L.; Esswein, A. J.; Gray, T. G.; Hodgkiss, J. M.; Manke, D. R.; Lockett, T. D.; Pistorio, B. J.; Veige, A. S.; Nocera, D. G. *Coord. Chem. Rev.* **2005**, *249*, 1316.
109. Bard, A. J.; Fox, M. A. *Acc. Chem. Res.* **1995**, *28*, 141.
110. Du, P. W.; Schneider, J.; Jarosz, P.; Eisenberg, R. *J. Am. Chem. Soc.* **2006**, *128*, 7726.
111. Heyduk, A. F.; Nocera, D. G. *Science* **2001**, *293*, 1639.
112. Gray, T. G.; Nocera, D. G. *Chem. Commun.* **2005**, 1540.
113. Esswein, A. J.; Veige, A. S.; Nocera, D. G. *J. Am. Chem. Soc.* **2005**, *127*, 16641.
114. Ozawa, H.; Yokoyama, Y.; Haga, M.; Sakai, K. *Dalton Trans.* **2007**, 1197.
115. Ozawa, H.; Haga, M. A.; Sakai, K. *J. Am. Chem. Soc.* **2006**, *128*, 4926.
116. Rau, S.; Schafer, B.; Gleich, D.; Anders, E.; Rudolph, M.; Friedrich, M.; Gorls, H.; Henry, W.; Vos, J. G. *Angew. Chem. Int. Ed. Engl.* **2006**, *45*, 6215.
117. Lei, P.; Hedlund, M.; Lomoth, R.; Rensmo, H.; Johansson, O.; Hammarstrom, L. *J. Am. Chem. Soc.* **2008**, *130*, 26.
118. Elvington, M.; Brown, J. R.; Zigler, D. F.; Brewer, K. J. *Proc. of SPIE* **2006**, *6340*, 63400W.
119. Goodwin, H. A.; Lions, F. *J. Am. Chem. Soc.* **1959**, *81*, 6415.
120. Sahai, R.; Rillema, D. P. *J. Chem. Soc., Chem. Commun.* **1986**, 1133.
121. Brown, J. R.; Elvington, M.; Mongelli, M. T.; Zigler, D. F.; Brewer, K. J. *Proc. of SPIE* **2006**, *6340*, 634017.
122. Brumleve, T. R.; Osteryoung, R. A.; Osteryoung, J. *Analytical Chemistry* **1982**, *54*, 782.
123. Molnar, S. M. *Ph.D. Dissertation: Synthesis and photophysical investigation of supramolecular complexes developed for photoinitiated electron collection* **1996**.
124. Purwanto; Deshpande, R. M.; Chaudhari, R. V.; Delmas, H. *J. Chem. Eng. Data* **1996**, *41*, 1414.
125. Buckingham, D. A.; Dwyer, F. P.; Goodwin, H. A.; Sargeson, A. M. *Aust. J. Chem.* **1964**, *17*, 325.
126. Constable, E. C.; Seddon, K. R. *J. Chem. Soc., Chem. Commun.* **1982**, 34.
127. Kober, E. M.; Meyer, T. J. *Inorg. Chem.* **1983**, *22*, 1614.
128. Puntoriero, F.; Serroni, S.; Licciardello, A.; Venturi, M.; Juris, A.; Ricevuto, V.; Campagna, S. *J. Chem. Soc., Dalton Trans.* **2001**, 1035.
129. Asara, J. M.; Uzelmeier, C. E.; Dunbar, K. R.; Allison, J. *Inorg. Chem.* **1998**, *37*, 1833.
130. Hunsucker, S. W.; Watson, C. R.; Tissue, B. M. *Rapid Commun. Mass Spectrom.* **2001**, *15*, 1334.
131. Liang, X. Q.; Suwanrumpha, S.; Freas, R. B. *Inorg. Chem.* **1991**, *30*, 652.
132. Lou, X.; van Buijtenen, J.; Bastiaansen, J. J. A. M.; de Waal, B. F. M.; Langeveld, B. M. W.; van Dongen, J. L. *J. Mass Spectrom.* **2005**, *40*, 654.
133. Campagna, S.; Serroni, S.; Bodige, S.; MacDonnell, F. M. *Inorg. Chem.* **1999**, *38*, 692.

134. MacDonnell, F. M.; Bodige, S. *Inorg. Chem.* **1996**, *35*, 5758.
135. Berger, R. M.; Mcmillin, D. R. *Inorg. Chem.* **1988**, *27*, 4245.
136. Murphy, W. R.; Brewer, K. J.; Gettliffe, G.; Petersen, J. D. *Inorg. Chem.* **1989**, *28*, 81.
137. Johnson, S. R.; Westmoreland, T. D.; Caspar, J. V.; Barqawi, K. R.; Meyer, T. J. *Inorg. Chem.* **1988**, *27*, 3195.
138. Richter, M. M.; Jensen, G. E.; Brewer, K. J. *Inorg. Chim. Acta* **1995**, *230*, 35.
139. Balzani, V.; Juris, A.; Venturi, M.; Campagna, S.; Serroni, S. *Chem. Rev.* **1996**, *96*, 759.
140. Elvington, M.; Brewer, K. J. *Inorg. Chem.* **2006**, *45*, 5242.
141. Anderson, C. P.; Salmon, D. J.; Meyer, T. J.; Young, R. C. *J. Am. Chem. Soc.* **1977**, *99*, 1980.
142. Galus, Z.; Adams, R. N. *J. Am. Chem. Soc.* **1962**, *84*, 2061.
143. Mizoguchi, T.; Adams, R. N. *J. Am. Chem. Soc.* **1962**, *84*, 2058.
144. Lide, D. R. *Handbook of Chemistry and Physics 88th Edition: CRC Press* **2007-2008**.
145. Elvington, M.; Brown, J.; Arachchige, S. M.; Brewer, K. J. *J. Am. Chem. Soc.* **2007**, *129*, 10644.
146. Kirch, M.; Lehn, J. M.; Sauvage, J. P. *Helvetica Chimica Acta* **1979**, *62*, 1345.
147. Lehn, J. M.; Sauvage, J. P.; Ziessel, R. *Nouveau Journal De Chimie-New Journal of Chemistry* **1981**, *5*, 291.
148. Schwarz, H. A.; Cruetz, C. *Inorg. Chem.* **1983**, *22*, 707.
149. Chou, M.; Creutz, C.; Mahajan, D.; Sutin, N.; Zipp, A. P. *Inorg. Chem.* **1982**, *21*, 3989.
150. Creutz, C.; Keller, A. D.; Sutin, N.; Zipp, A. P. *J. Am. Chem. Soc.* **1982**, *104*, 3618.
151. Zhang, B.; Seki, S.; Akiyama, K.; Tsutsui, K.; Li, T.; Nagao, K. *Acta Med. Okayama* **1992**, *46*, 427.
152. Vinograd, J.; Lebowitz, J. *J. Gen. Physiol.* **1966**, *49*, 103.
153. Friedman, A. E.; Chambron, J. C.; Sauvage, J. P.; Turro, N. J.; Barton, J. K. *J. Am. Chem. Soc.* **1990**, *112*, 4960.
154. Liu, Y.; Chouai, A.; Degtyareva, N. N.; Lutterman, D. A.; Dunbar, K. R.; Turro, C. *J. Am. Chem. Soc.* **2005**, *127*, 10796.
155. Holmlin, R. E.; Barton, J. K. *Inorg. Chem.* **1995**, *34*, 7.
156. Elvington, M.; Brewer, K. J. *Inorg. Chem.* **2006**, *45*, 5242.

Appendix

Table of Contents

Table of Contents	134
Figure A.1 400 MHz ¹ H NMR of [(bpy) ₂ Ru(dpp)](PF ₆) ₂ in CD ₃ CN	136
Figure A.2 400 MHz ¹ H NMR of [(bpy) ₂ Os(dpp)](PF ₆) ₂ in CD ₃ CN	136
Figure A.3 400 MHz ¹ H NMR of [{(bpy) ₂ Os(dpp)} ₂ Ru(dpq)](PF ₆) ₆ in DMSO	137
Figure A.4 400 MHz ¹ H NMR of [{(bpy) ₂ Ru(dpp)} ₂ Ru(dpp)](PF ₆) ₆ in DMSO	137
Figure A.5 400 MHz ¹ H NMR of [{{(bpy) ₂ Os(dpp)} ₂ Ru} ₂ (dpq)](PF ₆) ₁₂ in DMSO	138
Figure A.6 Cyclic voltammogram of the tetrametallic complex	139
[{{(bpy) ₂ Ru(dpp)} ₂ Ru(dpp)PtCl ₂](PF ₆) ₆ and the trimetallic complex	
[{{(bpy) ₂ Ru(dpp)} ₂ Ru(dpp)](PF ₆) ₆	
Figure A.7 Cyclic voltammogram of the trimetallic complex	140
[{{(bpy) ₂ Ru(dpp)} ₂ Ru(dpq)](PF ₆) ₆ and the tetrametallic complex	
[{{(bpy) ₂ Ru(dpp)} ₂ Ru(dpq)PtCl ₂](PF ₆) ₆	
Figure A.8 Electronic absorption spectra of [{{(bpy) ₂ Ru(dpp)} ₂ Ru(dpp)](PF ₆) ₆ ,	141
[{{(bpy) ₂ Ru(dpp)} ₂ Ru(dpq)](PF ₆) ₆ and [{{(bpy) ₂ Os(dpp)} ₂ Ru(dpq)](PF ₆) ₆	
Figure A.9 DMA quenching experiments on room temperature emission	141
of the tetrametallic complex [{{(bpy) ₂ Ru(dpp)} ₂ Ru(dpp)PtCl ₂](PF ₆) ₆	
Figure A.10 DMA quenching experiments on room temperature emission	142
of the tetrametallic complex [{{(bpy) ₂ Ru(dpp)} ₂ Ru(dpq)PtCl ₂](PF ₆) ₆	
Figure A.11 FAB-MS spectrum of [{{(bpy) ₂ Os(dpp)} ₂ Ru(dpq)](PF ₆) ₆	143
Figure A.12 MALDI-TOF-MS spectrum of [{{(bpy) ₂ Os(dpp)} ₂ Ru(dpq)](PF ₆) ₆	144
Figure A.13 FAB-MS spectrum of [{{(bpy) ₂ Ru(dpp)} ₂ Ru(dpp)](PF ₆) ₆	145
Figure A.14 FAB-MS spectrum of [{{(bpy) ₂ Ru(dpp)} ₂ Ru(dpq)](PF ₆) ₆	146
Figure A.15 FAB-MS spectrum of [{{(bpy) ₂ Os(dpp)} ₂ Ru} ₂ (dpq)](PF ₆) ₁₂	147
Figure A.16 MALDI-TOF-MS spectrum of [{{(bpy) ₂ Os(dpp)} ₂ Ru} ₂ (dpq)](PF ₆) ₁₂	148
Figure A.17 FAB-MS spectrum of [{{(bpy) ₂ Ru(dpp)} ₂ Ru(dpp)PtCl ₂](PF ₆) ₆	149
Figure A.18 MALDI-TOF-MS spectrum of [{{(bpy) ₂ Ru(dpp)} ₂ Ru(dpp)PtCl ₂](PF ₆) ₆	150

Figure A.19 FAB-MS spectrum of $[\{(bpy)_2Ru(dpp)\}_2Ru(dpq)PtCl_2](PF_6)_6$	151
Figure A.20 FAB-MS spectrum of $[\{(bpy)_2Os(dpp)\}_2Ru(dpq)PtCl_2](PF_6)_6$	152

$[(bpy)_2Ru(dpp)](PF_6)_2$ at 400 MHz in CD_3CN

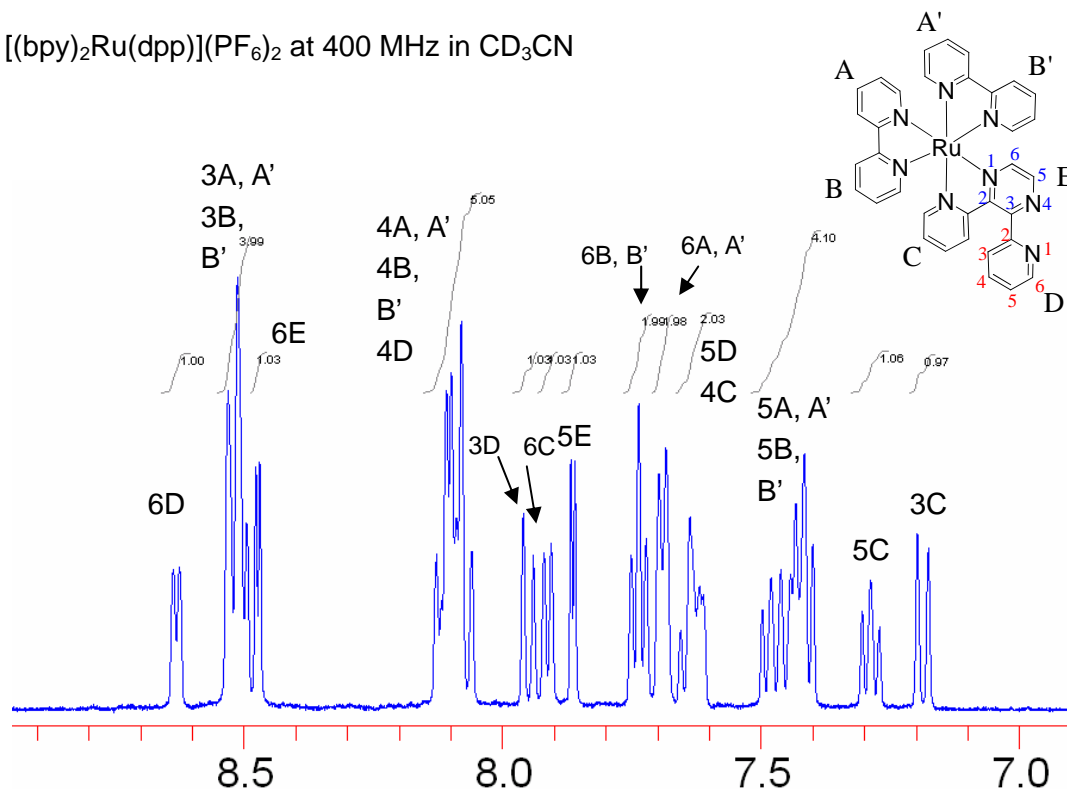


Figure A.1 400 MHz 1H NMR of $[(bpy)_2Ru(dpp)](PF_6)_2$ in CD_3CN (bpy = 2,2'-bipyridine, dpp = 2,3-bis(2-pyridyl)pyrazine).

$[(bpy)_2Os(dpp)](PF_6)_2$ at 400 MHz in CD_3CN

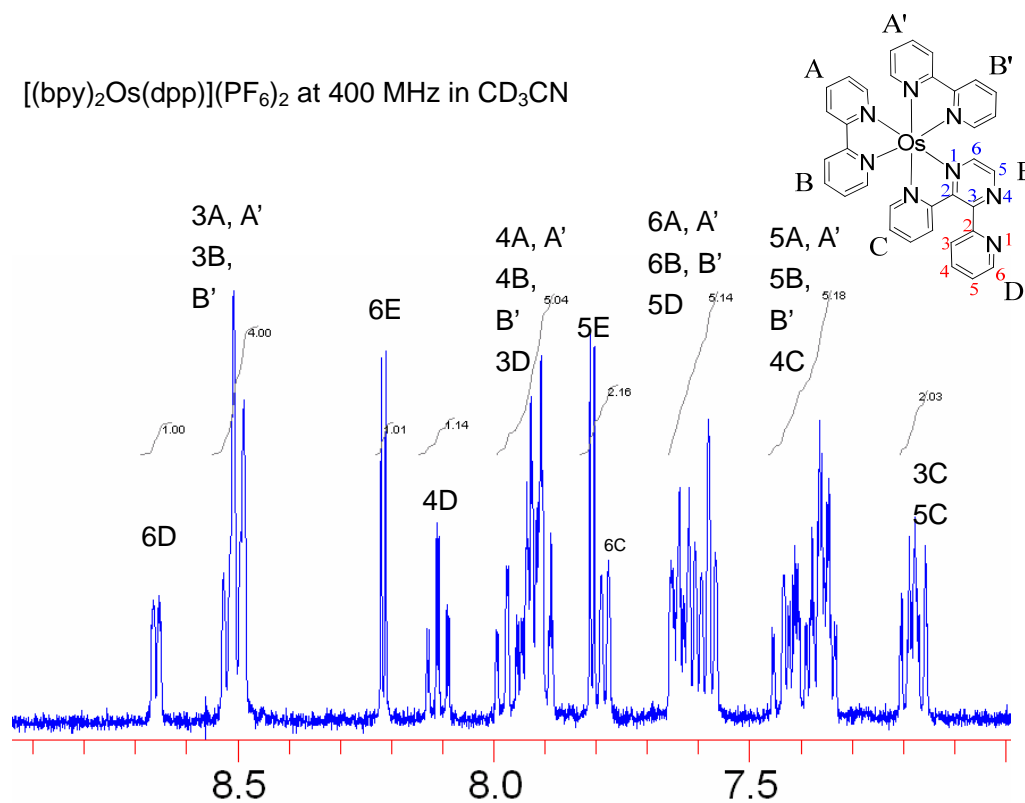


Figure A.2 400 MHz 1H NMR of $[(bpy)_2Os(dpp)](PF_6)_2$ in CD_3CN (bpy = 2,2'-bipyridine, dpp = 2,3-bis(2-pyridyl)pyrazine).

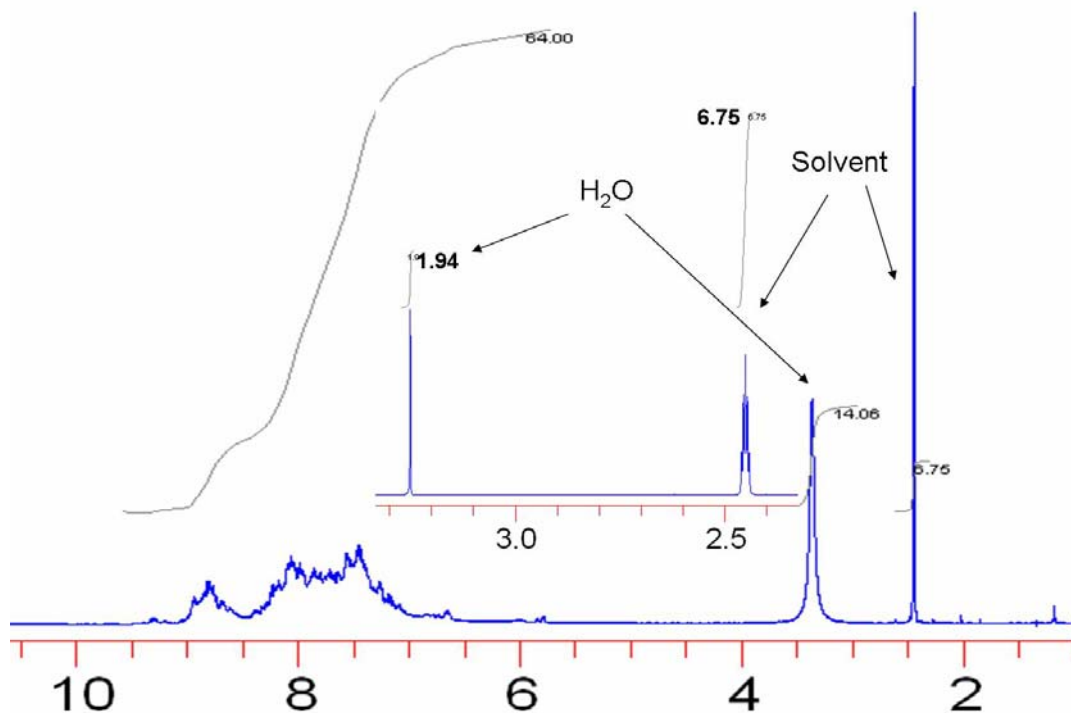


Figure A.3 400 MHz ^1H NMR of $[\{(\text{bpy})_2\text{Os}(\text{dpp})\}_2\text{Ru}(\text{dpq})](\text{PF}_6)_6$ in DMSO (bpy = 2,2'-bipyridine, dpp = 2,3-bis(2-pyridyl)pyrazine and dpq = 2,3-bis(2-pyridyl)quinoxaline). The inserted NMR is the spectrum of DMSO solvent.

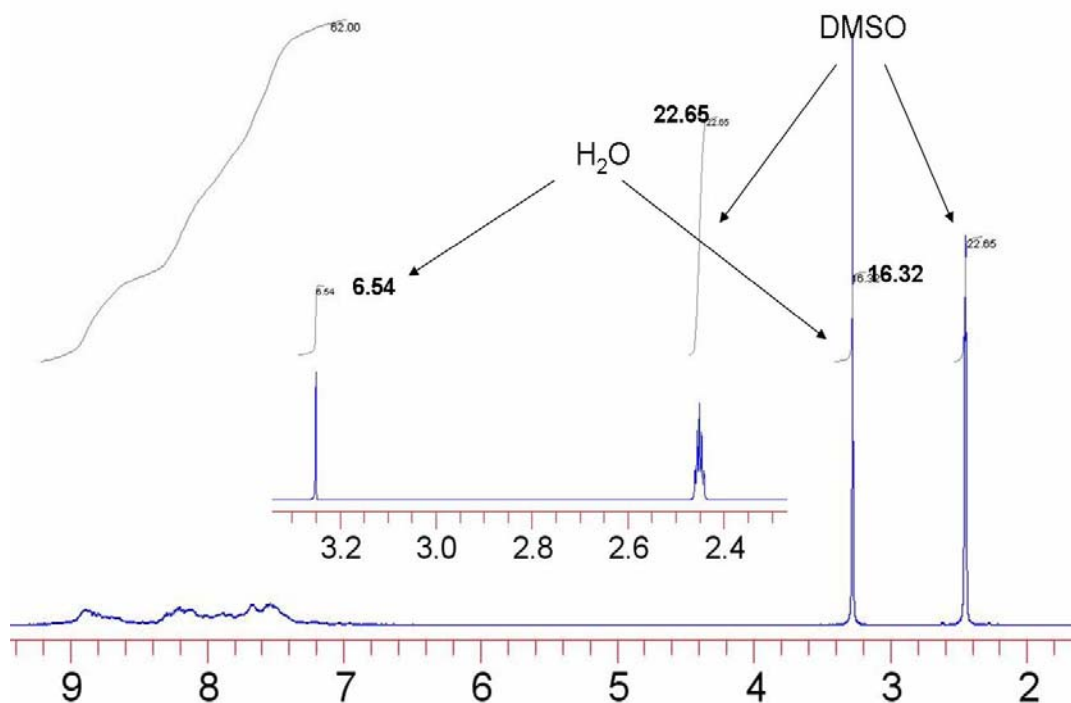


Figure A.4 400 MHz ^1H NMR of $[\{(\text{bpy})_2\text{Ru}(\text{dpp})\}_2\text{Ru}(\text{dpp})](\text{PF}_6)_6$ in DMSO (bpy = 2,2'-bipyridine and dpp = 2,3-bis(2-pyridyl)pyrazine). The inserted NMR is the spectrum of DMSO solvent.

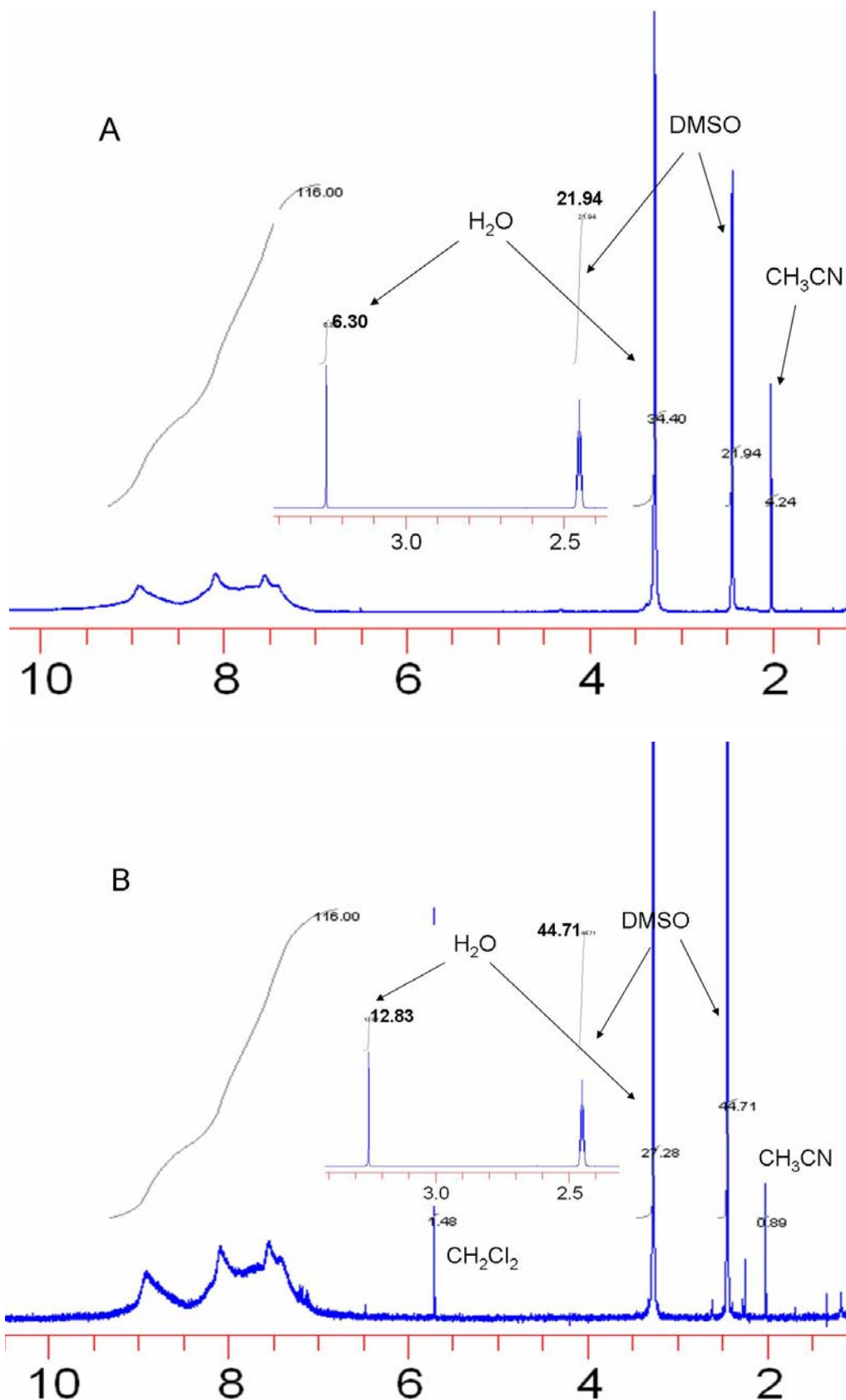


Figure A.5 400 MHz ^1H NMR of $[\{[(\text{bpy})_2\text{Os}(\text{dpp})]_2\text{Ru}\}_2(\text{dpq})](\text{PF}_6)_{12}$ in DMSO (A. B. are spectra from different batches. bpy = 2,2'-bipyridine, dpp = 2,3-bis(2-pyridyl)pyrazine and dpq = 2,3-bis(2-pyridyl)quinoxaline). The inserted NMR is the spectrum of DMSO solvent.

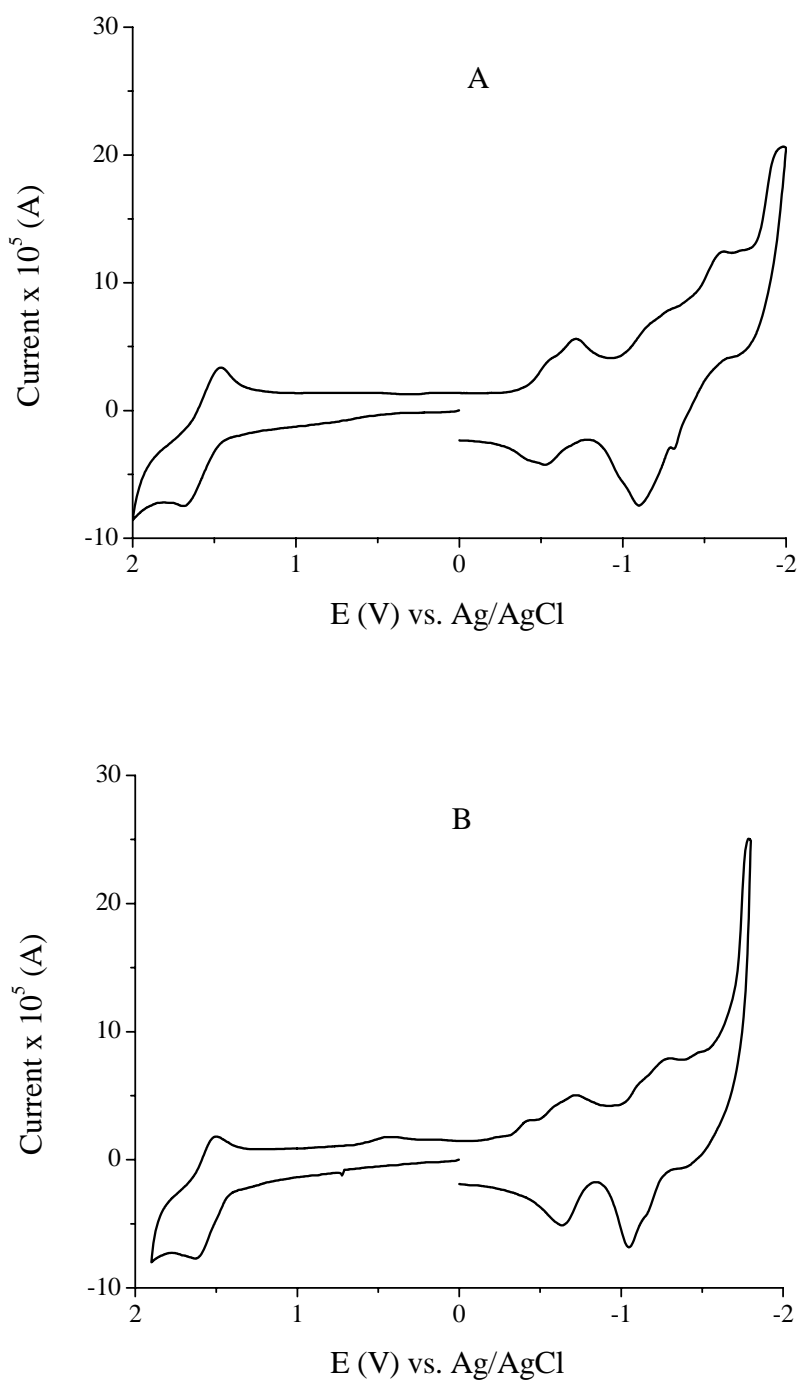


Figure A.6 Cyclic voltammogram of the tetrametallic complex $[\{ (\text{bpy})_2\text{Ru}(\text{dpp}) \}_2\text{Ru}(\text{dpp})\text{PtCl}_2](\text{PF}_6)_6$ (A) and the trimetallic complex $[\{ (\text{bpy})_2\text{Ru}(\text{dpp}) \}_2\text{Ru}(\text{dpp})](\text{PF}_6)_6$ (B) measured in 0.1 M Bu_4NPF_6 CH_3CN solution at room temperature at a scan rate 200 mV/s (potential reported vs. Ag/AgCl; bpy = 2,2'-bipyridine, dpp = 2,3-bis(2-pyridyl)pyrazine).

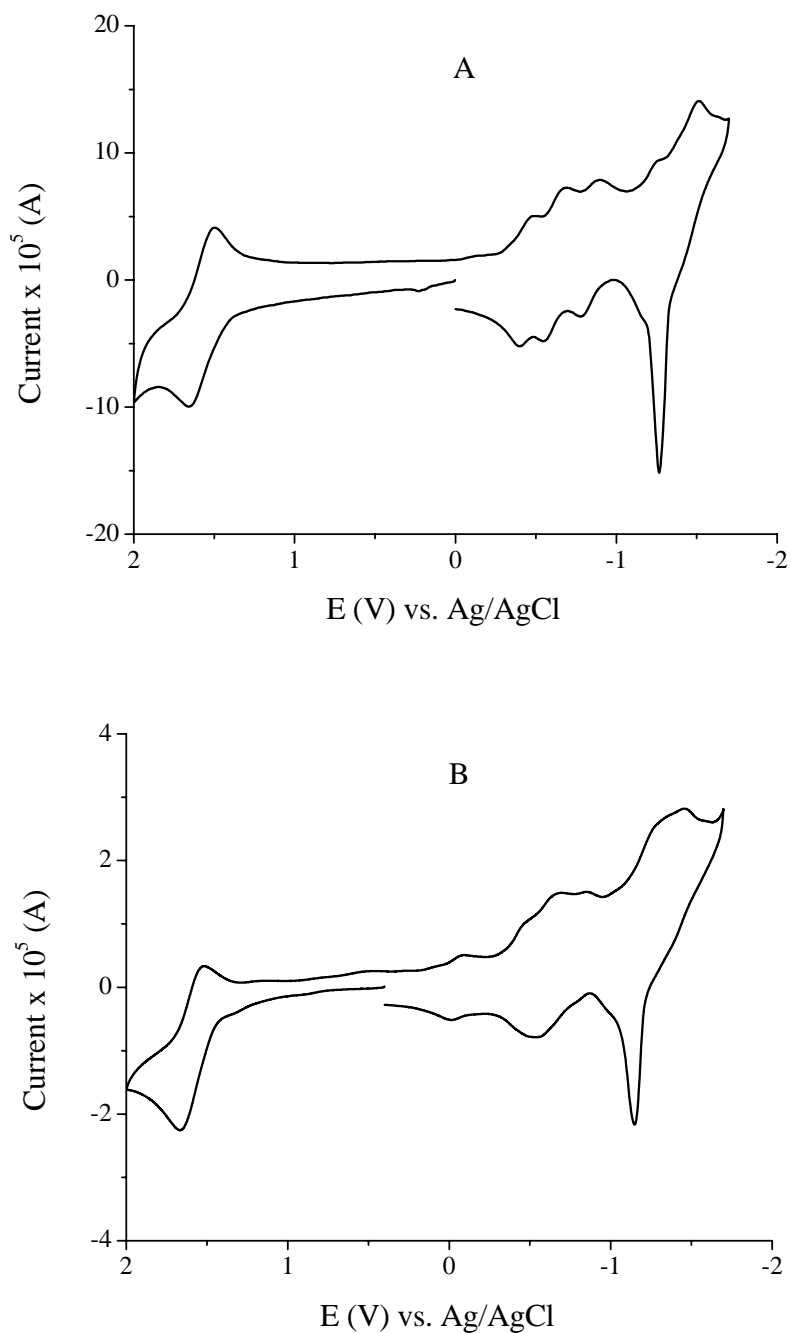


Figure A.7 Cyclic voltammogram of the trimetallic complex $[\{(\text{bpy})_2\text{Ru}(\text{dpp})\}_2\text{Ru}(\text{dpq})](\text{PF}_6)_6$ (A) and the tetrametallic complex $[\{(\text{bpy})_2\text{Ru}(\text{dpp})\}_2\text{Ru}(\text{dpq})\text{PtCl}_2](\text{PF}_6)_6$ (B) measured in 0.1 M Bu_4NPF_6 CH_3CN solution at room temperature at a scan rate 200 mV/s (potential reported vs. Ag/AgCl; bpy = 2,2'-bipyridine, dpp = 2,3-bis(2-pyridyl)pyrazine, dpq = 2,3-bis(2-pyridyl)quinoxaline).

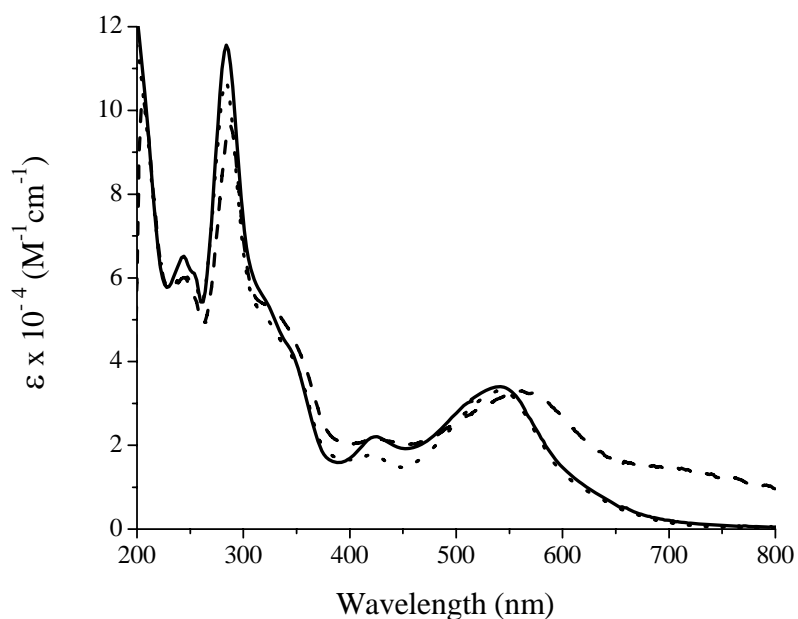


Figure A.8 Electronic absorption spectra of $[\{(\text{bpy})_2\text{Ru}(\text{dpp})\}_2\text{Ru}(\text{dpp})](\text{PF}_6)_6$ (—), $[\{(\text{bpy})_2\text{Ru}(\text{dpp})\}_2\text{Ru}(\text{dpq})](\text{PF}_6)_6$ (⋯), $[\{(\text{bpy})_2\text{Os}(\text{dpp})\}_2\text{Ru}(\text{dpq})](\text{PF}_6)_6$ (---), measured in CH_3CN solvent at room temperature (bpy = 2,2'-bipyridine, dpp = 2,3-bis(2-pyridyl)pyrazine and dpq = 2,3-bis(2-pyridyl)quinoxaline).

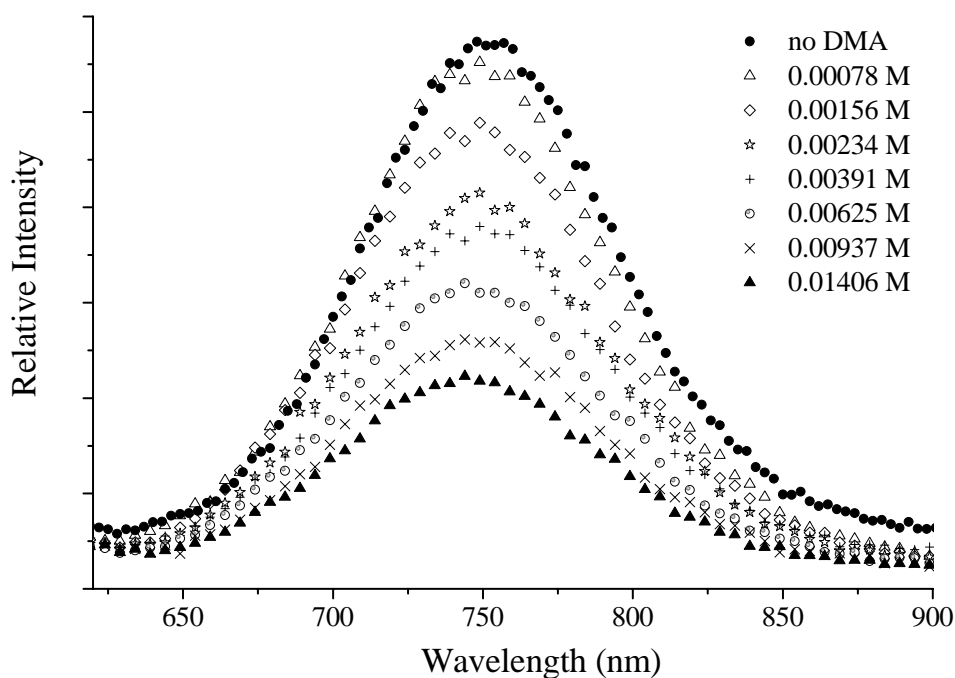


Figure A.9 DMA quenching experiments on room temperature emission of the tetrametallic complex $[\{(\text{bpy})_2\text{Ru}(\text{dpp})\}_2\text{Ru}(\text{dpp})\text{PtCl}_2](\text{PF}_6)_6$ in CH_3CN (bpy = 2,2'-bipyridine, dpp = 2,3-bis(2-pyridyl)pyrazine, dpq = 2,3-bis(2-pyridyl)quinoxaline).

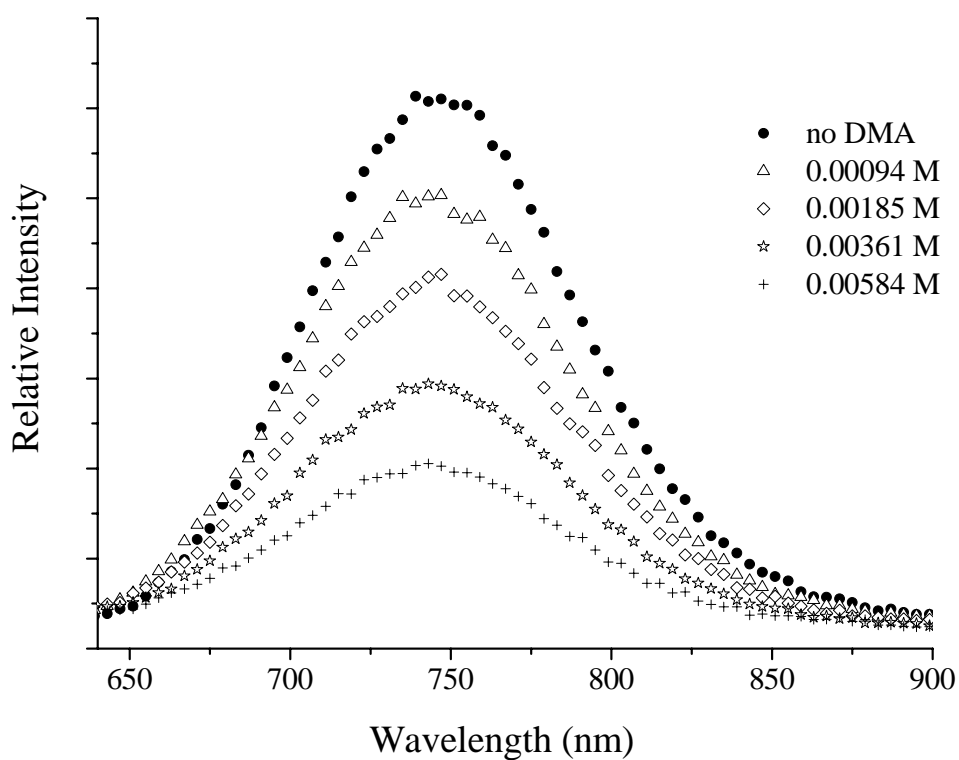


Figure A.10 DMA quenching experiments on room temperature emission of the tetrametallic complex $[\{(bpy)_2Ru(dpp)\}_2Ru(dpq)PtCl_2](PF_6)_6$ in CH_3CN ($bpy = 2,2'$ -bipyridine, $dpp = 2,3$ -bis(2-pyridyl)pyrazine, $dpq = 2,3$ -bis(2-pyridyl)quinoxaline).

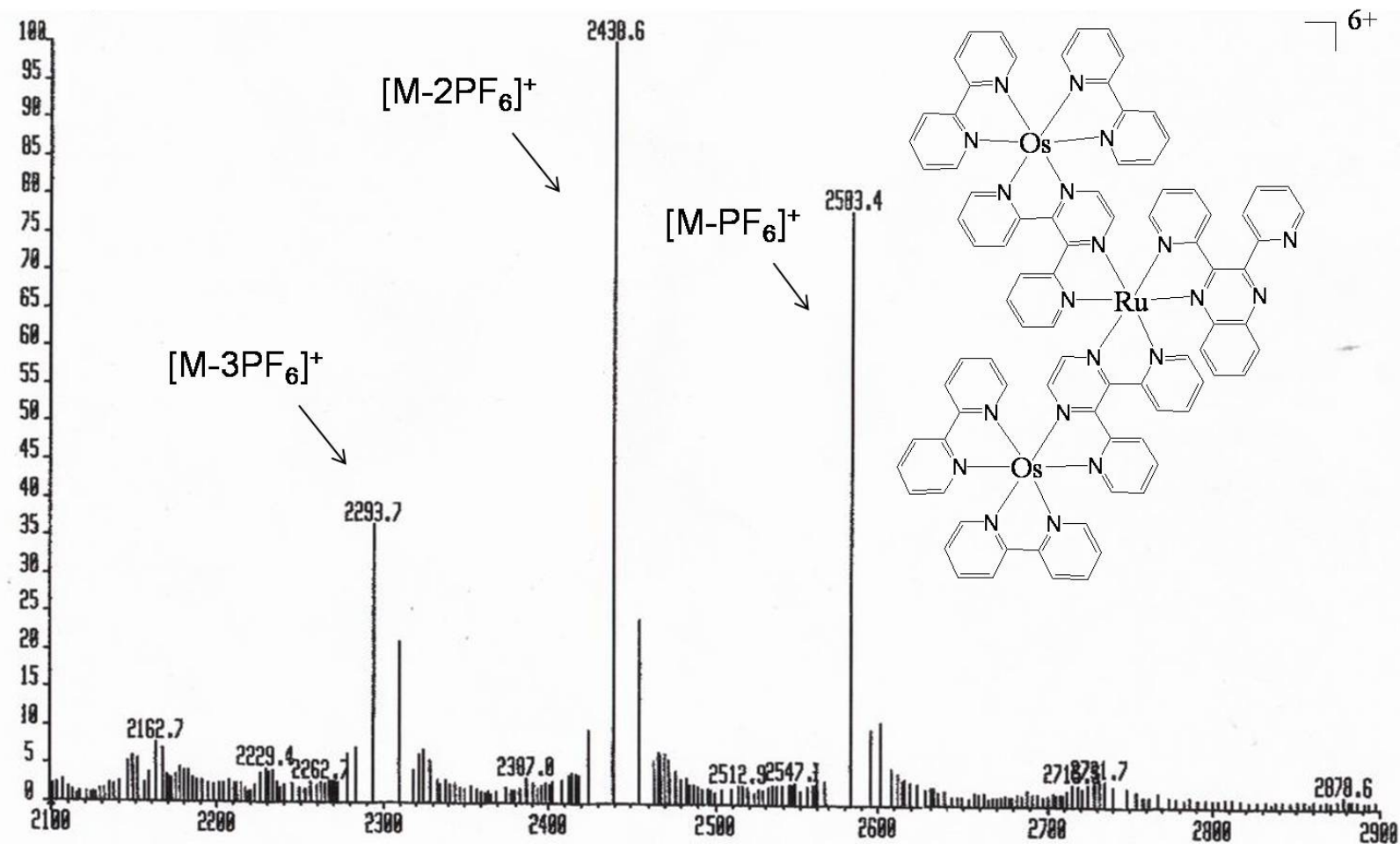


Figure A.11 FAB-MS spectrum of $[\{(bpy)_2Os(dpp)\}_2Ru(dpq)](PF_6)_6$ ($bpy = 2,2'$ -bipyridine, $dpp = 2,3$ -bis(2-pyridyl)pyrazine, $dpq = 2,3$ -bis(2-pyridyl)quinoxaline). (FAB-MS = fast-atom-bombardment mass spectrometry. The FAB-MS was performed on a VG Analytical ZAB 2-SE high field mass spectrometer using *m*-nitrobenzyl alcohol as a matrix).

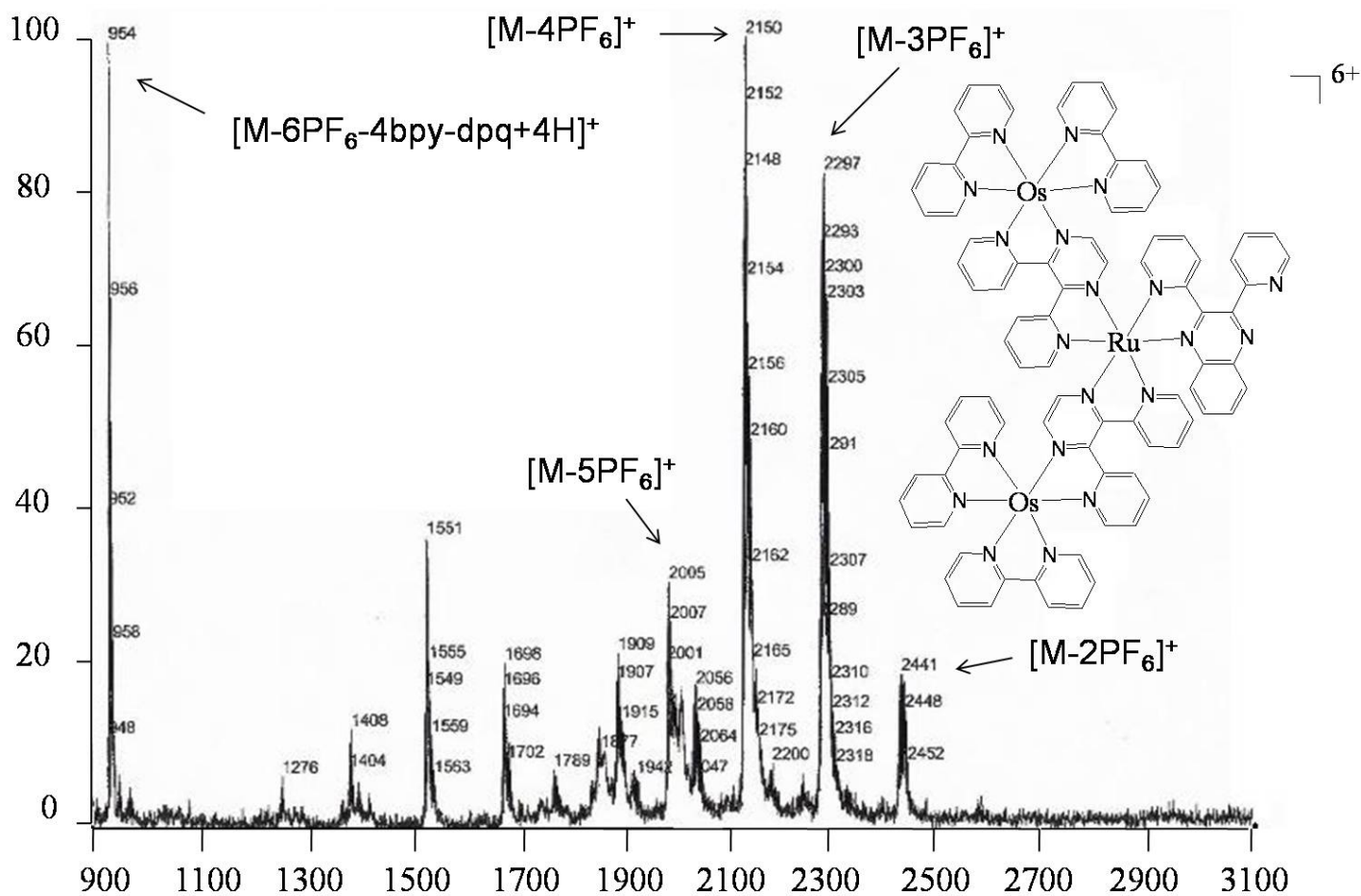


Figure A.12 MALDI-TOF-MS spectrum of $[(bpy)_2Os(dpp)]_2Ru(dpq)(PF_6)_6$ (bpy = 2,2'-bipyridine, dpp = 2,3-bis(2-pyridyl)pyrazine, dpq = 2,3-bis(2-pyridyl)quinoxaline). (MALDI-TOF-MS = matrix-assisted laser desorption/ionization time of flight mass spectrometry. MALDI-TOF MS was performed on an Applied Biosystems Voyager-DE Pro using 2,5-dihydroxybenzoic acid as a matrix and 337 nm as the excitation wavelength).

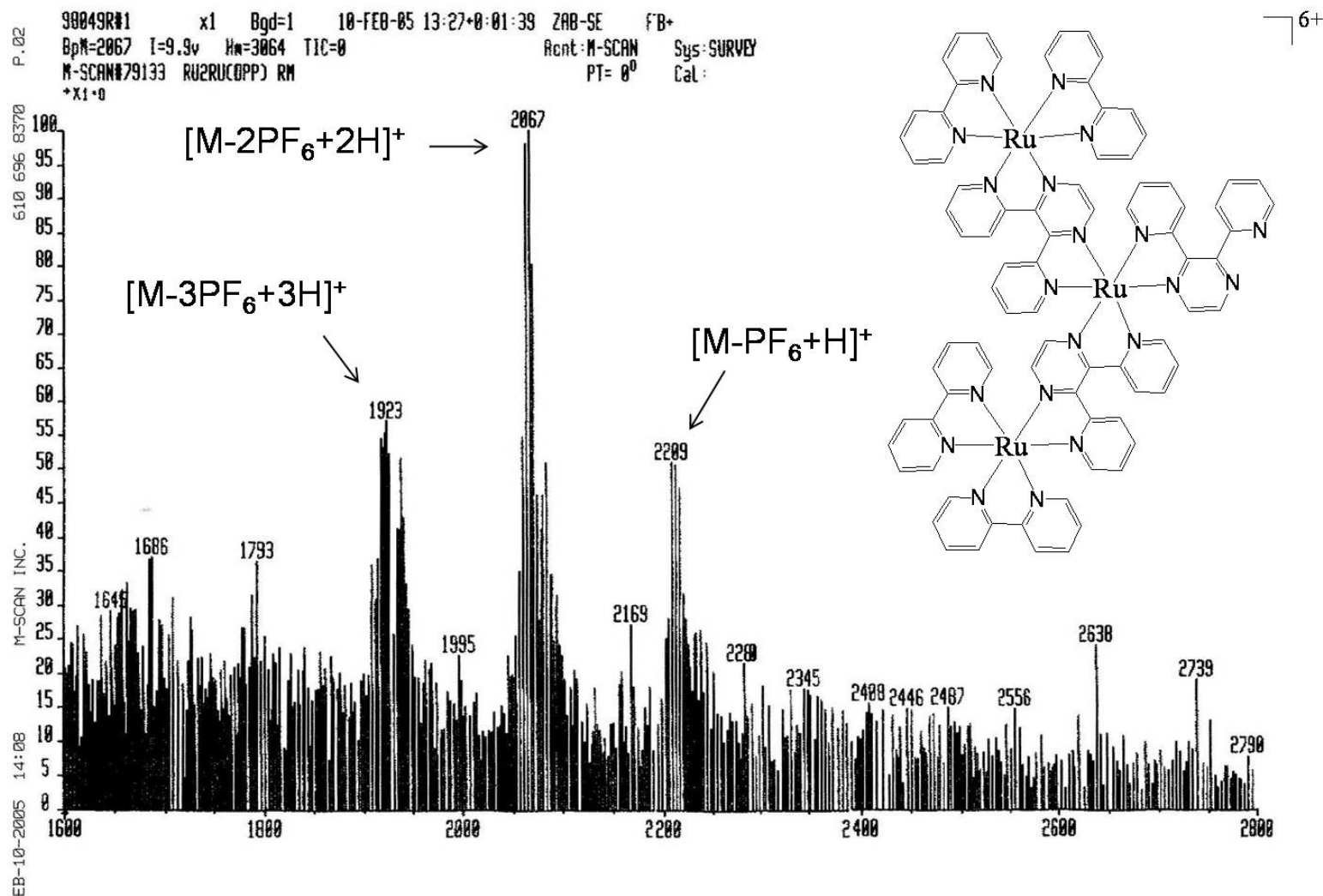


Figure A.13 FAB-MS spectrum of $[\{(bpy)_2Ru(dpp)\}_2Ru(dpp)](PF_6)_6$ ($bpy = 2,2'$ -bipyridine, $dpp = 2,3$ -bis(2-pyridyl)pyrazine). (FAB-MS = fast-atom-bombardment mass spectrometry. The FAB-MS was performed on a VG Analytical ZAB 2-SE high field mass spectrometer using *m*-nitrobenzyl alcohol as a matrix).

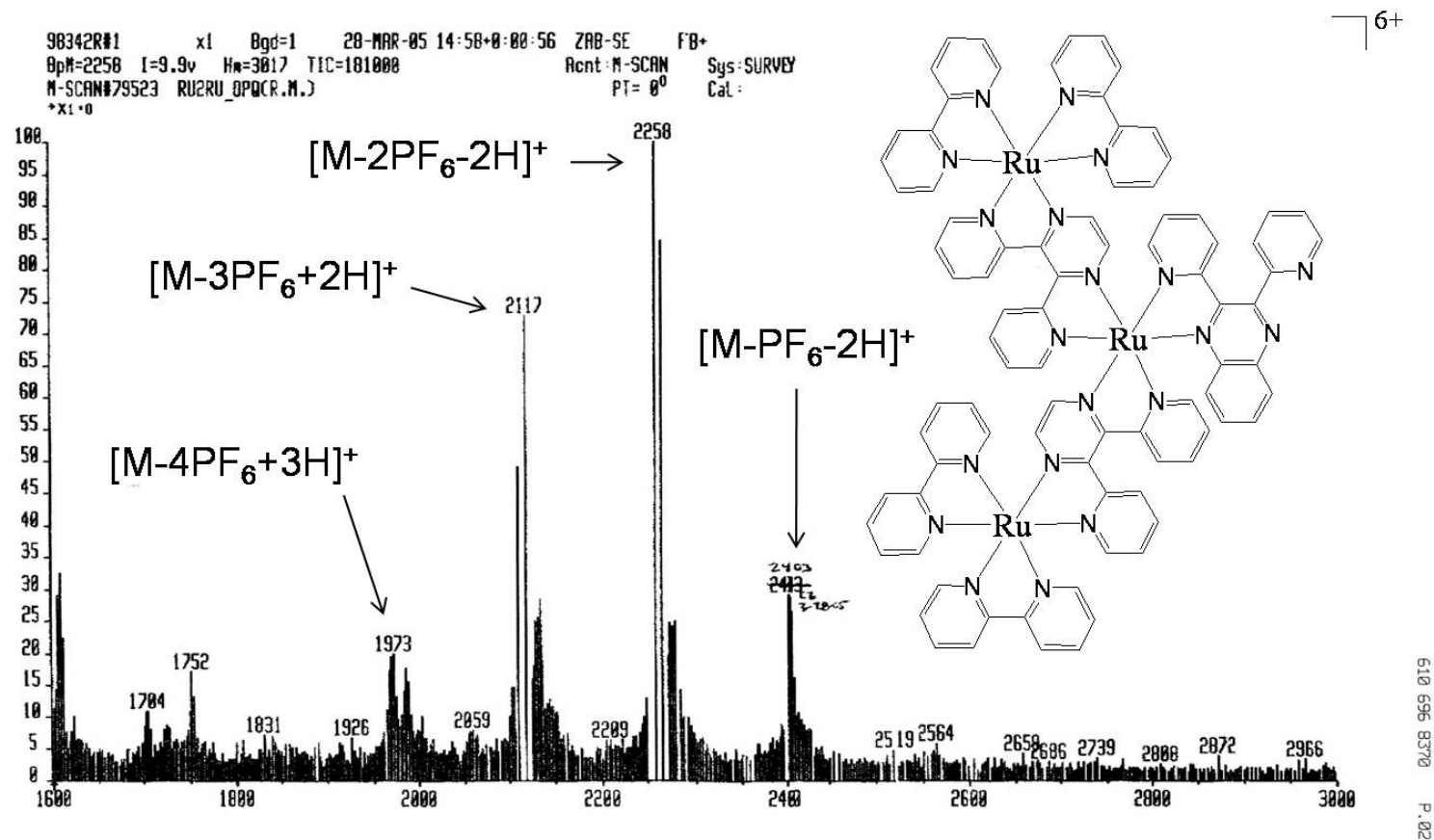


Figure A.14 FAB-MS spectrum of $[\{(bpy)_2Ru(dpp)\}_2Ru(dpq)](PF_6)_6$ ($bpy = 2,2'$ -bipyridine, $dpp = 2,3$ -bis(2-pyridyl)pyrazine, $dpq = 2,3$ -bis(2-pyridyl)quinoxaline). (FAB-MS = fast-atom-bombardment mass spectrometry. The FAB-MS was performed on a VG Analytical ZAB 2-SE high field mass spectrometer using *m*-nitrobenzyl alcohol as a matrix).

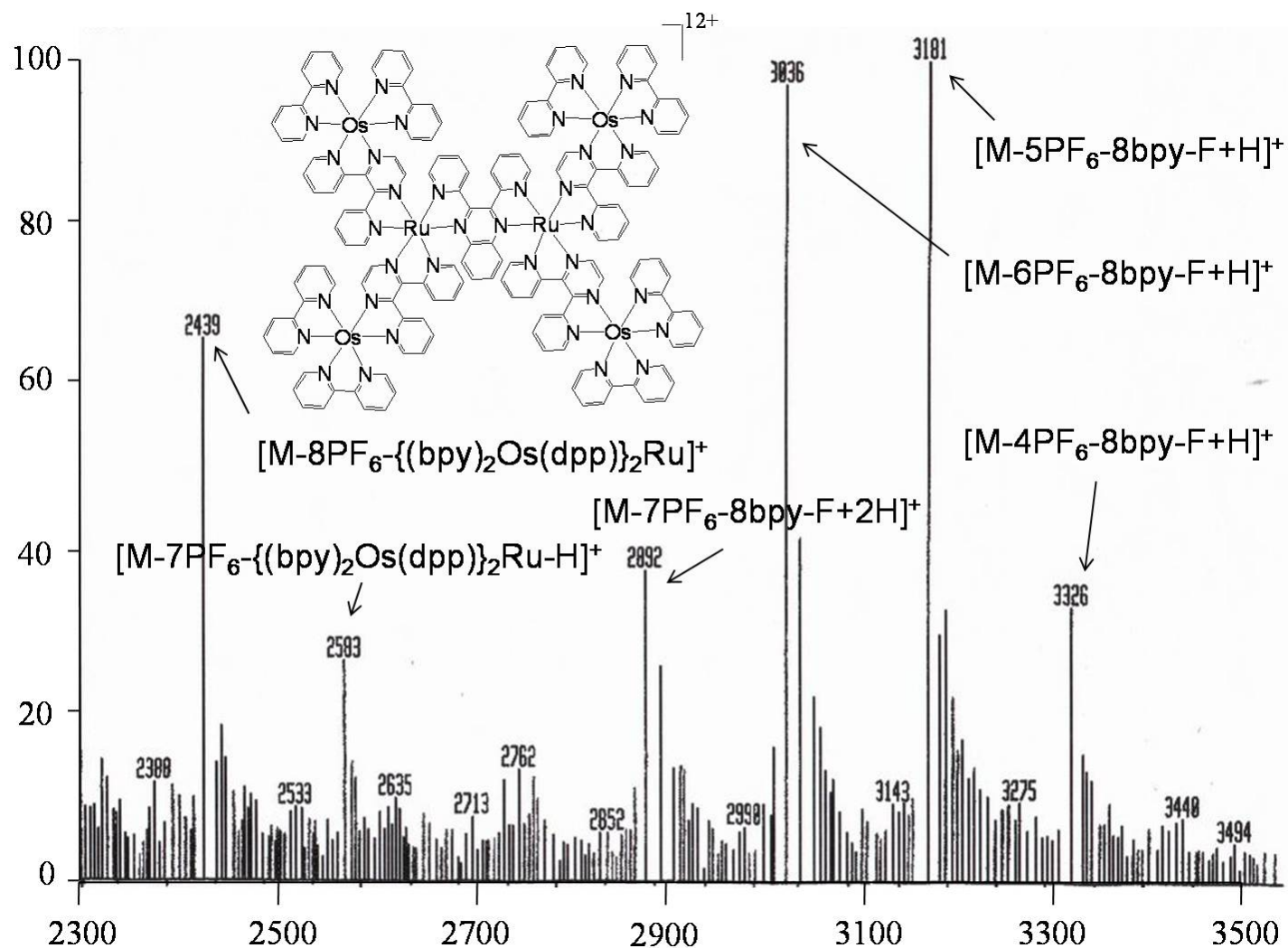


Figure A.15 FAB-MS spectrum of $\{[(bpy)_2Os(dpp)]_2Ru\}_2(dpq)(PF_6)_{12}$ (bpy = 2,2'-bipyridine, dpp = 2,3-bis(2-pyridyl)pyrazine, dpq = 2,3-bis(2-pyridyl)quinoxaline). (FAB-MS = fast-atom-bombardment mass spectrometry. The FAB-MS was performed on a VG Analytical ZAB 2-SE high field mass spectrometer using m-nitrobenzyl alcohol as a matrix).

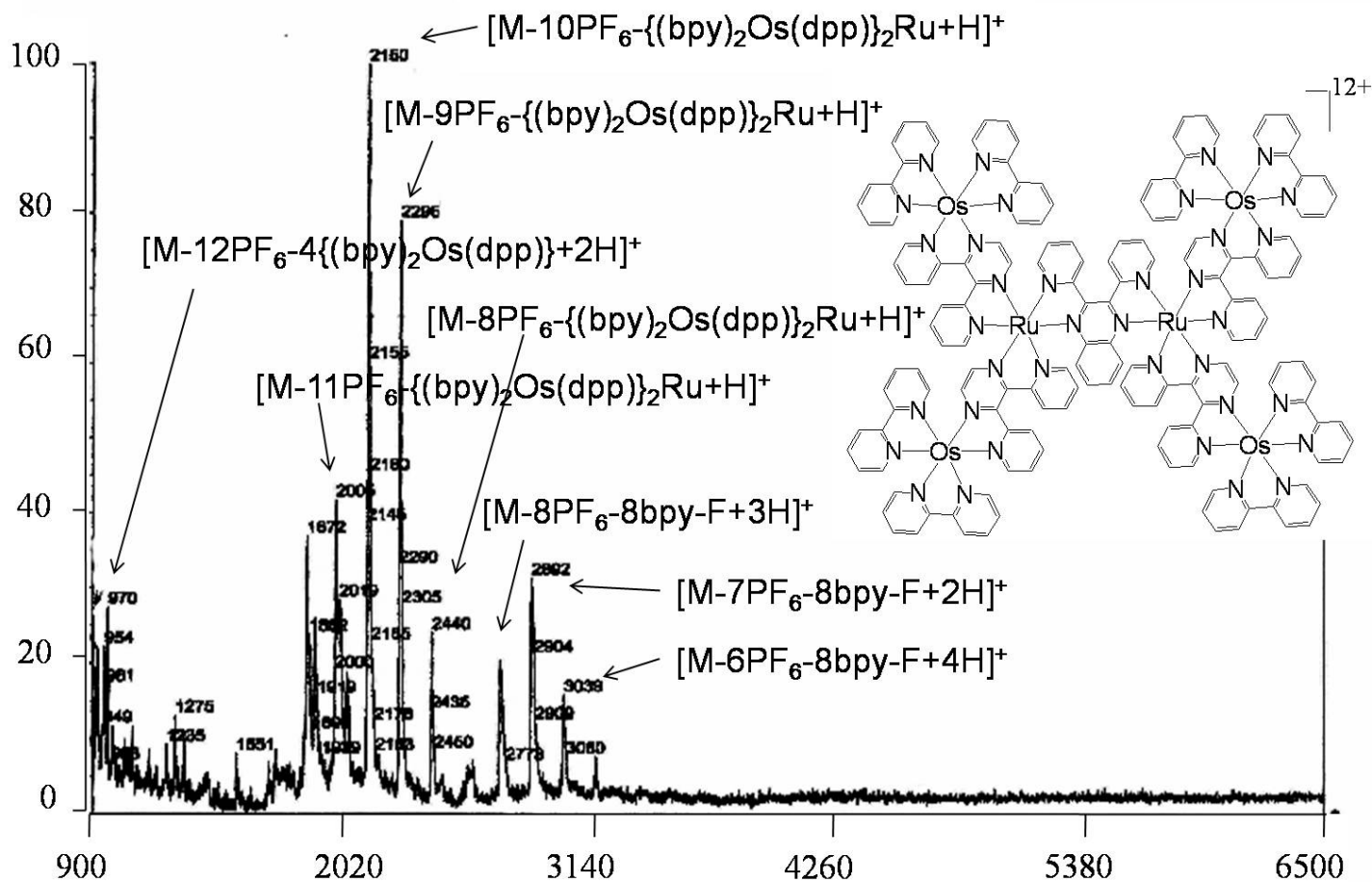


Figure A.16 MALDI-TOF-MS spectrum of $\{[\{(bpy)_2Os(dpp)\}_2Ru]_2(dpq)(PF_6)_{12}\}$ ($bpy = 2,2'$ -bipyridine, $dpp = 2,3$ -bis(2-pyridyl)pyrazine, $dpq = 2,3$ -bis(2-pyridyl)quinoxaline). (MALDI-TOF-MS = matrix-assisted laser desorption/ionization time of flight mass spectrometry. MALDI-TOF MS was performed on an Applied Biosystems Voyager-DE Pro using 2,5-dihydroxybenzoic acid as a matrix and 337 nm as the excitation wavelength).

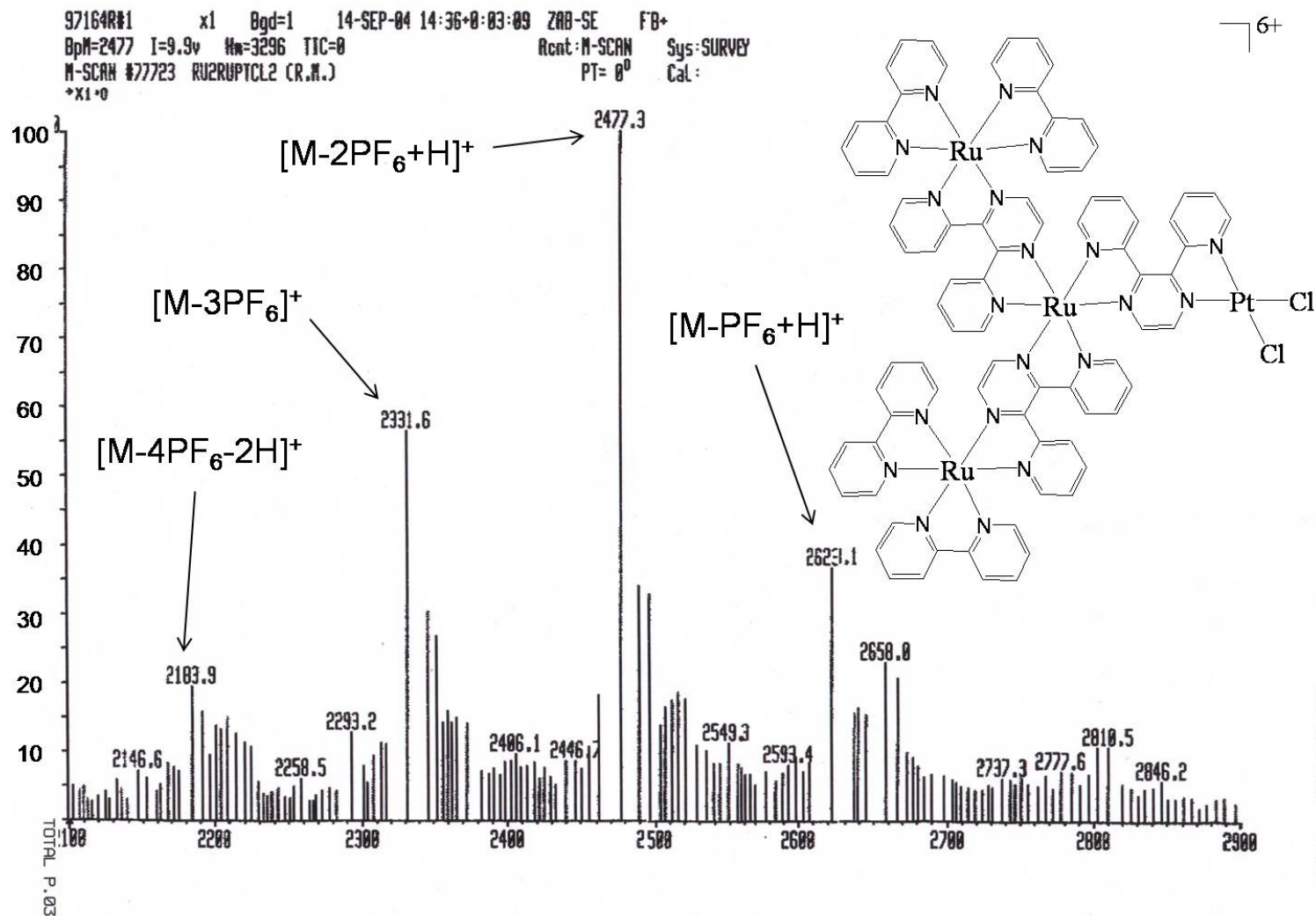


Figure A.17 FAB-MS spectrum of $[\{(bpy)_2Ru(dpp)\}_2Ru(dpp)PtCl_2](PF_6)_6$ ($bpy = 2,2'$ -bipyridine, $dpp = 2,3$ -bis(2-pyridyl)pyrazine). (FAB-MS = fast-atom-bombardment mass spectrometry. The FAB-MS was performed on a VG Analytical ZAB 2-SE high field mass spectrometer using *m*-nitrobenzyl alcohol as a matrix).

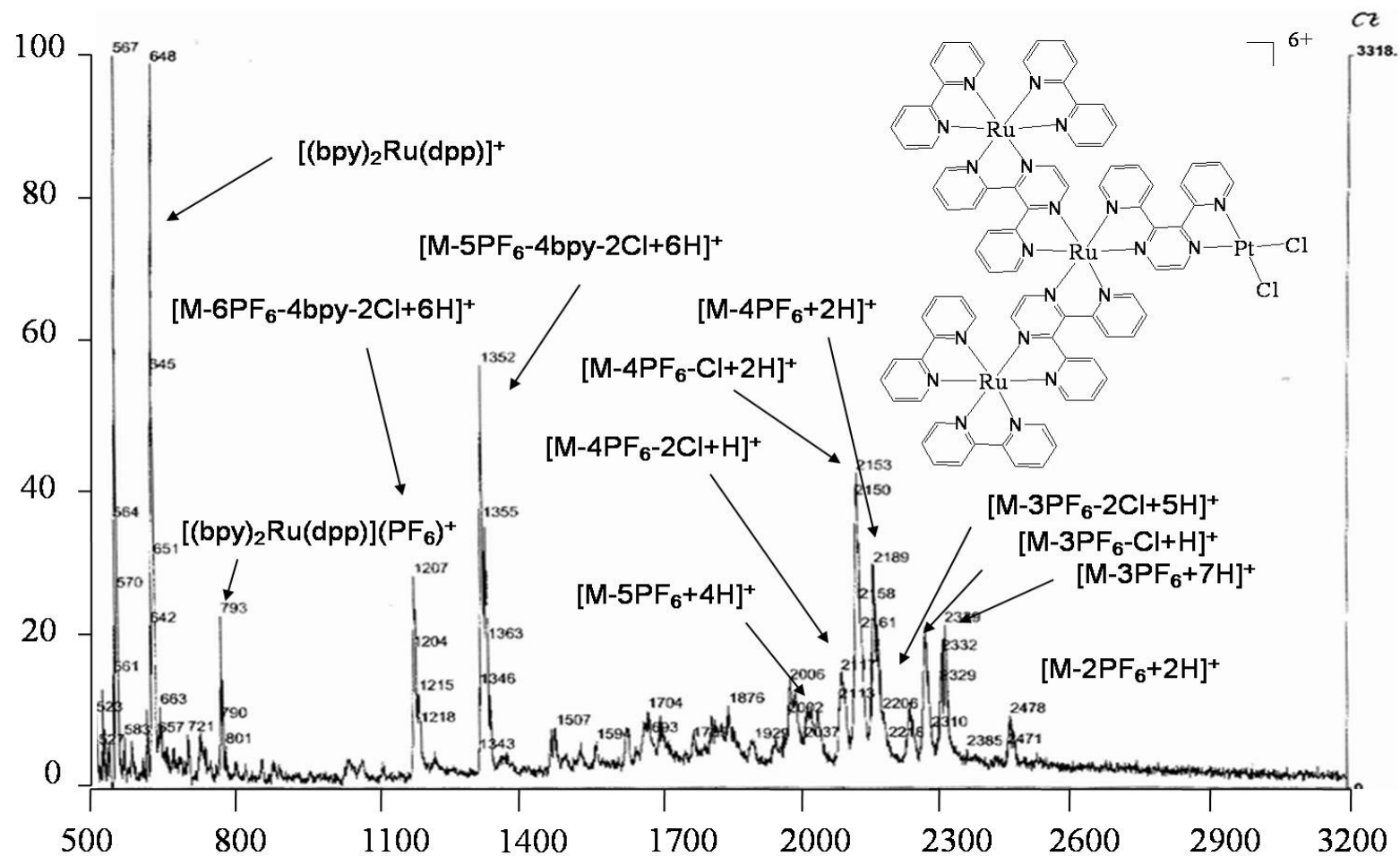


Figure A.18 MALDI-TOF-MS spectrum of $[(bpy)_2Ru(dpp)]_2Ru(dpp)PtCl_2(PF_6)_6$ ($bpy = 2,2'$ -bipyridine, $dpp = 2,3$ -bis(2-pyridyl)pyrazine). (MALDI-TOF-MS = matrix-assisted laser desorption/ionization time of flight mass spectrometry. MALDI-TOF MS was performed on an Applied Biosystems Voyager-DE Pro using 2,5-dihydroxybenzoic acid as a matrix and 337 nm as the excitation wavelength).

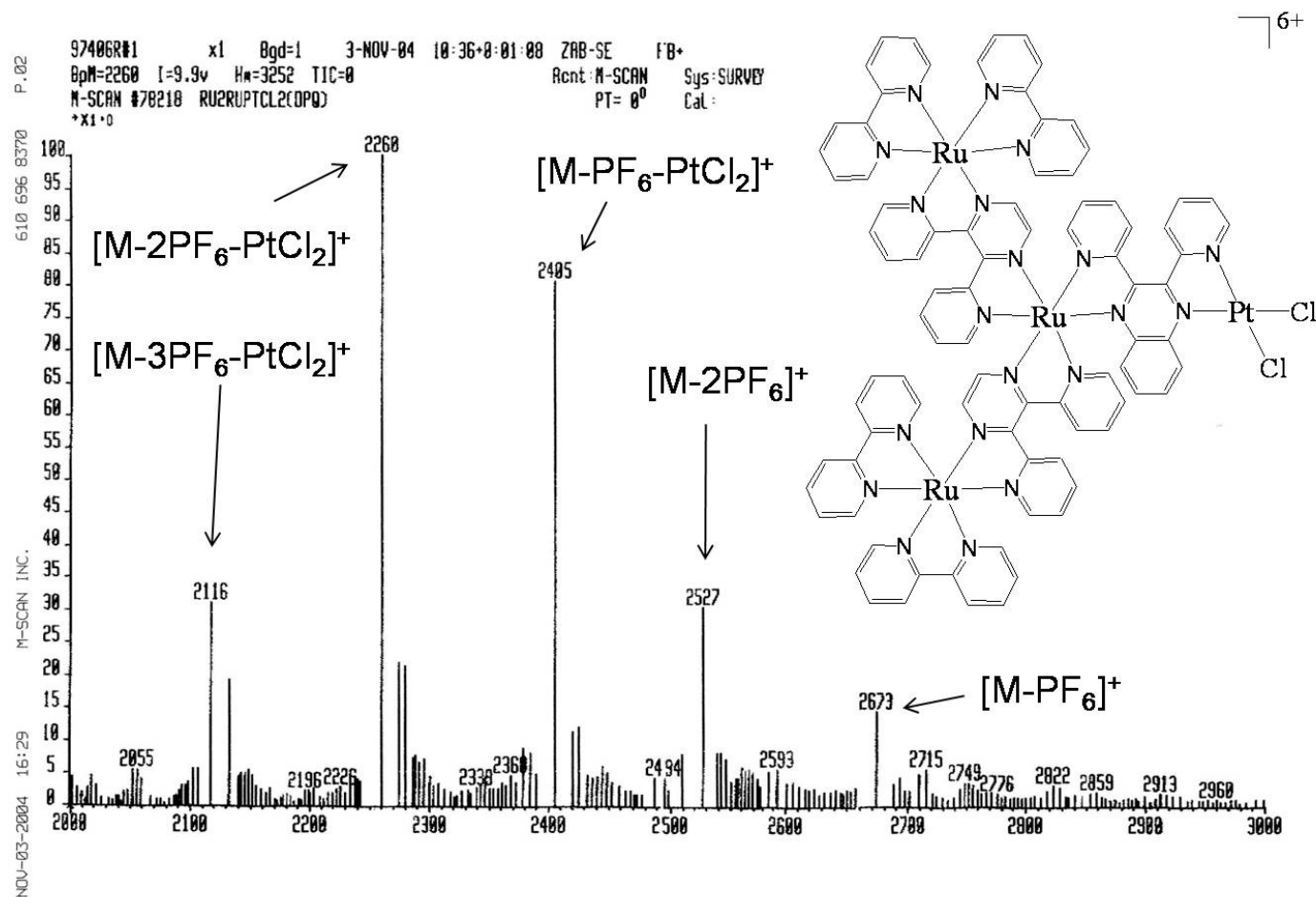


Figure A.19 FAB-MS spectrum of $[\{(bpy)_2Ru(dpp)\}_2Ru(dpq)PtCl_2](PF_6)_6$ (bpy = 2,2'-bipyridine, dpp = 2,3-bis(2-pyridyl)pyrazine, dpq = 2,3-bis(2-pyridyl)quinoxaline). (FAB-MS = fast-atom-bombardment mass spectrometry. The FAB-MS was performed on a VG Analytical ZAB 2-SE high field mass spectrometer using m-nitrobenzyl alcohol as a matrix).

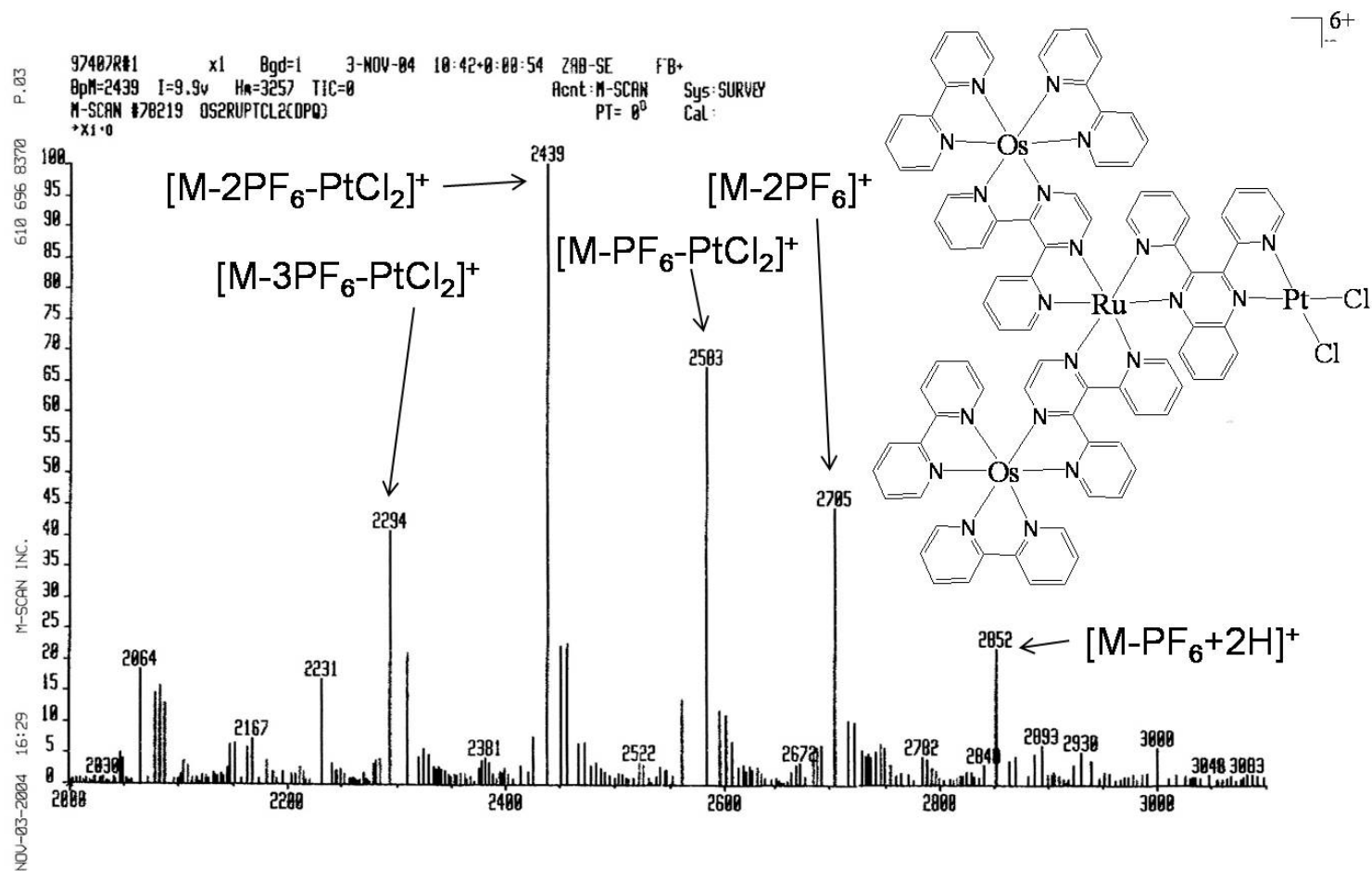


Figure A.20 FAB-MS spectrum of $[(bpy)_2Os(dpp)]_2Ru(dpq)PtCl_2](PF_6)_6$ ($bpy = 2,2'$ -bipyridine, $dpp = 2,3$ -bis(2-pyridyl)pyrazine, $dpq = 2,3$ -bis(2-pyridyl)quinoxaline). (FAB-MS = fast-atom-bombardment mass spectrometry. The FAB-MS was performed on a VG Analytical ZAB 2-SE high field mass spectrometer using *m*-nitrobenzyl alcohol as a matrix).